

A pFFT Accelerated High Order Panel Method

by

David Joe Willis

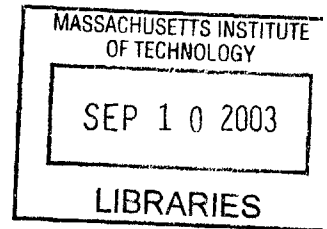
Submitted to the Department of Aeronautics and Astronautics
in partial fulfillment of the requirements for the degree of

Master of Science

at the

MASSACHUSETTS INSTITUTE OF TECHNOLOGY

February 2003



© Massachusetts Institute of Technology 2003. All rights reserved.

Author

Department of Aeronautics and Astronautics
February 1, 2003


Certified by ..


Jaime Peraire
Professor
Thesis Supervisor

Certified by


Jacob K. White
Professor
Thesis Supervisor

Accepted by ...


Edward M. Greitzer
H.N. Slater Professor of Aeronautics and Astronautics Chair,
Committee on Graduate Students

A pFFT Accelerated High Order Panel Method

by

David Joe Willis

Submitted to the Department of Aeronautics and Astronautics
on February 1, 2003, in partial fulfillment of the
requirements for the degree of
Master of Science

Abstract

The theory and development of a precorrected Fast Fourier Transform (pFFT) accelerated, linear strength Panel Method is presented. The traditional approach is presented; however, direct and iterative solution methods are memory intensive and computationally costly. The pFFT algorithm reduces the complexity of the matrix vector product to $O(n \log n)$, while attaining an $O(n)$ memory efficiency. As a result the overall solution scales with $O(kn \log n)$, a significant improvement over $O(n^3)$ and $O(n^2)$ unaccelerated approaches.

The accelerated method shows a distinct improvement over iterative and direct methods. Prior to accelerated methods direct solution methods were limited by memory. Geometries in excess of 3,000-4,000 panels are the upper limit for analyses. The pFFT approach shows a significant improvement, allowing cases with 50,000-100,000 surface panels to be analysed.

A method which computes both constant strength and linear strength panel integrals is presented. An investigation into the relative advantages of higher and lower order methods is performed. The linear strength panel integral approach is found to be slightly more computationally expensive (timewise) than the constant collocation scheme. It is determined that the computation of the three linear basis functions is 50 percent more expensive than computing a single constant strength panel integral. In addition, significant improvement in the simulation accuracy is attained, however, the convergence rate is limited by the flat panel discretization error.

The implemented pFFT accelerated linear strength case is not memory optimal. Several suggestions are presented to facilitate more optimal memory usage. One of which facilitates a memory requirement of about $\frac{1}{2}$ to $\frac{2}{3}$ the memory requirement of the constant case, however is has a resulting overall time penalty.

Thesis Supervisor: Jaime Peraire
Title: Professor

Thesis Supervisor: Jacob K. White
Title: Professor

Acknowledgments

My deepest gratitude to my advisors, Professor Jacob White, and Professor Jaime Peraire. A better Master's project could not have been dreamt up. You were both extremely understanding during a personally tough year. I would also like to thank professor Mark Drela for all of his help with aerodynamics. In addition to my advisors, I would like to thank the Singapore-MIT Alliance for their funding of this project. Working as both a researcher and a teaching assistant has been exceptionally rewarding.

A big thank you to my family for their support and belief in me. I know this may seem like another one of those crazy projects. I would like to thank my Mom and Dad for their belief in me and encouraging me all the way. My sisters, Tasha and Suzie for keeping me balanced. Without such an amazing and supporting family this would not have been possible!

I would like to thank those professors who have imparted knowledge throughout my educational career. A special thanks to Professor Angelo Mingarelli, who brought mathematics to life. Thanks to Professor Steen Sjolander for his introductions to the world of fluid dynamics and aerodynamics. Also, Professors C.L. Tan, and J. Salinas for their encouragement in the world of engineering. I would like to thank Paul Vickers, Ian Morrison, and last but not least Nancy Alford for her attempts to convert me to writing. There are many other teachers and professors that have selflessly imparted knowledge and helped me grow to be the person I am, I can't mention you all here, but thank you.

I would like to thank those who have been around me. I know towards the end of this work, when I came down with mononucleosis I was in need of friends and support. Ivan Skopovi for selflessly helping all the way through this thesis. For providing encouragement to get it done, and providing a solid theoretical sounding board. For all of the things, both work related and non-work related, thank you. Also, to Kayla Riccio. Your discussions on everything other than engineering were what kept me sane much of the time. You provide an invaluable outlet to the real

world outside of the engineering bubble I'm prone to live in. I appreciate all of the support, understanding and encouragement you have provided during this project. Thank you for being there for me.

I would also like to thank both Zhenhai Zhu and Ben Song for making available their constant collocation pFFT++ code and allowing me to modify it to suit my needs. Without it, I would have had a formidable task. I'd like to show my sincere gratitude to Ben Song. His understanding of the code and his willingness to explain the intricacies of C++ to a fledging aerodynamics engineer was priceless. In addition, Carlos Pinto Coehlo, you managed to convince me EMACS running GBD might just be one of the best programs on earth, although the jury is still out on C++.

Last, but not least, those people who had to put up with my antics and mess in the laboratory we call home. My lab mates, Xin Wang, Jay, Annie, Carlos, Dmitri, Xin Hu, Luke, Derek, Junghoon, Ben, Hür, Michal, Luca, Zhenhai, Tom, and Dennis. Also, to Grace, the watchful Grandmother.

Last, but not least, thanks to lil' buddy Willis at the pool.

For those I have neglected, and despite everything have remained a source of support, encouragement and love. This is for all of you. Thank you all for believing.

Contents

1	Introduction	27
1.1	Computational Aerodynamics : A Brief History	28
1.2	Motivation : The Goals of this Work	31
1.2.1	A Brief Overview of What was Done	31
1.2.2	The Use Of Linear Strength Panels	32
1.3	The pFFT Algorithm	32
1.3.1	History of the pFFT Algorithm and its Usage	33
1.4	Aircraft Axes	33
2	Theory : Potential Flow	35
2.1	Introduction : Chapter Overview	35
2.2	The Governing Differential Equations	35
2.2.1	Conservation of Mass : Differential Form	36
2.2.2	Perturbation Expression of the Potential Flow Equation and Associated Boundary Conditions	40
2.2.3	Conservation of Linear Momentum : In Differential Form	41
2.2.4	Postprocessing for Forces and Pressure Coefficients	44
2.3	Lifting Bodies and the Kutta Condition	44
2.3.1	The Fundamentals of Lift [1]	45
2.3.2	Potential Flow Considerations : The Generation of Lift	47
2.4	The Boundary Integral Equations	54
2.4.1	Determining the BIE expression for the <i>evaluation point</i> , \bar{x}' Inside of the Laplace Domain [2],[3]	57

2.4.2	Determining the BIE Expression for the <i>evaluation point</i> , \vec{x}' Outside of the Laplace Domain [2],[3]	59
2.5	Solution Formulations	59
2.6	The Potential Formulation : The Direct BIE Formulation	60
2.7	The Indirect Formulation	63
2.7.1	The Pure Source Case : The Indirect BIE Formulation [4]	65
2.7.2	The Pure Dipole Case : The Indirect BIE Formulation [4]	69
2.8	A Comparison of the Solution Approaches	72
2.9	Chapter Summary	73
3	The Boundary Element Method Implementation	75
3.1	Introduction	75
3.1.1	General Solution Flow Chart	75
3.2	Discrete Solution Procedure	76
3.2.1	The Discrete Equations	77
3.2.2	Discretizing the Surface of the Body	77
3.3	Computing the Panel Integrals	79
3.3.1	(1) Transforming Triangular Panels from (x, y, z) to (ξ, η, z') Coordinates [5]	79
3.3.2	2) Transforming Evaluation Points from (x, y, z) to (ξ, η, z') Co- ordinates [5]	80
3.3.3	(3) Computing the Panel Integrals	80
3.4	Computing the Analytic Panel Integrals	80
3.4.1	Hess and Smith [6]: Analytic Panel Integrals	80
3.4.2	Newman [7]: Analytic Panel Integrals	82
3.5	The Panel Integrals : The Constant Strength Basis Function Equations	83
3.5.1	Constant Strength Double Layer/Doublet Panel Integrals	86
3.5.2	Constant Strength Single Layer Panel Influence Integral	89
3.5.3	The Velocity Formulation Integrals : Constant Strength	90
3.5.4	Constant Double Layer Gradient : Panel Influence Integral	92

3.5.5	Constant Single Layer Gradient Panel Influence Integral [8], [7], [6]	96
3.6	The Linear Strength Basis Function Panel Influence Integral Equations	99
3.6.1	Shape Functions: Linear Shape Functions On Triangular Panels	99
3.6.2	Linear Strength Panel Influence Integral Computation Methodology	101
3.6.3	Linear Shape Function Computation Methods	102
3.6.4	Linear Strength Double Layer, and Single Layer Panel Influence Integrals	104
3.7	Analytic Expressions of the Linear Panel Influence Integrals	105
3.7.1	Integral Simplification	105
3.7.2	Linear Variation Double Layer Panel Influence Integral Expression	106
3.7.3	Linear Variation for the Single Layer Panel Influence Integral .	111
3.7.4	Computing the Linear Velocity Influence Integrals	111
3.7.5	The Gradient Equations for the Linear Double Layer Equations	115
3.7.6	Single Layer Gradient Equations	121
3.7.7	Comparing the Linear and Constant Strength Panel Integrals	126
3.7.8	Conclusion of Analytical Panel Influence Integrals	126
3.8	Matrix of Influence Coefficients and the Direct Solution	133
3.8.1	Matrix of Influence coefficients-Galerkin vs. Collocation	133
3.8.2	Setting Up the Linear System for Constant Strength Panels .	135
3.8.3	Setting Up the Linear System : Linear Strength Galerkin Approach	137
3.9	The Lifting Cases : Including the Wakes	139
3.10	Conclusion: Discretization of the Boundary Integral Equations	141
4	Acceleration Via a precorrected Fast Fourier Transform Method – pFFT	143
4.1	Introduction to Faster Methods	143

4.1.1	Iterative methods	143
4.2	Fast Algorithms	144
4.2.1	Introduction to current pFFT Method, pFFT++ implementa- tion [9]	145
4.3	The pFFT Algorithm	145
4.3.1	Overview of the Components of the pFFT Fast Matrix Vector Product	146
4.4	Linear pFFT : Modifications to the Constant pFFT Method	149
4.4.1	Intuitive approach : Tent-to-Tent Interactions	149
4.4.2	pFFT++ Approach: Panel-to-Panel Interactions	150
4.5	The Modifications to the Implementation	153
4.5.1	Projection : The Theory and Linear Panels	153
4.5.2	Fast Fourier Transform	157
4.5.3	Grid-to-Panel Interpolation [10]	157
4.5.4	Direct Terms and Pre-Correction	159
4.5.5	Implementation Generalizations	160
4.5.6	Lifting Case : pFFT Implementation of the Kutta Condition .	161
4.6	The Flow Chart for the pFFTflow Implementation	161
4.7	Conclusions	161
5	Solution Results and Examples	165
5.1	The Direct Method : Validation Through Spheres	165
5.1.1	Analytical Solution for a Sphere	165
5.1.2	Results for the Spheres	166
5.1.3	Boundary Condition Implementation	168
5.2	The pFFT-GMRES Accelerated Case : <i>Potential Formulation</i> . . .	169
5.2.1	Validation Results	169
5.2.2	Aeronautical Engineering Applications : Non-Lifting Bodies .	173
5.2.3	Aeronautical Engineering Applications : Lifting Body examples	173
5.3	pFFT Implementation Time Considerations, and Memory Requirements	176

5.3.1	Time Requirements	179
5.3.2	Discussion of Time Requirements	179
5.3.3	Memory Requirements	181
5.4	Discussion of Results	182
6	Conclusions and Recommendations	183
6.1	Conclusions Based on Results from the Computer Code	183
6.2	Recommendations Based on Results and Current Code Status	184
6.3	Overall Recommendations	185
A	Transform the panel	187
B	Test Spheres	189

List of Figures

1-1	An F-18 outlining the coordinate system convention for the problem. In addition various other defined properties are presented.	34
2-1	The flowfield under consideration. The body is considered to be stationary with a forced freestream flow around it. This is the total flowfield reference frame	36
2-2	The rotational and irrotational flow zones in the domain. Notice, that the scale of the boundary layer is exaggerated. There is significant magnification of the boundary layer	38
2-3	The perturbation flowfield. The perturbation form of the governing equations considers a reference frame in which the body is moving, and the flowfield is stationary	39
2-4	Circulation combined with the free stream and body effects causes an appropriate lifting body flow field.	45
2-5	The physical manifestation of circulation and vorticity. The boundary layer "induces" vorticity in the flow, and as a result of a non-zero integral of the boundary layer vorticity, the net circulation around the body is non-zero, and hence produces lift.	46
2-6	The pressure matching at the upper and lower surfaces produces a flow which leaves the trailing edge of the lifting body smoothly.	47
2-7	The introduction of a cut into the domain to account for the vorticity shed into the wake. The wake is later modeled as a single sheet of infinitesimal thickness.	48

2-8 The two types of trailing edge flows. For a finite angle trailing edge a stagnation point results. In the cusped airfoil case, the upper and lower velocities are non-zero, and the flow is parallel to the trailing edge mean angle. 49

2-9 The schematic description of a wing as seen from above. Notice the linearization involves the equality of the upper and lower perpendicular velocities. 50

2-10 The flow at the trailing edge. The main velocity is in the local-freestream approximated direction, while the velocities in the directions perpendicular to that are assumed to be negligibly small 51

2-11 The linearized Kutta condition at the trailing edge. The wake potential is presented as a single sheet with a potential jump, ϕ_w due to the assumption that the wake is of infinitesimal thickness 53

2-12 The representation of the fundamental solution of the 3-Dimensional Laplaces Equation. An impulse is applied at \vec{x} , and the solution is evaluated at \vec{x}' 55

2-13 The domain under consideration. Here V is the volume of the domain, while S is the boundary of the domain, including the wake, the body, and the outer boundary, $S = S_W + S_B + S_\infty$ 57

2-14 The flow thickness effect is modeled with a source singularity on the surface. This will mimic a doublet in the farfield, hence, there will be a $\frac{1}{|\vec{x}|^2}$ potential decay. 62

2-15 The Green's Theorem representation. The single layer mimics the body thickness by applying the body boundary condition, while the dipole layer augments the solution to provide lift and the potential result. . . 62

2-16 The external potential equation, expresses the computed potential at a point \vec{x}' in the domain for the external potential problem. 63

2-17 The internal potential equation, expresses the computed potential at a point \vec{x}' in the domain for the internal potential problem. 64

2-18	The flow modeled with a source singularity on the surface, will mimic a doublet in the farfield, hence have $\frac{1}{x^2}$ potential decay.	69
2-19	The flow modeled with a doublet singularity on the surface, will mimic a doublet in the farfield, hence have $\frac{1}{ \vec{x} ^2}$ potential decay.	72
3-1	General Flow Chart of the solution, and chapter overview.	76
3-2	The coordinate transform. Here the triangle in x, y, z is transformed to an in-plane, ξ, η, z' representation.	79
3-3	Pictorial representation of the perimeter integral for a side of the triangle	81
3-4	Adding and subtracting the various perimeter integrals to attain the final panel integral result.	82
3-5	The Hess and Smith method is most accurate in the "near-in-plane" region of the space. The shaded grey wedge shaped regions outline the areas in which the integration method is most accurate.	82
3-6	A panel projected onto a unit sphere. The included angles and distortion of the panel is apparent in the inset diagram of the panel.	83
3-7	The area in which the Newman integration method is most appropriate. Contrary to the Hess and Smith method, Newman's method is most accurate in the regions directly above and below the panel.	84
3-8	The constant strength shape function used in the computations	84
3-9	A triangle outlining the notation for the panel integrals in the sections that follow. Notice the labeling of the vertices with respect to the ξ, η axes, since the computations for the linear shape functions rely heavily on the ordering.	85
3-10	A 3-D potential plot for a double layer sample panel with vertices $[V1(0, 2, 0), V2(1, -1, 0), V3(-1, -1, 0)]$, evaluated in the plane $z' = +\epsilon$	88
3-11	A 2-D potential plot for a double layer sample panel with vertices $[V1(0, 2, 0), V2(1, -1, 0), V3(-1, -1, 0)]$, evaluated in the plane $z' = +\epsilon$	88

3-12	A 2-D potential plot for a double layer sample panel with vertices $[V1(0, 2, 0), V2(1, -1, 0), V3(-1, -1, 0)]$, evaluated in the plane $\eta = 0$.	89
3-13	A 3-D potential mesh plot for a single layer constant sample panel integral with vertices $[V1(0, 2, 0), V2(1, -1, 0), V3(-1, -1, 0)]$, evaluated in the plane $z' = +\epsilon$.	91
3-14	A 2-D potential plot for a single layer constant sample panel integral with vertices $[V1(0, 2, 0), V2(1, -1, 0), V3(-1, -1, 0)]$, evaluated in the plane $z' = 0$.	91
3-15	A 2-D potential plot for a sample panel $[V1(0, 2, 0), V2(1, -1, 0), V3(-1, -1, 0)]$, evaluated in the plane $\eta = 0$.	92
3-16	A 2-D velocity vector plot for a double layer sample panel $[V1(0, 2, 0), V2(1, -1, 0), V3(-1, -1, 0)]$, evaluated in the plane $\eta = 0$. The solution is actually symmetric about $\xi = 0$, despite the figure showing a possible asymmetry. The apparent asymmetry is due to the evaluation scan points being modified to exclude the panel edge singularities.	96
3-17	A 2-D velocity vector plot for a double layer sample panel with vertices $[V1(0, 2, 0), V2(1, -1, 0), V3(-1, -1, 0)]$, evaluated in the plane $\xi = 0$.	97
3-18	A 2-D velocity vector plot for a single layer sample panel with vertices $[V1(0, 2, 0), V2(1, -1, 0), V3(-1, -1, 0)]$, evaluated in the plane $z' = +\epsilon$.	98
3-19	A 2-D velocity vector plot for a single layer sample panel with vertices $[V1(0, 2, 0), V2(1, -1, 0), V3(-1, -1, 0)]$, evaluated in the plane $\eta = 0$.	98
3-20	A 2-D velocity vector plot for a single layer sample panel with vertices $[V1(0, 2, 0), V2(1, -1, 0), V3(-1, -1, 0)]$, evaluated in the plane $\xi = 0$.	99
3-21	The 3-Nodal based shape functions for the linear strength panel influence integrals. Notice, these shape functions are identical to those used in FEM approaches	100
3-22	The shape function footprint for the linear basis. The footprint represents the influence one shape function has on other neighboring shape functions	100

3-23	The rotation method: computing the linear shape function panel influence integrals through rotating the panel being computed.	102
3-24	A description of the computation of the orthogonal $\langle N1, N2, N3 \rangle$ shape function set, from the $\langle \xi, \eta, const \rangle$, basis function set. . . .	103
3-25	The 3-D SF1 potential scan for the double layer linear panel influence integral, for the panel $[V1(0, 2, 0), V2(1, -1, 0), V3(-1, -1, 0)]$, evaluated in the plane $z' = +\epsilon$	108
3-26	Potential scan for the SF2 double layer linear panel influence integral, for the panel $[V1(0, 2, 0), V2(1, -1, 0), V3(-1, -1, 0)]$, evaluated in the plane $z' = +\epsilon$	109
3-27	The 3-D potential scan for the SF2 double layer linear panel influence integral, for the panel $[V1(0, 2, 0), V2(1, -1, 0), V3(-1, -1, 0)]$, evaluated in the plane $z' = +\epsilon$	109
3-28	Potential scan for the SF3 double layer linear panel influence integral, for the panel $[V1(0, 2, 0), V2(1, -1, 0), V3(-1, -1, 0)]$, evaluated in the plane $z' = +\epsilon$	110
3-29	The 3-D potential scan for the SF3 double layer linear panel influence integral, for the panel $[V1(0, 2, 0), V2(1, -1, 0), V3(-1, -1, 0)]$, evaluated in the plane $z' = +\epsilon$	110
3-30	The potential scan for the SF1 single layer linear panel influence integral, for the panel $[V1(0, 2, 0), V2(1, -1, 0), V3(-1, -1, 0)]$, evaluated in the plane $z' = +\epsilon$	112
3-31	The 3-D potential scan for the SF1 single layer linear panel influence integral, for the panel $[V1(0, 2, 0), V2(1, -1, 0), V3(-1, -1, 0)]$, evaluated in the plane $z' = +\epsilon$	112
3-32	The potential scan for the SF2 single layer linear panel influence integral, for the panel $[V1(0, 2, 0), V2(1, -1, 0), V3(-1, -1, 0)]$, evaluated in the plane $z' = +\epsilon$	113

3-33	The 3-D potential scan for the SF2 single layer linear panel influence integral, for the panel $[V1(0, 2, 0), V2(1, -1, 0), V3(-1, -1, 0)]$, evaluated in the plane $z' = +\epsilon$	113
3-34	The potential scan for the SF3 single layer linear panel influence integral, for the panel $[V1(0, 2, 0), V2(1, -1, 0), V3(-1, -1, 0)]$, evaluated in the plane $z' = +\epsilon$	114
3-35	The 3-D potential scan for the SF3 single layer linear panel influence integral, for the panel $[V1(0, 2, 0), V2(1, -1, 0), V3(-1, -1, 0)]$, evaluated in the plane $z' = +\epsilon$	114
3-36	A 2-D velocity vector plot for a double layer sample panel with vertices $[V1(0, 2, 0), V2(1, -1, 0), V3(-1, -1, 0)]$, evaluated in the plane $\eta = 0$	118
3-37	A 2-D velocity vector plot for a double layer sample panel $[V1(0, 2, 0), V2(1, -1, 0), V3(-1, -1, 0)]$, evaluated in the plane $\xi = 0$	118
3-38	A 2-D velocity vector plot for a double layer sample panel $[V1(0, 2, 0), V2(1, -1, 0), V3(-1, -1, 0)]$, evaluated in the plane $\eta = 0$	119
3-39	A 2-D velocity vector plot for a double layer sample panel $[V1(0, 2, 0), V2(1, -1, 0), V3(-1, -1, 0)]$, evaluated in the plane $\xi = 0$	119
3-40	A 2-D velocity vector plot for a double layer sample panel $[V1(0, 2, 0), V2(1, -1, 0), V3(-1, -1, 0)]$, evaluated in the plane $\eta = 0$	120
3-41	A 2-D velocity vector plot for a double layer sample panel $[V1(0, 2, 0), V2(1, -1, 0), V3(-1, -1, 0)]$, evaluated in the plane $\xi = 0$	120
3-42	A 2-D velocity vector plot for a sample linear single layer panel influence integral, for the panel $[V1(0, 2, 0), V2(1, -1, 0), V3(-1, -1, 0)]$, evaluated in the plane $z' = +\epsilon$	125
3-43	A 2-D velocity vector plot for a sample linear single layer panel influence integral, for the panel $[V1(0, 2, 0), V2(1, -1, 0), V3(-1, -1, 0)]$, evaluated in the plane $\eta = 0$	125
3-44	A 2-D velocity vector plot for a sample linear single layer panel influence integral, for the panel $[V1(0, 2, 0), V2(1, -1, 0), V3(-1, -1, 0)]$, evaluated in the plane $\xi = 0$	126

3-45	A 2-D velocity vector plot for a sample linear single layer panel influence integral, for the panel $[V1(0, 2, 0), V2(1, -1, 0), V3(-1, -1, 0)]$, evaluated in the plane $z' = +\epsilon$	127
3-46	A 2-D velocity vector plot for a sample linear single layer panel influence integral, for the panel $[V1(0, 2, 0), V2(1, -1, 0), V3(-1, -1, 0)]$, evaluated in the plane $\eta = 0$	127
3-47	A 2-D velocity vector plot for a sample linear single layer panel influence integral, for the panel $[V1(0, 2, 0), V2(1, -1, 0), V3(-1, -1, 0)]$, evaluated in the plane $\xi = 0$	128
3-48	A 2-D velocity vector plot for a sample linear single layer panel influence integral, for the panel $[V1(0, 2, 0), V2(1, -1, 0), V3(-1, -1, 0)]$, evaluated in the plane $z' = +\epsilon$	128
3-49	A 2-D velocity vector plot for a sample linear single layer panel influence integral, for the panel $[V1(0, 2, 0), V2(1, -1, 0), V3(-1, -1, 0)]$, evaluated in the plane $\eta = 0$	129
3-50	A 2-D velocity vector plot for a sample linear single layer panel influence integral, for the panel $[V1(0, 2, 0), V2(1, -1, 0), V3(-1, -1, 0)]$, evaluated in the plane $\xi = 0$	129
3-51	The single layer potential evaluated along the line $z' = \epsilon, \xi = 0$	130
3-52	The single layer potential evaluated along the line $z' = \epsilon, \eta = 0$	130
3-53	The double layer potential evaluated along the line $z' = \epsilon, \xi = 0$. . .	131
3-54	The double layer potential evaluated along the line $z' = 0.5, \xi = 0$. . .	131
3-55	The double layer potential evaluated along the line $z' = \epsilon, \eta = 0$. . .	132
3-56	The double layer potential evaluated along the line $z' = 0.5, \eta = 0$. . .	132
3-57	The collocation approach for constant strength shape functions. . . .	134
3-58	The Galerkin approach for linear strength shape functions, φ_S^G to the left and ζ_T^G . Here the Gauss quadrature integration points are apparent.	136
3-59	The pictorial description of the wake. The three trailing edge vertices are coincident in space, however, they are 3 distinct individual vertices as shown.	139

3-60	A high aspect ratio wing, with a trailing discretized wake. Note, the panel distribution, and panel aspect ratio is not optimal in this example, due to the net-like construction of the case	140
4-1	Basic flow chart of iterative methods.	144
4-2	pFFT++ algorithm flow chart.	145
4-3	The uniform FFT grid is overlayed on top of the geometry.	146
4-4	The panel charges are projected onto the uniform grid via a polynomial interpolation.	146
4-5	A FFT computes the convolution integral of the $\frac{1}{r}$ type integrals. This computes the grid potentials as a result of the prescribed grid charges.	147
4-6	The grid potentials resulting from the FFT are interpolated back onto the panels.	147
4-7	The nearby influences are computed directly and a correction is made to eliminate the influences of the grid-to-grid approximation of the nearby influences computed in the FFT approximation section.	148
4-8	The point charge is projected onto the uniform grid.	154
4-9	The Gaussian quadrature point charges are projected onto the uniform grid. Combined with the shape function b_j effect, the panel integration is computed discretely for the projection.	156
4-10	The pFFT, Fast Fourier Transform convolution.	157
4-11	The Grid potential is interpolated to a point in the domain.	158
4-12	The flow chart for the pFFT algorithm.	162
5-1	The computed direct result for the 48 panel sphere, using both Neumann and Dirichlet approaches.	166
5-2	The computed direct result for the 192 panel sphere, using both Neumann and Dirichlet approaches.	167
5-3	The computed direct result for the 768 panel sphere, using both Neumann and Dirichlet approaches.	167

5-4	The analytical error computed in the L_2 norm. The Linear result is shown for both a Code-Computed normal (less accurate at nodes), and the analytical surface integral at the vertex points (more accurate).	171
5-5	A display of the integrated error for the test Spheres. An attempt was made to extract some of the discretization area convergence effect from the computation. The plot shows preliminary results.	172
5-6	The pressure coefficient distribution for the NACA 0012 symmetric airfoil profile high aspect ratio wing at a 0° angle of attack. The result is compared with the 2-Dimensional result from XFOIL [11]	174
5-7	The discretization of a NACA 2412 profile high aspect ratio wing with a trailing wake	176
5-8	The Pressure coefficient for the 2-D XFOIL [11] case compared with the 3D Panel Method Case for $\alpha = 0^\circ$	177
5-9	The Pressure coefficient for the 2-D XFOIL [11] case compared with the 3D Panel Method Case for $\alpha = 2^\circ$	177
5-10	The Pressure coefficient for the 2-D XFOIL [11] case compared with the 3D Panel Method Case for $\alpha = 4^\circ$	178
5-11	The Pressure coefficient for the 2-D XFOIL [11] case compared with the 3D Panel Method Case for $\alpha = 6^\circ$	178
5-12	The solution time for the pFFT Approach compared with the direct solution approach. Notice the pFFT algorithm scales Like $O(n \log(n))$ here.	179
5-13	The time components of the linear solution for the spheres.	180
5-14	The plot of the projected memory requirements for the linear and constant pFFT method compared with the actual memory requirements for the direct method.	181
A-1	The coordinate transform. Here the triangle in x, y, z is transformed to an in-plane, ξ, η, z' representation.	187
B-1	The discretization of the 48 panel sphere	190

B-2	The discretization of the 192 panel sphere	191
B-3	The discretization of the 768 panel sphere	192
B-4	The discretization of the 3072 panel sphere	193
B-5	The discretization of the 6912 panel sphere	194
B-6	The discretization of the 10800 panel sphere	195

List of Tables

1.1	The Flow variables, and geometric data for the flow simulation	34
5.1	A comparison between the number of vertices and number of panels for the test sphere data	170
5.2	The information for the NACA 2412 geometry discretization	175

Chapter 1

Introduction

Oh I have slipped the surly bonds of earth
And danced the skies on laughter-silvered wings;
Sunward I've climbed, and joined the tumbling mirth
Of sun-split clouds... and done a hundred things
you have not dreamed of... wheeled and soared and swung
High in the sunlit silence. Hov'ring there.
I've chased the shouting wind along, and flung
my eager craft through footless halls of air.
Up, up the long, delirious, burning blue
I've topped the windswept heights with easy grace
Where never lark, or even eagle flew.
And, while with silent, lifting mind I've trod
the high untrespassed sanctity of space...
put out my hand, and touched the face of God!

John Gillespie Magee

1.1 Computational Aerodynamics : A Brief History

Flight. Humankind has obsessed about flight for millenia. Mimicking the elegant grace of birds has been the focus of billions of intellect hours, and trillions of dollars. From Daedalus to Kelly Johnson, from Leonardo Da Vinci to The Wright Brothers, many ideas have been conceived, developed and tested. Flight was something humankind could imagine, dream and materialize. It wasn't until the 1943, with ENIAC (Electronic Numerical Integrator), the first general purpose electrical computer, could humankind begin dreaming of a virtual wind tunnel. This advancement was not foreseeable. The coupling of aeronautical concepts of many dreamers with this century's most powerful invention – the computer – resulted in a plethora of tools that weren't even the slightest figment in the minds of many of the aeronautical pioneers. The continued development of computational tools for analysis and design of aircraft continues to provide our modern dreamers with methods to design faster, sleeker, more efficient aircraft than ever before.

Computational aerodynamics began to take form in the early 1960's. Analysis to that point was either being done experimentally in wind tunnels, or theoretically using singularity superposition methods. During the 1960's, Hess and Smith [12], two research scientists at Douglas Aircraft Company developed what is now known in the aerodynamics community as the *panel method*. Initially developed as a method to determine the potential flow properties around bodies of revolution, such as fuselages, Hess and Smith realized that the method could be extended to encapsulate both non-lifting and lifting bodies [6]. Furthermore, the method in which they participated was not exclusive to aerodynamics. Infact, it is applicable to many diverse engineering disciplines. More commonly known, in the mathematical and engineering community as the Boundary Element Method (BEM), this method has formed a niche for efficiently solving many common physical problems.

Hess and Smith finished their initial work at Douglas Aircraft Company, finding that they had enabled a computationally efficient approach to computing the aerody-

namics of aircraft. Their method was the Douglas Neumann Code [12], appropriately named due to the implementation of Neumann boundary conditions. The method was the first breakthrough in the Computational Aerodynamics world.

Not wanting to be eclipsed by technology, several other aircraft companies started development of similar methods. Some of the more well known codes that are still in existence are:

- **QUADPAN** (Quadrilateral Panel Aerodynamics Program)[13] : The QUAD-PAN code was a low order method for computing the potential flow using quadrilateral panel discretizations of the geometry.

- **VSAERO** and **USAERO** (Vortex Separation Aerodynamics Program) [14] : Similar to QUADPAN, the VSAERO and USAERO codes are low order panel methods. These codes were commercialized and are still in use today.

- **PANAIR** [15], otherwise known as A502: A High Order 3-Dimensional Panel Method developed by Boeing with additional support from NASA. PANAIR is still used for preliminary design studies at Boeing. PANAIR uses a potential approach implementing a high order quadratic strength double layer, with a constant strength single layer. The panel formulation is novel in that a quadrilateral panel is subdivided into triangular panels in order to facilitate the higher order doublet distribution. PANAIR was the state of the art panel method for much of the 1980s and 1990s.

- **PMARC/CMARC** (Panel Method Ames Research Center/The commercial version is CMARC) [16]: PMARC was developed in the late 1980's as an efficient low order panel method. With continued development, PMARC has incorporated a large array of additional analyses, such as boundary layer corrections, compressibility corrections and quasi-unsteady analyses.

Many of the above codes vary from the original Neumann implementation presented by Hess and Smith, since they use the Green's Theorem Potential approach. In addition during that period, several other panel methods were investigated, as found in [17] and [18].

Once PANAIR and PMARC were developed, there was a lull in Panel Methods. This lull was primarily due to the limitations of computer speed and memory, as well

as the relative maturity of the research area. With the direct method implementation, the solution of the dense system that resulted from early implementations of the BEM approach cost $O(n^3)$ in time and $O(n^2)$ in memory. Furthermore, to compute all of the entries in the dense matrix an expensive $O(n^2)$ process was required. Due to these limitations early panel methods could only compute very simple geometric flow problems. The number of panels in early panel method cases rarely exceeded 1,000-2,000 panels [19].

A revival of panel methods in the engineering community occurred with the development of iterative methods [19]. Iterative methods allowed more complex cases to be considered. In addition, research in computational aerodynamics had altered focus from developing the solution methods, to actually improving the linear potential flow analysis through corrections. Corrections include the development of compressibility corrections [20], for both two- and three- dimensional problems. Additionally, corrections for viscous effects were also investigated [21], [22].

In the early 1990s, Rohklin [23] and Greengard [24] published their work introducing Fast Multipole Methods. Within the hierarchical Fast Multipole Method, Rohklin and Greengard had developed an $O(n \log n)$ solution algorithm. The implementation of the FMM in a three-dimensional boundary element method was first performed by Nabors and White in FastCAP [25]. This rejuvenated the interest in panel methods. Several research groups, and companies have now developed $O(n \log n)$ approaches to the panel method implementing the FMM approach, such as the HISSS method [26], and others [27], and [28]. The FMM approach facilitates fast implementations of the panel method enabling analysis of cases with up to a million panels [28].

This thesis presents the acceleration of the panel method by the precorrected Fast Fourier Transform (pFFT) method. The algorithm originally developed by Philips and White [29], in the mid 1990s, displays significant advantages over the Fast Multipole Algorithm for several geometrical cases. The advantages of the pFFT over the FMM acceleration are observed in terms of memory efficiency and computational time for situations where the solution accuracy is limited to Engineering requirements. For higher accuracy than traditional engineering applications, the FMM is more compu-

tationally efficient than the pFFT. The current work represents a state of the art in panel methods. In addition, the development of a linear strength pFFT accelerated panel method marks the first implementation of the pFFT algorithm in computational aerodynamics, and also marks the first extension of the pFFT algorithm to a linear basis Galerkin algorithm.

1.2 Motivation : The Goals of this Work

The goals of this work are to deliver a near real time method of solving the 3-Dimensional potential flow problem. This is done using a Boundary Element Method approach, with linear basis panel strengths. The acceleration to a near-real time solver is attained through the use of the pFFT algorithm.

The work is intended to provide an efficient tool for aerodynamicists. Coupled with an optimization code it should provide a method for optimizing aircraft geometries efficiently and accurately in the early design stages. A preliminary goal is to enable 100,000 panel simulations in under an hour on a scientific workstation.

Furthermore, with linear basis panel strengths the addition of some of the common corrections in panel methods are facilitated. Corrections such as the viscous boundary layer effects are easily implemented due to the simple extraction of the velocities associated with each of the panels.

The development of a generalized code including both constant strength and linear strength panels is presented. This is done in order to provide the user with a code which is multifaceted, while also allowing a comparison between the relative merits of the methods.

1.2.1 A Brief Overview of What was Done

The direct solution method for both the velocity formulation and the potential formulation was tested for both linear and constant strength methods. Following that, an acceleration via the GMRES iterative method combined with the pFFT algorithm was performed for the potential based linear and constant basis function approaches.

1.2.2 The Use Of Linear Strength Panels

In order to justify the additional complexity of linear strength panels a brief discussion of the proposed benefits of linear strength basis functions is presented. Determining the validity of these statements is the purpose of some of this research.

Advantages

The advantages of the linear strength basis functions:

- 1) Linear strength panels should provide a more accurate representation of the solution distribution.
- 2) Implementing a Galerkin approach should provide a more accurate solution.
- 3) The gradients of the panel potential (the velocity) are easily computed.

Disadvantages

The disadvantages of the linear strength basis functions are:

- 1) The computation of the direct linear strength panel integrals will be more expensive.
- 2) The Galerkin approach adds a factor of complexity corresponding to the order of the number of quadrature evaluation points being used.

In several portions of this research, complexities were only implemented in the portions of code which were deemed to have further use. This is done in order to provide a first comparison between the linear and constant strength methods.

1.3 The pFFT Algorithm

Described in detail in Chapter 4, the pFFT algorithm makes use of a few simple operations. The algorithm exploits the computation of the farfield potential interactions using Fourier domain multiplication to compute the real domain convolution integral. This reduces the convolution to an $O(n\log(n))$ operation from the original $O(n^2)$.

1.3.1 History of the pFFT Algorithm and its Usage

Due to the generality of the pFFT algorithm, it has been implemented in a broad variety of applications:

- 1) Phillips and White, FASTCAP [29]. Aluru, Nadkarni, and White [30] : Capacitance extraction. In [30] the advancement through implementation fo a parallel pFFT.
- 2) Zhu, Song, and White, FastImp [10]: An Impedance extraction code
- 3) Wang, Ye and White, [31] FastStokes : A Stokes flow simulation package for MEM's devices.
- 4) Kuo, Bardhan, Lee and White, FastMolecule [32]: A bio-molecular simulation package for protein analysis.
- 5) H. Hu, D.T. Blaauw, V.Zolotov, K. Gala, R. Panda, S.S.Sapatnekar [33] : A Precorrected-FFT Method for Simulating On-chip Inductance.
- 6) Newman and Lee [34] : pFFT applied in WAMIT, a code for offshore structure analysis.

Several of these problems have been explored by multiple different sources. There are other implementations of the pFFT algorithm, however, from the above list, the broad application of the pFFT algorithm is apparent.

1.4 Aircraft Axes

The problem being solved in this work is conceptually simple. The flow field around an arbitrary 3-Dimensional object is desired. In Figure 1-1 the coordinate system and the various flow properties are outlined for the problem under consideration. Table 1.1 describes the main properties of the flow.

Variable	Symbol	Description
Axes	X, Y, Z	The main coordinate axes
Freestream	\vec{V}_∞	The freestream flow
Angle of Attack	α	The angle of attack of the aircraft rotated about its Y axis
Sideslip angle	β	The angle of attack of the aircraft rotated about its Z axis
Bank Angle	ϕ	The angle of attack of the aircraft rotated about its X axis
Velocity	$\vec{v}_x, \vec{v}_y, \vec{v}_z$	The perturbation velocity at a field point \vec{x}
Velocity	$\vec{V}_x, \vec{V}_y, \vec{V}_z$	The total velocity at a field point \vec{x}
Position	$\vec{x} = (x, y, z)$	The x,y, and z coordinates
Span	b	The wing span for the case
Chord	c	The wing chord at a station y
Average Wing chord	\bar{c}	The average wing chord

Table 1.1: The Flow variables, and geometric data for the flow simulation

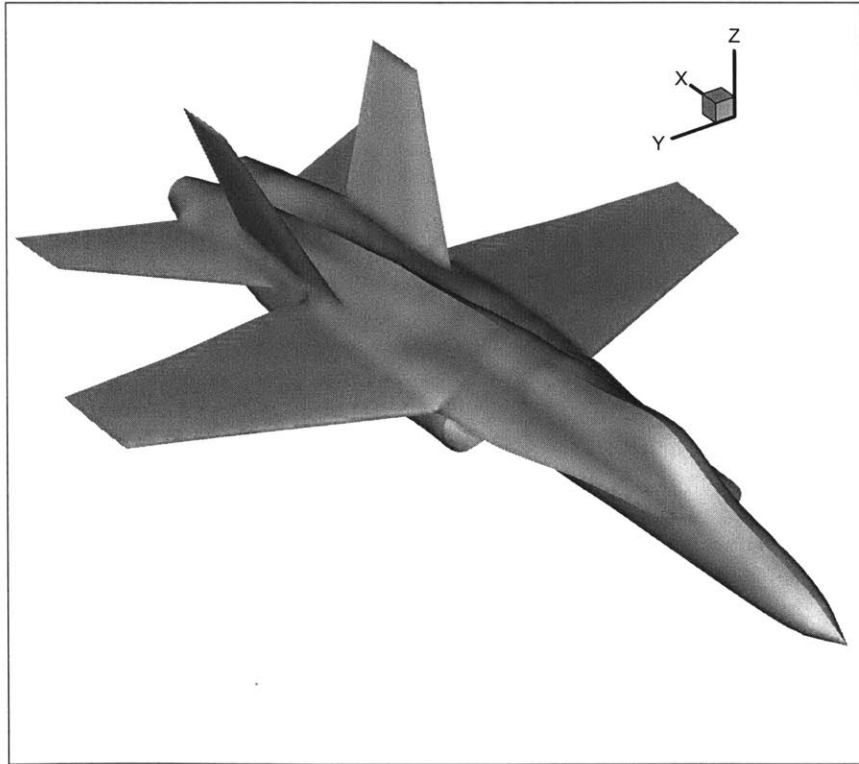


Figure 1-1: An F-18 outlining the coordinate system convention for the problem. In addition various other defined properties are presented.

Chapter 2

Theory : Potential Flow

2.1 Introduction : Chapter Overview

This chapter is divided into three main sections:

- 1) The derivation of the differential equations governing the flow.
 - a) *The Potential Flow Equation*: Total and perturbation forms.
 - b) *Bernoulli Equation*. A relation between velocity and pressure.
 - c) The forces, and pressure coefficient computation.
- 2) The application of a lifting body analysis.
 - a) The physical description of lifting body flows.
 - b) The modifications to the potential flow analysis.
 - c) The applicable Kutta conditions for the flow.
- 3) The determination of the Integral Equations.
 - a) The Direct Potential Formulation.
 - b) The Indirect Source - Velocity Formulation.
 - c) The Indirect Dipole - Velocity Formulation.

2.2 The Governing Differential Equations

The following chapter describes the derivation of the potential flow equations in both differential and integral form. The derivations start from the fundamental equations

of fluid dynamics – the *conservation of mass*, and the *conservation of momentum*.

2.2.1 Conservation of Mass : Differential Form

The expression for the conservation of mass for an infinitesimal volume, at a point, \vec{x} in a fluid domain (see figure 2-1), for a compressible, unsteady fluid flow is:

$$\frac{\partial \rho}{\partial t} + \nabla \cdot (\rho \vec{V}) = 0$$

Where,

t : is the time dimension.

ρ : Is the density of the fluid, at position \vec{x} at time t .

\vec{V} : Is the *total* velocity, at position \vec{x} , at time, t .

Notes:

- The fluid properties are expressed in an Eulerian form for a point \vec{x} in the domain.
- The velocity \vec{V} is a *total velocity*. It is the velocity at a point \vec{x} resulting from a fixed body with a forced freestream flow around it. The body is in a fixed, stationary reference frame.
- Derivations of the above conservation of mass statement can be found in most elementary fluids texts, such as White, and Anderson [35], [1].

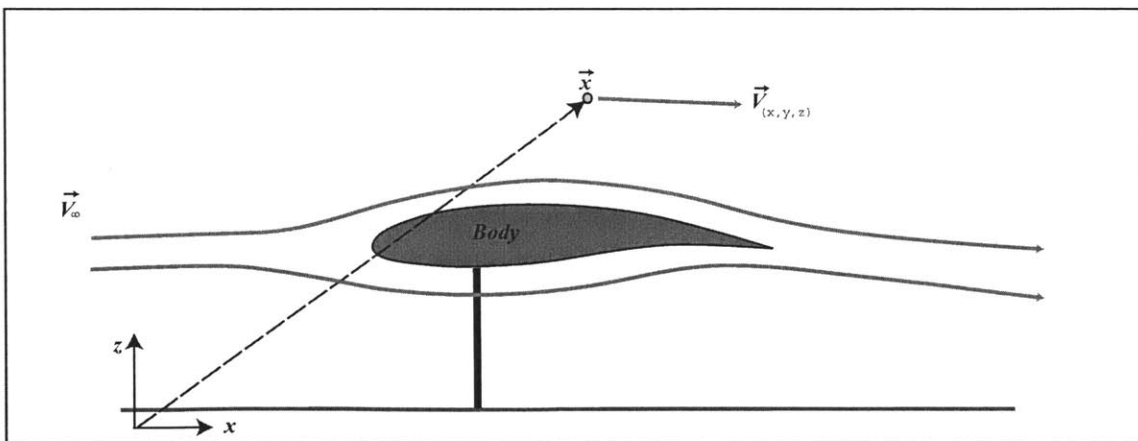


Figure 2-1: The flowfield under consideration. The body is considered to be stationary with a forced freestream flow around it. This is the total flowfield reference frame

Assumptions About the Flow

The conservation of mass statement for external aerodynamics can be simplified by making the following assumptions.

Steady Flow

Since the flowfield under consideration is independent of time ($\frac{\partial \rho}{\partial t} = 0$), it is assumed to be *steady*. As a result the flow is dependent only on the spatial coordinates. The conservation of mass statement reduces to:

$$\nabla \cdot (\rho \vec{V}) = 0$$

Incompressible Flow

The flow is assumed to have a subsonic freestream velocity (the flow velocity is actually assumed to be less than $\frac{1}{3}$ the speed of sound). As a consequence of the low Mach Number and the steady flow assumption, the flowfield under consideration is assumed to have a *constant density* throughout. First, consider the expanded expression of the above conservation of mass statement:

$$(\vec{V} \cdot \nabla)\rho + \rho \nabla \cdot (\vec{V}) = 0$$

Where, for a *constant density flow*, the density, ρ is spatially invariant, thus $(\vec{V} \cdot \nabla)\rho = 0$. Thus the conservation of mass statement reduces to:

$$\nabla \cdot (\vec{V}) = 0$$

Irrotational Flow (Inviscid Flow)

In physical reality there are thin boundary layers around a translating body. In addition there exists a thin trailing shear layer. These thin boundary layer effects are a result of viscous effects. They are the zones in which the flow is strongly *rotational*. The rest of the fluid domain can be considered *irrotational*. Figure 2-2 outlines the

regions of rotational and irrotational flow in a typical fluid domain.

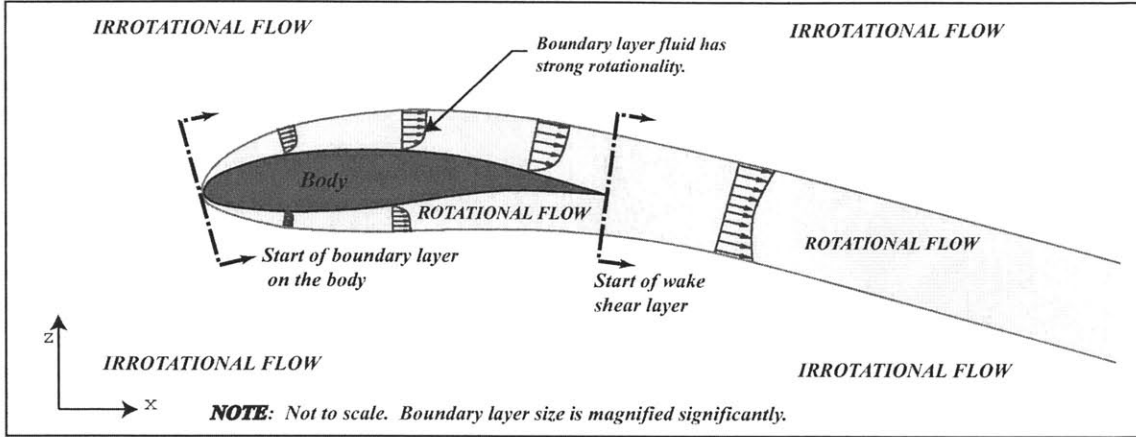


Figure 2-2: The rotational and irrotational flow zones in the domain. Notice, that the scale of the boundary layer is exaggerated. There is significant magnification of the boundary layer

Irrotational flow by definition has a zero curl of the velocity:

$$\nabla \times (\vec{V}) = 0$$

By assuming the entire domain contains irrotational flow, a *total velocity potential*, Φ , can be defined ($\vec{V} = \nabla\Phi$), such that:

$$\nabla \times (\nabla\Phi) = 0$$

Assuming that an irrotational flow assumption is valid, the conservation of mass reduces to:

$$\nabla \cdot (\vec{V}) = \nabla \cdot (\nabla\Phi) = 0$$

Which, is the Laplace equation on the velocity potential:

$$\nabla^2\Phi = \left(\frac{\partial^2\Phi}{\partial x^2} + \frac{\partial^2\Phi}{\partial y^2} + \frac{\partial^2\Phi}{\partial z^2} \right) = 0$$

Perturbation Potential Form from Total Potential Form

The potential flow equation can be presented in both a total and a perturbation form. The perturbation form of the equation considers a reference frame where the fluid is stationary, and the body translates. An advantage of the perturbation approach is the solution does not have the large freestream flow properties included. This allows more accurate numerical representation of the flow characteristics when small perturbations occur. Figure 2-3 describes the perturbation flowfield.

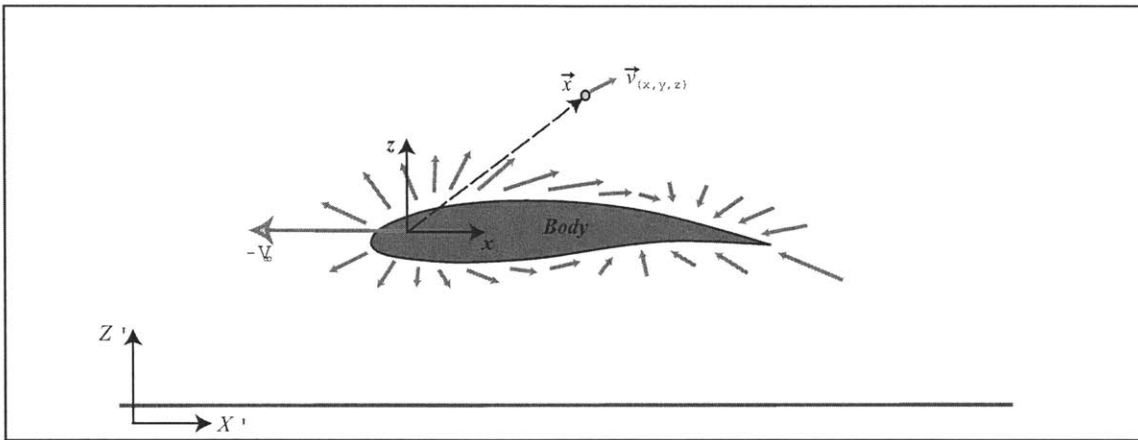


Figure 2-3: The perturbation flowfield. The perturbation form of the governing equations considers a reference frame in which the body is moving, and the flowfield is stationary

The relationship between the perturbation and total velocities is as follows:

$$\vec{V} = \vec{V}_\infty + \vec{v}$$

Where,

\vec{V}_∞ : Represents the uniform freestream velocity.

\vec{v} : Represents the perturbation velocity.

Correspondingly, the relationship between the perturbation and total potential is:

$$\Phi = \Phi_\infty + \phi$$

Where,

ϕ : Represents the perturbation potential, and, $\vec{v} = \nabla\phi$.

Φ_∞ : represents the freestream potential effect. It can be computed for a uniform freestream as:

$$\Phi_\infty = \vec{V}_\infty \cdot \vec{x}$$

2.2.2 Perturbation Expression of the Potential Flow Equation and Associated Boundary Conditions

For the analysis, the perturbation form of the Laplace equation is chosen.

Governing Fluid Flow Equation

The perturbation form of Laplace equation representing a potential flow is presented:

$$\nabla^2\phi = \left(\frac{\partial^2\phi}{\partial x^2} + \frac{\partial^2\phi}{\partial y^2} + \frac{\partial^2\phi}{\partial z^2} \right) = 0$$

Boundary Conditions

In order to define the potential flow problem uniquely, boundary conditions must be implemented.

Boundary Conditions on the Body

Normal Boundary Condition : No Fluid Penetration Situation

The normal derivative boundary condition on the surface of the body, at a point, \vec{x} , is:

$$\frac{\partial\phi}{\partial n} = -\vec{V}_\infty \cdot \hat{n}_{\vec{x}}$$

This is a statement satisfies the no-penetration body boundary condition.

No-Slip Tangential Flow Condition

The no-slip tangential velocity boundary condition which exists in physical flows is not satisfied in the potential flow model of the fluid. Due to the assumptions of irrotationality, hence inviscid flow, the satisfaction of this boundary condition is not mathematically possible.

Boundary Conditions at Infinity

Considering a closed surface with radius $r(s)$, surrounding the rigid body, the conservation of mass expression implies a zero net mass-flux across the surface:

$$\oint_S \vec{v} \cdot \hat{n} dS = 0$$

As $r(s) \rightarrow \infty$, the above expression implies that $\vec{v} \cdot \hat{n} \rightarrow 0$ faster than r^2 .

Considering a point \vec{x} in the domain. In the limit as \vec{x} approaches ∞ :

$$\lim_{\vec{x} \rightarrow \infty} \vec{v}(x) \rightarrow \frac{1}{|\vec{x}^3|}$$

As a consequence the perturbation potential decays as, $\frac{1}{|\vec{x}|^2}$ in the farfield.

Summary of the Conservation of Mass

The conservation of mass statement reduces to the governing potential flow equation. By solving the potential flow equation, both the potential and velocity of the fluid can be determined. Once the velocity and potential are determined, postprocessing of these results to include momentum effects such as surface pressures, forces, and moments can be performed.

2.2.3 Conservation of Linear Momentum : In Differential Form

The conservation of linear momentum for an infinitesimal fluid element at a point \vec{x} for an incompressible Newtonian flow is expressed as:

$$\rho \frac{\partial \vec{V}}{\partial t} + \rho(\vec{V} \cdot \nabla)\vec{V} = -\nabla p + \rho \vec{g} + \mu(\nabla^2 \vec{V})$$

where,

p : The static pressure at the point \vec{x}

μ : The kinematic viscosity of the fluid.

\vec{g} : The body force. Gravity would be an example of a body force. The body forces are assumed negligible.

By imposing the same flow assumptions used in the conservation of mass, the momentum equation can also be reduced to a simpler form.

Steady Flow

Assuming a steady flow, or quasi steady flow, all time derivatives are reduced to zero, resulting in:

$$\rho(\vec{V} \cdot \nabla)\vec{V} = -\nabla p + \mu(\nabla^2\vec{V}).$$

Irrotational Flow (Inviscid Flow)

Expressing the steady, incompressible equations in a non-dimensional form, the following equation results:

$$(\vec{V}' \cdot \nabla')\vec{V}' = -\frac{\nabla p}{\rho|\vec{V}'_\infty|^2} + \frac{\mu}{\rho|\vec{V}'_\infty|L} \cdot (\nabla'^2\vec{V}'),$$

where,

\vec{V}' : Is a normalized velocity.

∇' : Is a normalized gradient operator.

By definition the Reynold's Number is:

$$Re = \frac{\rho|\vec{V}'_\infty|L}{\mu}.$$

The Reynold's number is an expression relating the inertial effects to the viscous effects in the fluid domain. Most external aerodynamic flows have high Reynold's Numbers ($10^5 - 10^7$ are typical wing chord Reynolds numbers for aircraft).

By re-expressing the momentum equation using the following vector identities:

$$\nabla^2\vec{V} = \nabla(\nabla \cdot \vec{V}) - \nabla \times (\nabla \times \vec{V}),$$

and:

$$(\vec{V} \cdot \nabla)\vec{V} = \nabla \left(\frac{\vec{V} \cdot \vec{V}}{2} - \vec{V} \times (\nabla \times \vec{V}) \right),$$

the momentum equation can be written as:

$$\rho \left(\nabla \left(\frac{\vec{V} \cdot \vec{V}}{2} \right) - \vec{V} \times (\nabla \times \vec{V}) \right) = -\nabla p + \mu (\nabla(\nabla \cdot \vec{V}) - \nabla \times (\nabla \times \vec{V}))$$

The resulting equation, after assuming an irrotational flow ($\nabla \times \vec{V} = 0$), and exploiting the fact that incompressibility implies $\nabla \cdot \vec{V} = 0$, is:

$$\rho \left(\nabla \left(\frac{\vec{V} \cdot \vec{V}}{2} \right) \right) = -\nabla p$$

Reorganizing,

$$\nabla \left(\rho \frac{\vec{V} \cdot \vec{V}}{2} + p \right) = 0$$

As a result the following must be true:

$$\left(\rho \frac{\vec{V} \cdot \vec{V}}{2} + p \right) = \text{Constant} = P_\infty$$

where,

P_∞ : Is the total stagnation pressure in the flow. The stagnation pressure refers to the pressure that is present at any point in the flow should the moving flow be isentropically reduced to a zero velocity. This is much like the ideal stagnation point on the leading edge of an airfoil.

Final Statement of Bernoulli's Equation

The Bernoulli Equation used in this work is:

$$\left(\rho \frac{\vec{V} \cdot \vec{V}}{2} + p \right) = \text{Constant} = P_\infty$$

2.2.4 Postprocessing for Forces and Pressure Coefficients

Surface Force Components

The pressure is by definition the normal stress in a fluid. The differential force, $d\vec{F}$ on any infinitesimal area, $d\vec{S}$, due to a pressure, p , is:

$$d\vec{F} = (p \cdot d\vec{S})$$

In order to compute a directional force over a surface, an integral over the surface of the dot product of the infinitesimal force and the unit normal of the direction is computed. For example the force in the x -direction, \vec{F}_x , over surface S , of the body is:

$$\vec{F}_x = \int \int_S \hat{n}_x d\vec{F} = \int \int_S \hat{n}_x \cdot (p \cdot d\vec{S})$$

Similarly, equations can be written for all components of the force vector \vec{F} .

Additional analysis for computing the forces due to a lifting body in a flow domain can be performed using a Trefftz Plane Analysis (see Katz and Plotkin for more details [8]).

Surface Pressure Coefficients

The surface pressure coefficient, C_P , is computed as:

$$C_P(\vec{x}) = 1 - \left(\frac{|\vec{V}|^2}{|\vec{V}_\infty|^2} \right)$$

The surface pressure coefficient is a non-dimensional representation of the surface pressures.

2.3 Lifting Bodies and the Kutta Condition

The potential flow problem does not satisfy the conditions required to resolve a lifting body flow. Most aerodynamic analyses involve the development of lift. In order to

introduce a lifting body analysis into the potential flow solution, the physical concept of lift must be investigated. After which, the physical concepts are used to modify the potential flow model.

2.3.1 The Fundamentals of Lift [1]

In this section, the physics of lifting body fluid dynamics are presented.

The Kutta-Joukowski Theorem

For a lifting body the *Kutta-Joukowski* theorem must be satisfied. The Kutta-Joukowski theorem states that lift per unit span, L' , is generated by a circulation, Γ around the lifting body:

$$L' = \rho |\vec{V}_\infty| \Gamma$$

Where the circulation around the lifting body section, Γ can be written as,

$$\Gamma = \oint_S \vec{V} \cdot d\vec{S} = - \int \int_V (\nabla \times \vec{V}) \cdot dV$$

The circulation and lifting body flowfield is presented in figure 2-4.

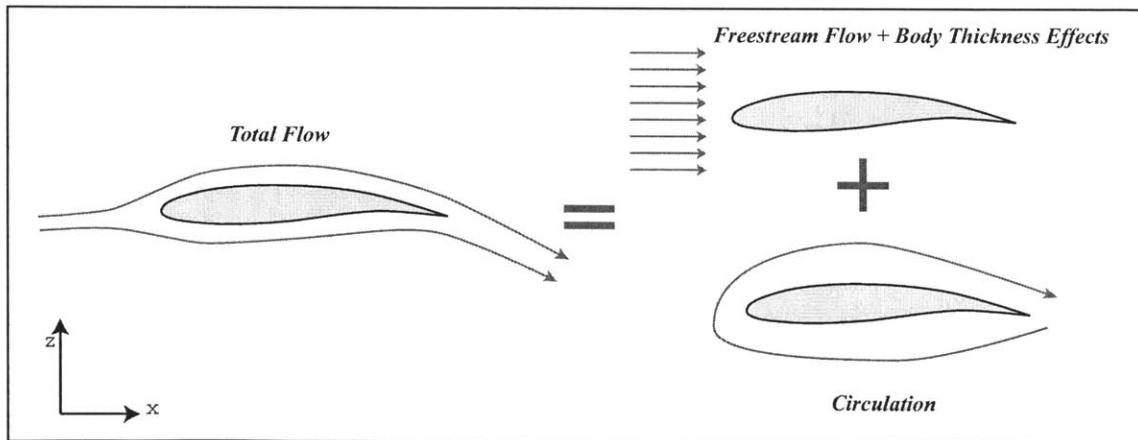


Figure 2-4: Circulation combined with the free stream and body effects causes an appropriate lifting body flow field.

The rotation of the fluid particles occurs in the thin boundary layers around the body. The lift-producing circulation is the result of the net vorticity in the boundary

layer of the flow, as shown in figure 2-5.

Kelvin's Theorem : Conservation of Vorticity in the Domain

In addition, by Kelvin's Theorem [8], a conservation of vorticity must be satisfied in the flowfield. The conservation statement implies vorticity cannot be created or destroyed, only conserved within the domain (Kelvin's Theorem assumes a non-dissipative flowfield). Therefore, the vorticity created on the lifting body is shed into the wake, and downstream behind the airfoil.

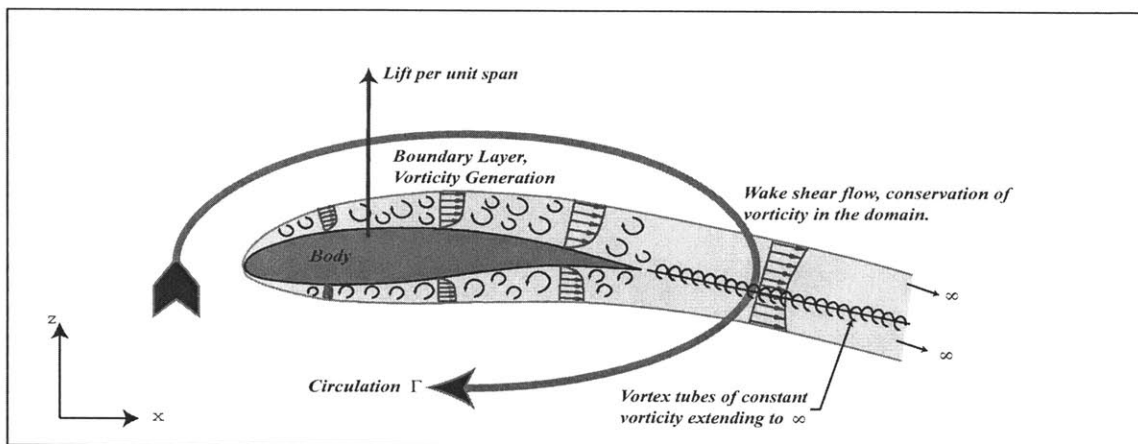


Figure 2-5: The physical manifestation of circulation and vorticity. The boundary layer "induces" vorticity in the flow, and as a result of a non-zero integral of the boundary layer vorticity, the net circulation around the body is non-zero, and hence produces lift.

Kutta Condition : Trailing Edge Condition

The Kutta condition at the trailing edge describes a relation which can be used to compute the correct circulation for the flow.

The Kutta condition implies a pressure equality for two flows meeting at the trailing edge of a body. As a consequence, the pressure at a point just above the body trailing edge, is equal to the pressure at a point just below the trailing edge as presented in figure 2-6.

By ensuring that the pressure Kutta condition is satisfied, the magnitude of the lift, and circulation will be determined as a part of the flowfield solution.

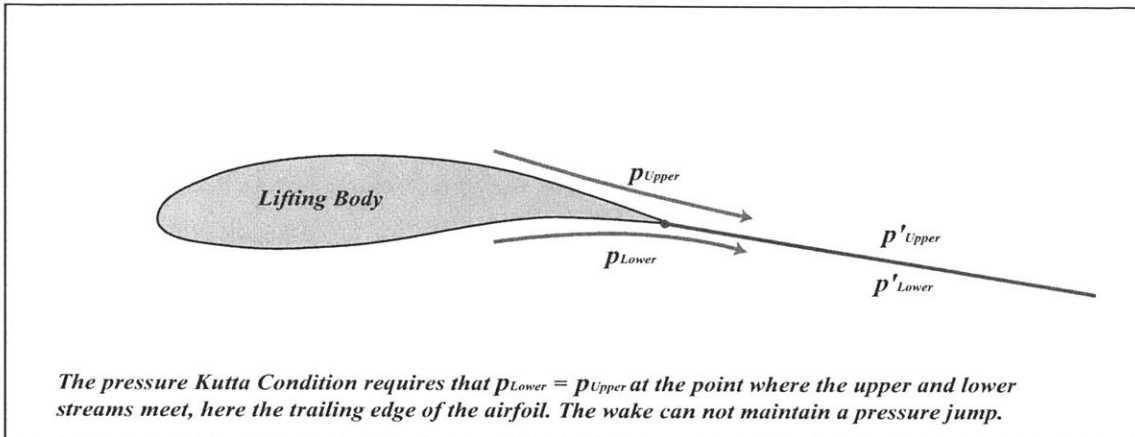


Figure 2-6: The pressure matching at the upper and lower surfaces produces a flow which leaves the trailing edge of the lifting body smoothly.

2.3.2 Potential Flow Considerations : The Generation of Lift

In this section a lifting model for the potential flow is presented. First the domain modifications are presented, followed by the application of the Kutta condition at the trailing edge of the lifting body.

The Domain Under Consideration

Due to Kelvin's Conservation of vorticity statement, the lifting model requires a sheet of vorticity in the domain. Since the governing potential flow equations are limited to irrotational flow, a cut is introduced into the fluid domain at the approximate position in which the wake lies. Iteration of the non-linear problem is required to determine the exact wake position, should it be desired. The wake surface cut is presented in figure 2-7.

In traditional panel methods, the length of the wake surface is approximately 20-30 times the length of the lifting body chord (or other flow wise length scale). In addition, the wake surface follows as closely as is practical to the fluid streamlines.

Kutta Conditions for the Potential Flow

In order to determine an expression for the surface potential of the wake, the Kutta condition is applied at the lifting body trailing edge.

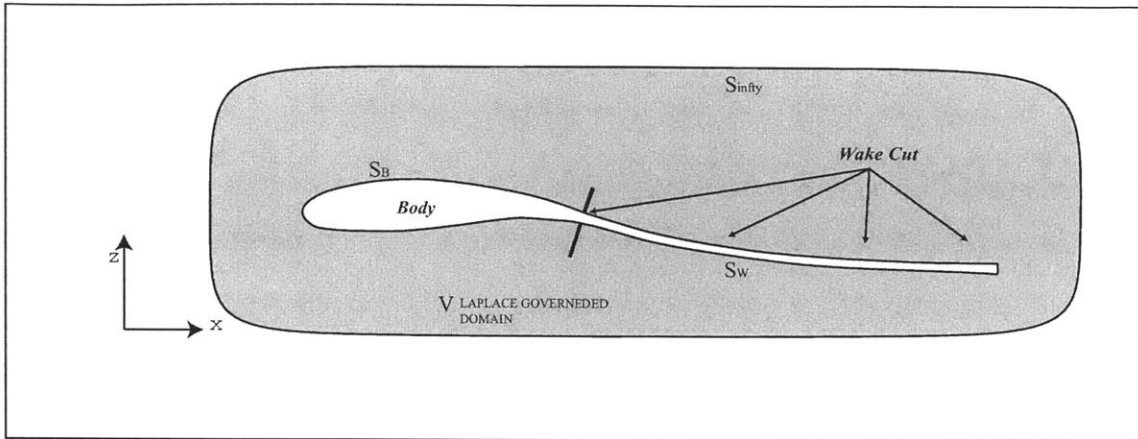


Figure 2-7: The introduction of a cut into the domain to account for the vorticity shed into the wake. The wake is later modeled as a single sheet of infinitesimal thickness.

The Non-Linear Pressure Kutta Condition [19]

Early developers of panel methods [19], [12] suggested implementing the pressure-Kutta condition:

$$p_{upper} = p_{lower}$$

By application of Bernoulli's equation:

$$\frac{(\vec{V})_u \cdot (\vec{V})_u}{2} = \frac{(\vec{V})_l \cdot (\vec{V})_l}{2}$$

This further reduces to:

$$|\nabla(\Phi)|_u \cdot |\nabla(\Phi)|_u = |\nabla(\Phi)|_l \cdot |\nabla(\Phi)|_l$$

This is the statement of the non-linear *pressure*-Kutta condition. The solution of the non-linear problem is computationally expensive. As a result a linearization is considered.

Linearization of the Pressure Kutta Condition

The non-linear Kutta condition expressed simply as:

$$|\vec{V}|_u = |\vec{V}|_l$$

In order to linearize the Kutta condition, several assumptions can be made.

1) The geometry of the wake is prescribed *a priori*. The actual non-linear *relaxed wake* condition requires that the wake be aligned with the freestream flow. The solution of the relaxed wake problem requires iteration, as seen in Ramsey's work [36]. The accuracy of the linearized wake analysis will be affected by the placement of the wake. As seen in figure 2-8, the flow at the trailing edge of the airfoil can be approximated as the bisector of the trailing edge angle. As the wake proceeds downstream, the re-alignment of the wake with the freestream is recommended.

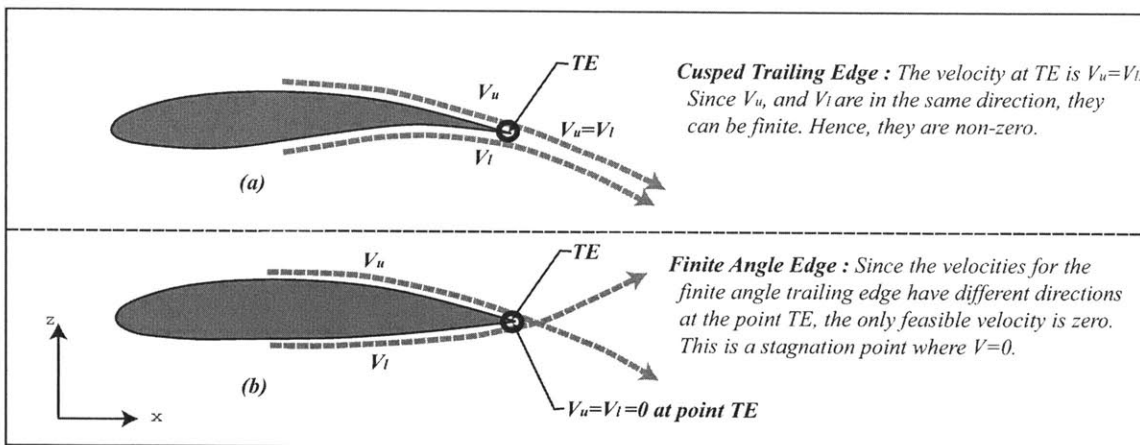


Figure 2-8: The two types of trailing edge flows. For a finite angle trailing edge a stagnation point results. In the cusped airfoil case, the upper and lower velocities are non-zero, and the flow is parallel to the trailing edge mean angle.

2) The wake position will also enforce a condition on the lines of the constant jump in potential (between the upper and lower surfaces of the wake) along the length of the wake. Since the potential jump between upper and lower wake surfaces is constant along a line spanning the length of the wake (as a requirement of Kelvin's Theorem), the user defined wake position will have a significant influence on the location and orientation of these lines. If the lines of constant potential jump are not adequately

aligned with the approximate freestream potential along the wake, the breakdown of the linearized Kutta condition is observed (the regions of large transverse wing tip flow of high-lift wings are an example of this).

3) The equality of the $L2 - norm$ of the velocity in the non-linear Kutta condition is by definition non-linear. An assumption must be made in order to linearize the expression. In this analysis, the flow is assumed to leave the upper and lower surfaces of the trailing edge in the direction of the prescribed wake panel. As a result, the user specifies the direction in which the linearization of the Kutta condition occurs.

For the sake of clarity, the direction of optimal wake placement is assumed to be known.

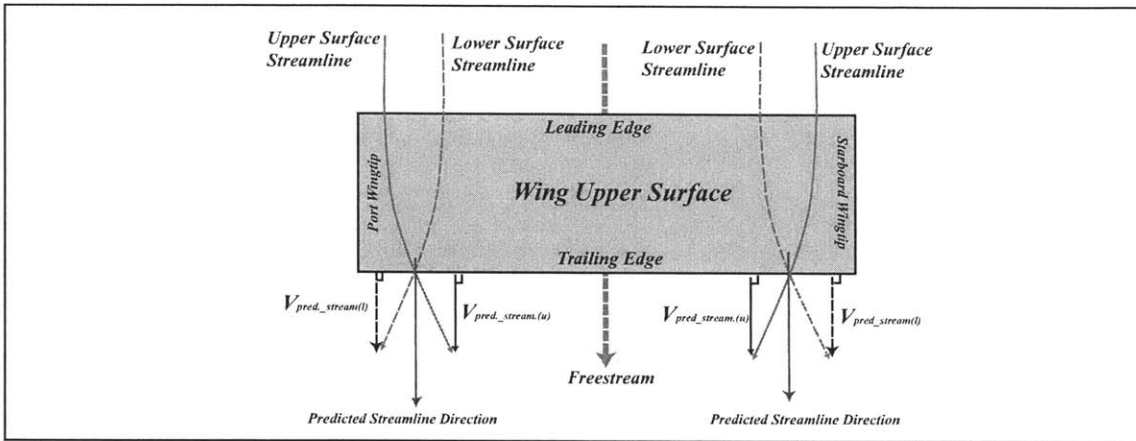


Figure 2-9: The schematic description of a wing as seen from above. Notice the linearization involves the equality of the upper and lower perpendicular velocities.

Figure 2-9 is a schematic depiction of a typical flow over a 3-Dimensional wing. The velocity in the direction parallel with the freestream (as seen from above the airfoil) is considered to be the dominant velocity direction. Combining this direction with the flows shown in figure 2-8, a trailing edge flow can be determined as shown in figure 2-10.

As a result a linearization of the non-linear velocity relationship condition can be performed:

$$|\vec{V}|_u = \sqrt{V_{Predicted-Streamline}^2 + V_{Normal_1}^2 + V_{Normal_2}^2} = \sqrt{V_{Predicted-Streamline}^2} = V_{Predicted-Streamline}$$

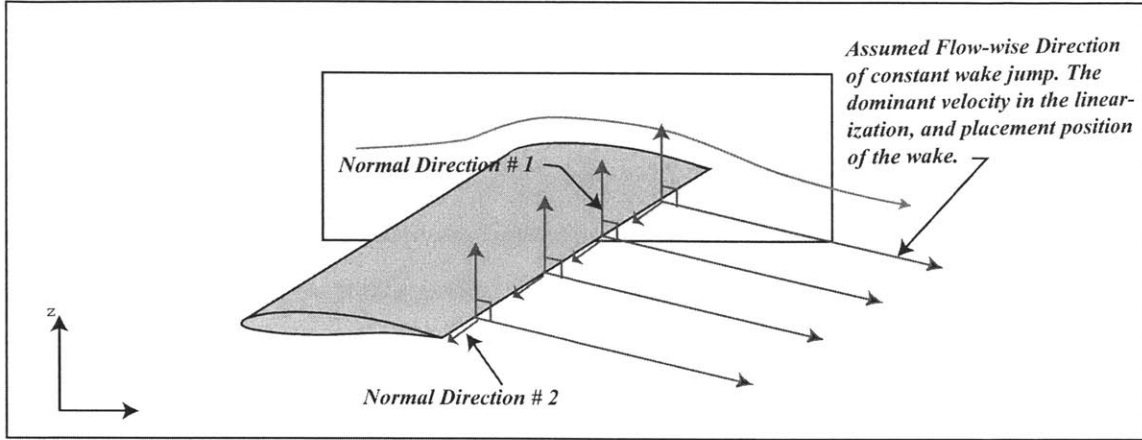


Figure 2-10: The flow at the trailing edge. The main velocity is in the local-freestream approximated direction, while the velocities in the directions perpendicular to that are assumed to be negligibly small

Where,

$V_{Predicted-Streamline}$: Is the direction along which the user defines the lines of constant potential jump in the wake.

$V_{Normal_1}, V_{Normal_2}$: Are two orthogonal velocity directions, normal to the user defined dominant velocity direction. Assuming a well chosen wake position, these velocities should be small. Regions of the domain where, V_{Normal_1} , and V_{Normal_2} are not small (such as wingtip regions and highly swept trailing edge flows), will have a breakdown of the linearized Kutta condition. Figure 2-10 shows the $Normal_1$, and $Normal_2$ velocity directions.

By the linearization above, the Kutta condition becomes

$$\vec{V}_l \cdot \hat{i}_{Predicted-Streamline} = \vec{V}_u \cdot \hat{i}_{Predicted-Streamline}$$

where:

$\hat{i}_{Predicted-Streamline}$: is the user defined wake position based on the freestream flow.

As a consequence of the above linearized equation there exists no local vorticity, $\gamma(L)$ in the direction perpendicular to the $\hat{i}_{Predicted-Streamline}$ direction at that

particular location of the trailing edge:

$$\gamma(L) = \nabla \times (\vec{V}_u \cdot \hat{i}_{\text{Predicted-Streamline}} - \vec{V}_l \cdot \hat{i}_{\text{Predicted-Streamline}}) = 0$$

As a result, the expression can be rewritten in terms of the potential on the upper and lower points of the trailing edge:

$$\nabla \cdot \hat{i}_{\text{Predicted-Streamline}}(\Phi_u - \Phi_l) = 0$$

Hence, the difference between the upper and lower total potential at the trailing edge and the potential jump between the upper and lower surface points of the infinitely thin wake surface is a constant.

$$\Phi_u - \Phi_l = \text{const.}$$

The expression can be re-written in a perturbation form as:

$$\phi_u - \phi_l + (\vec{V}_\infty \cdot \vec{r}_{u-l}) = \Delta\phi_w$$

where,

\vec{r}_{u-l} : is the relative position of the upper evaluation point compared with the lower evaluation point. This condition is non-zero when the potential evaluation points do not lie on coincident perpendiculars to the freestream flow.

$\Delta\phi_w$: represents the wake potential jump, assuming a single thin sheet representing the wake, as in figure 2-11. Since the normals of the upper and lower surfaces are opposite in direction, one can see that the potential difference between upper and lower surfaces can be defined as a single potential jump, of $\Delta\phi$. In the integral formulation presented later, the use of a thin sheet approximation for the wake results in a single double layer sheet with a strength $\Delta\phi_w$. This is just an effect approximating the integral of the infinitely thin wake sheet with opposing normals over the upper and lower surfaces as an integral over a single surface with a strength $\Delta\phi$.

If the freestream potential at the upper and lower points is the same (through discretization, or choice of control points), then the linearized Kutta condition can be expressed in perturbation form as:

$$\phi_u - \phi_l = \text{const.} = \Delta\phi_w$$

The linearized Kutta condition presented provides a relationship between the lower-upper surface wake potential jump and the potential at the upper and lower surfaces of the trailing edge of a lifting body.

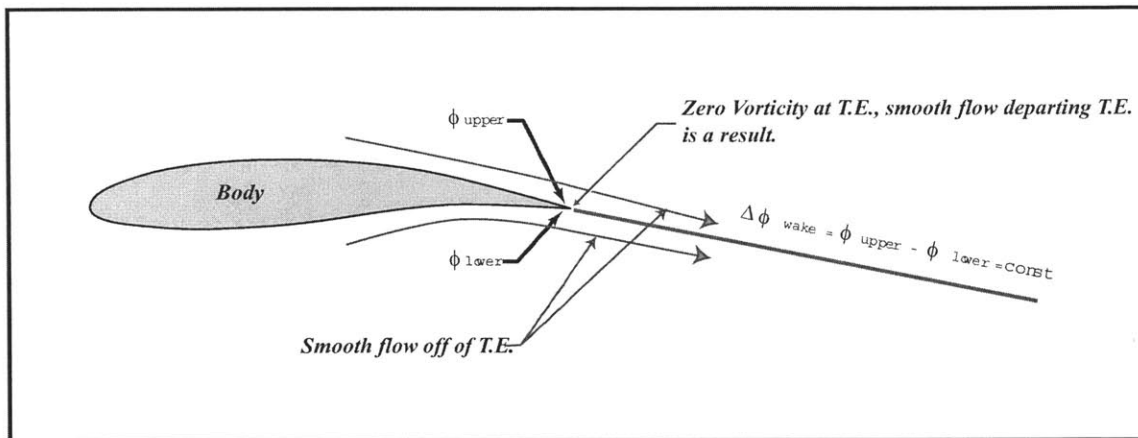


Figure 2-11: The linearized Kutta condition at the trailing edge. The wake potential is presented as a single sheet with a potential jump, ϕ_w due to the assumption that the wake is of infinitesimal thickness

This is one of the simplest and most effective expressions determining the trailing wake strength. When implementing Kutta conditions in panel methods, the potential is an easily accessible value, and can easily be used in the manipulation. It is the sole Kutta condition used in the presented discrete implementation.

Application of the Linearized Potential Kutta Condition

At first glance, the practical numerical application of the above Kutta condition appears to be flawed. As the upper, u , and lower, l , potential evaluation points tend towards the trailing edge, intuition suggests that, ϕ_u and ϕ_l will converge to the same

value, ϕ_{ul} .

$$\lim_{\vec{x}_u \rightarrow (T.E), \vec{x}_l \rightarrow (T.E)} (\phi_u - \phi_l) = 0$$

As a result, the potential in the wake is argued to be zero. Since ϕ_u and ϕ_l can be said to have multiple values, the resulting system is deemed singular.

This however is not seen in the practical applications of this Kutta condition (finite wings with sharp, low angle trailing edges). When applied to the sharp trailing edge of an airfoil the lifting flow is resolved. The trailing edge nodes can have unique values for the upper and lower surface potentials.

In the case where a continuous surface is analyzed (or geometrically close to continuous), the result is not seen to converge to a distinct value for the linear panel case. The case where a rotating cylinder in a freestream was analyzed, with increased panel discretization the solution does not converge rapidly to a distinct solution. It does however suggest that a lifting solution exists.

As a result of the $(\phi_u - \phi_l) \rightarrow 0$ suggested breakdown in the Kutta condition, this linearized Kutta condition is cautiously implemented (with additional time and resources, a more robust Kutta condition implementation is recommended).

Several lifting airfoil sections were tested, and all showed good agreement with experimental results (see Chapter 5). In the limit, where the panels are infinitely small, this condition may indeed break down. For cases where the resolution of the Kutta condition is of great importance, it is recommended to revisit the implemented Kutta condition for more insight and potential modification.

Additional linearized Kutta conditions are implementable. Conditions enforcing tangential velocity at the trailing edge are feasible and it is highly recommended that they should be investigated. It is left as a recommendation for future work to implement a more robust Kutta condition in the resulting computer code.

2.4 The Boundary Integral Equations

The Boundary Element Method(BEM) implements the Boundary Integral Equations(BIE) in the solution. Starting from the differential form, the boundary in-

tegral equations are derived. Additional insight may be found in works dedicated to boundary integral equation expressions [3], [8], [37].

The governing differential perturbation potential flow equation is:

$$\nabla^2 \phi(\vec{x}) = 0$$

With boundary conditions:

$$\lim_{\vec{x} \rightarrow \infty} \nabla \phi(\vec{x}) \rightarrow \frac{1}{|\vec{x}|^3}$$

$$\nabla \phi(\vec{x}_b) \cdot \hat{n}(\vec{x}_b) = -\vec{V}_\infty \cdot \hat{n}(\vec{x}_b)$$

The *fundamental solution* is defined as the solution at \vec{x}' , of the governing equation when it is excited by an impulse at \vec{x} :

$$\nabla^2 G(\vec{x}, \vec{x}') = 4\pi\delta(\vec{x}, \vec{x}')$$

This is pictorially depicted in Figure 2-12. $G(\vec{x}, \vec{x}')$ represents the potential at \vec{x}' due to the impulse at \vec{x} .

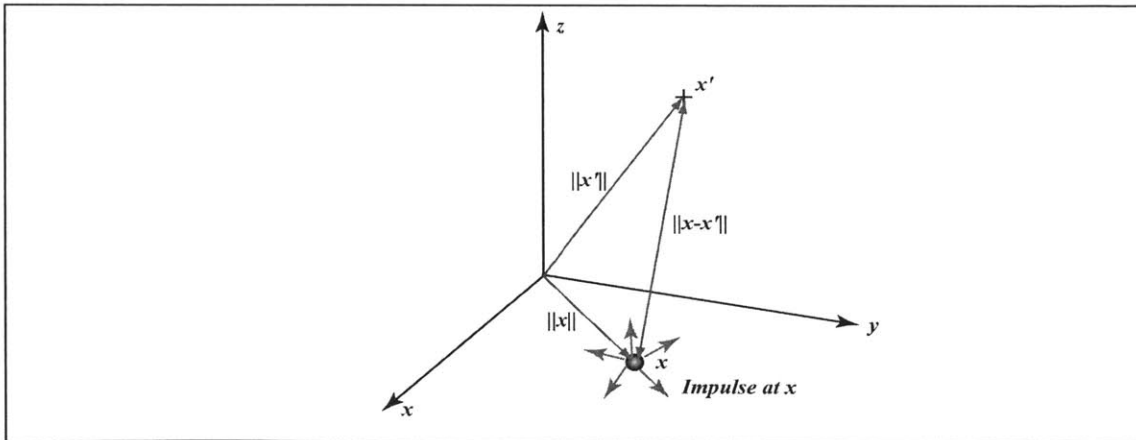


Figure 2-12: The representation of the fundamental solution of the 3-Dimensional Laplaces Equation. An impulse is applied at \vec{x} , and the solution is evaluated at \vec{x}' .

Solving the above equation gives the *fundamental solution* or *kernel* for Laplaces

equation in 3-Dimensions. In its most general form:

$$G(\vec{x}, \vec{x}') = \frac{1}{|\vec{x} - \vec{x}'|} + F(\vec{x}, \vec{x}')$$

Where, here the $F(\vec{x}, \vec{x}')$ is a valid solution to Laplaces equation ($\nabla^2 F(\vec{x}, \vec{x}') = 0$). This expression demonstrates the addition of a particular fundamental solution, $\frac{1}{|\vec{x} - \vec{x}'|}$, to a function that already satisfies Laplaces equation, $F(\vec{x}, \vec{x}')$, will yield a valid solution to Laplaces equation.

In the interest of simplicity, the more concise form of the fundamental solution is used:

$$\psi(\vec{x}, \vec{x}') = \frac{1}{|\vec{x} - \vec{x}'|}$$

This is a particular fundamental solution of the Laplace equation.

By observation, when \vec{x} and \vec{x}' are coincident points, the fundamental solution does not exist due to a local $\frac{1}{r}$ singularity. At all other points in the domain the fundamental solution satisfies Laplaces equation exactly.

The full solution for the potential at a given point is formed by the superposition of an infinite number of weighted fundamental solutions over the entire domain and boundary. The weighting function, $\rho(\vec{x})$, is the volume source term (right hand side of the Poisson Equation).

Considering the domain in figure 2-13, and applying the fundamental solution, an expression for the volume of the domain results (this expression does not include the surface boundary effects yet). The resulting expression is:

$$\int \int \int_V \frac{1}{\|\vec{x} - \vec{x}'\|} \nabla^2 \phi dV = \int \int \int_V \left(\phi \cdot \nabla^2 \left(\frac{1}{\|\vec{x} - \vec{x}'\|} \right) \right) dV = 0$$

The coincident (x, x') integration point, and the body and infinity boundary surfaces are not included in the above expression. By applying the divergence theorem to the above domain expression, the boundary equations are expressed easily:

$$\int \int \int_V \left(\phi \cdot \nabla^2 \left(\frac{1}{\|\vec{x} - \vec{x}'\|} \right) \right) dV =$$

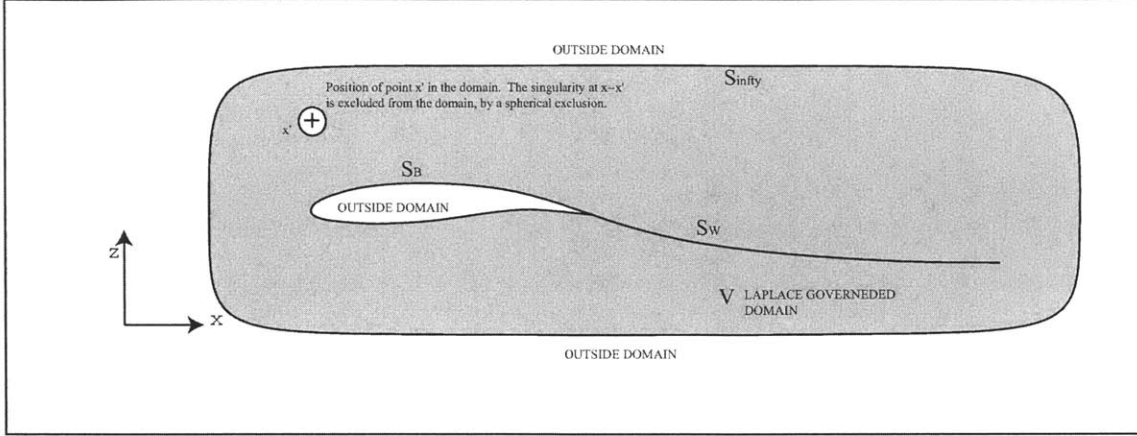


Figure 2-13: The domain under consideration. Here V is the volume of the domain, while S is the boundary of the domain, including the wake, the body, and the outer boundary, $S = S_W + S_B + S_\infty$.

$$\int \int_{S_W + S_B + S_\infty + S_{Sphere}} \left(\phi \cdot \nabla \left(\frac{1}{\|\vec{x} - \vec{x}'\|} \right) \right) - \left(\left(\frac{1}{\|\vec{x} - \vec{x}'\|} \right) \cdot \nabla \phi \right) \cdot \hat{n} dS + \int \int \int_V \left(\frac{1}{\|\vec{x} - \vec{x}'\|} \cdot (\nabla^2 \phi) \right) dV$$

Due to the simplification of the volume terms, the Boundary Integral Equation representing a Laplace equation is:

$$\int \int_{S_W + S_B + S_\infty + S_{Sphere}} \left(\phi \cdot \nabla \left(\frac{1}{\|\vec{x} - \vec{x}'\|} \right) - \left(\frac{1}{\|\vec{x} - \vec{x}'\|} \right) \cdot \nabla \phi \right) \cdot \hat{n} dS = 0$$

2.4.1 Determining the BIE expression for the *evaluation point*, \vec{x}' Inside of the Laplace Domain [2],[3]

By evaluating the BIE for the various components of the boundary ($S_W + S_B + S_\infty + S_{Sphere}$), an appropriate governing integral equation can be determined.

First the boundary at infinity is considered:

$$\int \int_{S_\infty} \left(\phi \cdot \nabla \left(\frac{1}{\|\vec{x} - \vec{x}'\|} \right) - \left(\frac{1}{\|\vec{x} - \vec{x}'\|} \right) \cdot \nabla \phi \right) \cdot \hat{n} dS$$

As, \vec{x}' approaches S_∞ , the potential, ϕ decays like $\frac{1}{\|\vec{x} - \vec{x}'\|^2}$. As a result the boundary integral over this surface will tend to zero as the evaluation point \vec{x}' approaches

infinity.

Next, the integral over the surface of the infinitesimal sphere which excludes the coincident \vec{x} and \vec{x}' singularity from the domain is considered. This integral is evaluated for $r = \epsilon$, where $\epsilon \rightarrow 0$. The resulting surface integral is:

$$\int \int_{S_{sphere}} \left(\frac{1}{\|\vec{x} - \vec{x}'\|} \nabla \phi - \phi \nabla \frac{1}{\|\vec{x} - \vec{x}'\|} \right) \cdot \hat{n} dS$$

As suggested by Katz, and Plotkin [8], the exclusion integral is evaluated over the surface using a local spherical coordinate system, centered at the point \vec{x}' , so that , the integral can be expressed as:

$$- \int \int_{sphere} \left(\frac{1}{r} \cdot \frac{\partial \phi}{\partial r} + \frac{\phi}{r^2} \right) dS$$

Furthermore, the first term in the spherical surface integral will disappear if the potential in the sphere is not varying rapidly. The integration of the second term yields:

$$\int \int_{\epsilon \rightarrow 0} \left(\frac{\phi}{r^2} \right) dS = -4\pi \phi(\vec{x}')$$

The remaining surface expressions are for the boundary surface and wake surface evaluation, in which no simplification is made. This results in a final boundary integral expression as presented below.

Final BIE Expression for the *evaluation point*, \vec{x}' Inside of the Laplace Domain

$$\phi(\vec{x}') = \frac{1}{4\pi} \int \int_{S_B} \left(\frac{\partial \phi}{\partial n} \frac{1}{\|\vec{x} - \vec{x}'\|} \right) dS_B - \frac{1}{4\pi} \int \int_{S_{B+W}} \left(\phi \frac{\partial}{\partial n} \left(\frac{1}{\|\vec{x} - \vec{x}'\|} \right) \right) dS_{B+W}$$

The result is a boundary integral expression of the potential at a point \vec{x}' , due to the surface distributions of the potential ϕ , and its surface normal derivative $\frac{\partial \phi}{\partial n}$. Note: The second integral on the RHS, is evaluated over both the wake and the body, while the first integral is evaluated only over the body. The first integral has a zero value on the wake surface, while the second integral specifying ϕ is a necessary condition for the lifting body flow in which a wake is present, and has a non-zero value if lift is

present in the analysis.

2.4.2 Determining the BIE Expression for the *evaluation point, \vec{x}' Outside of the Laplace Domain* [2],[3]

Here the BIE is derived for a point outside of the Laplace domain. The only difference between this case and the case for the *evaluation point* inside the Laplace domain is in the spherical exclusion integral. If the evaluation point lies outside of the Laplace domain, there is no coincident \vec{x}, \vec{x}' term. Thus the relation reduces to the following boundary integral equation.

Final BIE Expression for the *evaluation point, \vec{x}' Outside of the Laplace Domain*

The resulting boundary integral equation can be written for the potential, $\phi(\vec{x}')$ at a point \vec{x}' outside of the domain:

$$0 = \frac{1}{4\pi} \iint_{S_B} \left(\frac{\partial \phi}{\partial n} \frac{1}{\|\vec{x} - \vec{x}'\|} \right) dS_B - \frac{1}{4\pi} \iint_{S_{B+W}} \left(\phi \frac{\partial}{\partial n} \left(\frac{1}{\|\vec{x} - \vec{x}'\|} \right) \right) dS_{B+W}$$

2.5 Solution Formulations

The integral equations derived to this point express the potential at a point \vec{x}' due to the surface values ϕ and $\frac{\partial \phi}{\partial n}$. Values of both, ϕ and $\frac{\partial \phi}{\partial n}$ are required to resolve the potential at the point \vec{x}' . The determination of a set of boundary integral equations, which solve the potential flow boundary value problem is considered in this section.

In order to use the boundary integral formulation to solve the potential flow problem, physical flow boundary conditions must be introduced. This approach is discussed in the sections that follow. For additional insight into alternate explanations the reader is directed to [4] [8],[38], [37], [1] and [39].

In the sections that follow, three solution formulations are presented.

Direct Methods:

1) *The potential formulation* : As the name suggests, the solution yields the surface potential. This is the only non-velocity formulation considered. It is based on the Green's Theorem result for the boundary integral equation.

Indirect Methods

2) *The source velocity approach*: This is based on the physical flow Neumann boundary condition. The result is an expression of the potential at a point \vec{x}' based only on the surface single layer singularity strength.

3) *The dipole velocity approach*: This formulation is also based on the physical flow Neumann boundary condition. The result is an expression of the potential at a point, \vec{x}' , based only on the surface double layer singularity strength.

2.6 The Potential Formulation : The Direct BIE Formulation

The first solution approach presented is the potential formulation of the boundary integral equation.

The potential approach is similar to the traditional source-doublet approach in aerodynamics. The formulation is attributed to Morino [40] in the aerodynamics community.

From the physical flow boundary condition, it is known that:

$$\frac{\partial \phi}{\partial n} = -\vec{V}_\infty \cdot \hat{n}_{\vec{x}}$$

The resulting expression for the potential at a point in the domain is expressed as:

$$\phi(\vec{x}) = \frac{1}{4\pi} \int \int_{S_B} -\vec{V}_\infty \cdot \hat{n}_{\vec{x}} \frac{1}{\|\vec{x} - \vec{x}'\|} dS_B - \frac{1}{4\pi} \int \int_{S_{B+W}} \phi(\vec{x}) \frac{\partial}{\partial n} \left(\frac{1}{\|\vec{x} - \vec{x}'\|} \right) dS_{B+W}$$

With a fixed single layer distribution $(-\vec{V}_\infty \cdot \hat{n}_{\vec{x}})$, the only unknown in the formulation is the double layer distribution strength, ϕ , which is the boundary value of the potential. By placing control points on the surface of a discretized body, the potential

at each control point is identically the double layer strength.

Resolution of the Farfield Behavior for the Direct Integral Equation

The boundary condition on the farfield requires that the potential decays as:

$$\lim_{\vec{x} \rightarrow \infty} \vec{v}(x) \rightarrow \frac{1}{|\vec{x}^3|}$$

As a consequence the perturbation potential decays as, $\frac{1}{|\vec{x}|^2}$ in the farfield.

In the direct BIE implementation, there is both a single layer and double layer singularity to consider. The double layer potential contribution, by definition will decay as $\frac{1}{|\vec{x}|^2}$. The single layer potential however suggests a slower $\frac{1}{|\vec{x}|}$ decay. Initially this seems to pose an inconsistency in the boundary conditions. In order for the correct farfield decay to be satisfied, a particular distribution of single layer must be present. In this case, the single layer strength is specified, through the boundary condition as:

$$\vec{V}_{\infty} \cdot \hat{n}_{\vec{x}} = \frac{\partial \phi}{\partial n}$$

Integrating this over the surface of the body, as $\vec{x} \rightarrow \infty$, results in an effect which looks like a dipole aligned in the flowwise-wise direction. The following details explain intuitively why this effect is seen:

- 1) The single layer surface strength has a zero total surface integral. As a result, in the farfield the $\frac{1}{\vec{x}}$ effect is canceled out.
- 2) Since there is a lumping of positive single layer strength in the front of a body and a lumping of negative single layer in the trailing region of a body (by property of the surface boundary condition), the farfield effect looks like a doublet aligned in the flowwise direction. Essentially defining the correct $\frac{1}{\vec{x}^2}$ decay of the perturbation potential.

Figure 2-14 demonstrates this created doublet effect for an infinite span elliptical cross section member.

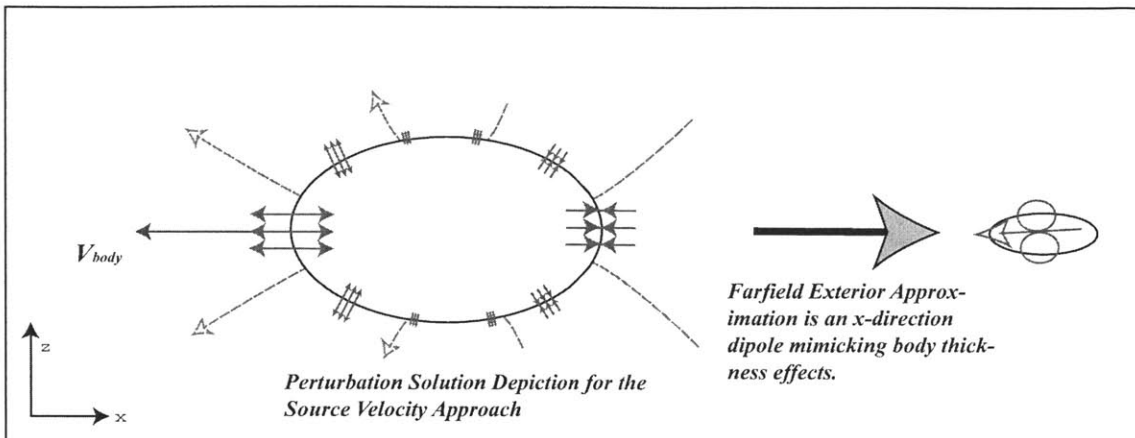


Figure 2-14: The flow thickness effect is modeled with a source singularity on the surface. This will mimic a doublet in the farfield, hence, there will be a $\frac{1}{|x|^2}$ potential decay.

Physical Intuition

Figure 2-15 outlines the physical interpretation of the above Green's Function BIE. The single layer distribution on the body forces the no-penetration boundary condition for the external aerodynamic flow. As a result, the corresponding potential on the surface is determined from the solution of the direct boundary integral equation.

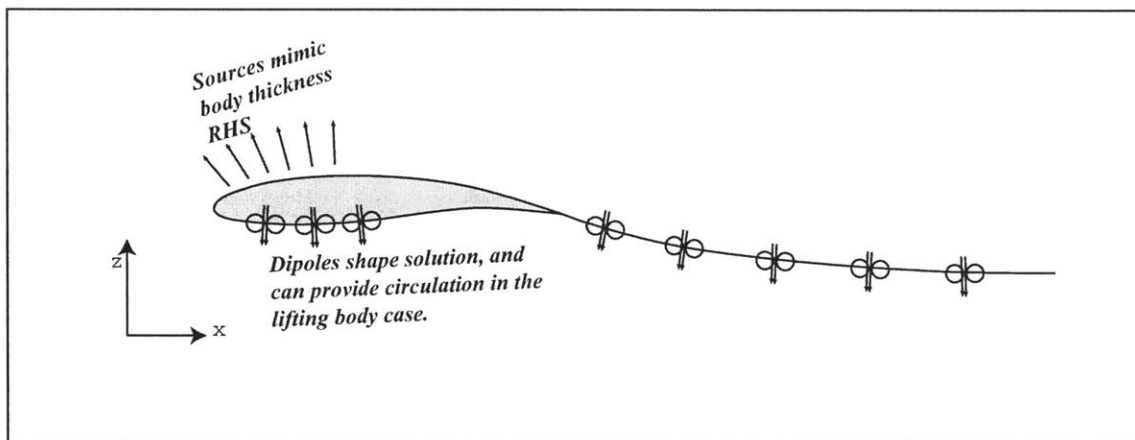


Figure 2-15: The Green's Theorem representation. The single layer mimics the body thickness by applying the body boundary condition, while the dipole layer augments the solution to provide lift and the potential result.

The potential formulation presented assumes that the internal-to-the-body flow-field is arbitrary in the solution.

2.7 The Indirect Formulation

Following the presentation of the direct potential BIE, is the presentation of the indirect BIE's for the velocity formulation. First a general internal-external BIE is presented.

For the closed body problem there are two domains. There is the external flow domain, which is the fluid domain of interest. In addition, there is also an internal-to-the-body domain, which, is often neglected.

The External Flow Domain

Considering the external domain (figure 2-16), the expressions for the potential at a point \vec{x}' are:

$$\phi(\vec{x}') = \frac{1}{4\pi} \int \int_{S_B} \left[\frac{\partial \phi}{\partial n} \right]_e \frac{1}{\|\vec{x} - \vec{x}'\|} dS_B - \frac{1}{4\pi} \int \int_{S_{B+W}} [\phi(\vec{x})]_e \frac{\partial}{\partial n} \left(\frac{1}{\|\vec{x} - \vec{x}'\|} \right) dS_{B+W}$$

where:

e : The subscript e represents the external surface singularity distributions of ϕ and $\frac{\partial \phi}{\partial n}$.

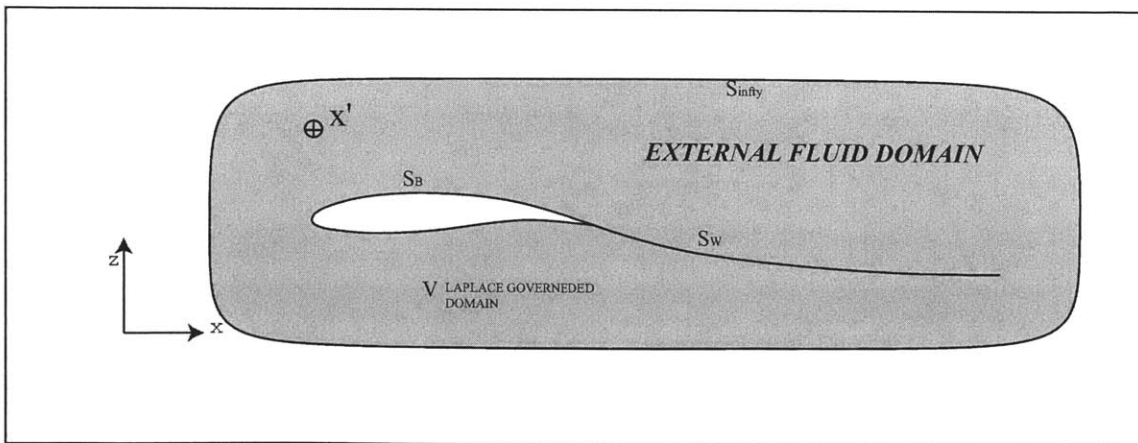


Figure 2-16: The external potential equation, expresses the computed potential at a point \vec{x}' in the domain for the external potential problem.

The Internal Flow Domain

A potential BIE for the internal domain can also be determined. The potential at a point, \vec{x}' , in the external domain as a result of the internal potential problem (see figure 2-17):

$$0 = \frac{1}{4\pi} \iint_{S_B} \left[\frac{\partial \phi}{\partial n} \right]_i \frac{1}{\|\vec{x} - \vec{x}'\|} dS_B - \frac{1}{4\pi} \iint_{S_B} [\phi(\vec{x})]_i \frac{\partial}{\partial n} \left(\frac{1}{\|\vec{x} - \vec{x}'\|} \right) dS_B$$

Where:

i : The subscript i represents the internal surface singularity distributions of ϕ and $\frac{\partial \phi}{\partial n}$.

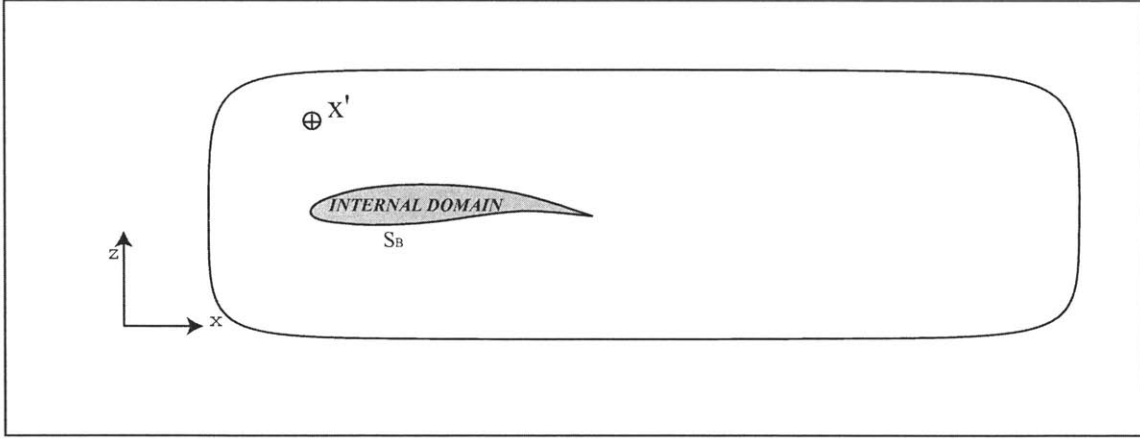


Figure 2-17: The internal potential equation, expresses the computed potential at a point \vec{x}' in the domain for the internal potential problem.

Subtracting the Internal and External Potential Equations

By linearity, the superposition of two valid Laplace solutions yields yet another Laplace solution. The difference of the potential expression for the external problem and internal problem is presented:

$$\phi(\vec{x}') = \frac{1}{4\pi} \iint_{S_B} \left(\left[\frac{\partial \phi}{\partial n} \right]_e - \left[\frac{\partial \phi}{\partial n} \right]_i \right) \frac{1}{\|\vec{x} - \vec{x}'\|} dS_B - \frac{1}{4\pi} \iint_{S_B} ([\phi(\vec{x})]_e - [\phi(\vec{x})]_i) \frac{\partial}{\partial n} \left(\frac{1}{\|\vec{x} - \vec{x}'\|} \right) dS_B - \frac{1}{4\pi} \iint_{S_W} [\phi(\vec{x})]_e \frac{\partial}{\partial n} \left(\frac{1}{\|\vec{x} - \vec{x}'\|} \right) dS_W$$

Introducing the Source, σ and Dipole/Doublet, μ

In order to simplify the internal-external equation, the definition of the following surface distributions is given:

A source, σ , is defined as:

$$\sigma = \left[\frac{\partial \phi}{\partial n} \right]_e - \left[\frac{\partial \phi}{\partial n} \right]_i$$

A dipole or doublet, μ , is defined as:

$$\mu = [\phi(\vec{x})]_e - [\phi(\vec{x})]_i$$

The resulting internal-external BIE is:

$$\begin{aligned} \phi(\vec{x}') &= \frac{1}{4\pi} \iint_{S_B} \sigma \frac{1}{\|\vec{x} - \vec{x}'\|} dS_B - \\ &\frac{1}{4\pi} \iint_{S_B} \mu \frac{\partial}{\partial n} \left(\frac{1}{\|\vec{x} - \vec{x}'\|} \right) dS_B - \frac{1}{4\pi} \iint_{S_W} [\phi(\vec{x})]_W \frac{\partial}{\partial n} \left(\frac{1}{\|\vec{x} - \vec{x}'\|} \right) dS_W \quad (BIE - 1) \end{aligned}$$

Where:

$[\phi(\vec{x})]_W$: Represents the prescribed wake strength. In this work, $[\phi(\vec{x})]_W = \phi(\vec{x})_u - \phi(\vec{x})_l$

2.7.1 The Pure Source Case : The Indirect BIE Formulation [4]

Applying the following relationship, as suggested by [8], to the internal-external BIE (equation-(BIE - 1)):

$$\phi_i = \phi_e,$$

at points \vec{x}' on the surface of the body S_B , it is obvious that the doublet term is eliminated from the expression. In addition, since there can be no generation of a vortex like effect on the body, the wake expression is dropped from the analysis (since the flow can not be a lifting one).

The resulting boundary integral equation for the potential at a point \vec{x}' in the

domain is presented as a single singularity BIE:

$$\phi(\vec{x}') = \frac{1}{4\pi} \int \int_{S_B} \left(\sigma \frac{1}{|\vec{x} - \vec{x}'|} \right) dS_B$$

The Velocity Boundary Condition Application : Source Only Formulation

The gradient of the potential is by definition the velocity. Here a velocity based single layer distribution is used to satisfy the governing fluid boundary condition. Earlier equations give the relation:

$$\phi(\vec{x}') = \frac{1}{4\pi} \int \int_{S_B} \sigma \frac{1}{\|\vec{x} - \vec{x}'\|} dS_B$$

To satisfy the velocity boundary conditions, a gradient of both sides is taken:

$$\vec{v}(\vec{x}') = \nabla_{\vec{x}'}(\phi(\vec{x}')) = \frac{1}{4\pi} \nabla_{\vec{x}'} \int \int_{S_B} \sigma \frac{1}{\|\vec{x} - \vec{x}'\|} dS_B$$

An integrable singularity occurs when the evaluation point \vec{x}' coincides with the surface source point \vec{x} . By placing a hemisphere, or a partial-hemisphere around the coincidental \vec{x} and \vec{x}' the singularity in the integral can be eliminated. This will separate the integral into an integrable singularity corresponding to the portion excluded by the hemisphere, and a surface integral over the rest of the body.

This results in the following second kind Fredholm integral equation for the velocity:

$$\vec{v}(\vec{x}') = \nabla_{\vec{x}'}(\phi) = \frac{c\sigma(\vec{x}')}{2} + \frac{1}{4\pi} \nabla_{\vec{x}'} \oint_{S_B} \sigma(\vec{x}) \frac{1}{\|\vec{x} - \vec{x}'\|} dS_B$$

Where, c is a constant related to the solid angle of the surface at evaluation point:

$$c = \frac{\Theta_{surf}}{\pi}$$

The Θ_{surf} here is merely the fraction of the hemisphere. In the case of a full sphere, Θ_{surf} would be 2π , and in the case of a semi-hemisphere, the value of Θ_{surf} would be π . It is $\frac{1}{2}$ of the remaining in domain area of a unit sphere centered at the evaluation

point cut by the surface of the body.

Boundary Integral Equation which is Solved

To satisfy the given boundary condition, $-\vec{V}_\infty(\vec{x}') \cdot \hat{n}_{\vec{x}'} = \vec{v}(\vec{x}') \cdot \hat{n}_{\vec{x}'}$, the dot product of the velocity formulation expressed at a point \vec{x}' , with the corresponding surface normal, $\hat{n}_{\vec{x}'}$, must be computed. As a result the final boundary integral equation to be solved is:

$$-\vec{V}_\infty(\vec{x}') \cdot \hat{n}_{\vec{x}'} = \vec{v}(\vec{x}') \cdot \hat{n}_{\vec{x}'} = \nabla_{\vec{x}'}(\phi) \cdot \hat{n}_{\vec{x}'} = \frac{c\sigma(\vec{x}')}{2} + \frac{1}{4\pi} \nabla_{\vec{x}'} \cdot \hat{n}_{\vec{x}'} \oint_{S_B} \sigma \frac{1}{\|\vec{x} - \vec{x}'\|} dS_B$$

Where the only unknown in the above expression is the surface source strength, σ .

Postprocessing the Solution

Once the single layer surface distribution is known, the potential at any point, \vec{x}' in the domain can be determined through back-substitution into:

$$\phi(\vec{x}') = \frac{1}{4\pi} \int \int_{S_B} \sigma \frac{1}{\|\vec{x} - \vec{x}'\|} dS_B$$

The velocity distribution may also be computed using:

$$\vec{v}(\vec{x}') = \nabla_{\vec{x}'}(\phi(\vec{x}')) = \frac{c\sigma(\vec{x}')}{2} + \frac{1}{4\pi} \nabla_{\vec{x}'} \oint_{S_B} \sigma \frac{1}{\|\vec{x} - \vec{x}'\|} dS_B$$

Physical Interpretation

Traditional aerodynamic courses will present an intuitive interpretation of the above equations. The source singularity is important for approximating many flowfield effects. Through the superposition of source and sink (negative sources) sheets, many diverse geometries in a flow can be analyzed. Here σ represents the surface mass emission density. The approach taken to solve a flow using the above formulation is to smear a single layer distribution with an unknown density over the surface of

the geometry. By placing a varying single layer source distribution over the entire body, a velocity field is set up. By adjusting the strength of the source distribution, so that the no-fluid-penetration boundary condition is satisfied, a unique solution of the Laplace governed potential flow results.

The Lack of a Lifting Model In the Source Only Formulation

The source only velocity formulation does not allow the specification of a lifting body problem. This is due to the inability of the source singularity to cause a net circulation around the body, through a potential jump. In order to satisfy a lifting body formulation, a non-zero circulation around the airfoil must be imposed. In order to do this in the source only formulation, the addition of a singularity capable of producing a vortex-like effect is necessary

Resolution of the Farfield Behavior for the Direct Integral Equation

The boundary condition on the farfield requires that the potential decays as:

$$\lim_{\vec{x} \rightarrow \infty} \vec{v}(\vec{x}) \rightarrow \frac{1}{|\vec{x}^3|}$$

As a consequence the perturbation potential decays as, $\frac{1}{|\vec{x}|^2}$ in the farfield. The single layer potential will decay as $\frac{1}{\vec{x}}$ in most applications. If a net zero integrated source exists on the body, the potential will decay as $\frac{1}{\vec{x}^2}$. The boundary condition applied in this case is:

$$\vec{V}_{\infty} \cdot \hat{n}_{\vec{x}} = \vec{v} \cdot \hat{n}$$

This boundary condition on the single layer velocity has a net zero integral on the surface. The resulting source distribution also has a net zero surface integral. This results in a similar situation as seen in the Direct Potential case. Once again the source strength is seen to produce an x-wise doublet-like effect in the farfield. Once again, this is due to:

1) The single layer surface strength has a zero total surface integral. As a result, in

the farfield the $\frac{1}{x}$ effect is canceled out.

2) Since there is a lumping of positive single layer strength in the front of a body and a lumping of negative single layer in the trailing region of a body (by property of the surface boundary condition), the farfield effect looks like a doublet aligned in the flowwise direction. Essentially defining the correct $\frac{1}{|\vec{x}|^2}$ decay of the perturbation potential.

Figure 2-18 demonstrates this created doublet effect for an infinite span elliptical cross section member.

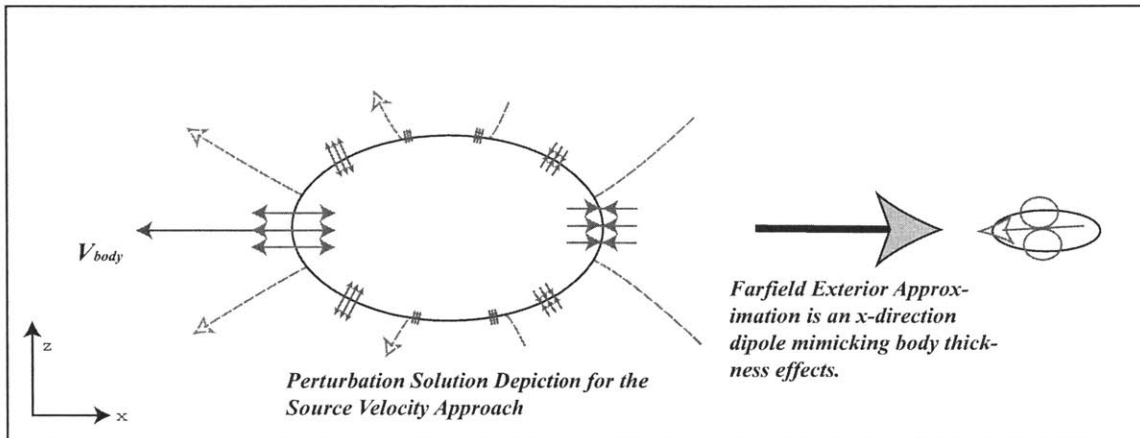


Figure 2-18: The flow modeled with a source singularity on the surface, will mimic a doublet in the farfield, hence have $\frac{1}{x^2}$ potential decay.

2.7.2 The Pure Dipole Case : The Indirect BIE Formulation

[4]

With the velocity formulation for the single layer distribution described, the analogue for the double layer is determined in the current sub-section.

Starting again from the expression for the internal-external problem and forcing the following relation (Equation - (BIE - 1)):

$$\left[\frac{\partial \phi}{\partial n} \right]_i = \left[\frac{\partial \phi}{\partial n} \right]_e$$

for points, \vec{x} on the surface of the body, S_B , it is obvious that the elimination of

the source term in the external-internal BIE will occur. The resulting BIE for the potential at a point, \vec{x}' , is expressed:

$$\phi(\vec{x}') = \frac{1}{4\pi} \int \int_{S_B} \left(\mu \frac{\partial}{\partial n_x} \frac{1}{|\vec{x} - \vec{x}'|} \right) dS_B$$

The Velocity Boundary Condition Application

With an equation expressing the potential based solely on the double layer singularity distribution, μ , the solution of the BIE implementing the physical flow boundary conditions is approached. Starting from:

$$\phi(\vec{x}') = \frac{1}{4\pi} \int \int_{S_{B+W}} \mu \frac{\partial}{\partial n_x} \frac{1}{\|\vec{x} - \vec{x}'\|} dS_{B+W}$$

Expressing the BIE in terms of a velocity expression on the flow, a gradient of both sides is taken:

$$\vec{v}(\vec{x}') = \nabla_{\vec{x}'}(\phi(\vec{x}')) = \frac{1}{4\pi} \nabla_{\vec{x}'} \int \int_{S_{B+W}} \mu \frac{\partial}{\partial n_x} \frac{1}{\|\vec{x} - \vec{x}'\|} dS_{B+W}$$

The self term, when \vec{x} and \vec{x}' are coincident, is in fact a hypersingular expression.

Boundary Integral Equation which is Solved

To satisfy the given boundary equations, $-\vec{V}_\infty(\vec{x}') \cdot \hat{n}_{\vec{x}'} = \vec{v}(\vec{x}') \cdot \hat{n}_{\vec{x}'}$, the dot product of the expressed velocity at a point \vec{x}' , with the surface normal must be computed, at the point, \vec{x}' , where the boundary condition is to be satisfied. This is the dipole, or double layer induced surface normal velocity at that point.

$$-\vec{V}_\infty(\vec{x}') \cdot \hat{n}_{\vec{x}'} = \vec{v}(\vec{x}') \cdot \hat{n}_{\vec{x}'} = \nabla_{\vec{x}'}(\phi(\vec{x}')) \cdot \hat{n}_{\vec{x}'} = \frac{1}{4\pi} \nabla_{\vec{x}'} \cdot \hat{n}_{\vec{x}'} \int \int_{S_{B+W}} \mu \frac{\partial}{\partial n_x} \frac{1}{\|\vec{x} - \vec{x}'\|} dS_{B+W}$$

The unknown distribution of the double layer, μ , can be determined from this expression.

Postprocessing the Solution

Once the distribution of the doublet has been computed, the potential at any point \vec{x}' in the domain, can be determined by back substitution into:

$$\phi(\vec{x}') = \frac{1}{4\pi} \int \int_{S_{B+W}} \mu \frac{\partial}{\partial n_x} \frac{1}{\|\vec{x} - \vec{x}'\|} dS_{B+W}$$

The velocity distribution may also be computed using:

$$\vec{v}(\vec{x}') = \nabla_{\vec{x}'}(\phi(\vec{x}')) = \frac{1}{4\pi} \nabla_{\vec{x}'} \int \int_{S_{B+W}} \mu \frac{\partial}{\partial n_x} \frac{1}{\|\vec{x} - \vec{x}'\|} dS_{B+W}$$

Resolution of the Farfield Behavior for the Integral Equations: Indirect Dipole Velocity Formulation

The boundary condition on the farfield requires the potential decays as:

$$\lim_{|\vec{x}| \rightarrow \infty} \vec{v}(x) \rightarrow \frac{1}{|\vec{x}^3|}$$

As a consequence the perturbation potential decays as, $\frac{1}{|\vec{x}|^2}$ in the farfield.

The double layer satisfies the infinity boundary condition by definition. Since the double layer potential decays as $\frac{1}{|\vec{x}|^2}$, and the velocity decays as $\frac{1}{|\vec{x}|^3}$ in the limit as infinity is approached. Hence, as a result the double layer automatically satisfies the decay condition at infinity.

Looking at the example for a translating infinite cylinder (figure 2-19), it is seen that the cylinder doublet strengths approximate an overall doublet.

Physical Interpretation

Traditional aerodynamic courses will present an intuitive interpretation of the above equations. A partial surface with a doublet/dipole strength μ , will emit a net zero volume mass flow. By placing a varying double layer or doublet distribution over the entire body, a velocity field is set up. By adjusting the strength of the distribution so that the no-fluid-penetration boundary condition is satisfied, a unique solution of

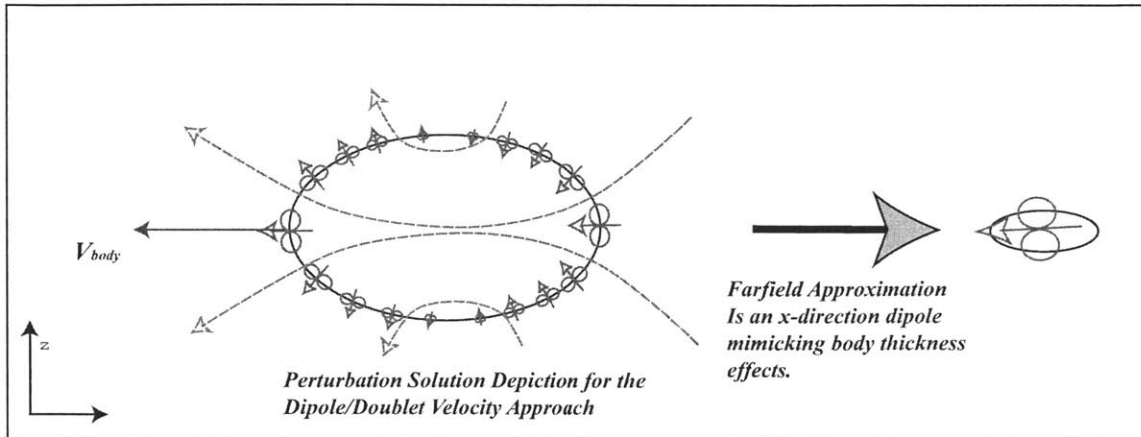


Figure 2-19: The flow modeled with a doublet singularity on the surface, will mimic a doublet in the farfield, hence have $\frac{1}{|\vec{x}|^2}$ potential decay.

the Laplace governed potential flow for the case results. The resulting singularity distribution on the surface will define the potential uniquely at all points in the domain.

2.8 A Comparison of the Solution Approaches

The optimal panel method formulation is problem dependent. The following discussion outlines the various differences, advantages and disadvantages of the direct potential and indirect velocity formulations:

Potential Based Direct Formulation

- Optimal method for closed bodies with finite thickness
- The potential solution is easy to compute
- The lifting and non-lifting solutions can be computed without distinction

Neumann Velocity Based Indirect Formulations

- The only method available for thin membrane analysis (yacht sails)
- The velocity solution requires the computation of the gradient, a more costly operation

- Lifting solutions require a mixed formulation

2.9 Chapter Summary

In this chapter the theoretical foundation was laid for the Boundary Integral Equation representation of the potential flow problem. First a potential flow expression was defined for the external aerodynamics problem. Following this the boundary integral equations were derived from a differential statement of the potential flow equation. As a result two separate approaches were explored, the potential approach, and the velocity approach. The velocity approach was seen to have a dual implementation, one for the double layer, and the other for the single layer.

A summary of the boundary integrals derived, which will be used in the discrete solution:

Single Layer Neumann Velocity Boundary Integral Equation:

$$-\vec{V}_\infty(\vec{x}') \cdot \hat{n}_{\vec{x}'} = \vec{v}(\vec{x}') \cdot \hat{n}_{\vec{x}'} = \nabla_{\vec{x}'}(\phi) \cdot \hat{n}_{\vec{x}'} = \frac{c\sigma(\vec{x}')}{2} + \frac{1}{4\pi} \nabla_{\vec{x}'} \cdot \hat{n}_{\vec{x}'} \oint_{S_B} \sigma \frac{1}{\|\vec{x} - \vec{x}'\|} dS_B$$

Double Layer Neumann Velocity Boundary Integral Equation:

$$-\vec{V}_\infty(\vec{x}') \cdot \hat{n}_{\vec{x}'} = \vec{v}(\vec{x}') \cdot \hat{n}_{\vec{x}'} = \nabla_{\vec{x}'}(\phi(\vec{x}')) \cdot \hat{n}_{\vec{x}'} = \frac{1}{4\pi} \nabla_{\vec{x}'} \cdot \hat{n}_{\vec{x}'} \int \int_{S_B} \mu \frac{\partial}{\partial n_x} \frac{1}{\|\vec{x} - \vec{x}'\|} dS_B$$

Potential Based Dirichlet Equation:

$$\phi(\vec{x}) = \frac{1}{4\pi} \int \int_{S_B} -\vec{V}_\infty \cdot \hat{n} \frac{1}{\|\vec{x} - \vec{x}'\|} dS_B - \frac{1}{4\pi} \int \int_{S_{B+W}} \phi \frac{\partial}{\partial n} \left(\frac{1}{\|\vec{x} - \vec{x}'\|} \right) dS_{B+W}$$

Finally the lifting body problem is considered. A Morino Kutta condition [40] will be implemented in the discrete version of the solution. The wake strength is governed by:

$$\phi_{wake} = \phi_u - \phi_l$$

Following this chapter, the discrete solution of the Boundary Integral Equations, by a Boundary Element Method (BEM) is presented. The Boundary Element Method implementation is described in some detail in the following chapter.

Chapter 3

The Boundary Element Method Implementation

3.1 Introduction

The numerical solution of the Boundary Integral Equations for potential flow is described in this chapter. The following sections outline the multistep process of setting up a linear system of equations. The majority of this chapter is the presentation of both constant strength and linear strength planar panel integral influences are presented.

The linear Galerkin, the constant Galerkin and constant collocation schemes are investigated later in the chapter. The presentation provides the direct Boundary Element Method(BEM) approach without any simplification. In Chapter 4, acceleration using a pFFT algorithm is described.

3.1.1 General Solution Flow Chart

The implementation of the direct solver boundary element method approach is summarized in figure 3-1:

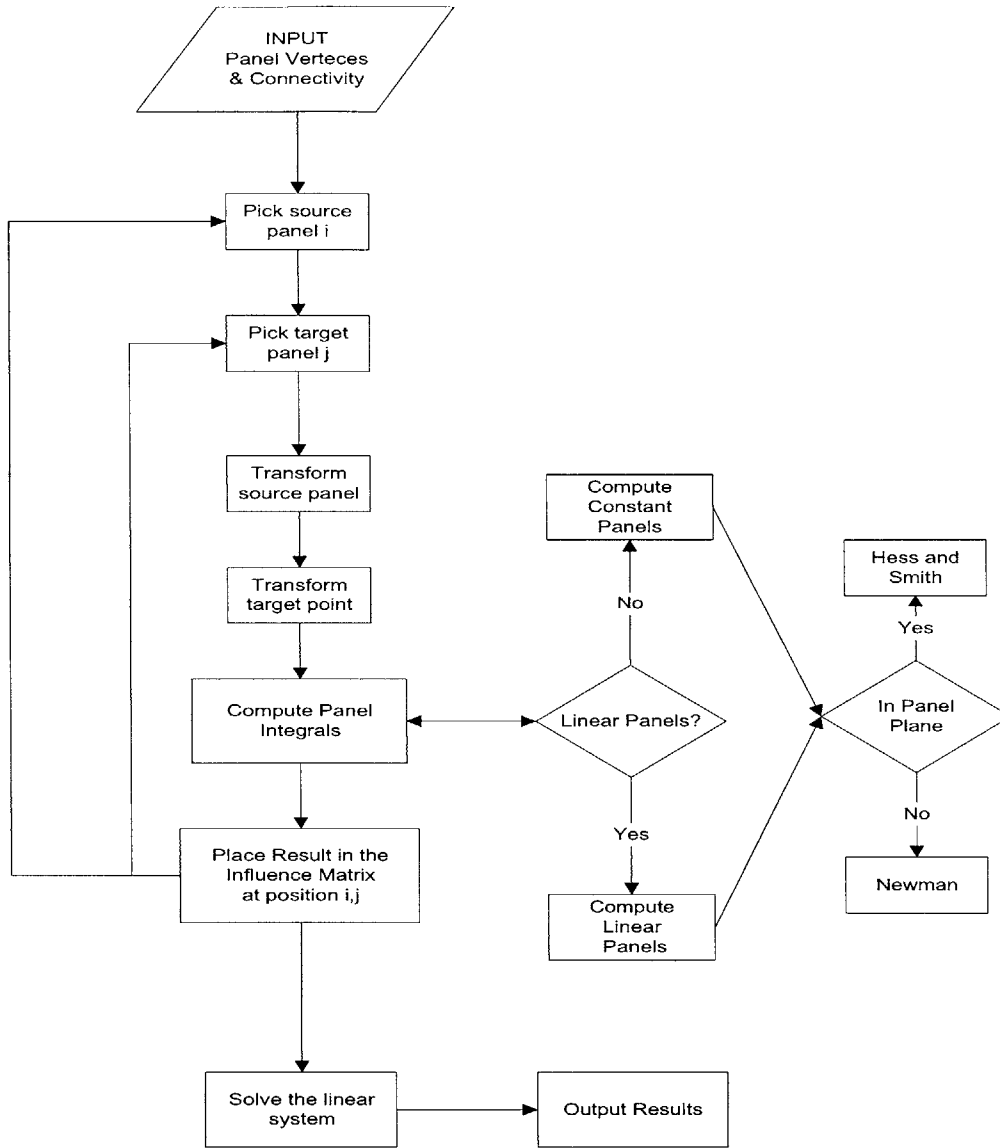


Figure 3-1: General Flow Chart of the solution, and chapter overview.

3.2 Discrete Solution Procedure

The discrete form of the Boundary Integral Equations, derived in Chapter 2, are used in the Boundary element solution. By discretizing the body surface into *panels* and forcing the boundary conditions at *control points* or *evaluation points*, a linear system representing the surface integral formulation is formed.

3.2.1 The Discrete Equations

As a result of the discretization, the boundary integral equations are expressed discretely. The continuous integrals over the surface of the body, become summations over a finite set of panels covering the surface of the body.

Source - Velocity Indirect Formulation

$$\vec{v}(\vec{x}') \cdot \hat{n}_{\vec{x}'} = \nabla_{\vec{x}'}(\phi(\vec{x}')) \cdot \hat{n}_{\vec{x}'} = \frac{c\sigma\delta_{ii}}{2} + \frac{1}{4\pi} \sum_{n=1}^{n=NP} \nabla_{\vec{x}'} \cdot \hat{n}_{\vec{x}'} \oint_{S_{Panel_n}} \sigma(\vec{x}) \frac{1}{\|\vec{x} - \vec{x}'\|} dS_{Panel_n}$$

Dipole - Velocity Indirect Formulation

Double Layer Neumann Velocity Boundary Integral Equation:

$$\vec{v}(\vec{x}') \cdot \hat{n}_{\vec{x}'} = \nabla_{\vec{x}'} \cdot \hat{n}_{\vec{x}'} \phi(\vec{x}) = -\frac{1}{4\pi} \sum_{n=1}^{n=NP} \frac{\partial}{\partial \hat{n}_{\vec{x}'}} \int \int_{S_{Panel_n}} \mu(\vec{x}) \left(\frac{\partial}{\partial \hat{n}_{\vec{x}}} \left(\frac{1}{\|\vec{x} - \vec{x}'\|} \right) \right) dS_{Panel_n}^{B+W}$$

Potential - Direct Formulation

Potential Based Dirichlet Equation:

$$\phi(\vec{x}) = \frac{1}{4\pi} \sum_{n=1}^{n=NP} \int \int_{S_{Panel_n}} -V_{\infty} \cdot \hat{n} \frac{1}{\|\vec{x} - \vec{x}'\|} dS_{Panel_n} - \frac{1}{4\pi} \sum_{n=1}^{n=NP} \int \int_{S_{Panel_n}} \phi \frac{\partial}{\partial n} \left(\frac{1}{\|\vec{x} - \vec{x}'\|} \right) dS_{Panel_n}^{B+W}$$

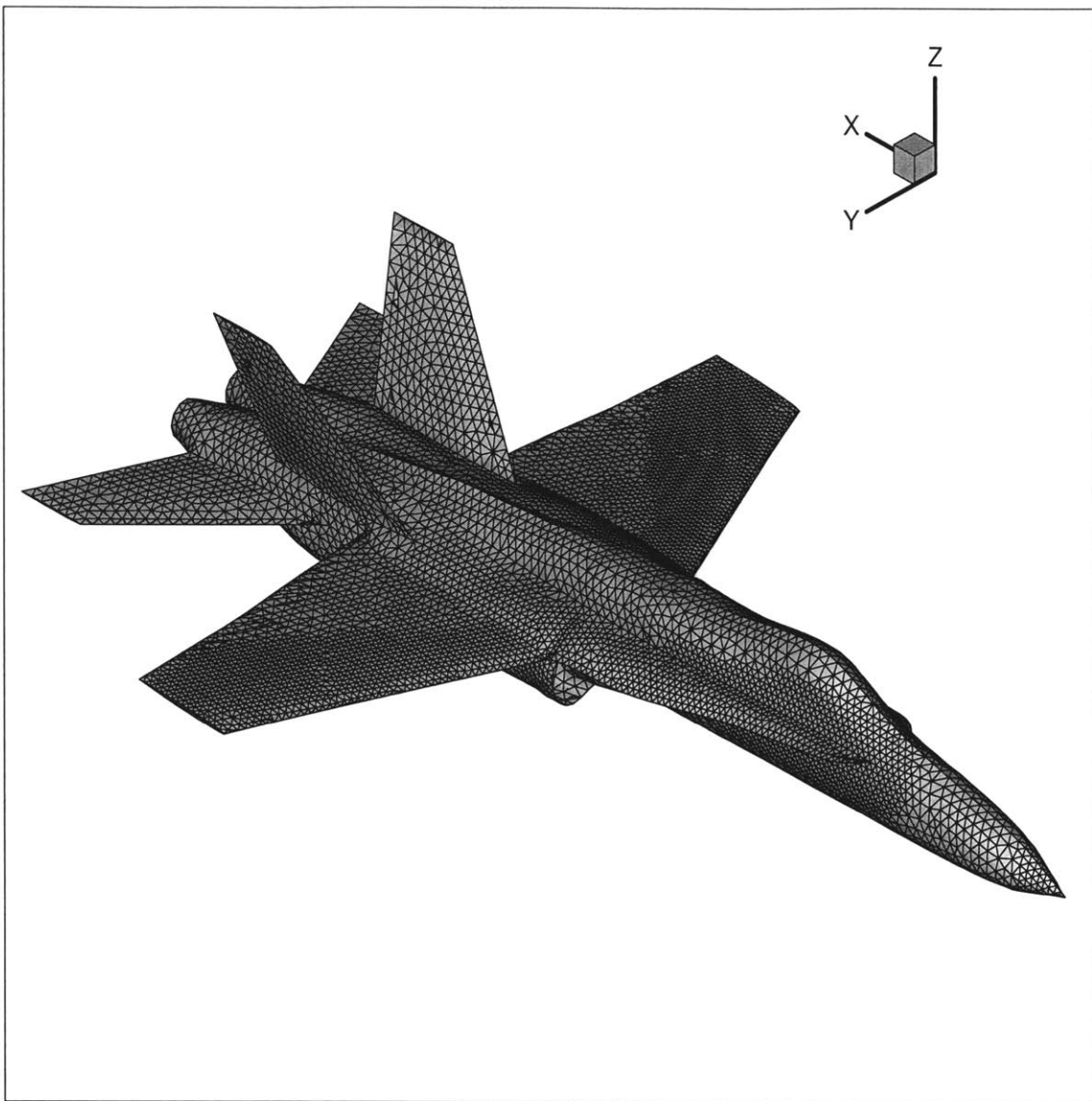
3.2.2 Discretizing the Surface of the Body

In this work the body is discretized using surface triangular panels. Figure 3.2.2 shows an F18 surface discretization without wake panels.

Why Triangular Panels?

Advantages of using triangles are:

- 1) Triangles model arbitrary surfaces without leaks. Higher order flat polygonal shapes allow leakage between panels.
- 2) Triangular panels have simple linear basis functions. They are independent of bilinear shape functions.
- 3) There are several commercial and research codes available to generate triangular



F-18 Fighter Jet, without a wake model, discretized using triangular panels [41]

surface discretizations.

4) Triangles are the basic polygon in creating other higher order 2-D polygons. All discretizations can be reduced to their sub-triangles.

5) Triangular meshes can be expressed in a consistent and simple manner using vertex coordinate data and connectivity data. This simplifies the computation of the linear basis footprint, and it allows a generic input file.

The presentation of most of the formulae in this chapter are general enough to extend to higher dimensional planar elements.

3.3 Computing the Panel Integrals

Expressions of the surface panel integrals must be determined. The steps taken to compute a surface panel integral are:

- 1) The panel is first transformed into a new panel based coordinate system (ξ, η, z') .
- 2) The evaluation point(s) are also transformed to the new coordinate system.
- 3) The appropriate panel integrals are computed.

The following section describes the above steps.

3.3.1 (1) Transforming Triangular Panels from (x, y, z) to (ξ, η, z') Coordinates [5]

Figure 3-2 outlines the transformation from an arbitrary 3-Dimensional space (x, y, z) , to a pseudo 2-Dimensional panel based coordinate system (ξ, η, z') :

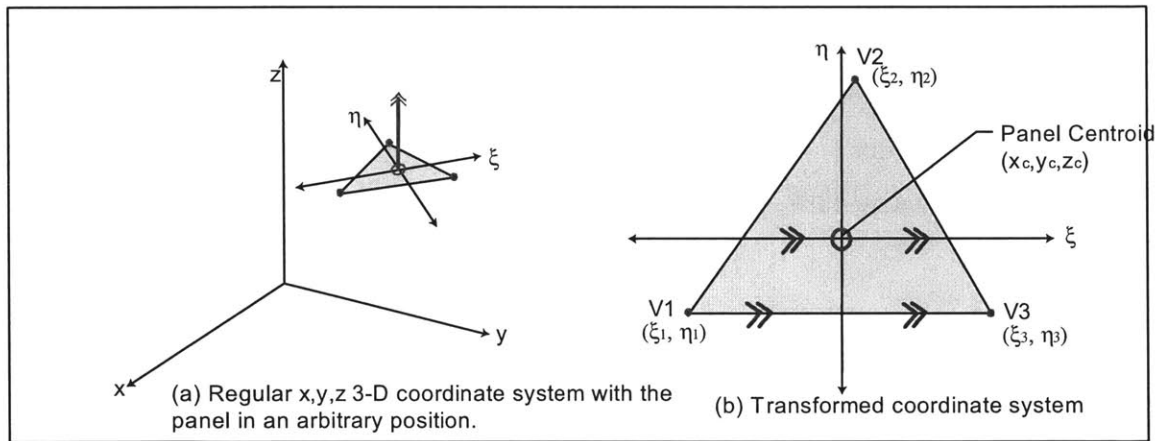


Figure 3-2: The coordinate transform. Here the triangle in x, y, z is transformed to an in-plane, ξ, η, z' representation.

Properties of the transformation:

- The panel lies in the $z' = 0$ plane.
- The panel centroid lies at the (ξ, η, z') coordinate origin.
- Side 2 of the panel is parallel with the ξ axis.
- The panel is not rescaled at all during the transformation.

The panel transform algorithm is outlined in more detail in Appendix A. It is identical

to that presented by White [5]. The coordinate transform chosen is particularly suited to the linear panel integral approach presented later in the chapter.

3.3.2 2) Transforming Evaluation Points from (x, y, z) to (ξ, η, z') Coordinates [5]

The evaluation points and normals are also transformed into the panel based coordinate system. This is done to ensure consistency in the computation of the panel integrals.

3.3.3 (3) Computing the Panel Integrals

There are several different methods to evaluate the panel integral equations.

- 1) Analytic panel integrals [6], [7]
- 2) Multipole expansions [23], [24]
- 3) Quadrature based integrals

Analytic panel integrals are described in depth.

3.4 Computing the Analytic Panel Integrals

The analytic panel integrals for the potential flow problem are presented. Methods by Hess and Smith, [6], and Newman [7] are presented in overview. Following that, the analytic panel influence integrals for the constant and linear panel basis functions are presented.

3.4.1 Hess and Smith [6]: Analytic Panel Integrals

Hess and Smith suggest a panel integral evaluation in their early work [6]. For a detailed derivation the reader is referred to their original paper on the subject [6]. The pertinent approach is presented to allow the reader insight into the method's behavior.

Hess and Smith suggest a variable substitution in the integrand, in effect forming an integration over the z' plane. The integral:

$$\phi(\vec{x}') = \int \int_S \frac{1}{\|\vec{x} - \vec{x}'\|} dS$$

is transformed through a variable substitution ($\|\vec{x} - \vec{x}'\| = \sqrt{(R^2 + h^2)}$) to:

$$\phi = \oint_{\text{Perimeter}} \int_0^R \frac{RdRd\theta}{\sqrt{(R^2 + z^2)}}$$

The perimeter integral is evaluated for each side of the panel, as presented in figure 3-3.

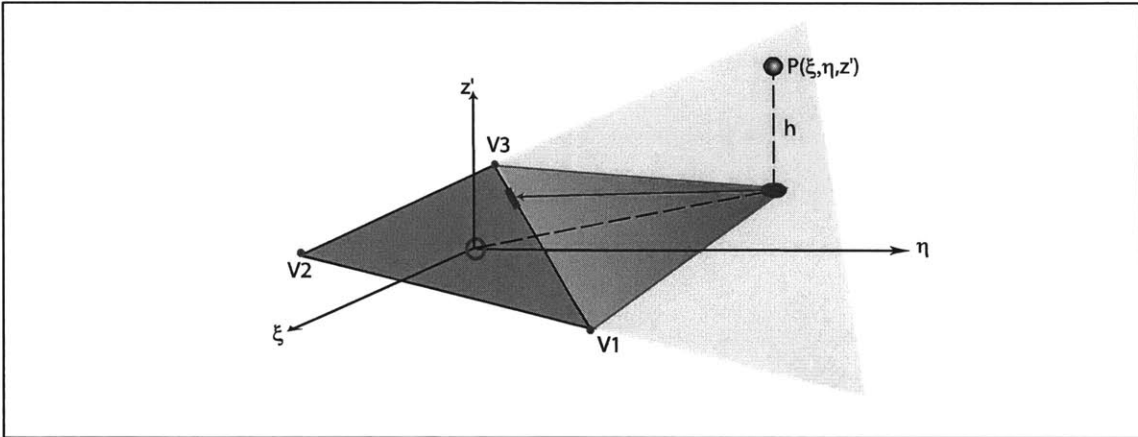


Figure 3-3: Pictorial representation of the perimeter integral for a side of the triangle

By summing up the perimeter integrals appropriately, the computation of the full integral results (see figure 3-4).

Comments on the Hess and Smith Method:

The Hess and Smith panel integral influence computation is most appropriate when the evaluation point, (\vec{x}') , lies in the region, or near the region of the extended plane of the panel (see figure 3-5. This is due to the substitution of variables leading to an "in-plane" computation of the integral.

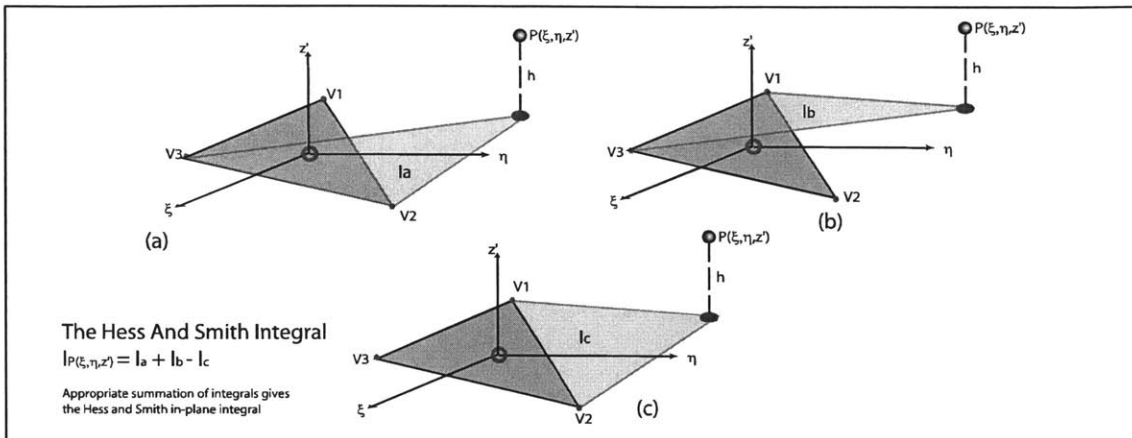


Figure 3-4: Adding and subtracting the various perimeter integrals to attain the final panel integral result.

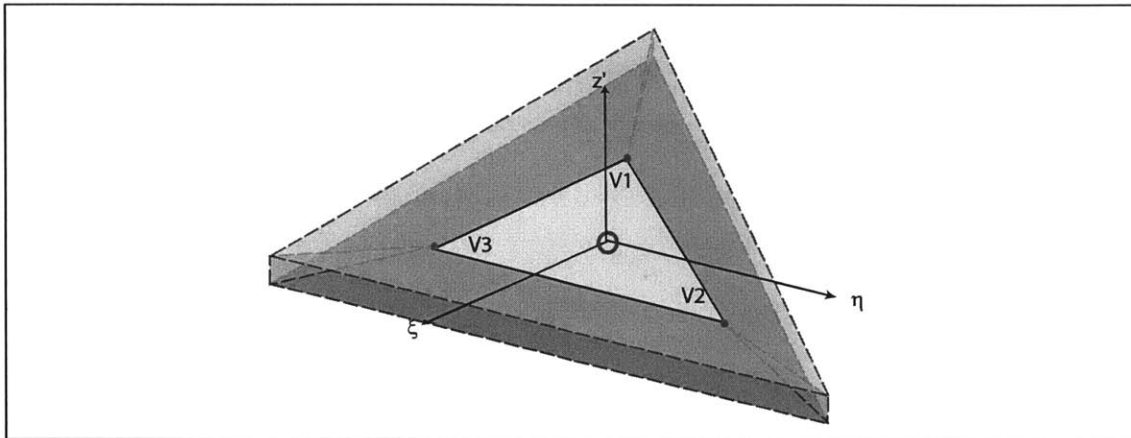


Figure 3-5: The Hess and Smith method is most accurate in the "near-in-plane" region of the space. The shaded grey wedge shaped regions outline the areas in which the integration method is most accurate.

3.4.2 Newman [7]: Analytic Panel Integrals

Another approach to determining the panel integral influence was presented by Newman [7]. Once again the reader is recommended to consult the appropriate references for additional in depth-derivations pertaining to the method.

Newman suggested the use of a fundamental theorem of differential geometry, the Gauss-Bonnet theorem. In his approach, the evaluation point is surrounded by a unit sphere. Following this, the panel is projected onto the unit sphere. At this point, the Gauss-Bonnet theorem provides a relationship between the panel influence integral

and the projected panel's solid angle(essentially the summation of deformed angles on the spherical surface). Figure 3-6 shows the general principle. In addition, the warping of the panel when projected on the unit sphere is shown. The mechanics of the solid angle summation are presented in detail in Newman's original paper on the subject.

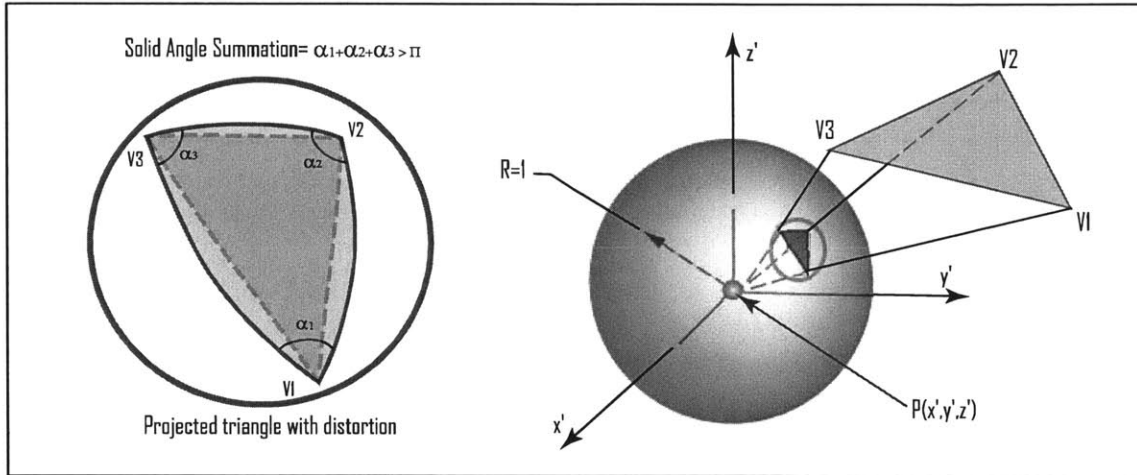


Figure 3-6: A panel projected onto a unit sphere. The included angles and distortion of the panel is apparent in the inset diagram of the panel.

Comments on the Newman Method

The Newman integration method yields particularly accurate results when the field point lies in the region above the panel (see figure 3-7). When the evaluation point approaches the plane of the panel, the projected panel becomes a line, which causes inaccuracies in the computation of the solid angle.

3.5 The Panel Integrals : The Constant Strength Basis Function Equations

The specific panel influence integrals which are used in the computation of the resulting linear BEM system are presented. Both Newman and Hess and Smith approaches are presented. Figure 3-8 shows the constant basis shape function.

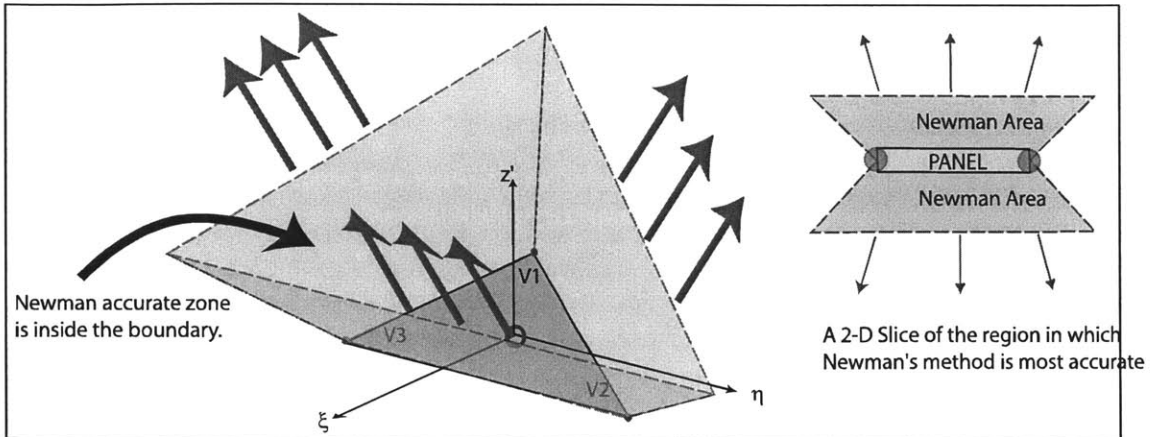


Figure 3-7: The area in which the Newman integration method is most appropriate. Contrary to the Hess and Smith method, Newman's method is most accurate in the regions directly above and below the panel.

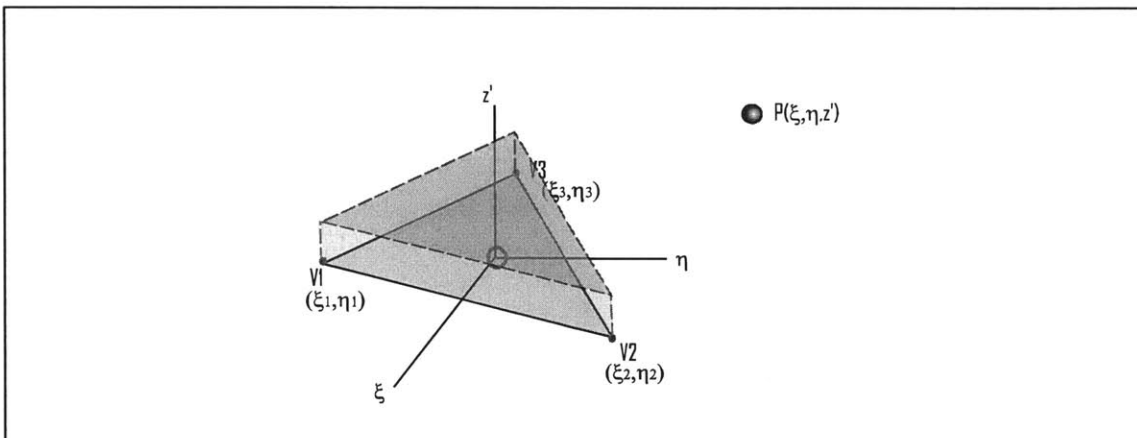


Figure 3-8: The constant strength shape function used in the computations

Panel Integral Notation:

The notation used for the panel influence integrals is outlined in figure 3-9.

In Mathematical form:

Panel Side length:

$$l_i = \sqrt{(\xi_{i+1}^S - \xi_i^S)^2 + (\eta_{i+1}^S - \eta_i^S)^2}$$

Component lengths:

$$l_i^\xi = \xi_{i+1}^S - \xi_i^S$$

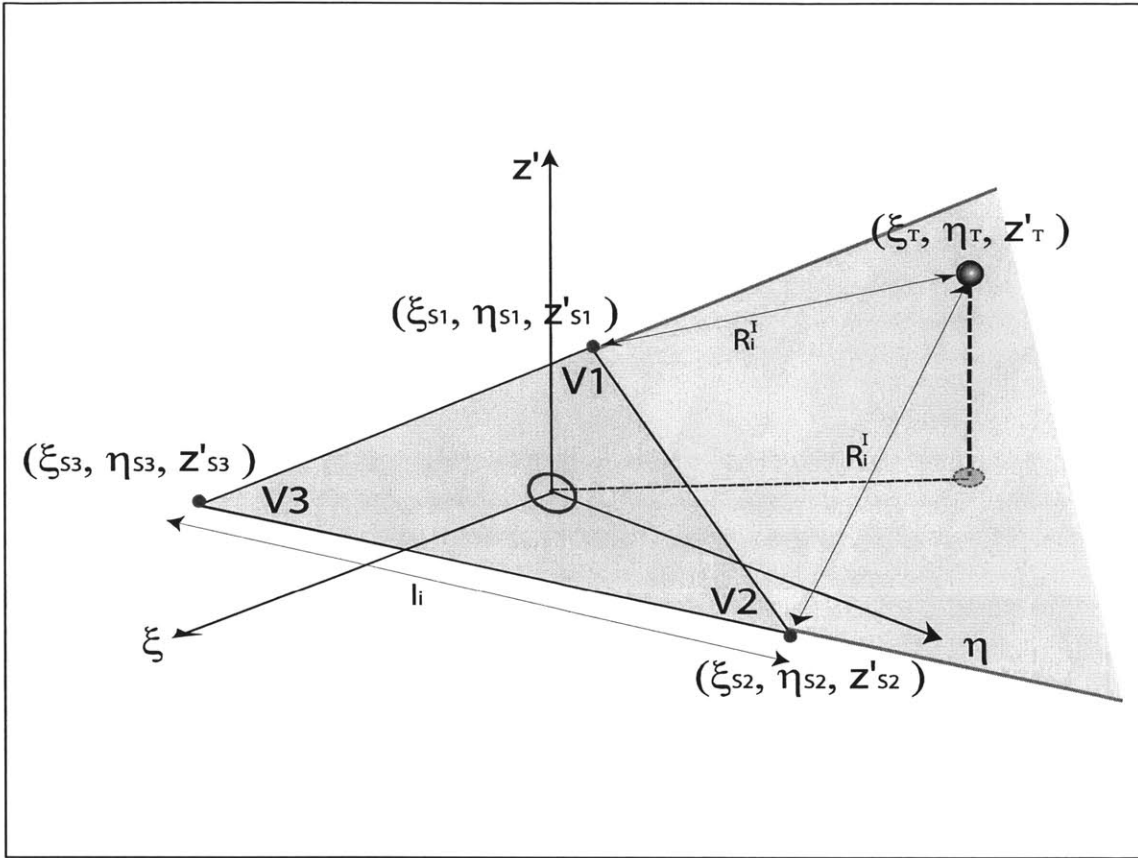


Figure 3-9: A triangle outlining the notation for the panel integrals in the sections that follow. Notice the labeling of the vertices with respect to the ξ, η axes, since the computations for the linear shape functions rely heavily on the ordering.

$$l_i^\eta = \eta_{i+1}^S - \eta_i^S$$

Panel trigonometric relations:

$$\sin(\theta_i^P) = \frac{l_i^\eta}{l_i}$$

$$\cos(\theta_i^P) = \frac{l_i^\xi}{l_i}$$

Side length delta's:

$$\Delta \xi_i^{ST} = \xi_i^S - \xi_i^T$$

$$\Delta \eta_i^{ST} = \eta_i^S - \eta_i^T$$

$$\Delta z_i'^{ST} = z_i'^S - z_i'^T$$

The in-plane vertex radius:

$$R_i^I = \sqrt{(\Delta\xi_i^{ST})^2 + (\Delta\eta_i^{ST})^2 + (\Delta z_i^{ST})^2}$$

A defined value Q_i :

$$Q_i = \log \left(\frac{R_i^I + R_{i+1}^I + l_i}{R_i^I + R_{i+1}^I - l_i} \right)$$

The panel integrals presented are applicable to any n -sided polygonal shape.

3.5.1 Constant Strength Double Layer/Doublet Panel Integrals

The constant strength double layer integral is the basic building block of all of the subsequent panel integrals. This is because the double layer influence is the panel normal derivative of the single layer influence. The double layer integral being computed is:

$$\psi_M^c(\xi^T, \eta^T, z^T) = \int \int_{Panel} \rho_c \cdot \frac{\partial}{\partial \hat{n}_{Panel}} \frac{1}{\|\vec{x} - \vec{x}'\|} dS_{Panel}$$

Where, $\psi_M^c(\xi^T, \eta^T, z^T)$: Is the potential (denoted ψ to distinguish it is a double layer), due to a constant basis (denoted c), evaluated at a target field point (T), with coordinates (ξ^T, η^T, z^T) , using computation method M (M is *H.S.* for a Hess and Smith approach, and *N* for a Newman approach).

ρ_c : represents the density per surface area of the constant shape function. In this computation, $\rho = 1$

Hess and Smith – Constant Double Layer Panel Influence Integral Expression [6]

The Hess and Smith computed potential at a target evaluation point (ξ^T, η^T, z'^T) , due to a double layer panel (the panel is denoted the source, S):

$$\psi_{H.S}^c(\xi^T, \eta^T, z'^T) = \sum_{i=1}^{i=NV} \left(\arctan \left[\frac{l_i^\eta \cdot \left((\Delta \xi_i^{ST})^2 + (\Delta z_i'^{ST})^2 \right) - (\Delta \xi_i^{ST})(\Delta \eta_i^{ST})}{(\Delta z_i'^{ST}) \cdot \sqrt{(\Delta \xi_i^{ST})^2 + (\Delta \eta_i^{ST})^2 + (\Delta z_i'^{ST})^2}} \right] - \right. \\ \left. \sum_{i=1}^{i=NV} \arctan \left[\frac{l_i^\eta \cdot \left((\Delta \xi_{i+1}^{ST})^2 + (\Delta z_{i+1}'^{ST})^2 \right) - (\Delta \xi_{i+1}^{ST})(\Delta \eta_{i+1}^{ST})}{(\Delta z_{i+1}'^{ST}) \cdot \sqrt{(\Delta \xi_{i+1}^{ST})^2 + (\Delta \eta_{i+1}^{ST})^2 + (\Delta z_{i+1}'^{ST})^2}} \right] \right)$$

Newman – Constant Double Layer Panel Influence Integral Expression [7]

In order to compute the integral for the Newman method, several terms are defined :

$$s_i^a = l_i^\eta \cdot \left((\Delta \xi_i^{ST})^2 + (\Delta z_0'^{ST})^2 - l_i^\xi \cdot \Delta \xi_i^{ST} \cdot \Delta \eta_i^{ST} \right)$$

$$s_i^b = l_i^\eta \cdot \left((\Delta \xi_{i+1}^{ST})^2 + (\Delta z_0'^{ST})^2 - l_i^\xi \cdot \Delta \xi_{i+1}^{ST} \cdot \Delta \eta_{i+1}^{ST} \right)$$

$$c_i^a = R_i^I \cdot \Delta z_0'^{ST} \cdot l_i^\xi$$

$$c_i^b = R_{i+1}^I \cdot \Delta z_0'^{ST} \cdot l_i^\xi$$

The final result is:

$$\psi_N^c(\xi^T, \eta^T, z'^T) = - \sum_{i=1}^{i=NV} \arctan \left(\frac{s_i^a \cdot c_i^b - s_i^b \cdot c_i^a}{c_i^a \cdot c_i^b + s_i^a \cdot s_i^b} \right)$$

Potential Scans for the Constant Double Layer Panel Integrals

Potential scans for the double layer panel potential influence integral are presented in figures 3-10 through 3-12. These are plots outlining the values of the potential due to the panel at various points on a designated plane.

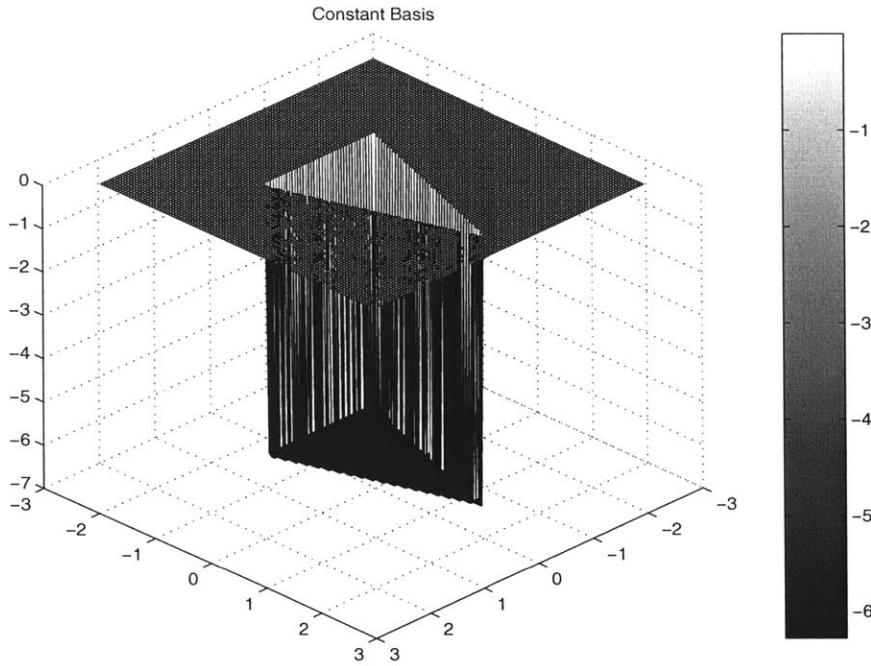


Figure 3-10: A 3-D potential plot for a double layer sample panel with vertices $[V1(0, 2, 0), V2(1, -1, 0), V3(-1, -1, 0)]$, evaluated in the plane $z' = +\epsilon$.

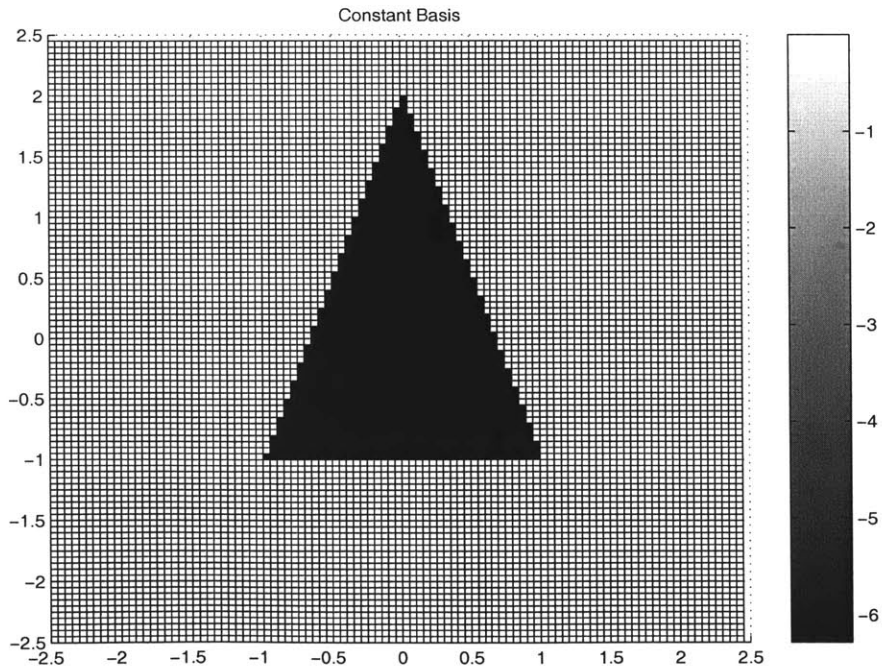


Figure 3-11: A 2-D potential plot for a double layer sample panel with vertices $[V1(0, 2, 0), V2(1, -1, 0), V3(-1, -1, 0)]$, evaluated in the plane $z' = +\epsilon$.

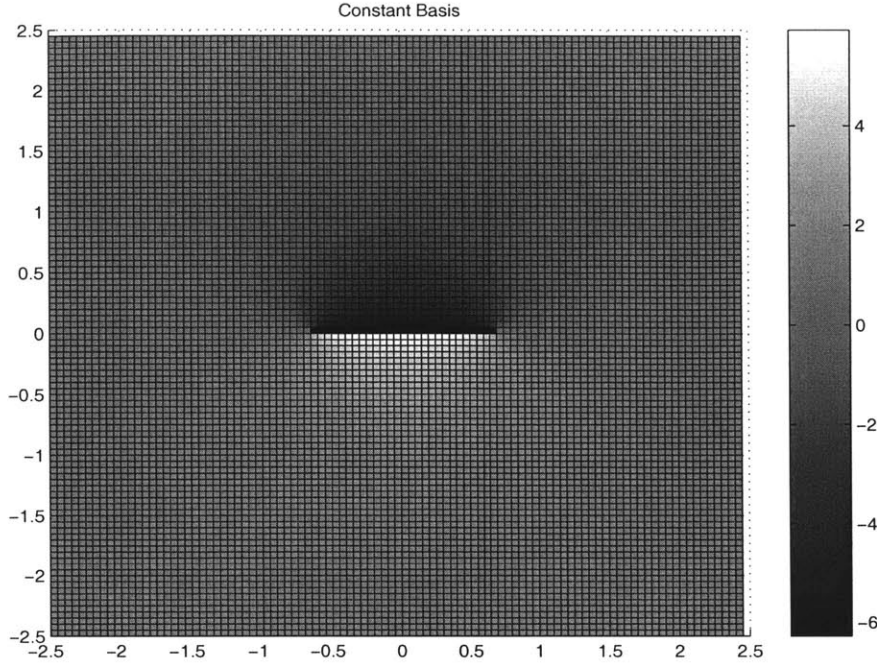


Figure 3-12: A 2-D potential plot for a double layer sample panel with vertices $[V1(0, 2, 0), V2(1, -1, 0), V3(-1, -1, 0)]$, evaluated in the plane $\eta = 0$.

3.5.2 Constant Strength Single Layer Panel Influence Integral

The single layer panel influence integral computation is expressed over a panel:

$$\phi_M^c(\xi^T, \eta^T, z'^T) = \int \int_{Panel} \rho_c \cdot \frac{1}{\|\vec{x} - \vec{x}'\|} dS_{Panel}$$

Where,

$\phi_M^c(\xi^T, \eta^T, z'^T)$: Is the potential (denoted ϕ to distinguish it is a single layer), due to a constant basis (denoted c), evaluated at a target point (T), with coordinates (ξ^T, η^T, z'^T) , using computation method M (M is *H.S.* for a Hess and Smith approach, and N for a Newman approach).

ρ_c : represents the density per surface area of the constant shape function. In this computation, $\rho = 1$.

By recognizing the double layer integral is the panel normal derivative of the single layer potential, the integration in is simplified.

Hess and Smith – Single Layer Potential Panel Influence Integral Evaluation [6]

The potential at a target point (T) due to a single layer panel (S), computed using the Hess and Smith Approach [6], [8] is:

$$\phi_{H.S}^c(\eta_T, \xi_T, z_T) = -\Delta z_0'^{ST} \cdot \psi_{H.S}^c(\eta^T, \xi^T, z^T) + \sum_{i=1}^{i=NV} Q_i \cdot (\Delta \xi_i^{ST} \cdot \sin(\theta_i^P) - \Delta \eta_i^{ST} \cdot \cos(\theta_i^P))$$

Newman – Single Layer Potential Panel Influence Integral Evaluation [7]

The potential at a target point (T) due to a single layer panel (S), computed using the Newman Approach [7] is:

$$\phi_N^c(\eta^T, \xi^T, z^T) = -\Delta z_0'^{ST} \cdot \psi_N^c(\eta^T, \xi^T, z^T) + \sum_{i=1}^{i=NV} Q_i \cdot (\Delta \xi_i^{ST} \cdot \sin(\theta_i^P) - \Delta \eta_i^{ST} \cdot \cos(\theta_i^P))$$

Comments and Comparison : Hess and Smith vs. Newman Methods

The Newman and Hess & Smith expressions are *identical*, apart from the double layer term ($\psi_{H.S}^c(\eta^T, \xi^T, z^T)$). Therefore, with the double layer integral computed previously, there is a single computation for the single layer (Hess and Smith [6], or Newman [7]).

Potential Scans for the Constant Single Layer Panel Influence Integrals

Scans of the potential due to the evaluation of a single layer panel influence integral are presented in figures 3-13-3-15.

3.5.3 The Velocity Formulation Integrals : Constant Strength

The indirect BIE, leading to the velocity formulation requires the gradient of the panel influence integrals, evaluated at the target point, T . In the following sections the velocity influences for a double and single layer constant strength integral are presented. The expressions compute the velocity influence of a panel in the three transformed coordinate directions, for the double and single layers respectively.

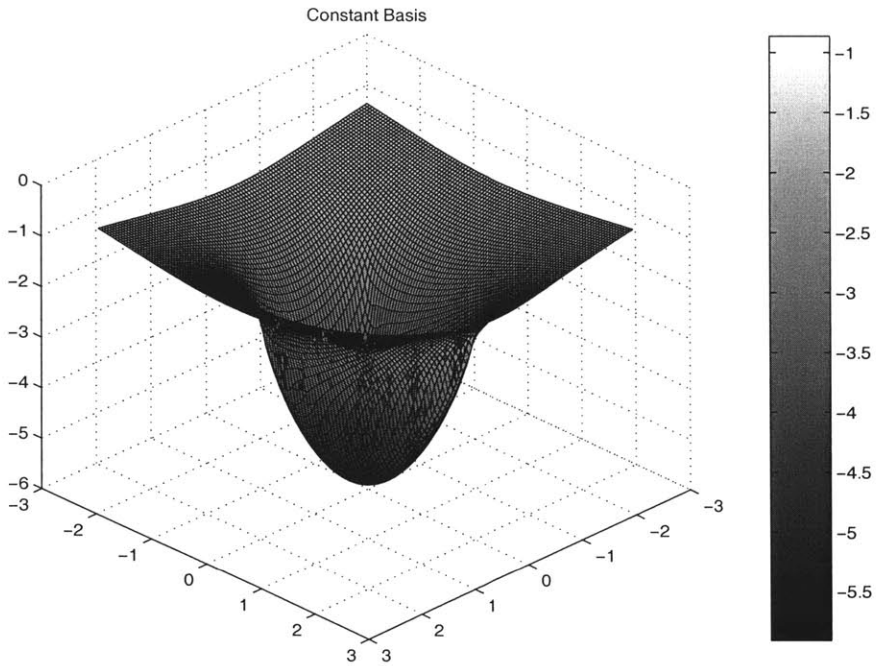


Figure 3-13: A 3-D potential mesh plot for a single layer constant sample panel integral with vertices $[V1(0, 2, 0), V2(1, -1, 0), V3(-1, -1, 0)]$, evaluated in the plane $z' = +\epsilon$.

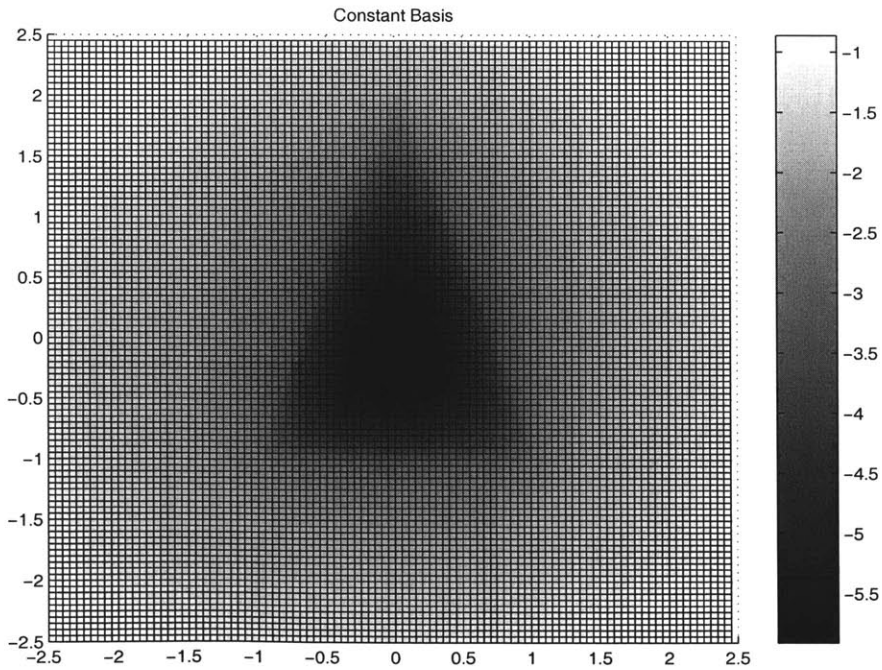


Figure 3-14: A 2-D potential plot for a single layer constant sample panel integral with vertices $[V1(0, 2, 0), V2(1, -1, 0), V3(-1, -1, 0)]$, evaluated in the plane $z' = 0$.

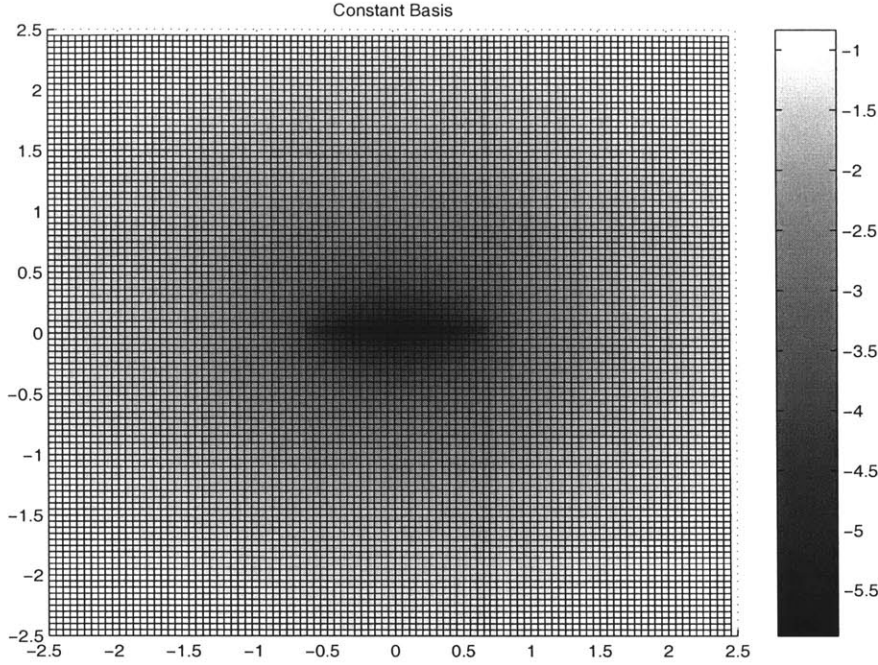


Figure 3-15: A 2-D potential plot for a sample panel $[V1(0, 2, 0), V2(1, -1, 0), V3(-1, -1, 0)]$, evaluated in the plane $\eta = 0$.

3.5.4 Constant Double Layer Gradient : Panel Influence Integral

The panel influence integral of the double layer gradient at a target point T , computes the following relation:

$$\nabla_T \left(\psi_M^c(\xi^T, \eta^T, z^T) \right) = \vec{v}(\xi^T, \eta^T, z^T) = \nabla_T \left(\int \int_{Panel} \rho_c \cdot \frac{\partial}{\partial \hat{n}_{Panel}} \frac{1}{\|\vec{x} - \vec{x}'\|} dS_{Panel} \right)$$

Where,

∇_T : Is the gradient evaluated at the target point, T . The gradient term is presented as the individual components in each of the transformed coordinate directions.

Hess and Smith – Constant Double Layer Gradient Panel Influence Integral [8]

If $\Delta z_0^{ST} = 0$, ie. the point is in the panel plane, a simplified panel influence integral exists.

First a simplification for the denominator term:

$$D_0 = \left((R_i^I)^2 \cdot (R_{i+1}^I)^2 + \Delta\xi_i^{ST} \cdot \Delta\xi_{i+1}^{ST} + \Delta\eta_i^{ST} \cdot \Delta\eta_{i+1}^{ST} \right)$$

The resulting in-plane, $\Delta z_0'^{ST} = 0$, panel integrals are:

The velocity in the ξ -direction:

$$\frac{\partial}{\partial \xi^T} (\psi_{H.S}^c(\xi^T, \eta^T, z'^T)) = 0$$

The velocity in the η -direction:

$$\frac{\partial}{\partial \eta^T} (\psi_{H.S}^c(\xi^T, \eta^T, z'^T)) = 0$$

The velocity in the z' -direction:

$$\frac{\partial}{\partial z'^T} (\psi_{H.S}^c(\xi^T, \eta^T, z'^T)) = \sum_{i=1}^{i=NV} \left(\frac{(\Delta\xi_{i+1}^{ST} \cdot \Delta\eta_i^{ST} - \Delta\xi_i^{ST} \cdot \Delta\eta_{i+1}^{ST}) \cdot (R_i^I + R_{i+1}^I)}{D_0} \right)$$

The velocity in the ξ - and η -directions is zero at the panel plane. This is due to the nature of the double layer singularity, which has a z' velocity only at the panel surface. Notice, that computing the influence at a point on the boundary of the panel will result in a hypersingularity, similar to a vortex singularity.

The $\Delta z_0'^{ST} \neq 0$ Case

If $\Delta z_0'^{ST} \neq 0$, ie. the point is not in the panel plane. The following is the simplified denominator term in this case:

$$D_1 = \left((R_i^I)^2 \cdot (R_{i+1}^I)^2 + \Delta\xi_i^{ST} \cdot \Delta\xi_{i+1}^{ST} + \Delta\eta_i^{ST} \cdot \Delta\eta_{i+1}^{ST} + \Delta z_0'^{ST} \cdot \Delta z_0'^{ST} \right)$$

The velocity in the ξ -direction:

$$\frac{\partial}{\partial \xi^T} (\psi_{H.S}^c(\xi^T, \eta^T, z'^T)) = - \sum_{i=1}^{i=NV} \left(\frac{\Delta z_0'^{ST} \cdot l_i^y (R_i^I + R_{i+1}^I)}{D_1} \right)$$

The velocity in the η -direction:

$$\frac{\partial}{\partial \eta^T}(\psi_{H.S}^c(\xi^T, \eta^T, z'^T)) = - \sum_{i=1}^{i=NV} \left(\frac{\Delta z_0'^{ST} \cdot l_i^x (R_i^I + R_{i+1}^I)}{D_1} \right)$$

The velocity in the z' -direction:

$$\frac{\partial}{\partial z'^T}(\psi_{H.S}^c(\xi^T, \eta^T, z'^T)) = \sum_{i=1}^{i=NV} \left(\frac{(\Delta \xi_{i+1}^{ST} \cdot \Delta \eta_i^{ST} - \Delta \xi_i^{ST} \cdot \Delta \eta_{i+1}^{ST}) \cdot (R_i^I + R_{i+1}^I)}{D_1} \right)$$

Newman – Constant Double Layer Gradient Panel Influence Integral Expression [7]

The following equations were derived based on the Newman Approach [7]. Newman and all other known sources do not present these equations in their explicit form for the discrete panel integral. They were derived and implemented in the final version of the discrete solver.

In order to simplify the implementation, the following notation is introduced:

$$Num_i^1 = l_i^\eta \cdot ((\Delta \xi_i^{ST})^2 + (\Delta z_0'^{ST})^2) - l_i^\xi \cdot (\Delta \xi_i^{ST})(\Delta \eta_i^{ST})$$

and:

$$Num_i^2 = l_i^\eta \cdot ((\Delta \xi_{i+1}^{ST})^2 + (\Delta z_0'^{ST})^2) - l_i^\xi \cdot (\Delta \xi_{i+1}^{ST})(\Delta \eta_{i+1}^{ST})$$

The gradient of the $\tan \zeta$ term is outlined:

$$\delta^1 \tan_i = \frac{R_i^I \cdot \Delta z_0'^{ST} \cdot l_i^\xi}{(R_i^I \cdot \Delta z_0'^{ST} \cdot l_i^\xi) + (Num_i^1)^2}$$

and:

$$\delta^2 \tan_i = \frac{R_{i+1}^I \cdot \Delta z_0'^{ST} \cdot l_i^\xi}{(R_{i+1}^I \cdot \Delta z_0'^{ST} \cdot l_i^\xi) + (Num_i^2)^2}$$

The $\Delta z_0'^{ST} \neq 0$ Case

If $\Delta z_0'^{ST} \neq 0$, the following equations are used (the case where $\Delta z_0'^{ST} = 0$, $\Delta z_0'^{ST}$ is modified by shifting the evaluation point by some small $\delta\epsilon$, such that, $\Delta z_0'^{ST} = \delta\epsilon$) :
The velocity in the ξ -direction at the field point due to a constant strength dipole panel.

$$\begin{aligned} \frac{\partial}{\partial \xi^T}(\psi_N^c(\xi^T, \eta^T, z'^T)) &= \sum_{i=1}^{i=NV} \left(2 \cdot l_i^\eta \cdot \Delta \xi_i^{ST} - l_i^\xi \cdot \Delta \eta_i^{ST} - \delta^1 \tan_i \frac{\Delta \xi_i^{ST}}{(R_i^I)^2 \cdot Num_i^1} \right) \\ &\quad - \sum_{i=1}^{i=NV} \left(2 \cdot l_i^\eta \cdot \Delta \xi_{i+1}^{ST} - l_i^\xi \cdot \Delta \eta_{i+1}^{ST} - \delta^2 \tan_i \frac{\Delta \xi_{i+1}^{ST}}{(R_{i+1}^I)^2 \cdot Num_i^2} \right) \end{aligned}$$

The velocity in the η -direction at the field point due to a constant strength dipole panel.

$$\begin{aligned} \frac{\partial}{\partial \eta^T}(\psi_n^c(\xi^T, \eta^T, z'^T)) &= \sum_{i=1}^{i=NV} \left(\delta^1 \tan_i \left(\frac{(-l_i^\xi \cdot \Delta \xi_i^{ST}) - \Delta \eta_i^{ST} \cdot Num_i^1}{(R_i^I)^2} \right) \right) \\ &\quad - \sum_{i=1}^{i=NV} \left(\delta^2 \tan_i \left(\frac{(-l_i^\xi \cdot \Delta \xi_{i+1}^{ST}) - \Delta \eta_{i+1}^{ST} \cdot Num_i^2}{(R_{i+1}^I)^2} \right) \right) \end{aligned}$$

The velocity in the z' -direction at the field point due to a constant strength dipole panel.

$$\begin{aligned} \frac{\partial}{\partial z'^T}(\psi_n^c(\xi^T, \eta^T, z'^T)) &= \sum_{i=1}^{i=NV} \left(\frac{2 \cdot l_i^\eta \cdot \Delta z_i'^{ST} - \Delta z_i'^{ST} \cdot Num_i^1}{(R_i^I)^2} - \frac{\delta^1 \tan_i \cdot Num_i^1}{\Delta z_i'^{ST}} \right) \\ &\quad \sum_{i=1}^{i=NV} \left(-\frac{2 \cdot l_i^\eta \cdot \Delta z_{i+1}'^{ST} - \Delta z_{i+1}'^{ST} \cdot Num_i^2}{(R_{i+1}^I)^2} - \frac{\delta^2 \tan_i \cdot Num_i^2}{\Delta z_{i+1}'^{ST}} \right) \end{aligned}$$

Velocity Scans for the Gradient of the Constant Double Layer Panel Influence Integrals

Scans for the double layer panel influence velocity are presented. For convenience a vector scan is used to plot the results for easy viewing. The doublet/dipole effect is clearly seen in figures 3-16 to 3-17. It is seen that there is a hyper-singularity on the edges of the panel. This singularity, when describing a constant strength integral,

essentially mimics a vortex tube along the panel edge.

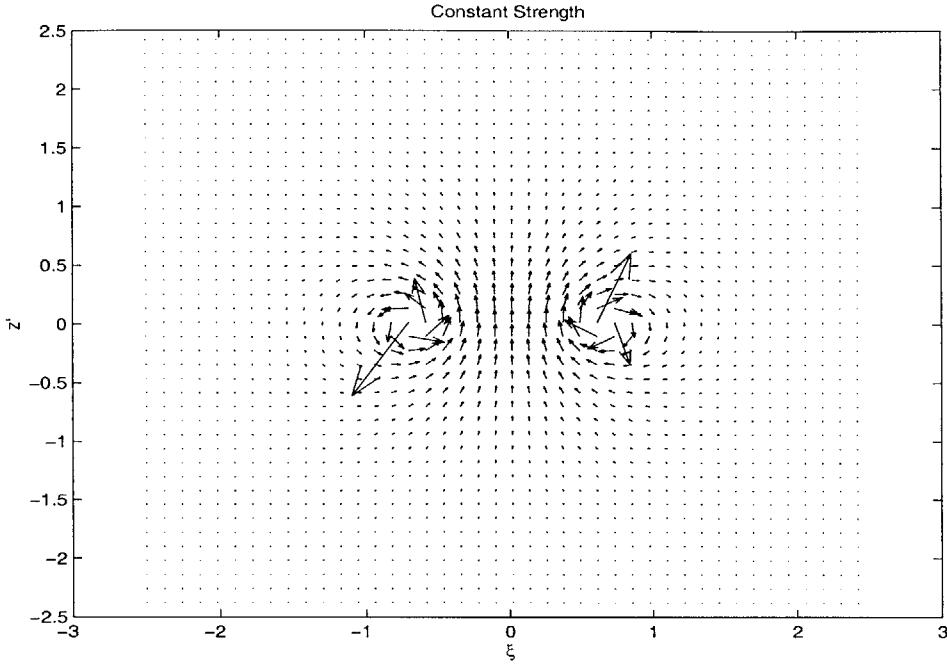


Figure 3-16: A 2-D velocity vector plot for a double layer sample panel $[V1(0, 2, 0), V2(1, -1, 0), V3(-1, -1, 0)]$, evaluated in the plane $\eta = 0$. The solution is actually symmetric about $\xi = 0$, despite the figure showing a possible asymmetry. The apparent asymmetry is due to the evaluation scan points being modified to exclude the panel edge singularities.

3.5.5 Constant Single Layer Gradient Panel Influence Integral [8], [7], [6]

The gradient of the constant single layer results in an expression providing the velocity at a target point (T), due to a constant strength single layer panel. The following is an expression of the integral being computed:

$$\nabla_T \left(\phi_M^c(\xi^T, \eta^T, z^T) \right) = \vec{v}(\xi^T, \eta^T, z^T) = \nabla_T \left(\int \int_{Panel} \rho_c \cdot \frac{1}{|\vec{x} - \vec{x}'|} dS_{Panel} \right)$$

Hess and Smith, and Newman Relations

For both the Hess and Smith, and the Newman approaches, the velocity influence integral for the single layer singularity is expressed simply as:

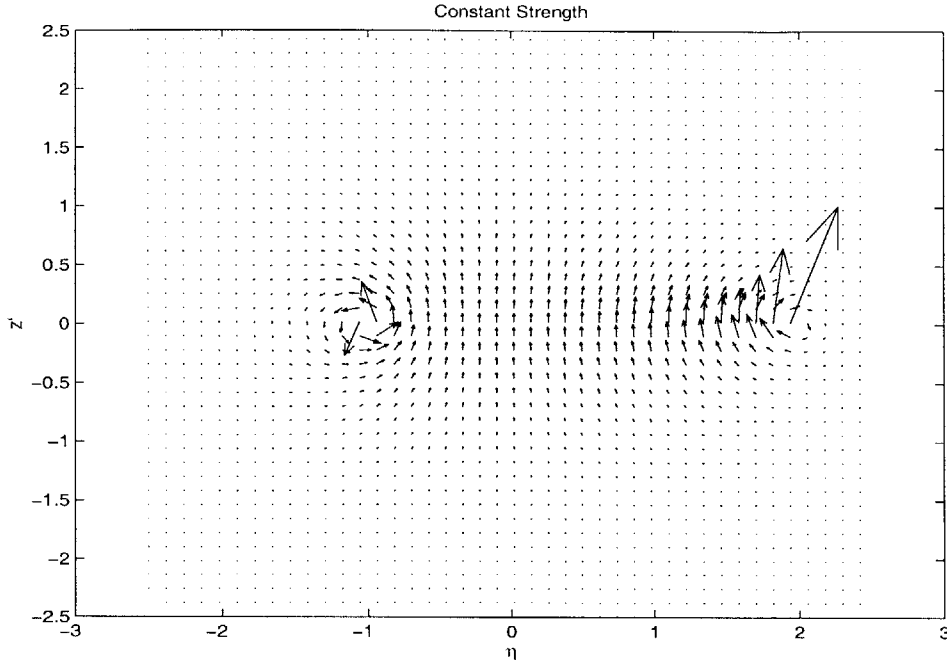


Figure 3-17: A 2-D velocity vector plot for a double layer sample panel with vertices $[V1(0, 2, 0), V2(1, -1, 0), V3(-1, -1, 0)]$, evaluated in the plane $\xi = 0$.

The ξ -direction velocity at the target point (T):

$$\frac{\partial}{\partial \xi^T}(\phi_{H.S,N}^c(\xi^T, \eta^T, z^T)) = - \sum_{i=1}^{i=N} \sin(\theta_i) \cdot Q_i$$

The η -direction velocity at the target point (T):

$$\frac{\partial}{\partial \eta^T}(\phi_{H.S,N}^c(\xi^T, \eta^T, z^T)) = \sum_{i=1}^{i=N} \cos(\theta_i) \cdot Q_i$$

The z' -direction velocity at the target point (T):

$$\frac{\partial}{\partial z^T}(\phi_{H.S,N}^c(\xi^T, \eta^T, z^T)) = \psi_{H.S,N}^c(\eta^T, \xi^T, z^T)$$

Potential Scans for the Gradient of the Constant Single Layer Panel Influence Integrals

Velocity scans for the single layer velocity result are presented in figures 3-18 - 3-20.

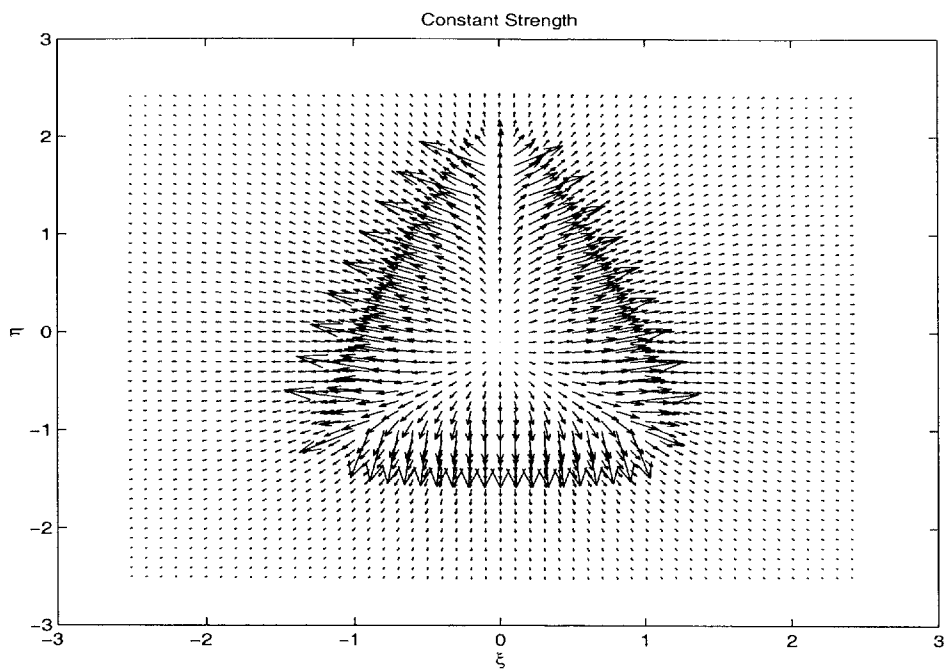


Figure 3-18: A 2-D velocity vector plot for a single layer sample panel with vertices $[V1(0, 2, 0), V2(1, -1, 0), V3(-1, -1, 0)]$, evaluated in the plane $z' = +\epsilon$.

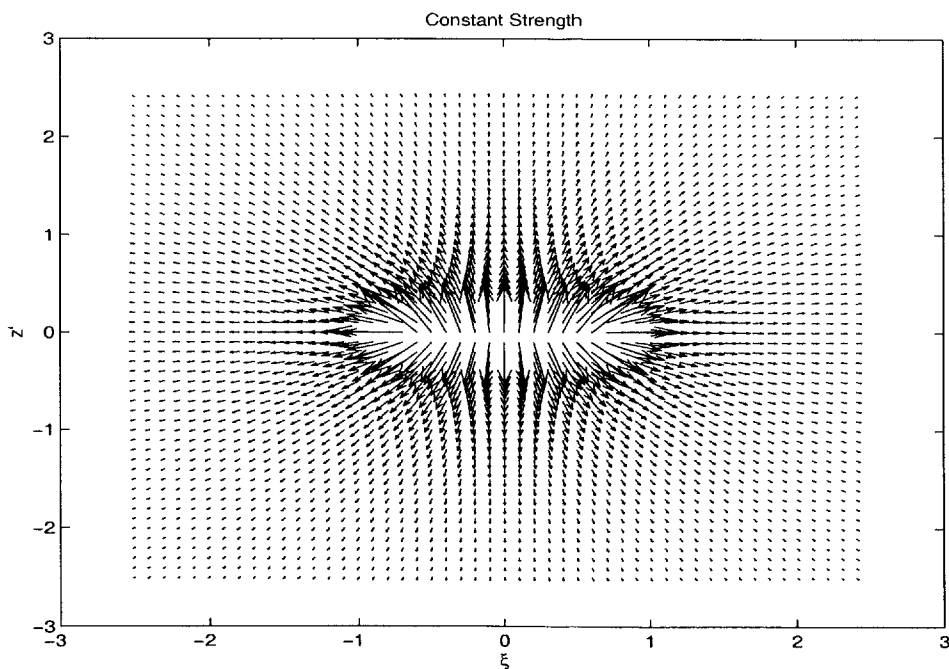


Figure 3-19: A 2-D velocity vector plot for a single layer sample panel with vertices $[V1(0, 2, 0), V2(1, -1, 0), V3(-1, -1, 0)]$, evaluated in the plane $\eta = 0$.

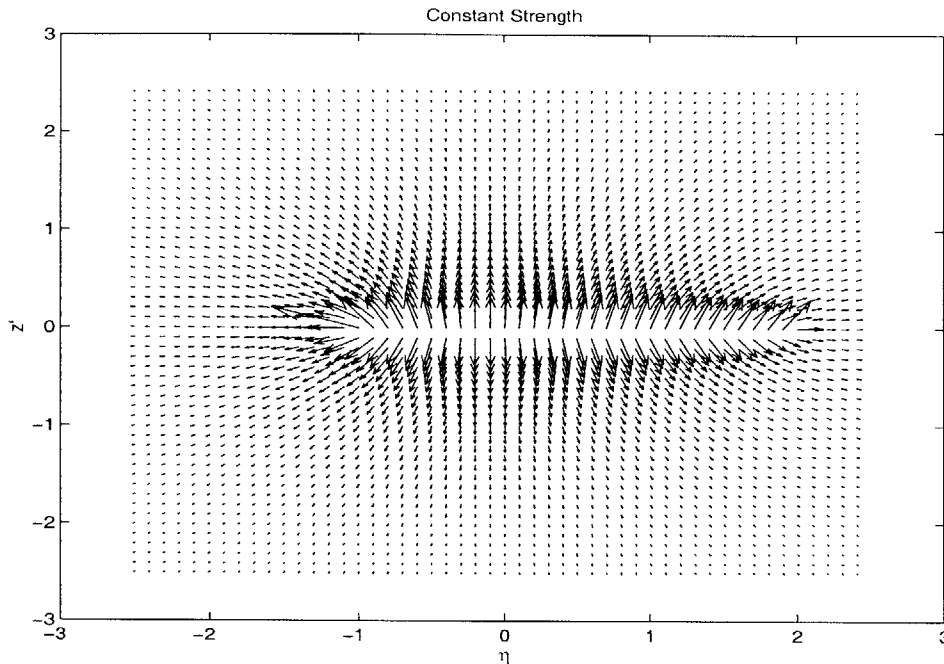


Figure 3-20: A 2-D velocity vector plot for a single layer sample panel with vertices $[V1(0, 2, 0), V2(1, -1, 0), V3(-1, -1, 0)]$, evaluated in the plane $\xi = 0$.

3.6 The Linear Strength Basis Function Panel Influence Integral Equations

In this section the panel influence integrals for a linear distribution on the panel are presented. The mechanics involved in computing the linear influence integrals, as well as the final expressions are presented.

3.6.1 Shape Functions: Linear Shape Functions On Triangular Panels

The linear shape function considered is a vertex based, compact support shape function. Before analyzing the linear panel influence integrals, a brief description of the linear shape functions and their manipulation is presented. Figure 3-21 outlines the three nodal based linear shape functions for an arbitrary triangle.

Since the shape functions have a nodal basis, their support extends to all panels associated with the vertex. The support-”footprint” of the shape function is presented

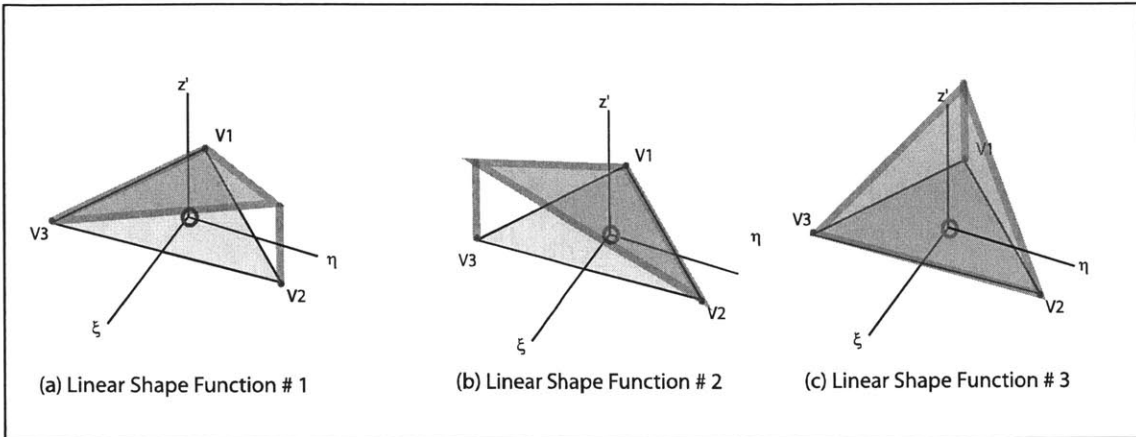


Figure 3-21: The 3-Nodal based shape functions for the linear strength panel influence integrals. Notice, these shape functions are identical to those used in FEM approaches

in figure 3-22. Notice that this footprint is larger than the panel based collocation approach.

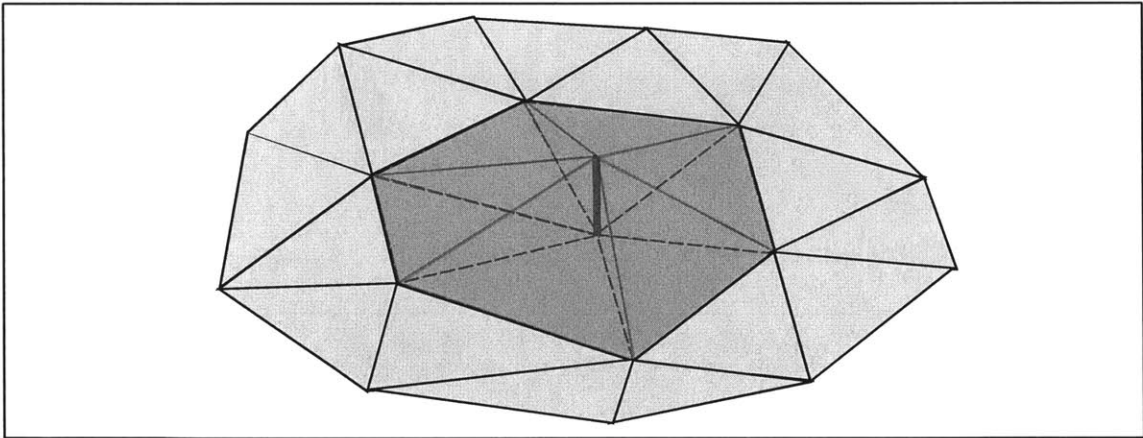


Figure 3-22: The shape function footprint for the linear basis. The footprint represents the influence one shape function has on other neighboring shape functions

Since the governing equation is linear, the total shape function is the superimposed influence of the individual triangle shape functions sharing a common vertex. As such, panel integrals can be computed independently, and added to form the total influence.

$$Influence_{Vertex_i} = Influence_{1_{Vertex_i}} + Influence_{2_{Vertex_i}} + \dots + Influence_{N_{Vertex_i}}$$

3.6.2 Linear Strength Panel Influence Integral Computation Methodology

In order to compute the linear variation of singularity strength on the panel the following approach was taken.

The expressions for the single layer panel influence integrals are presented by Newman [7] as:

$$\psi_{\xi} = \int \int (f(\xi)) \frac{1}{|\vec{x} - \vec{x}'|} d\xi d\eta$$

with $(f(\xi)) = (\xi)$, and correspondingly for the η -direction variation:

$$\psi_{\eta} = \int \int (f(\eta)) \frac{1}{|\vec{x} - \vec{x}'|} d\xi d\eta$$

with $(f(\eta)) = (\eta)$.

The linear variation is computed by extending the ξ and η variations in the integrand to mimic shape functions, or density distributions. The idea is to mimic the following:

$$\psi_{\xi} = \int \int (\rho_{\xi}) \frac{1}{|\vec{x} - \vec{x}'|} d\xi d\eta$$

$$\psi_{\eta} = \int \int (\rho_{\eta}) \frac{1}{|\vec{x} - \vec{x}'|} d\xi d\eta$$

Where,

ρ_l : is a linear panel shape function. ρ_l varies from $[0, 1]$ over the panel, in the direction of the linear variation, l of the shape function. The integral is computed by generalizing the mathematics to the point at which an analytic panel integral can be formed. This is done by allowing a panel translation (in both the ξ - and η -directions) and an appropriate scaling of the result (also occurring in both the ξ - and η -directions). The following sections present the resulting linear panel integrals, while also presenting some of the mechanics involved in attaining a consistent and general linear $\langle \xi - \eta - const \rangle$ shape function system for the linear integrals.

3.6.3 Linear Shape Function Computation Methods

Since variations in the ξ and η directions are easily computed in the transformed coordinate system, there are two approaches for computing the linear panel influence integrals. The two descriptions are presented below.

The Rotation Method

The rotation method computes the nodal based linear shape functions in the following steps:

- 1) Align the panel's i th shape function with a primary axis
- 2) Compute the linear influence (Shape function i)
- 3) Rotate the panel such that the $i + 1$ th shape function aligns with the primary axis.
- 4) Repeat steps 1-3, until all shape functions have been computed.

The rotation method is presented pictorially in figure 3-23

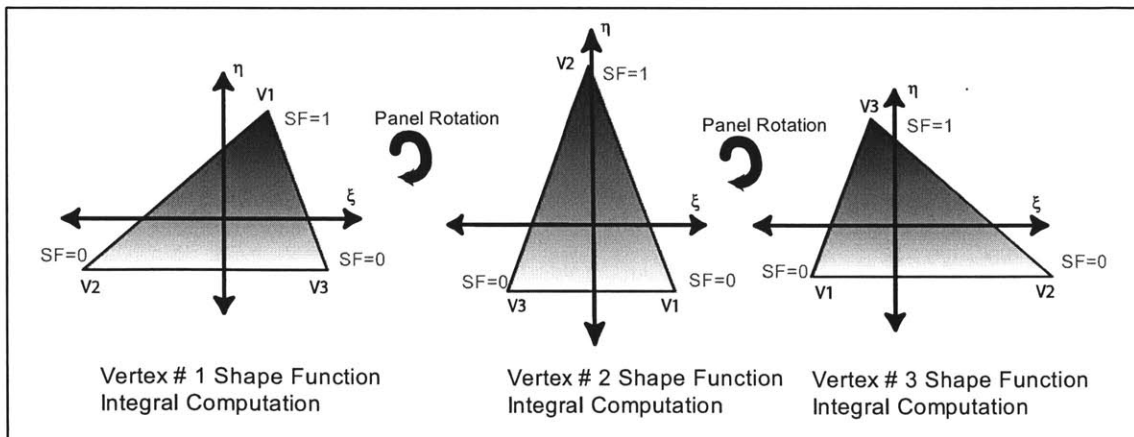


Figure 3-23: The rotation method: computing the linear shape function panel influence integrals through rotating the panel being computed.

Due to the computational complexity involved in computing three transformations, and three separate linear panel integrals, the method is inefficient and very slow at run-time. This method was implemented, but later removed for a more efficient approach, outlined below.

Shape Function - $\langle \xi, \eta, const \rangle$ Method

The $\langle \xi, \eta, const \rangle$ method makes use of the linear variation in the ξ - and η -directions. Combining the independent $\langle \xi, \eta, const \rangle$ shape functions appropriately, the three orthogonal nodal $\langle N1, N2, N3 \rangle$ shape functions can be computed. Figure 3-24 shows the pictorial representation of the ξ - and η - linear variation shape functions. The reduction of the $\langle \xi, \eta, const \rangle$ to $\langle N1, N2, N3 \rangle$, is performed in the following steps:

$$N^1 = N^\eta$$

$$N^2 = N^\xi - \frac{\xi_1 - \xi_2}{\xi_1 - \xi_3} \cdot N^\eta$$

$$N^3 = N^c - N^1 - N^2$$

where, $\frac{\xi_1 - \xi_2}{\xi_1 - \xi_3}$: is a scaling factor, denoted in further references as PCT_ξ . The scaling factor is the percentage of the N^η shape function, which must be removed from the N^ξ shape function, to produce a N^2 shape function.

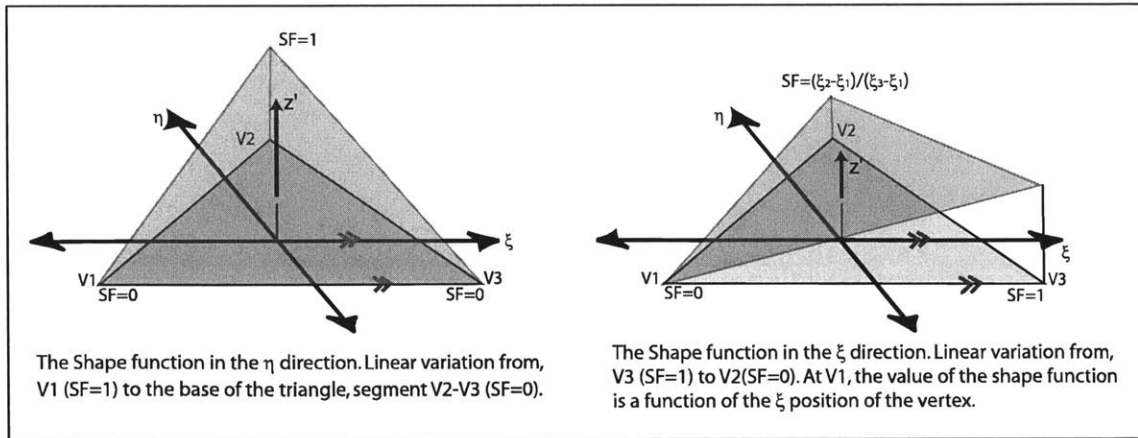


Figure 3-24: A description of the computation of the orthogonal $\langle N1, N2, N3 \rangle$ shape function set, from the $\langle \xi, \eta, const \rangle$, basis function set.

This method proves to be significantly more efficient than the *rotation method*. The following benefits arise from using the $\langle \xi, \eta, const \rangle$ approach for the linear panel influence integrals:

- 1) Computing the $\xi - \eta$ variations has a minimal additional cost over the constant strength integrals. Computing ξ, η and *constant* integrals requires only 40-50 %

additional time over the *constant* only integral.

- 2) Having to compute two linear shape functions, rather than three is less costly.
- 3) The third shape function, the constant strength one is already present in the computation.
- 4) Converting the $\langle \xi, \eta, constant \rangle$ shape function set to the $\langle N1, N2, N3 \rangle$ shape function set is simple.
- 5) Only one basic transform and panel variable setup is required to compute the integrals. This is why the transform presented earlier is so useful.

The computational overhead between computing the constant strength integral and three linear strength shape functions is approximated to be about 40-50 % when considering the $\langle \xi, \eta, const \rangle$ method with triangular elements. Hence, especially when implementing a low order Gauss-Quadrature-Galerkin routine, there is not a significant time penalty in the panel integral computation for linear strength panels over constant strength panels.

3.6.4 Linear Strength Double Layer, and Single Layer Panel Influence Integrals

Shift Factors, and Scaling Factors

In order to maintain consistency in the panel transform, several scaling factors must be added to the computation.

Scaling Factor

The scaling factor, S_l is implemented to ensure that the shape function has a value of unity at the appropriate node. Simply presented, the scaling factor is computed as:

For ξ linear variation:

$$S_\xi = \left| \frac{1}{\xi_1^S - \xi_3^S} \right|$$

For η linear variation:

$$S_\eta = \left| \frac{1}{\eta_2^S - \eta_1^S} \right|$$

Shift Factor

The Shift factor is a temporary panel and vertex transformation. The shift factor for the η - direction shifts the triangular panel upwards, such that the base of the triangle lies on the ξ axis. In the ξ - direction, the panel is shifted eastward such that the west-most vertex lies on the η -axis:

The shift factors are computed:

In the ξ - direction:

$$SF_{\xi} = -\xi_1$$

In the η - direction:

$$SF_{\eta} = \frac{\eta_2 - \eta_1}{3}$$

Pct_{ξ} : Shape Function Fraction

In the $\langle \xi - \eta - const \rangle$ shape function approach, a percentage of the linear η -variation shape function must be subtracted from the linear ξ -variation shape function. This percentage is determined from the position of vertex 2, V_2 , relative to the other vertices:

$$PCT_{\xi} = \frac{\xi_1 - \xi_2}{\xi_1 - \xi_3}$$

3.7 Analytic Expressions of the Linear Panel Influence Integrals

The analytic expressions of the linear panel influence integrals are presented.

3.7.1 Integral Simplification

The following terms are introduced to simplify the final panel integral expressions.

$$S_i^1 = -\Delta\xi_i^{ST} \cdot \cos(\theta_i^P) + -\Delta\eta_i^{ST} \cdot \sin(\theta_i^P)$$

and,

$$S_i^2 = -\Delta\xi_{i+1}^{ST} \cdot \cos(\theta_i^P) + -\Delta\eta_{i+1}^{ST} \cdot \sin(\theta_i^P)$$

and,

$$PC_i = \frac{1}{2} \left(S_i^1 \cdot R_i^I - S_i^2 \cdot R_i^{I+1} - Q_i \cdot \left((R_i^I)^2 - (S_i^1)^2 \right) \right)$$

The physical meaning of these terms is irrelevant. They are some common computations found in many of the influence integrals.

3.7.2 Linear Variation Double Layer Panel Influence Integral Expression

The computation of the following integral over a panel is expressed analytically:

$$\psi_M^{l\xi,\eta}(\xi^T, \eta^T, z'^T) = \int \int_{Panel} \rho_{l\xi,\eta} \cdot \frac{\partial}{\partial \hat{n}_{Panel}} \frac{1}{|\vec{x} - \vec{x}'|} dS_{Panel}$$

where,

$\psi_M^{l\xi,\eta}(\xi^T, \eta^T, z'^T)$: Is the potential (denoted ψ to distinguish it is a double layer), due to a linear basis (denoted l – this will represent the direction of singularity distribution variation ξ or η), evaluated at a target field point (T), with coordinates (ξ^T, η^T, z'^T) , using computation method M (M is *H.S.* for a Hess and Smith approach, and N for a Newman approach).

ρ_c : represents the density per surface area of the constant shape function. In this computation, $\rho = 1$ at the appropriate vertex in the linear variation, and linearly varies across the panel to a value of *zero*.

Newman, and Hess and Smith Integrals For Linear Variation of the Double Layer Panel Potential Influence

In order to compute the panel influence integrals, an intermediate step is taken. The computation of the *linear* "correction", to be applied to the constant strength result:

$$SD_{\xi} = \sum_{i=1}^{i=NV} Q_i \cdot \sin(\theta_i^P)$$

$$SD_{\eta} = \sum_{i=1}^{i=NV} -Q_i \cdot \cos(\theta_i^P)$$

The resulting linear variation panel integrals are: The potential due to a ξ -direction linear double layer distribution at a target point T :

$$\psi_{N,H.S}^{\xi}(\xi^T, \eta^T, z'^T) = S_{\xi} \left((SF_{\xi} + \xi^T) \cdot \psi_{N,H.S}^c(\xi^T, \eta^T, z'^T) - z'^T \cdot SD_{\xi} \right)$$

The potential due to a η -direction linear double layer distribution at a target point T :

$$\psi_{N,H.S}^{\eta}(\xi^T, \eta^T, z'^T) = S_{\eta} \left((SF_{\eta} + \eta^T) \cdot \psi_{N,H.S}^c(\xi^T, \eta^T, z'^T) - z'^T \cdot SD_{\eta} \right)$$

The potential due to a constant double layer distribution at a target point T :

$$\psi_{N,H.S}^{z'}(\xi^T, \eta^T, z'^T) = \psi_{N,H.S}^c(\xi^T, \eta^T, z'^T)$$

The Linear Double Layer Potential Panel Influence Integral Plots

The following plots outline the linear variation of the potential due to a double layer panel influence integral.

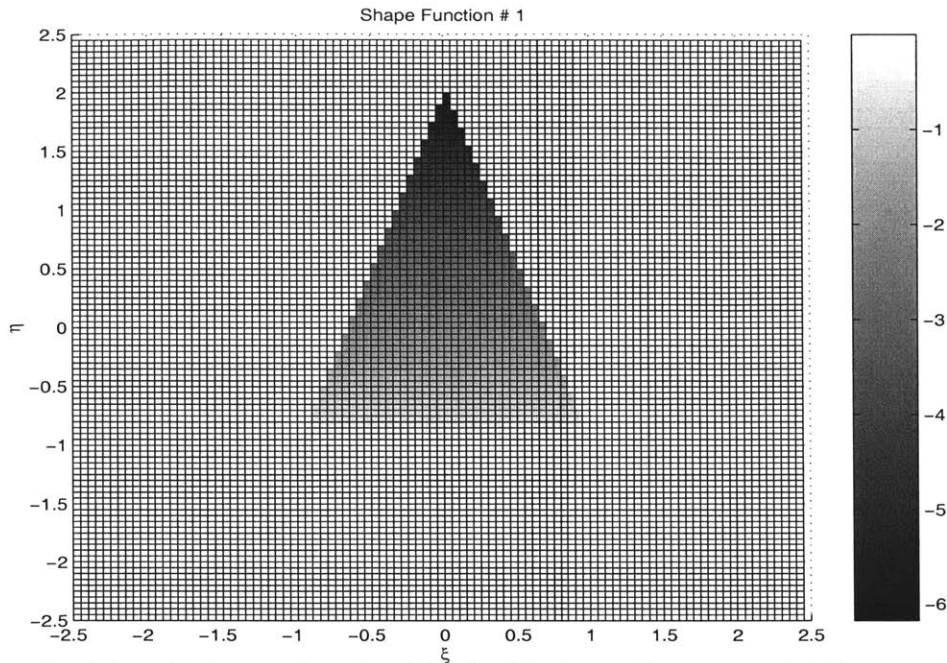


Figure 3-24: Potential scan for the SF1 double layer linear panel influence integral, for the panel $[V1(0, 2, 0), V2(1, -1, 0), V3(-1, -1, 0)]$, evaluated in the plane $z' = +\epsilon$.

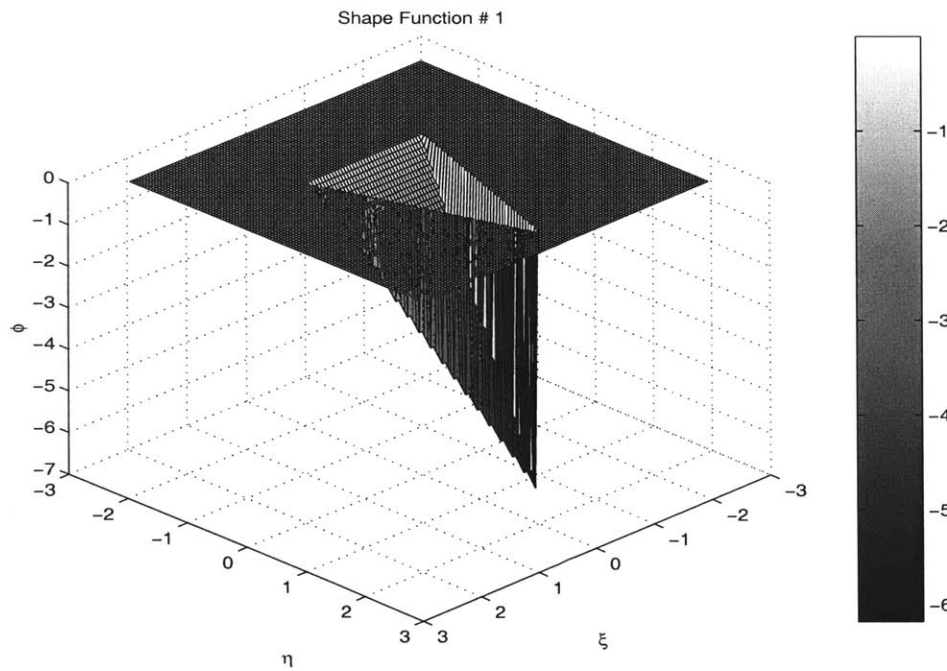


Figure 3-25: The 3-D SF1 potential scan for the double layer linear panel influence integral, for the panel $[V1(0, 2, 0), V2(1, -1, 0), V3(-1, -1, 0)]$, evaluated in the plane $z' = +\epsilon$.

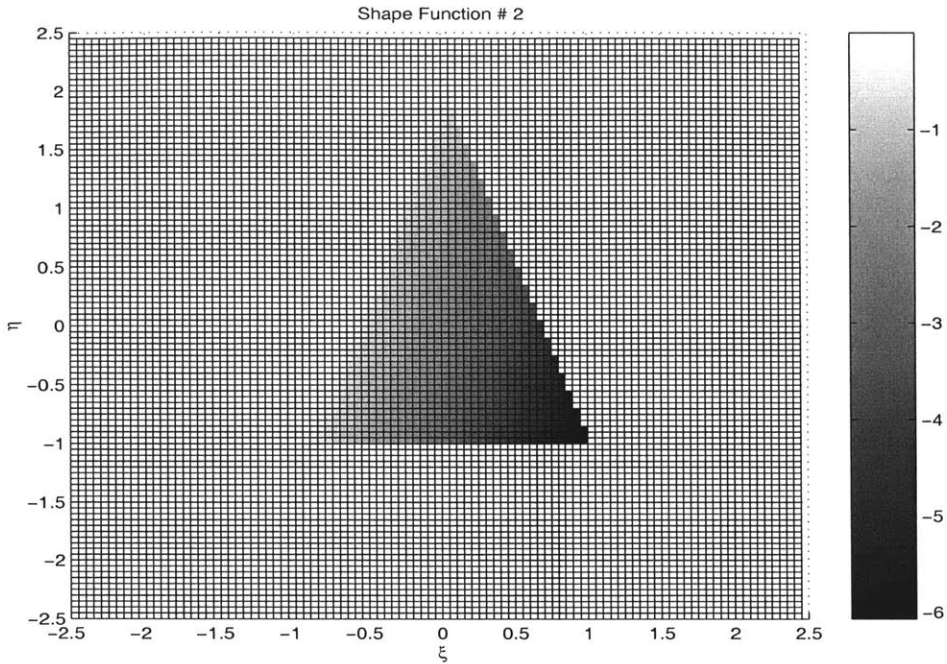


Figure 3-26: Potential scan for the SF2 double layer linear panel influence integral, for the panel $[V1(0, 2, 0), V2(1, -1, 0), V3(-1, -1, 0)]$, evaluated in the plane $z' = +\epsilon$.

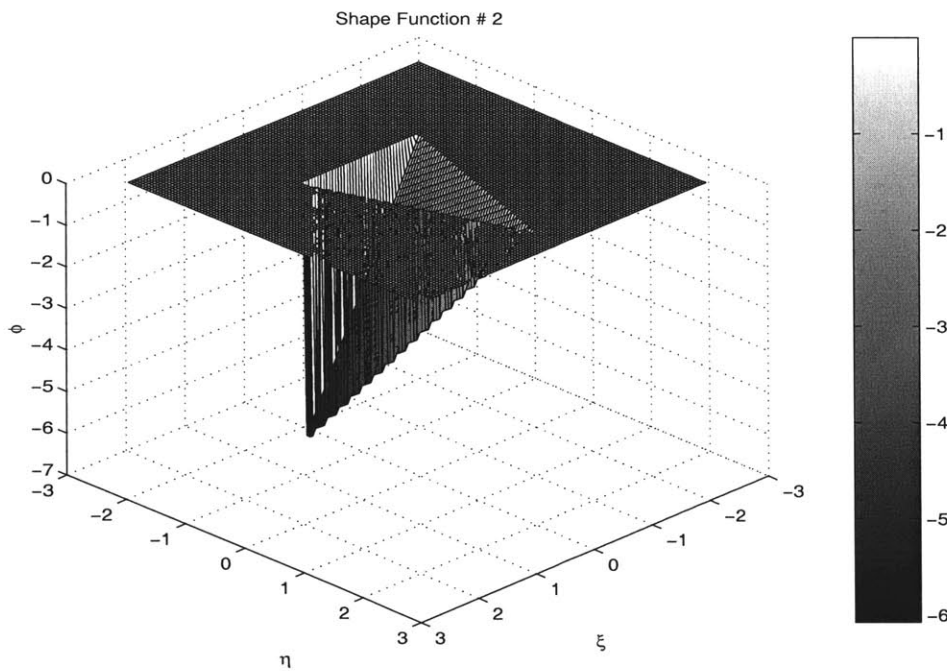


Figure 3-27: The 3-D potential scan for the SF2 double layer linear panel influence integral, for the panel $[V1(0, 2, 0), V2(1, -1, 0), V3(-1, -1, 0)]$, evaluated in the plane $z' = +\epsilon$.

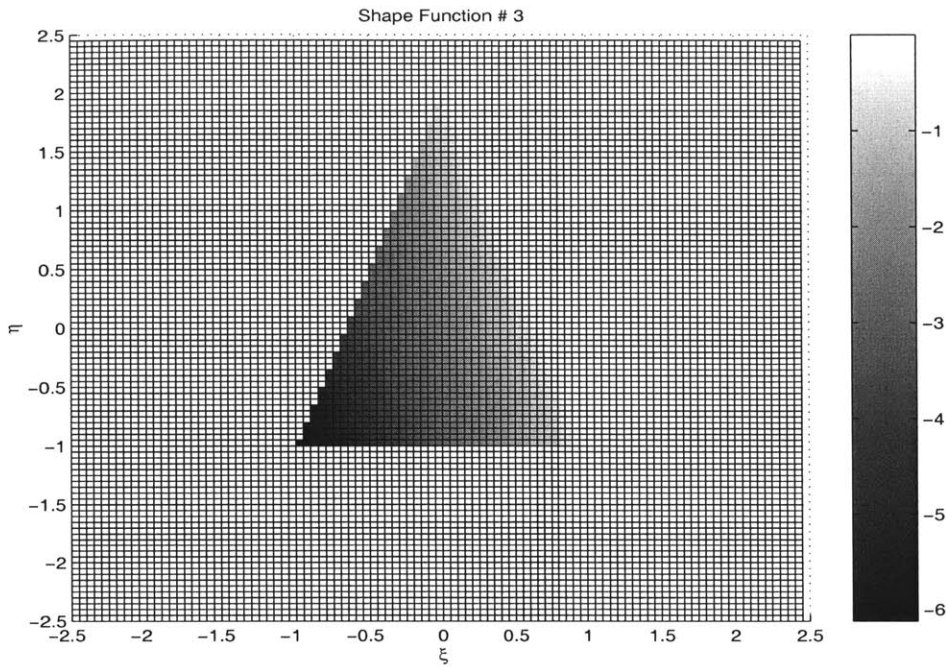


Figure 3-28: Potential scan for the SF3 double layer linear panel influence integral, for the panel $[V1(0, 2, 0), V2(1, -1, 0), V3(-1, -1, 0)]$, evaluated in the plane $z' = +\epsilon$.

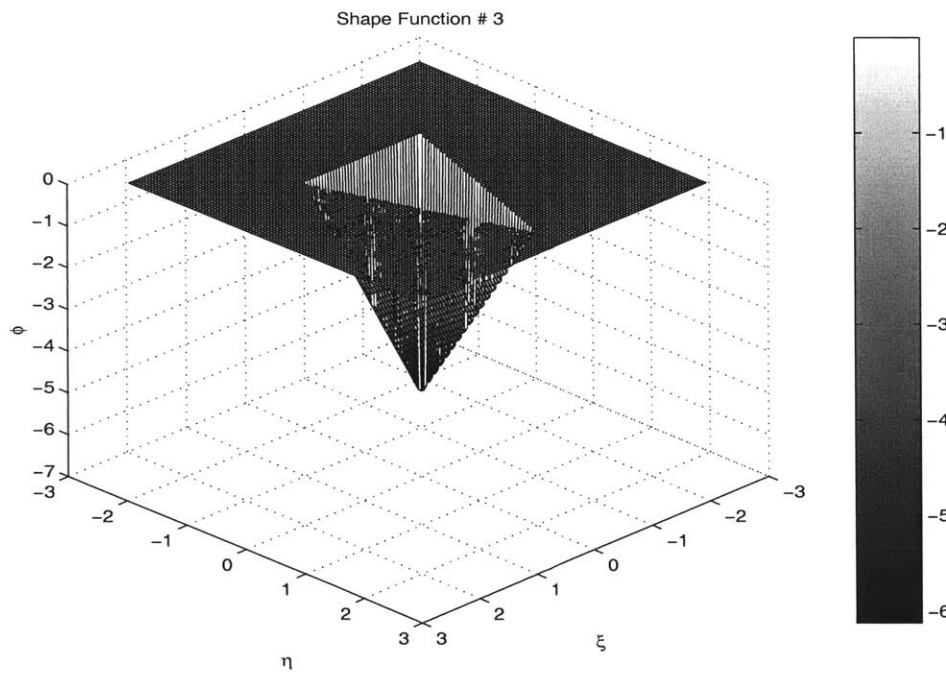


Figure 3-29: The 3-D potential scan for the SF3 double layer linear panel influence integral, for the panel $[V1(0, 2, 0), V2(1, -1, 0), V3(-1, -1, 0)]$, evaluated in the plane $z' = +\epsilon$.

3.7.3 Linear Variation for the Single Layer Panel Influence Integral

Here, the linear single layer panel influence integral is computed. This is an analytic expression of the following integral:

$$\phi_M^{l_{\xi,\eta}}(\xi^T, \eta^T, z'^T) = \int \int_{Panel} \rho_{l_{\xi,\eta}} \cdot \frac{1}{|\vec{x} - \vec{x}'|} dS_{Panel}$$

Newman, and Hess and Smith Integrals For Linear Variation of the Single Layer Panel Potential Influence

In order to compute the panel integrals, there is an intermediate step which is taken.

$$SS_{\xi} = \sum_{i=1}^{i=N_V} -PC_i \cdot \sin(\theta_i^P)$$

$$SS_{\eta} = \sum_{i=1}^{i=N_V} +PC_i \cdot \cos(\theta_i^P)$$

Following this, the integrals are computed. The expression of the ξ -variation single layer linear panel integral:

$$\phi_{N,H.S}^{\xi}(\xi^T, \eta^T, z'^T) = S_{\xi} \left((SF_{\xi} + \xi^T) \cdot \phi_{N,H.S}^c(\xi^T, \eta^T, z'^T) + SD_{\xi} \right)$$

The expression of the η -variation single layer linear panel integral:

$$\phi_n^{\eta}(\xi^T, \eta^T, z'^T) = S_{\eta} \left((SF_{\eta} + \eta^T) \cdot \phi_{N,H.S}^c(\xi^T, \eta^T, z'^T) + SD_{\eta} \right)$$

The Linear Single Layer Potential Panel Influence Integral Plots

Figures 3-30 through 3-35 outline the linear variation of the single layer, panel influence integral plots in $\langle N1, N2, N3 \rangle$.

3.7.4 Computing the Linear Velocity Influence Integrals

The velocity panel influence integrals are computed for the linear shape functions.

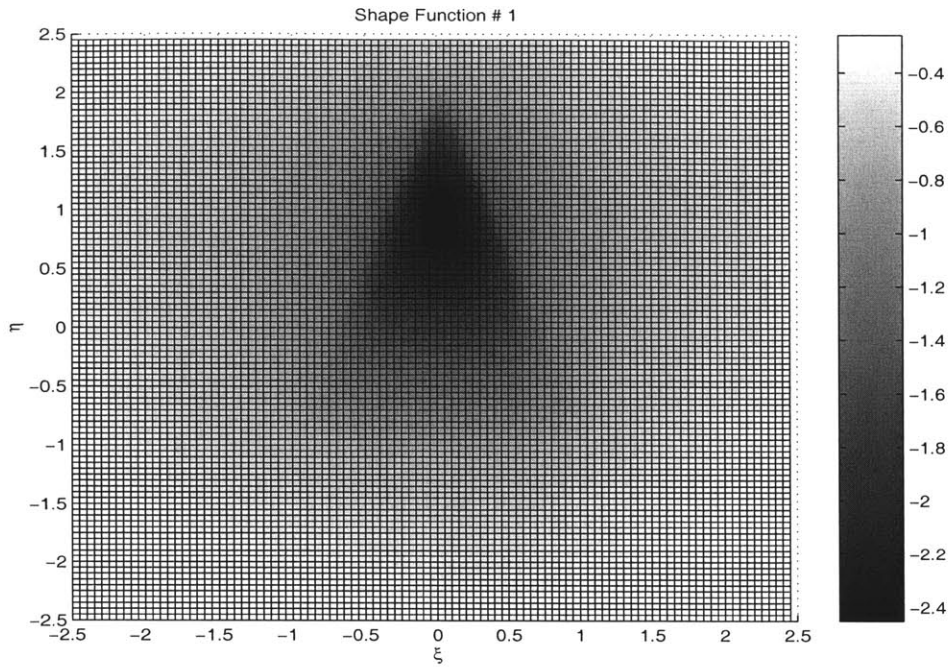


Figure 3-30: The potential scan for the SF1 single layer linear panel influence integral, for the panel $[V1(0, 2, 0), V2(1, -1, 0), V3(-1, -1, 0)]$, evaluated in the plane $z' = +\epsilon$.

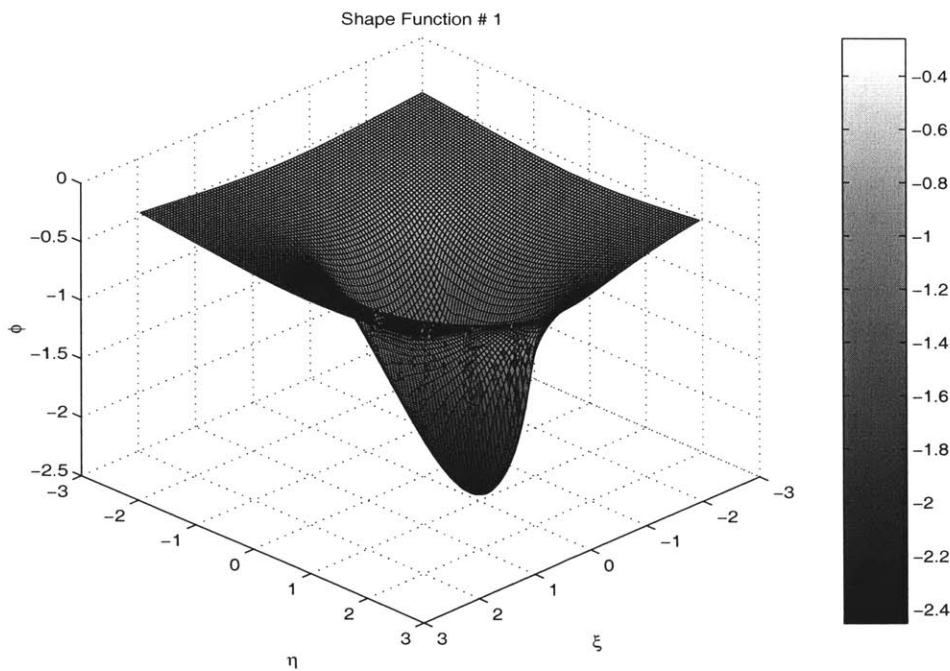


Figure 3-31: The 3-D potential scan for the SF1 single layer linear panel influence integral, for the panel $[V1(0, 2, 0), V2(1, -1, 0), V3(-1, -1, 0)]$, evaluated in the plane $z' = +\epsilon$.

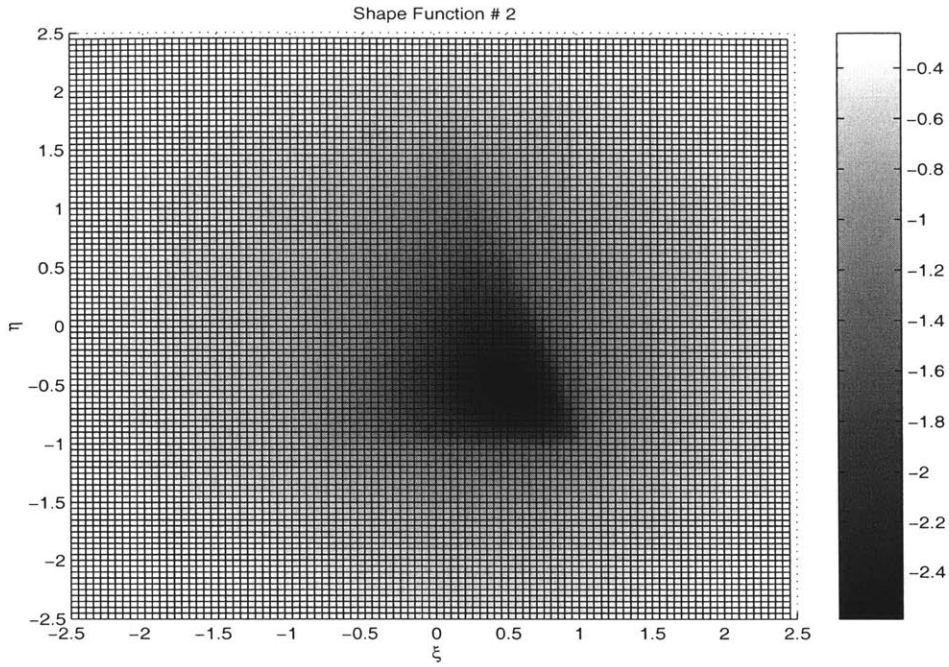


Figure 3-32: The potential scan for the SF2 single layer linear panel influence integral, for the panel $[V1(0, 2, 0), V2(1, -1, 0), V3(-1, -1, 0)]$, evaluated in the plane $z' = +\epsilon$.

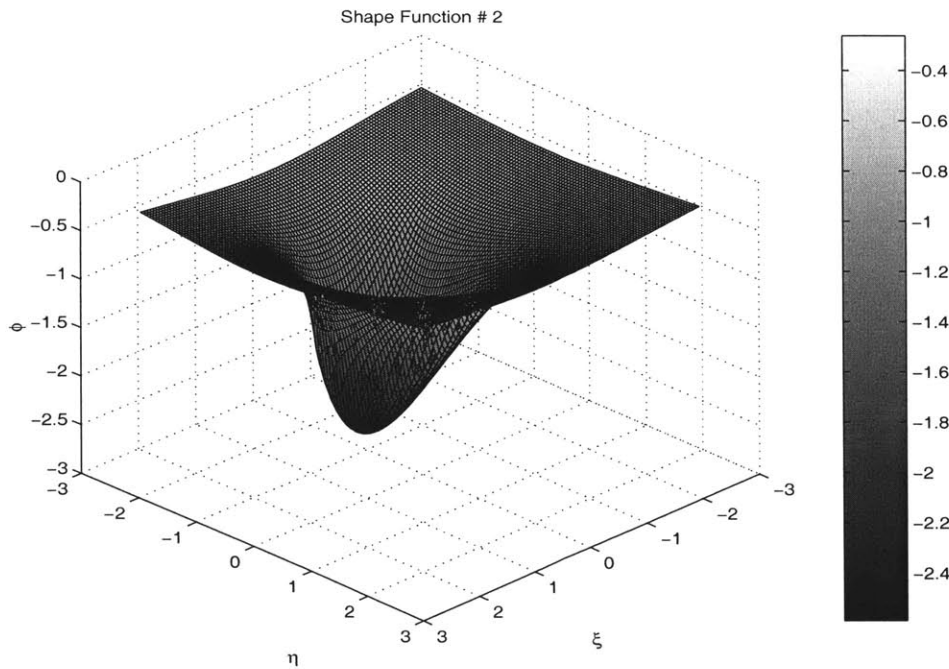


Figure 3-33: The 3-D potential scan for the SF2 single layer linear panel influence integral, for the panel $[V1(0, 2, 0), V2(1, -1, 0), V3(-1, -1, 0)]$, evaluated in the plane $z' = +\epsilon$.

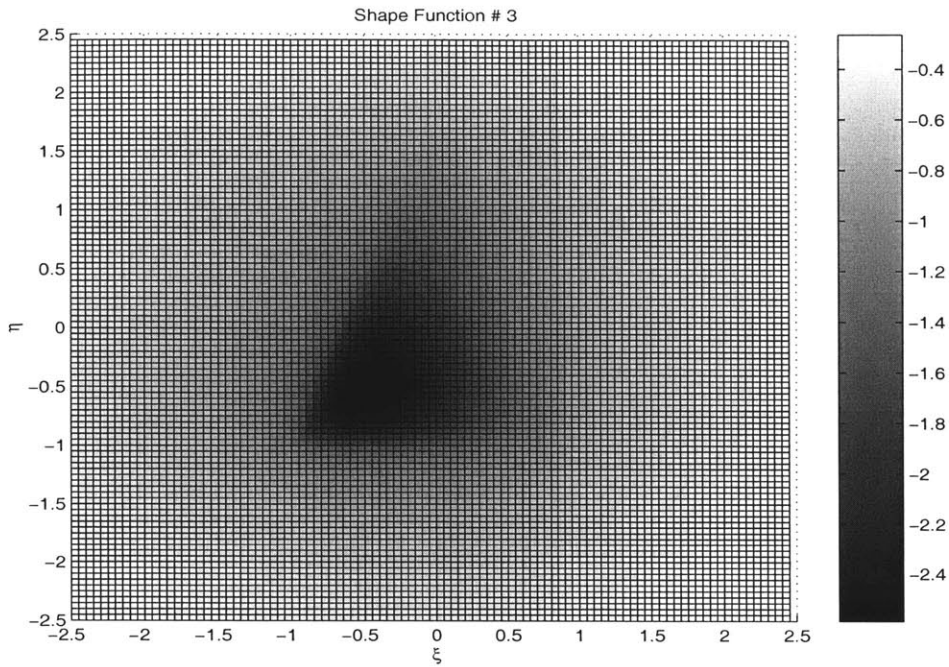


Figure 3-34: The potential scan for the SF3 single layer linear panel influence integral, for the panel $[V1(0, 2, 0), V2(1, -1, 0), V3(-1, -1, 0)]$, evaluated in the plane $z' = +\epsilon$.

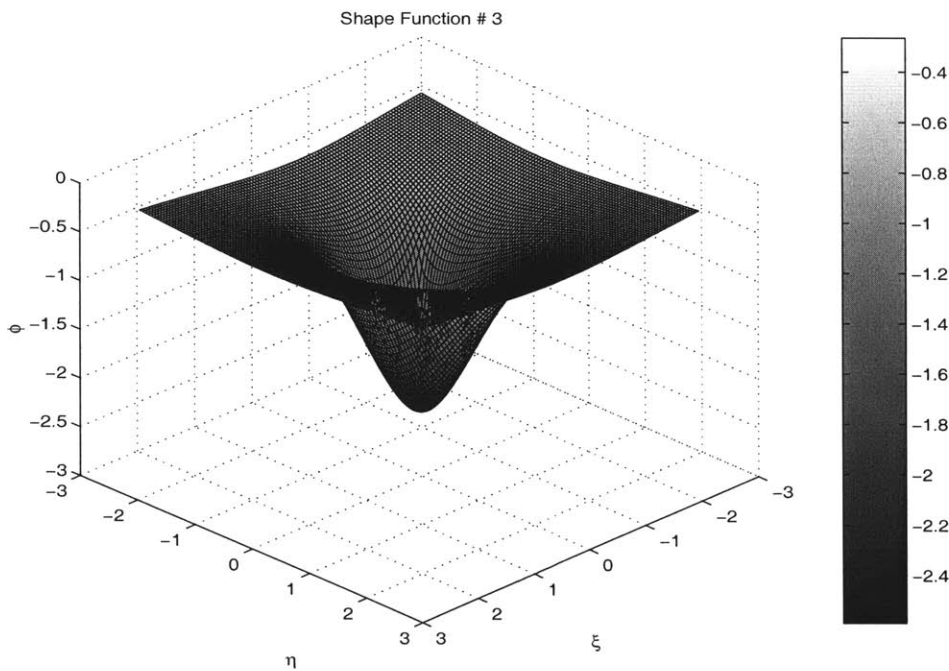


Figure 3-35: The 3-D potential scan for the SF3 single layer linear panel influence integral, for the panel $[V1(0, 2, 0), V2(1, -1, 0), V3(-1, -1, 0)]$, evaluated in the plane $z' = +\epsilon$.

3.7.5 The Gradient Equations for the Linear Double Layer Equations

The panel influence integral for the gradient of the double layer is computed in this section. The result is an analytic expression of the following panel integral:

$$\nabla_T \left(\psi_M^{l_{\xi,n}}(\xi^T, \eta^T, z'^T) \right) = \vec{v}(\xi^T, \eta^T, z'^T) = \nabla_T \left(\int \int_{Panel} \rho_{l_{\xi,n}} \cdot \frac{\partial}{\partial \hat{n}_{Panel}} \frac{1}{|\vec{x} - \vec{x}'|} dS_{Panel} \right)$$

Double Layer Gradient Equations : Setup of Preliminary Variables

The intermediate setup for the double layer panel integration:

$$S_i^1 = -\Delta \xi_i^{ST} \cdot \cos(\theta_i^P) + -\Delta \eta_i^{ST} \cdot \sin(\theta_i^P)$$

and:

$$S_i^2 = -\Delta \xi_{i+1}^{ST} \cdot \cos(\theta_i^P) + -\Delta \eta_{i+1}^{ST} \cdot \sin(\theta_i^P)$$

Further terms are computed for simplification of the final equations:

$$D_i = \sqrt{(\xi_{i+1}^S - \xi_i^S \cdot \xi_{i+1}^S - \xi_i^S) + (\eta_{i+1}^S - \eta_i^S \cdot \eta_{i+1}^S - \eta_i^S)}$$

The following additional intermediate terms are presented to simplify the final integral expression:

$$T_{\frac{\partial Q}{\partial \xi}} = \left(-2 \cdot D_i \frac{\left(\frac{-\Delta \xi_i^{ST}}{R_i^I} + \frac{-\Delta \xi_{i+1}^{ST}}{R_{i+1}^I} \right)}{(R_i^I + R_{i+1}^I - D_i) \cdot (R_i^I + R_{i+1}^I + D_i)} \right)$$

$$T_{\frac{\partial Q}{\partial \eta}} = \left(-2 \cdot D_i \frac{\left(\frac{-\Delta \eta_i^{ST}}{R_i^I} + \frac{-\Delta \eta_{i+1}^{ST}}{R_{i+1}^I} \right)}{(R_i^I + R_{i+1}^I - D_i) \cdot (R_i^I + R_{i+1}^I + D_i)} \right)$$

$$T_{\frac{\partial Q}{\partial z'}} = \left(-2 \cdot D_i \frac{\left(\frac{-\Delta z'^{ST}_i}{R_i^I} + \frac{-\Delta z'^{ST}_{i+1}}{R_{i+1}^I} \right)}{(R_i^I + R_{i+1}^I - D_i) \cdot (R_i^I + R_{i+1}^I + D_i)} \right)$$

The linear correction terms for the ξ linear variation shape function are computed next. These expressions can be thought of the terms that augment the constant strength computation:

$$LT_{\frac{\partial Q}{\partial \xi}}^{\xi} = \sum_{i=1}^{i=NV} \left(T_{\frac{\partial Q}{\partial \xi}} \cdot \Delta z_i'^{ST} \cdot \sin(\theta_i^P) \right)$$

$$LT_{\frac{\partial Q}{\partial \eta}}^{\xi} = \sum_{i=1}^{i=NV} \left(T_{\frac{\partial Q}{\partial \eta}} \cdot \Delta z_i'^{ST} \cdot \sin(\theta_i^P) \right)$$

$$LT_{\frac{\partial Q}{\partial z'}}^{\xi} = \sum_{i=1}^{i=NV} \left(T_{\frac{\partial Q}{\partial z'}} \cdot \Delta z_i'^{ST} \cdot \sin(\theta_i^P) \right)$$

$$LT_{Q \frac{\partial z'}{\partial \xi}}^{\xi} = \sum_{i=1}^{i=NV} \left(Q_i \cdot \sin(\theta_i^P) \right)$$

The linear Correction Terms for the η linear variation shape function are computed. Similar to the ξ variation terms, these are also used to augment the constant basis to a linear one:

$$LT_{\frac{\partial Q}{\partial \xi}}^{\eta} = \sum_{i=1}^{i=NV} \left(T_{\frac{\partial Q}{\partial \xi}} \cdot \Delta z_i'^{ST} \cdot \cos(\theta_i^P) \right)$$

$$LT_{\frac{\partial Q}{\partial \eta}}^{\eta} = \sum_{i=1}^{i=NV} \left(T_{\frac{\partial Q}{\partial \eta}} \cdot \Delta z_i'^{ST} \cdot \cos(\theta_i^P) \right)$$

$$LT_{\frac{\partial Q}{\partial z'}}^{\eta} = \sum_{i=1}^{i=NV} \left(T_{\frac{\partial Q}{\partial z'}} \cdot \Delta z_i'^{ST} \cdot \cos(\theta_i^P) \right)$$

$$LT_{Q \frac{\partial z'}{\partial \xi}}^{\eta} = \sum_{i=1}^{i=NV} \left(Q_i \cdot \cos(\theta_i^P) \right)$$

With all of the intermediate terms computed, the panel integrals can be computed.

Double Layer Gradient Equations : Linear in the ξ -Direction

The final expressions for the panel influence integrals for a linear panel singularity variation in the ξ - direction, are:

The velocity in the ξ - direction due to a linear ξ shape function:

$$\frac{\partial}{\partial \xi^T} (\psi_{N,H.S}^{\xi}(\xi^T, \eta^T, z'^T)) = S_{\xi} \left((SF_{\xi} + \xi^T) \cdot \frac{\partial}{\partial \xi^T} (\psi_{N,H.S}^c(\xi^T, \eta^T, z'^T)) + \psi_{N,H.S}^c(\xi^T, \eta^T, z'^T) + LT_{\frac{\partial Q}{\partial \xi}}^{\xi} \right)$$

The velocity in the η - direction due to a linear ξ shape function:

$$\frac{\partial}{\partial \eta^T}(\psi_{N,H.S}^\xi(\xi^T, \eta^T, z'^T)) = S_\xi \left((SF_\xi + \xi^T) \cdot \frac{\partial}{\partial \eta^T}(\psi_{N,H.S}^c(\xi^T, \eta^T, z'^T)) + LT_{\frac{\partial Q}{\partial \eta}}^\xi \right)$$

The velocity in the z' - direction due to a linear ξ shape function:

$$\frac{\partial}{\partial z'^T}(\psi_{N,H.S}^\xi(\xi^T, \eta^T, z'^T)) = S_\xi \left((SF_\xi + \xi^T) \cdot \frac{\partial}{\partial z'^T}(\psi_{N,H.S}^c(\xi^T, \eta^T, z'^T)) + LT_{\frac{\partial Q}{\partial z'}}^\xi + LT_{Q \frac{\partial z'}{\partial \eta}}^\xi \right)$$

Double Layer Gradient Equations : Linear in the η -Direction

The results of the double layer gradient, or velocity panel influence integrals are presented for the η -direction double layer variation across the panel:

The velocity in the ξ -direction due to a linear η shape function:

$$\frac{\partial}{\partial \xi^T}(\psi_{N,H.S}^\eta(\xi^T, \eta^T, z'^T)) = S_\eta \left((SF_\eta + \eta^T) \cdot \frac{\partial}{\partial \xi^T}(\psi_{N,H.S}^c(\xi^T, \eta^T, z'^T)) + LT_{\frac{\partial Q}{\partial \xi}}^\eta \right)$$

The velocity in the η -direction due to a linear η shape function:

$$\frac{\partial}{\partial \eta^T}(\psi_{N,H.S}^\eta(\xi^T, \eta^T, z'^T)) = S_\eta \left((SF_\eta + \eta^T) \cdot \frac{\partial}{\partial \eta^T}(\psi_{N,H.S}^c(\xi^T, \eta^T, z'^T)) + \psi_n^c(\xi^T, \eta^T, z'^T) + LT_{\frac{\partial Q}{\partial \eta}}^\eta \right)$$

The velocity in the z' -direction due to a linear η shape function:

$$\frac{\partial}{\partial z'^T}(\psi_{N,H.S}^\eta(\xi^T, \eta^T, z'^T)) = S_\eta \left((SF_\eta + \eta^T) \cdot \frac{\partial}{\partial z'^T}(\psi_{N,H.S}^c(\xi^T, \eta^T, z'^T)) + LT_{\frac{\partial Q}{\partial z'}}^\eta + LT_{Q \frac{\partial z'}{\partial \eta}}^\eta \right)$$

Double Layer Gradient Equations : $\langle N1, N2, N3 \rangle$ Plots

Figures 3-36 - 3-41 show the double layer velocity effects of the various individual $\langle N1, N2, N3 \rangle$ shape functions.

Commentary on the Double Layer Gradient Plots

The double layer velocity scans are particularly interesting. The linear variation of the double layer creates a line of vortex like elements across the panel surface in the direction of the linear variation. Figures Figures 3-36 - 3-41 show this panel surface

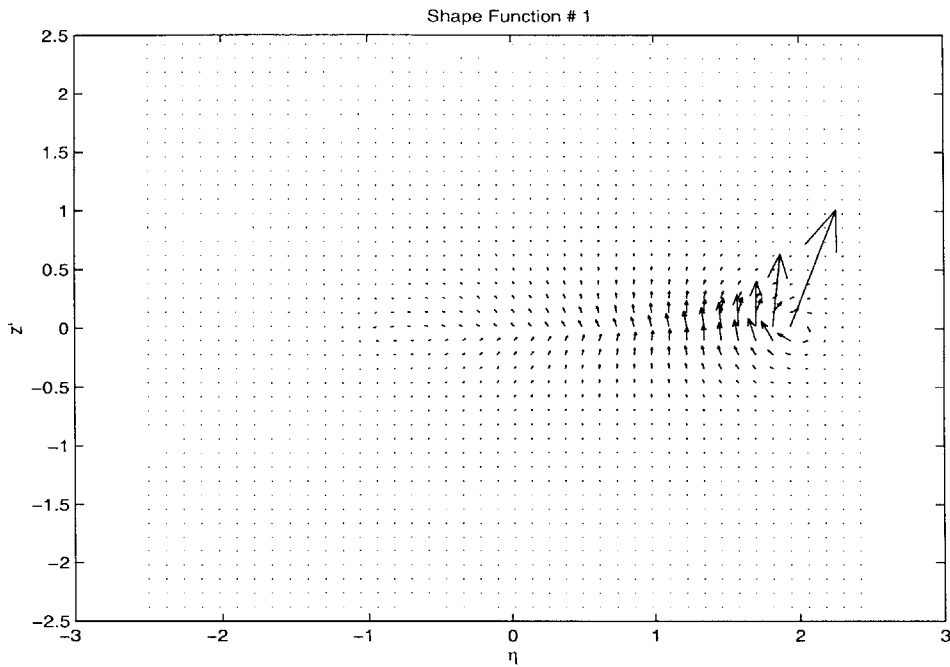


Figure 3-36: A 2-D velocity vector plot for a double layer sample panel with vertices $[V1(0, 2, 0), V2(1, -1, 0), V3(-1, -1, 0)]$, evaluated in the plane $\eta = 0$.

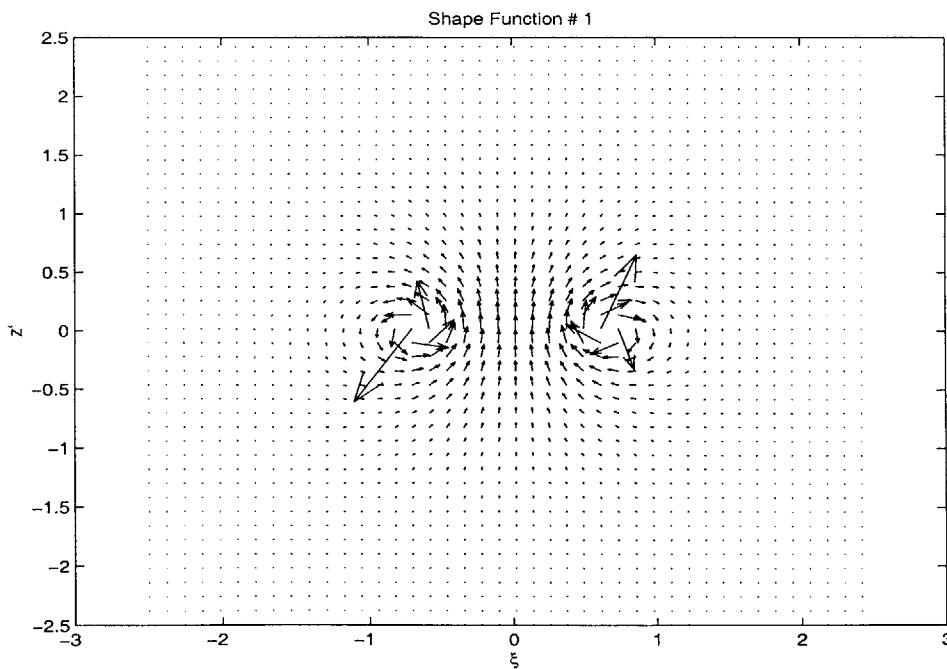


Figure 3-37: A 2-D velocity vector plot for a double layer sample panel $[V1(0, 2, 0), V2(1, -1, 0), V3(-1, -1, 0)]$, evaluated in the plane $\xi = 0$.

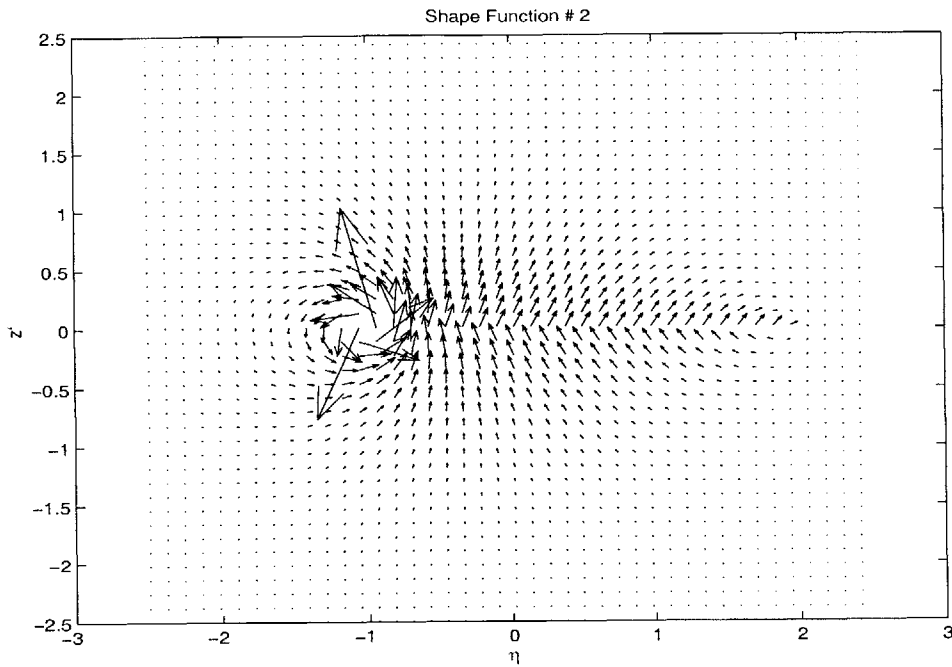


Figure 3-38: A 2-D velocity vector plot for a double layer sample panel $[V1(0, 2, 0), V2(1, -1, 0), V3(-1, -1, 0)]$, evaluated in the plane $\eta = 0$.

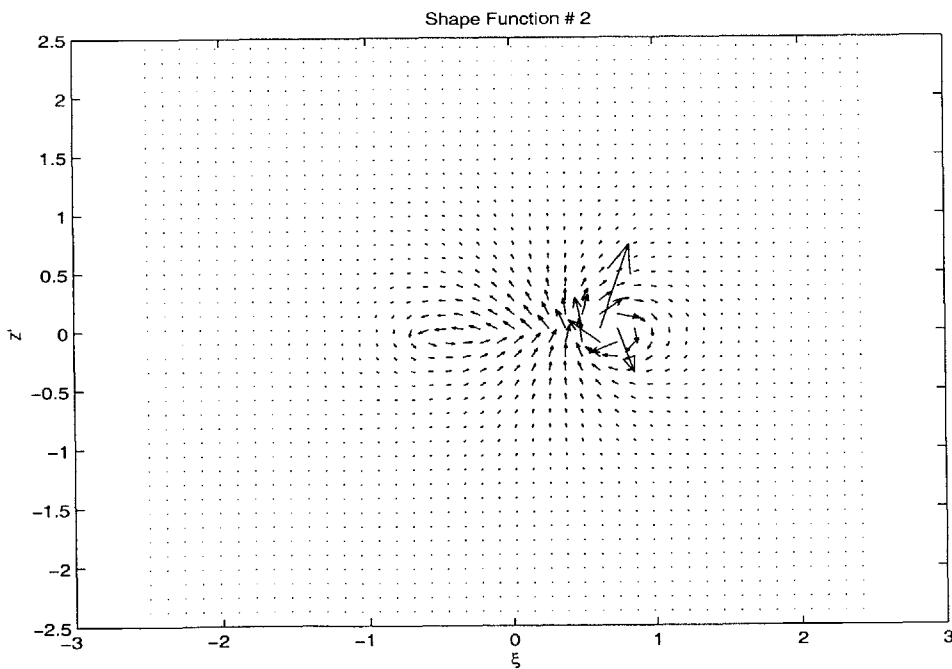


Figure 3-39: A 2-D velocity vector plot for a double layer sample panel $[V1(0, 2, 0), V2(1, -1, 0), V3(-1, -1, 0)]$, evaluated in the plane $\xi = 0$.

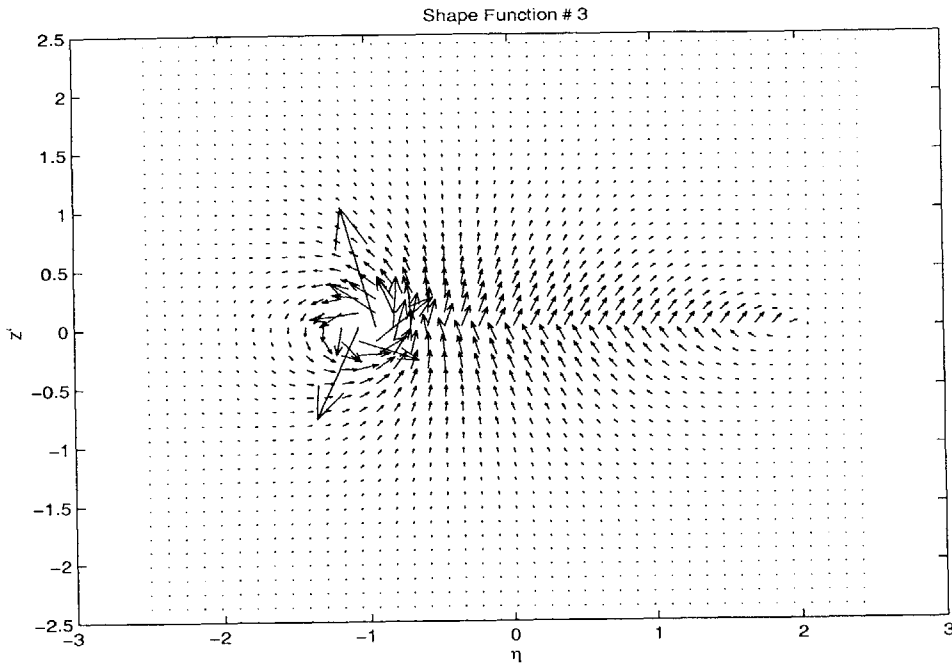


Figure 3-40: A 2-D velocity vector plot for a double layer sample panel $[V1(0, 2, 0), V2(1, -1, 0), V3(-1, -1, 0)]$, evaluated in the plane $\eta = 0$.

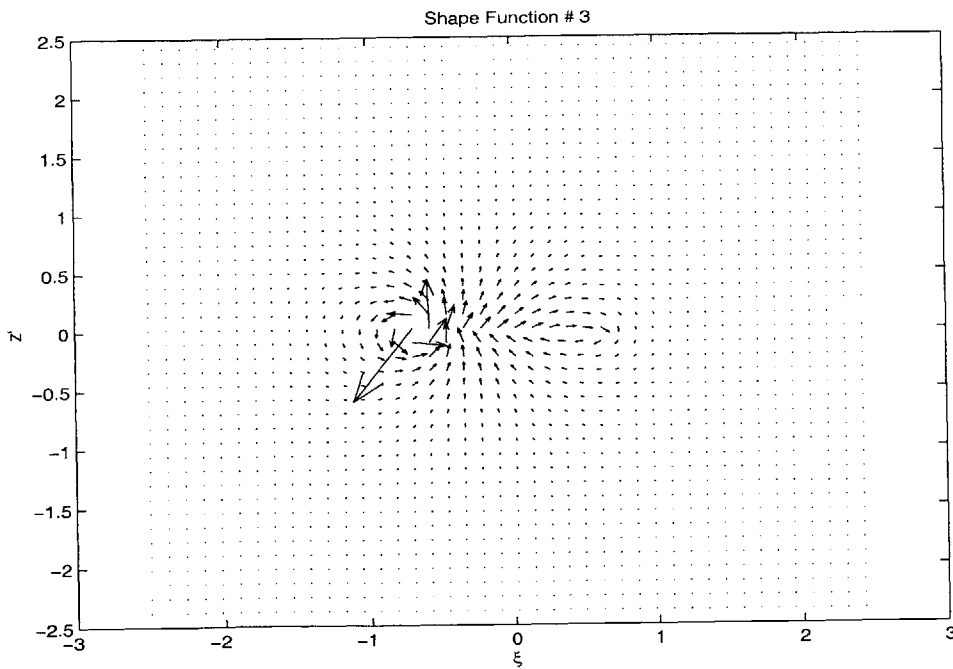


Figure 3-41: A 2-D velocity vector plot for a double layer sample panel $[V1(0, 2, 0), V2(1, -1, 0), V3(-1, -1, 0)]$, evaluated in the plane $\xi = 0$.

vortex like behavior clearly. The plots are particularly enlightening since they show the panel surface constant vortex distribution due to the linear doublet variation. The panel surface vortex distribution is equal and opposite in total strength to the vortex strength produced at the edge of the panel where the doublet strength has a step function like behavior from $\rho_\psi = 0$ just outside of the panel to $\rho_\psi = 1$ just on the panel. The linear variation of doublet strength is advantageous in the panel method due to the "smearing" of the important vortex effect over the panel element, rather than just at the edges of the panel as seen in the constant doublet case.

3.7.6 Single Layer Gradient Equations

The panel integral for the gradient of the single layer is computed in this section. This is an analytic expression of the following panel integral:

$$\nabla_T \left(\phi_M^{l_{\xi,\eta}}(\xi^T, \eta^T, z'^T) \right) = \vec{v}(\xi^T, \eta^T, z'^T) = \nabla_T \left(\int \int_{Panel} \rho_{l_{\xi,\eta}} \cdot \frac{1}{|\vec{x} - \vec{x}'|} dS_{Panel} \right)$$

Single Layer Gradient Equations : Variable Setup and Simplifications

Before computing the linear variation of the velocity-single layer panel integrals, some intermediate terms are defined in order to simplify the final expressions.

$$S_i^1 = -\Delta \xi_i^{ST} \cdot \cos(\theta_i^P) + -\Delta \eta_i^{ST} \cdot \sin(\theta_i^P)$$

and:

$$S_i^2 = -\Delta \xi_{i+1}^{ST} \cdot \cos(\theta_i^P) + -\Delta \eta_{i+1}^{ST} \cdot \sin(\theta_i^P)$$

and:

$$D_i = \sqrt{(\xi_{i+1}^S - \xi_i^S \cdot \xi_{i+1}^S - \xi_i^S) + (\eta_{i+1}^S - \eta_i^S \cdot \eta_{i+1}^S - \eta_i^S)}$$

The following intermediate terms are presented, once again to simplify the final integral expression. Here the ξ -singularity variation on the panel intermediate terms are presented:

$$T1_\xi = - \left(R_i^I \cdot \cos(\theta_i^P) + \left(\frac{S_i^1 \cdot \Delta \xi_i^{ST}}{R_i^I} \right) \right)$$

$$\begin{aligned}
T2_\xi &= \left(R_{i+1}^I \cdot \cos(\theta_i^P) + \left(\frac{S_i^2 \cdot \Delta \xi_{i+1}^{ST}}{R_{i+1}^I} \right) \right) \\
T3_\xi &= -Q_i \cdot \left(2 \cdot (-\Delta \xi_i^{ST}) + 2 \cdot (S_i^1) \cdot \cos(\theta_i^P) \right) \\
T4_\xi &= (R_i^I + R_{i+1}^I - D_i) \cdot (R_i^I + R_{i+1}^I + D_i) \\
T5_\xi &= \left(\frac{2 \cdot D_i \cdot ((R_i^I)^2 - (S_i^1)^2)}{T4_\xi^\eta} \right) \cdot \left(\frac{\Delta \xi_i^{ST}}{R_i^I} + \frac{\Delta \xi_{i+1}^{ST}}{R_{i+1}^I} \right)
\end{aligned}$$

The linear correction term is expressed:

For the ξ -linear variation of panel singularity strength expression for the linear correction to the velocity in the ξ -direction:

$$T6_\xi^\xi = \sum_{i=1}^{i=NV} \left(\frac{1}{2} \sin(\theta_i^P) (T1_\xi + T2_\xi + T3_\xi + T5_\xi) \right)$$

For the ξ -linear variation of panel singularity strength expression for the linear correction to the velocity in the η -direction:

$$T6_\xi^\eta = \sum_{i=1}^{i=NV} \left(\frac{1}{2} \cos(\theta_i^P) (T1_\xi + T2_\xi + T3_\xi + T5_\xi) \right)$$

And similarly for the η -variation linear shape function, the following expressions are temporary variable simplifications:

$$\begin{aligned}
T1_\eta &= - \left(R_i^I \cdot \sin(\theta_i^P) + \left(\frac{-S_i^1 \cdot \Delta \eta_i^{ST}}{R_i^I} \right) \right) \\
T2_\eta &= \left(R_{i+1}^I \cdot \sin(\theta_i^P) + \left(\frac{-S_i^2 \cdot \Delta \eta_{i+1}^{ST}}{R_{i+1}^I} \right) \right) \\
T3_\eta &= -Q_i \cdot \left(2 \cdot (-\Delta \eta_i^{ST}) + 2 \cdot (S_i^1) \cdot \sin(\theta_i^P) \right) \\
T4_\eta &= (R_i^I + R_{i+1}^I - D_i) \cdot (R_i^I + R_{i+1}^I + D_i) \\
T5_\eta &= \left(\frac{2 \cdot D_i \cdot ((R_i^I)^2 - (S_i^1)^2)}{T4_\eta^\eta} \right) \cdot \left(\frac{\Delta \eta_i^{ST}}{R_i^I} + \frac{\Delta \eta_{i+1}^{ST}}{R_{i+1}^I} \right)
\end{aligned}$$

The linear correction term, before addition to the scaled panel constant strength, is finally expressed. It turns out that the temporary terms double up in both the cases, and the final result is expressed. For the η linear variation of panel singularity strength expression for the linear correction to the velocity in the ξ -direction:

$$T6_{\eta}^{\xi} = \sum_{i=1}^{i=NV} \left(\frac{1}{2} \sin(\theta_i^P) (T1_{\eta}^{\eta} + T2_{\eta}^{\eta} + T3_{\eta}^{\eta} + T5_{\eta}^{\eta}) \right)$$

For the η linear variation of panel singularity strength expression for the linear correction to the velocity in the η -direction:

$$T6_{\eta}^{\eta} = \sum_{i=1}^{i=NV} \left(\frac{1}{2} \cos(\theta_i^P) (T1_{\eta}^{\eta} + T2_{\eta}^{\eta} + T3_{\eta}^{\eta} + T5_{\eta}^{\eta}) \right)$$

Single Layer Gradient Equations : Linear In ξ -Direction

The gradient of the single layer integral is evaluated at the field point. In this case the linear variation of the single layer lies in the ξ - direction:

The velocity in the ξ -direction, due to a linear variation in single layer in the ξ -direction:

$$\frac{\partial}{\partial \xi^T} (\phi_{H.S,N}^{\xi}(\xi^T, \eta^T, z'^T)) = S_{\xi} \left((SF_{\xi} + \xi^T) \cdot \frac{\partial}{\partial \xi^T} (\phi_{H.S,N}^c(\xi^T, \eta^T, z'^T)) + (\phi_{H.S,N}^c(\xi^T, \eta^T, z'^T)) - T6_{\xi}^{\xi} \right)$$

The velocity in the η -direction, due to a linear variation in single layer in the ξ -direction:

$$\frac{\partial}{\partial \eta^T} (\phi_{H.S,N}^{\xi}(\xi^T, \eta^T, z'^T)) = S_{\xi} \left((SF_{\xi} + \xi^T) \cdot \frac{\partial}{\partial \eta^T} (\phi_{H.S,N}^c(\xi^T, \eta^T, z'^T)) - T6_{\eta}^{\xi} \right)$$

The velocity in the z' -direction, due to a linear variation in single layer in the ξ -direction:

$$\frac{\partial}{\partial z'^T} (\phi_{H.S,N}^{\xi}(\xi^T, \eta^T, z'^T)) = \psi_{H.S,N}^{\xi}(\xi^T, \eta^T, z'^T)$$

Single Layer Gradient Equations : Linear In η -Direction

The gradient of the single layer integral is evaluated at the field point. In this case the linear variation on the source panel lies in the η -direction:

The velocity in the ξ -direction, due to a linear variation in single layer in the η -direction:

$$\frac{\partial}{\partial \xi^T}(\phi_{H.S,N}^\eta(\xi^T, \eta^T, z'^T)) = S_\eta \left((SF_\eta + \eta^T) \cdot \frac{\partial}{\partial \xi^T}(\phi_{H.S,N}^c(\xi^T, \eta^T, z'^T)) + T6_\xi^\eta \right)$$

The velocity in the η -direction, due to a linear variation in single layer in the η -direction:

$$\frac{\partial}{\partial \eta^T}(\phi_{H.S,N}^\eta(\xi^T, \eta^T, z'^T)) = S_\eta \left((SF_\eta + \eta^T) \cdot \frac{\partial}{\partial \eta^T}(\phi_{H.S,N}^c(\xi^T, \eta^T, z'^T)) + (\phi_{H.S,N}^c(\xi^T, \eta^T, z'^T)) + T6_\eta^\eta \right)$$

The velocity in the z' -direction, due to a linear variation in single layer in the η -direction:

$$\frac{\partial}{\partial z'^T}(\phi_{H.S,N}^\eta(\xi^T, \eta^T, z'^T)) = \psi_{H.S,N}^\eta(\xi^T, \eta^T, z'^T)$$

Single Layer Gradient Equations : $\langle N1, N2, N3 \rangle$ Results

These equations combined with the constant strength shape function, N^c , derived in earlier sections, makeup the $\langle N^\xi, N^\eta, N^c \rangle$ basis. The result should then be transformed through the basis transformation to compute the Linear $\langle N^1, N^2, N^3 \rangle$ basis.

The Gradient of the Single Layer Potential Panel Influence Integral Plots

Figures 3-42 to 3-50 outline the gradient of the linear variation of the single layer, panel influence integral plots as vector traces.

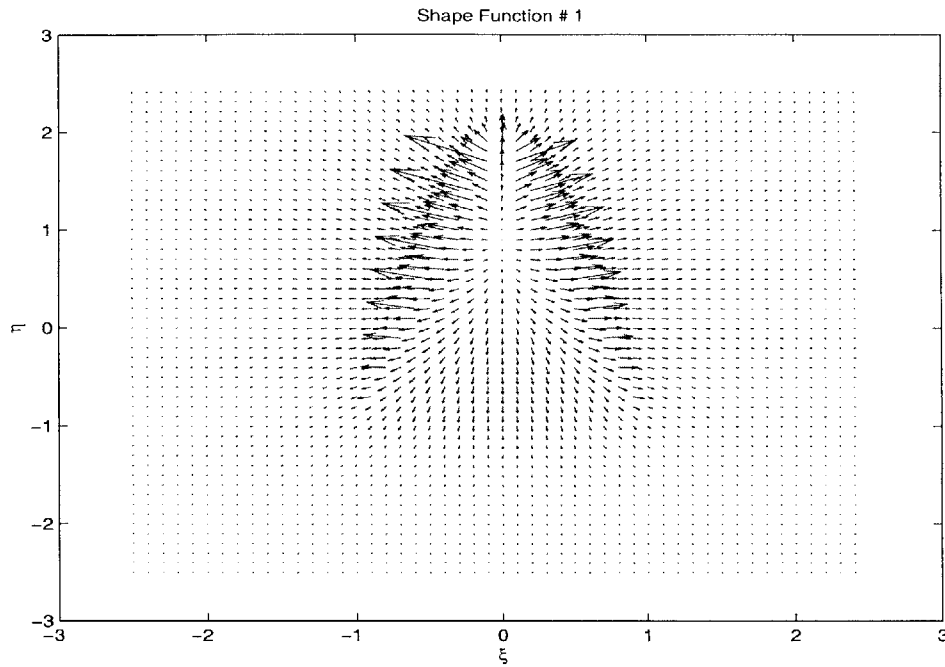


Figure 3-42: A 2-D velocity vector plot for a sample linear single layer panel influence integral, for the panel $[V1(0, 2, 0), V2(1, -1, 0), V3(-1, -1, 0)]$, evaluated in the plane $z' = +\epsilon$.

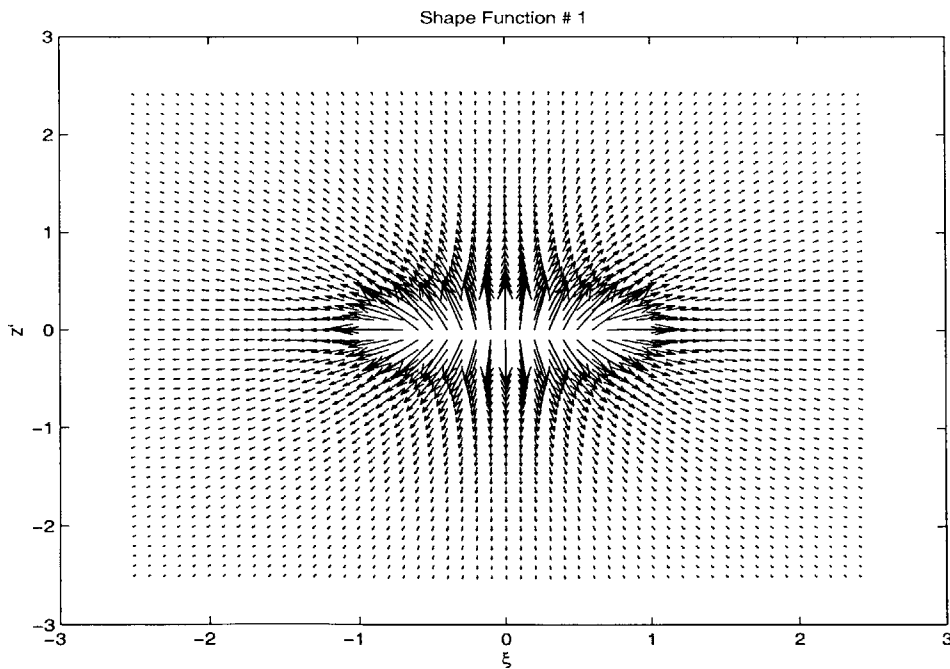


Figure 3-43: A 2-D velocity vector plot for a sample linear single layer panel influence integral, for the panel $[V1(0, 2, 0), V2(1, -1, 0), V3(-1, -1, 0)]$, evaluated in the plane $\eta = 0$.

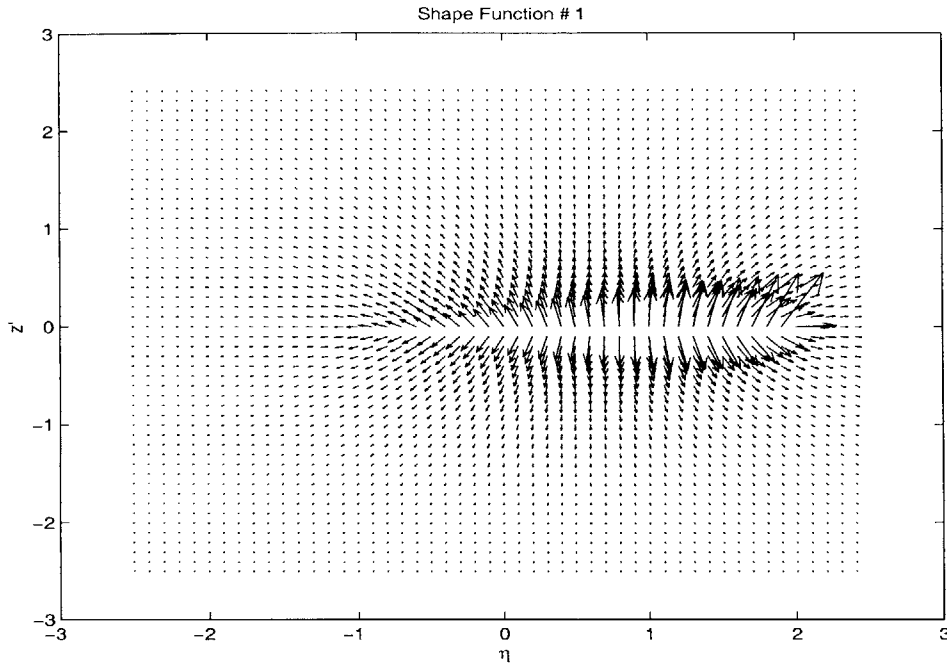


Figure 3-44: A 2-D velocity vector plot for a sample linear single layer panel influence integral, for the panel $[V1(0, 2, 0), V2(1, -1, 0), V3(-1, -1, 0)]$, evaluated in the plane $\xi = 0$.

3.7.7 Comparing the Linear and Constant Strength Panel Integrals

Figures 3-51 to 3-56 show the potential plot comparisons for the linear strength and constant strength integrals, for both the single and double layers. The comparison admits a conceptual feel for the decay of the linear effects with distance from the panel. Notice that the constant strength integral is presented as both a full result and a $\frac{1}{3}$ result corresponding to a similar density strength as the linear method (useful for the comparison of the approaches).

3.7.8 Conclusion of Analytical Panel Influence Integrals

The analytical integrals have a significant advantage since they allow very accurate computation of the panel influence integrals. However, several disadvantages are identified with the analytical panel integrals:

- They are costly to compute. The time taken to compute a panel integral is large

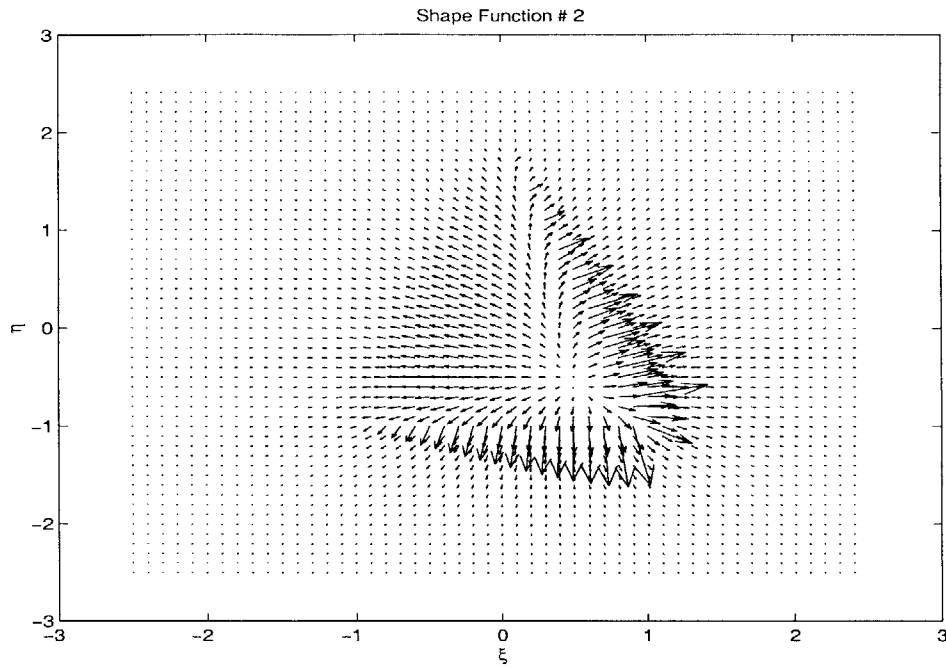


Figure 3-45: A 2-D velocity vector plot for a sample linear single layer panel influence integral, for the panel $[V1(0, 2, 0), V2(1, -1, 0), V3(-1, -1, 0)]$, evaluated in the plane $z' = +\epsilon$.

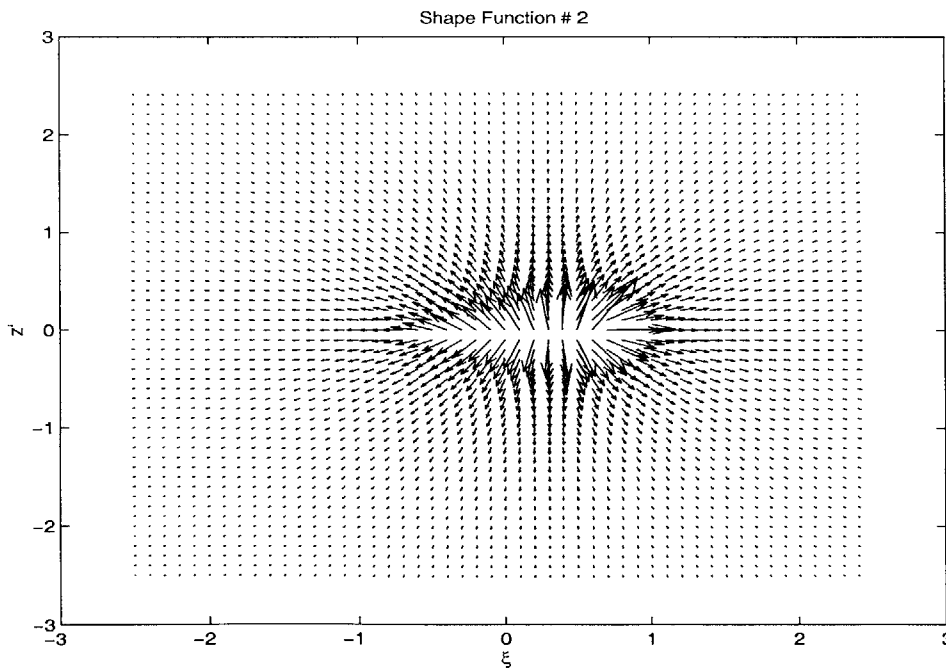


Figure 3-46: A 2-D velocity vector plot for a sample linear single layer panel influence integral, for the panel $[V1(0, 2, 0), V2(1, -1, 0), V3(-1, -1, 0)]$, evaluated in the plane $\eta = 0$.

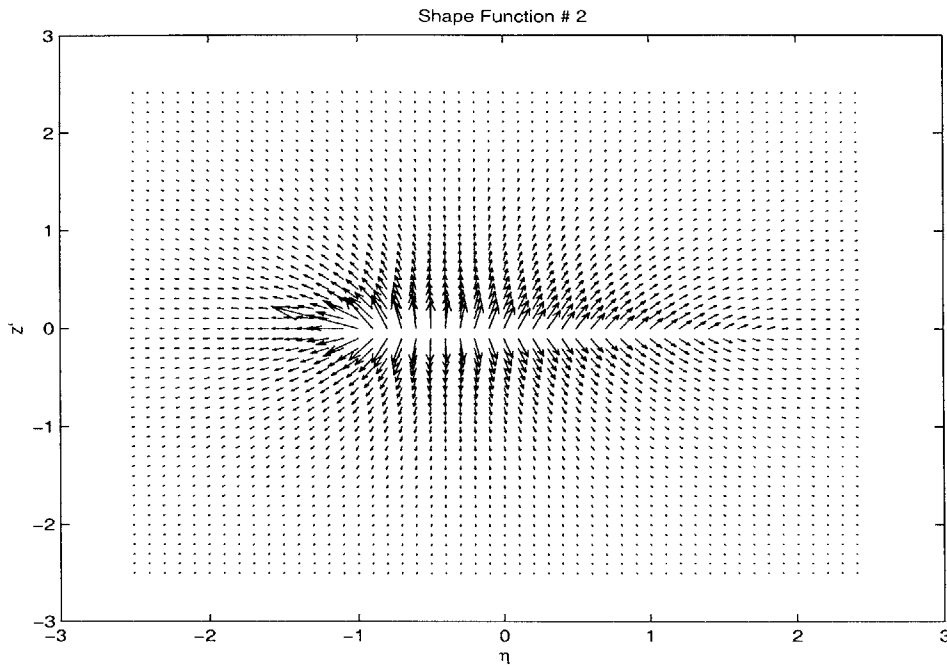


Figure 3-47: A 2-D velocity vector plot for a sample linear single layer panel influence integral, for the panel $[V1(0, 2, 0), V2(1, -1, 0), V3(-1, -1, 0)]$, evaluated in the plane $\xi = 0$.

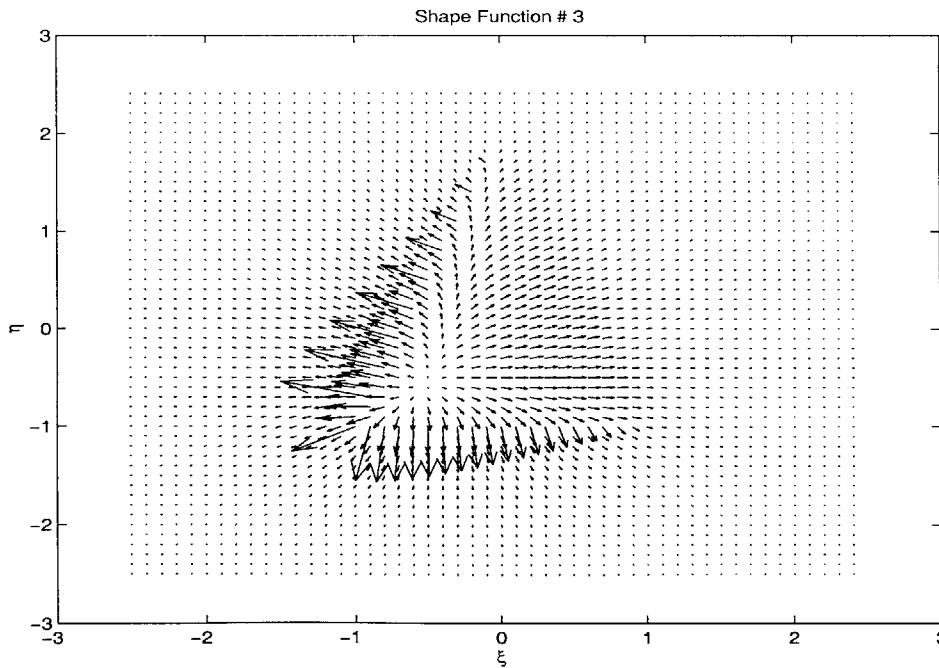


Figure 3-48: A 2-D velocity vector plot for a sample linear single layer panel influence integral, for the panel $[V1(0, 2, 0), V2(1, -1, 0), V3(-1, -1, 0)]$, evaluated in the plane $z' = +\epsilon$.

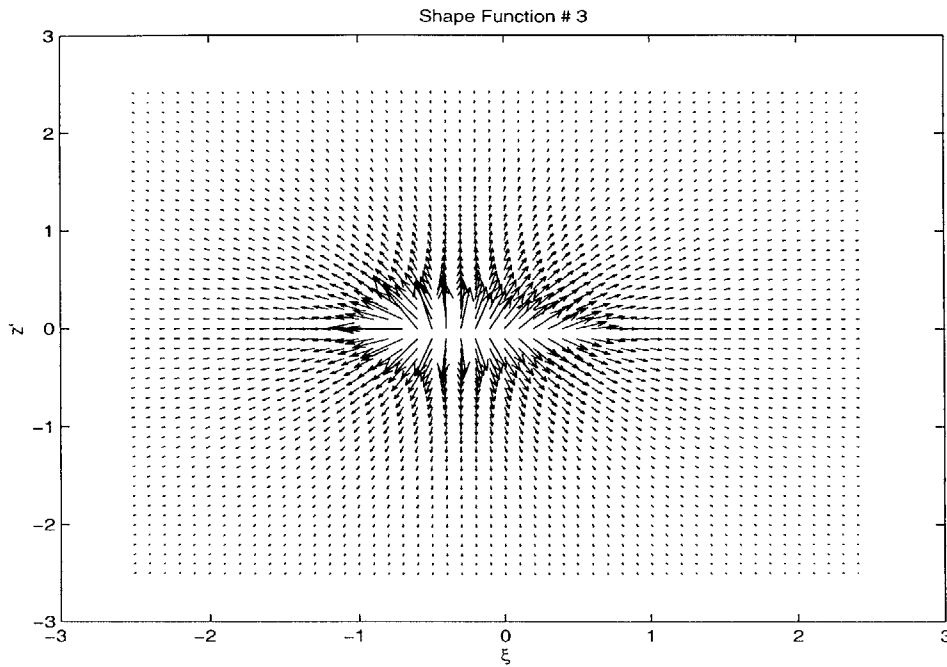


Figure 3-49: A 2-D velocity vector plot for a sample linear single layer panel influence integral, for the panel $[V1(0, 2, 0), V2(1, -1, 0), V3(-1, -1, 0)]$, evaluated in the plane $\eta = 0$.

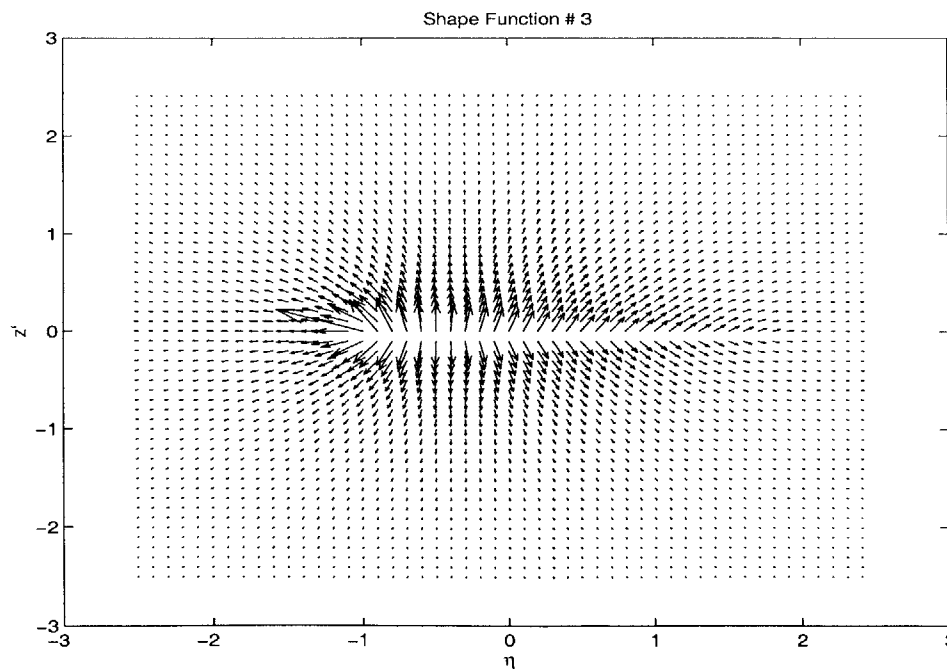


Figure 3-50: A 2-D velocity vector plot for a sample linear single layer panel influence integral, for the panel $[V1(0, 2, 0), V2(1, -1, 0), V3(-1, -1, 0)]$, evaluated in the plane $\xi = 0$.

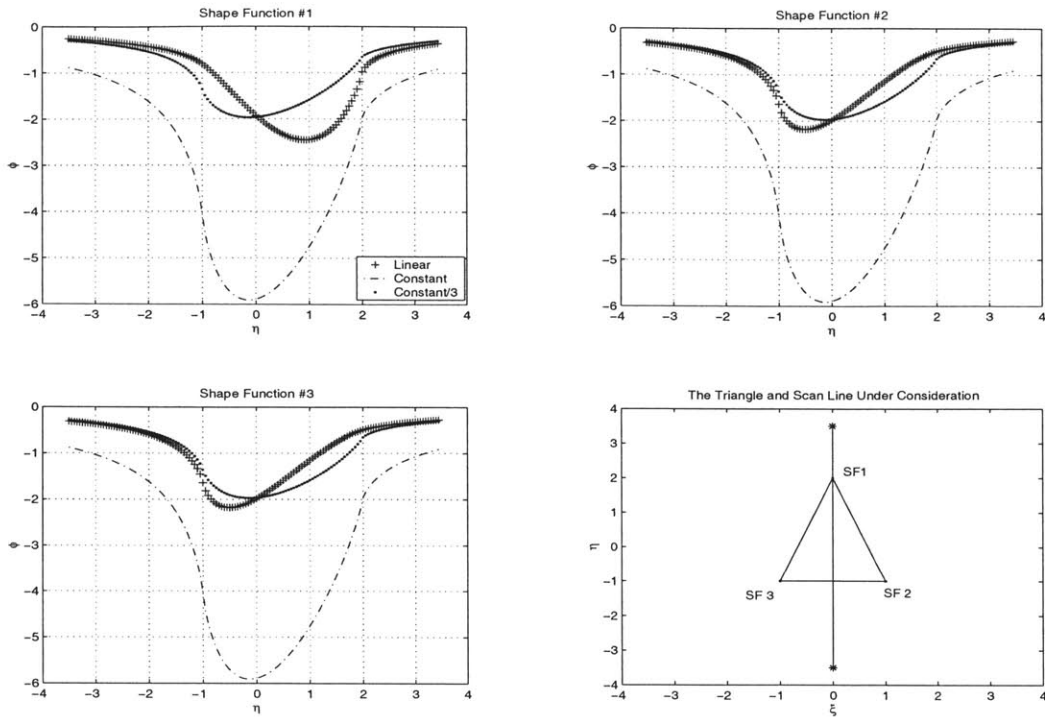


Figure 3-51: The single layer potential evaluated along the line $z' = \epsilon, \xi = 0$.

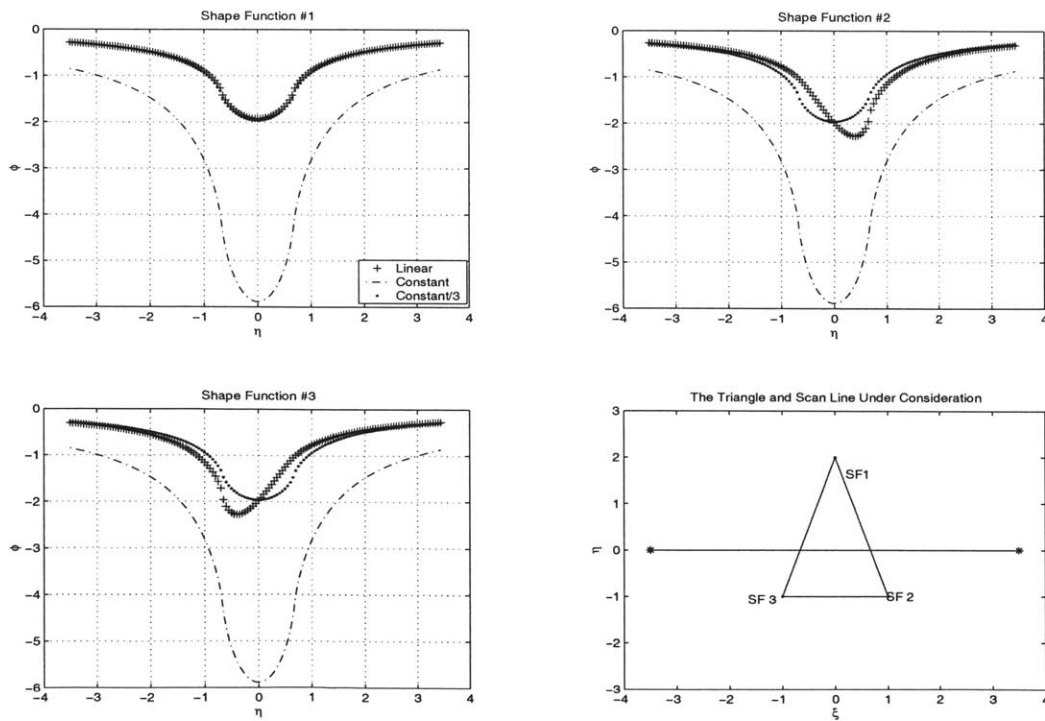


Figure 3-52: The single layer potential evaluated along the line $z' = \epsilon, \eta = 0$.

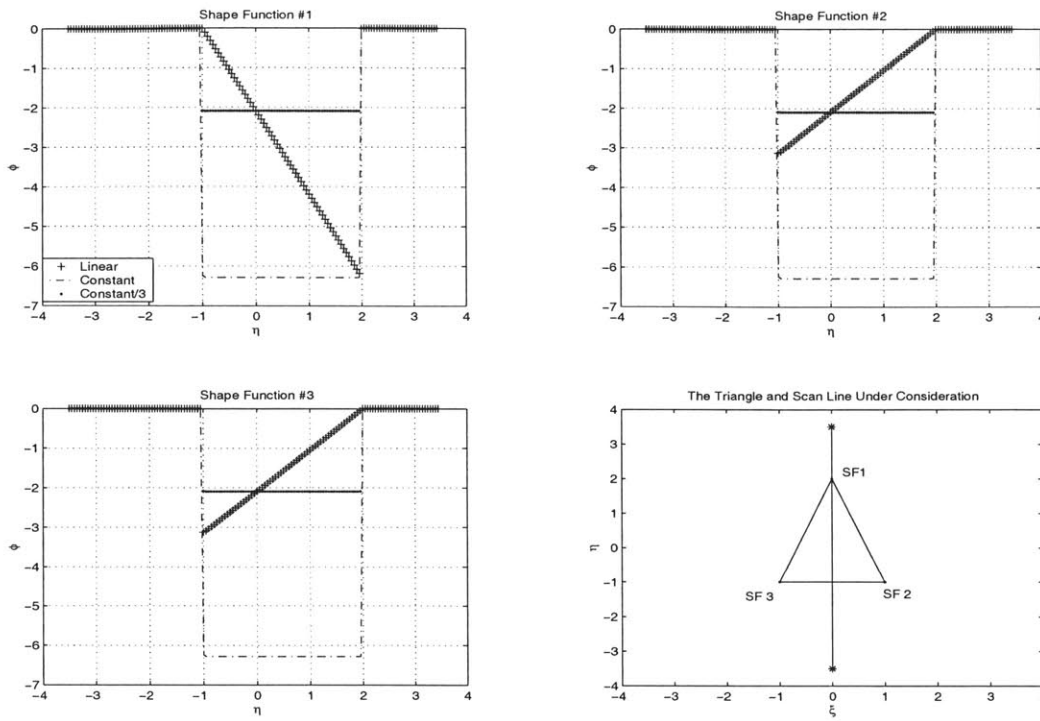


Figure 3-53: The double layer potential evaluated along the line $z' = \epsilon$, $\xi = 0$.

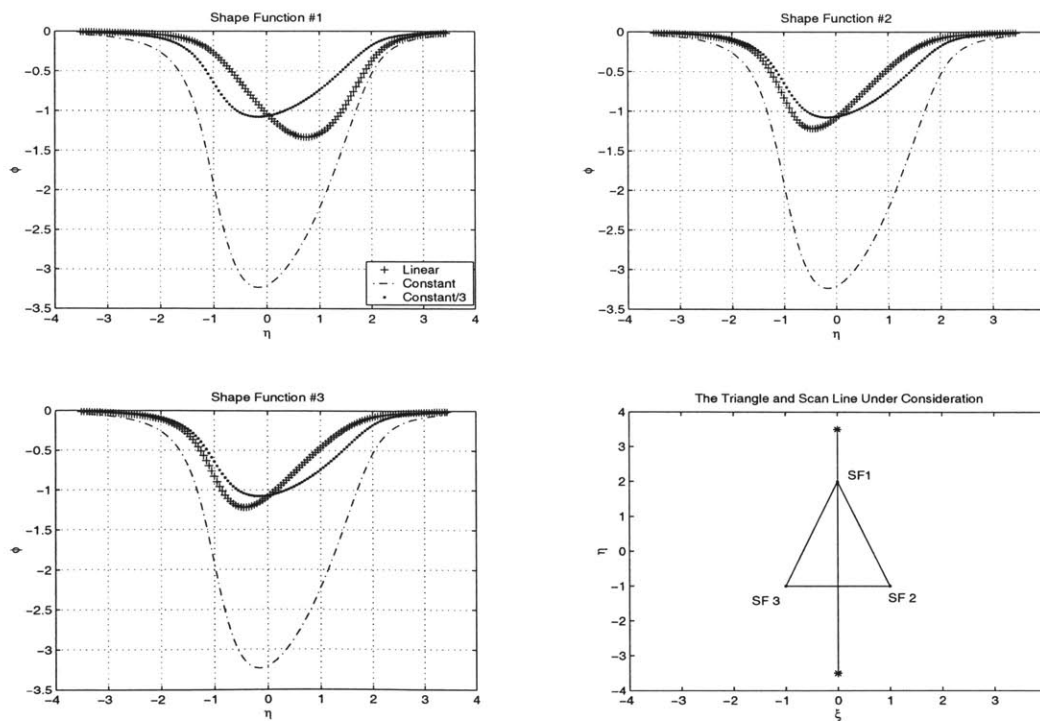


Figure 3-54: The double layer potential evaluated along the line $z' = 0.5$, $\xi = 0$.

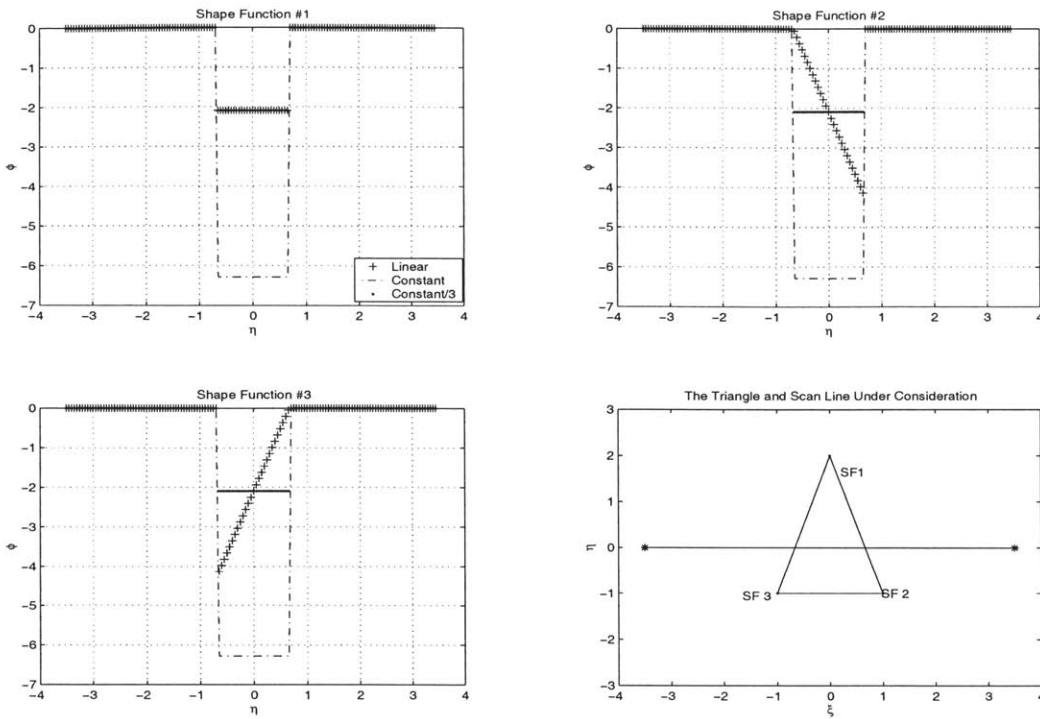


Figure 3-55: The double layer potential evaluated along the line $z' = \epsilon, \eta = 0$.

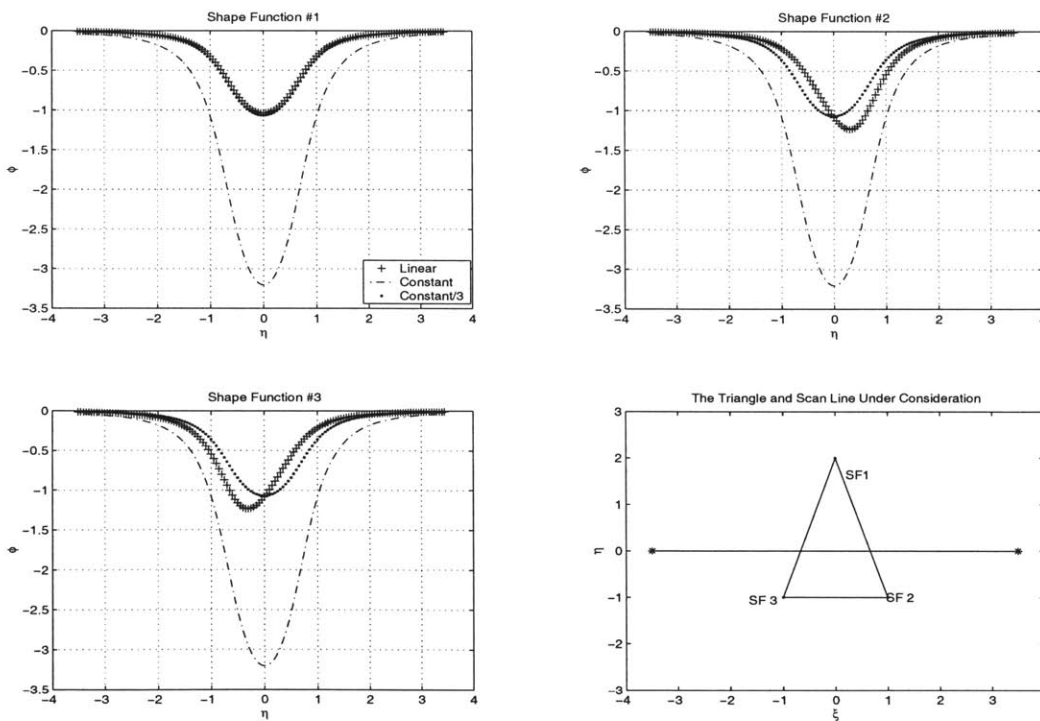


Figure 3-56: The double layer potential evaluated along the line $z' = 0.5, \eta = 0$.

due to the logarithmic and trigonometric relations involved. When computing several million direct interactions on a modern workstation, the time taken can be relatively significant.

- At great distances from the panel the analytical panel integrals become less accurate.

Fortunately, in the cases where the panel is a large distance from the evaluation point faster and more accurate means of computing the panel integral influence exist. These simplifications are the foundation of the fast methods which will be described in Chapter 4.

3.8 Matrix of Influence Coefficients and the Direct Solution

Once the panel integrals are computed, they need to be compiled in such a manner as to solve the linear system described by the initial discretized version of the equations. This is easily done by constructing a matrix of the panel integral influence coefficients.

3.8.1 Matrix of Influence coefficients-Galerkin vs. Collocation

Before describing the linear system, a brief investigation of the two methods of satisfying boundary conditions are presented. The simple collocation scheme, and the Galerkin Scheme.

Collocation Approaches

The Collocation Method is common in panel method implementations. It is presented here for the constant panel influence case.

Collocation is merely constraining the boundary condition at a single point on the panel. For the constant-collocation case, the panel centroid is the collocation point, as seen in figure 3-57.

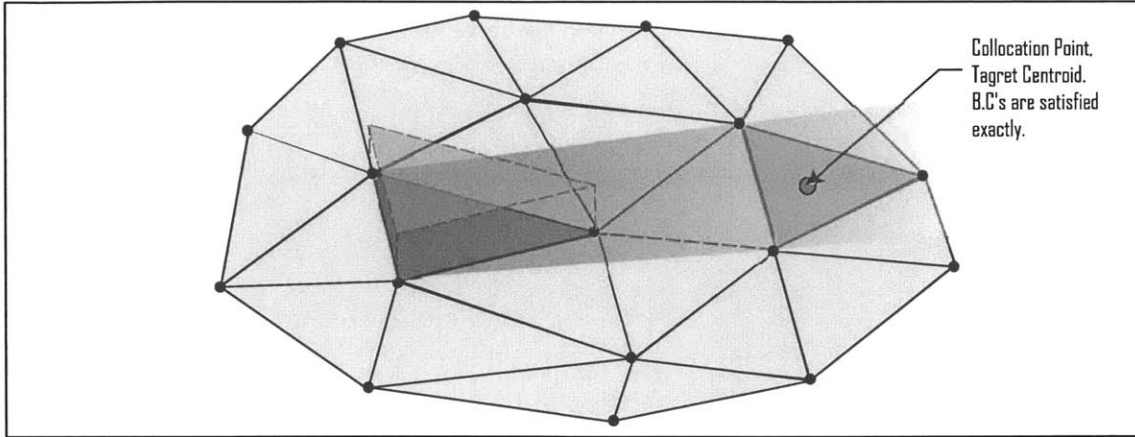


Figure 3-57: The collocation approach for constant strength shape functions.

Galerkin Approaches

The Galerkin Scheme is more commonly used in Finite Element Method approaches, however, it is fully compliant with the Boundary Element Method, and can add to the solution refinement in some cases. The Galerkin scheme is based on minimizing the residual of the orthogonal basis functions on the source and target panels respectively. The equations for the discrete system when expressed in a Galerkin form become:

Gradient Single Layer

Single Layer Neumann Velocity Boundary Integral Equation:

$$R_G = \int \int_{T_{Panel}} (\nabla_{\vec{x}'} \cdot \hat{n} \cdot \zeta_T^G(\phi(\vec{x}')))) dS_{T_{Panel}} - \int \int_{T_{Panel}} \zeta_T^G \left(\frac{c\varphi\delta_{ii}}{2} \right) dS_{T_{Panel}}$$

$$+ \frac{1}{4\pi} \nabla_{\vec{x}'} \cdot \hat{n} \sum_{n=1}^{n=NP} \int \int_{T_{Panel}} \zeta_T^G \left(\oint_{S_{Paneln}} \varphi_S^G(\vec{x}) \frac{1}{\|\vec{x} - \vec{x}'\|} dS_{S_{Paneln}} \right) dS_{T_{Panel}}$$

Gradient Double Layer

Double Layer Neumann Velocity Boundary Integral Equation:

$$R_G = \int \int_{T_{Panel}} \zeta_T^G (\nabla_{\vec{x}'} \cdot \hat{n} \cdot \varphi(\vec{x})) -$$

$$-\frac{1}{4\pi} \sum_{n=1}^{n=N_P} \nabla_{\vec{x}'} \cdot \hat{n} \int \int_{T_{Panel}} \zeta_T^G \left(\int \int_{S_{Panel_n}} \varphi_S^G \left(\frac{\partial}{\partial \hat{n}_{\vec{x}}} \left(\frac{1}{\|\vec{x} - \vec{x}'\|} \right) \right) dS_{Panel_n}^{B+W} \right) dS_{T_{Panel}}$$

Potential Method

Potential Equation:

$$\begin{aligned} R_G = & \int \int_{T_{Panel}} \zeta_T^G (\phi(\vec{x})) dS_{T_{Panel}} - \\ & \frac{1}{4\pi} \sum_{n=1}^{n=N_P} \int \int_{T_{Panel}} \zeta_T^G \left(\int \int_{S_{Panel_n}} -V_\infty \cdot \hat{n} \frac{1}{\|\vec{x} - \vec{x}'\|} dS_{Panel_n} \right) dS_{T_{Panel}} \\ & - \frac{1}{4\pi} \sum_{n=1}^{n=N_P} \int \int_{T_{Panel}} \zeta_T^G \left(\int \int_{S_{Panel_n}} \phi \frac{\partial}{\partial n} \left(\frac{1}{\|\vec{x} - \vec{x}'\|} \right) dS_{Panel_n}^{B+W} \right) dS_{T_{Panel}} \end{aligned}$$

Here φ is the shape function on the source panel, while ζ is the shape function on the target panel. By definition, the above expressions become a Galerkin formulation when the φ and ζ are identical orthogonal shape function sets. In this thesis, the φ and ζ distributions are either traditional constant or linear basis functions.

As a result of using a Galerkin scheme, the complexity of the system is increased. Only one of the area integrals can be computed analytically, the other must be computed numerically. A choice between the inner panel integral and the outer Galerkin integrals must be made. In this work, the outer integral is computed using a 2-D Surface Triangle Gauss Quadrature approach. In the implementation, several default quadrature orders and schemes are available. Figure 3-58 outlines the Galerkin approach.

3.8.2 Setting Up the Linear System for Constant Strength Panels

Most constant strength boundary element implementations make use of centroidal-collocation approaches. Here the more general Galerkin scheme is presented. For constant strength panels the Constant Collocation method is a Galerkin formulation using a single quadrature point.

The entries to the matrix are merely the panel j influence integrals, evaluated

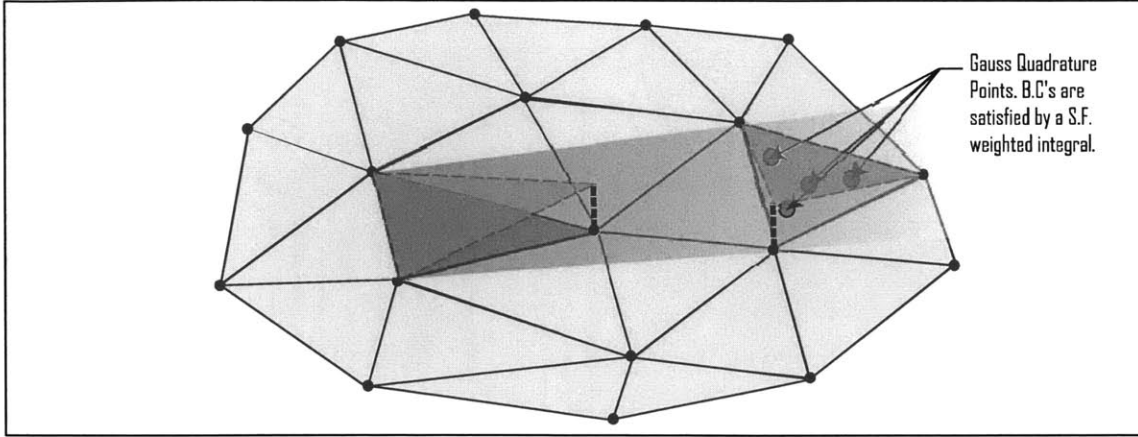


Figure 3-58: The Galerkin approach for linear strength shape functions, φ_S^G to the left and ζ_T^G . Here the Gauss quadrature integration points are apparent.

over target panel i (by collocation or Galerkin). The following linear system results:

$$[AIC] \vec{\rho}_D = B \cdot \vec{C}.$$

where, $\vec{\rho}_D$ is the unknown discrete panel singularity density, and $B \cdot \vec{C}$ is the boundary condition to be forced at each evaluation point.

The following is the full expression for the general constant collocation linear equation:

$$\begin{pmatrix} I_{T=1,S=1} & I_{T=1,S=2} & \dots & I_{T=1,S=NP} \\ I_{T=2,S=1} & I_{T=2,S=2} & \dots & I_{T=2,S=NP} \\ \vdots & \vdots & \vdots & \vdots \\ I_{T=NP,S=1} & I_{T=NP,S=2} & \dots & I_{T=NP,S=NP} \end{pmatrix} \begin{pmatrix} \rho_{D_{S=1}} \\ \rho_{D_{S=2}} \\ \vdots \\ \rho_{D_{S=NP}} \end{pmatrix} = \begin{pmatrix} B \cdot C_{T=1} \\ B \cdot C_{T=2} \\ \vdots \\ B \cdot C_{T=NP} \end{pmatrix}$$

The entries, $I_{T=2,S=1}$ are the analytic panel integrals presented earlier, in Galerkin or collocation form.

Considering each of the formulations used to solve the potential flow equation:

For the potential approach:

$$[AIC_{I_\psi^c}](\vec{\phi}) = [AIC_{I_\phi^c}](-V_\infty \cdot \hat{n})$$

For the single layer velocity approach:

$$[AIC_{I_\phi^c}](\vec{\sigma}) = (-V_\infty^{\vec{}} \cdot \hat{n})$$

For the double layer velocity approach:

$$[AIC_{I_\psi^c}](\vec{\mu}) = (-V_\infty^{\vec{}} \cdot \hat{n})$$

3.8.3 Setting Up the Linear System : Linear Strength Galerkin Approach

Since the linear-basis, vertex-based system has larger support footprint than the panel based approach, the resulting influence matrix must have inter-dependencies. Once again the general linear system resembles:

$$[AIC] \vec{\rho}_D = B \cdot \vec{C}.$$

where, $\vec{\rho}_D$ is the unknown discrete panel singularity density, and $B \cdot \vec{C}$ is the boundary condition to be forced at each evaluation point.

The following is an example of the construction of the system, including the influence matrix:

$$\begin{pmatrix} \sum I_{V_T=1, V_S=1}^P & \sum I_{V_T=1, V_S=2}^P & \cdots & \sum I_{V_T=1, V_S=NV}^P \\ \sum I_{V_T=2, V_S=1}^P & \sum I_{V_T=2, V_S=2}^P & \cdots & \sum I_{V_T=2, V_S=NV}^P \\ \vdots & \vdots & \vdots & \vdots \\ \sum I_{V_T=NP, V_S=1}^P & \sum I_{V_T=NP, V_S=2}^P & \cdots & \sum I_{V_T=NP, V_S=NV}^P \end{pmatrix} \begin{pmatrix} \rho_{D_S=1} \\ \rho_{D_S=2} \\ \vdots \\ \rho_{D_S=NP} \end{pmatrix} = \begin{pmatrix} \sum (B \cdot C_{T=1}) \\ \sum (B \cdot C_{T=2}) \\ \vdots \\ \sum (B \cdot C_{T=NV}) \end{pmatrix}$$

Where:

$\sum I_{V_T=NV, V_S=1}^P$ represents the sum of all of the source panels sharing vertex 1, and their influence on the target panels sharing vertex NV . Similarly, the right hand side of the equation must also be a summation over the panels sharing common vertices in the tent-like basis function, and $\sum (B \cdot C_{T=NP})$ represents the summation of the

common shape function panel boundary conditions at each vertex.

As observed in the above matrix representation of the vertex based approach, the panel influence integrals are added together on a vertex-by-vertex basis. The result of this is an $N_V \times N_V$ matrix. This is typically a reduced degree of freedom system for triangular panels when compared with constant basis approaches, since there are typically $\frac{1}{2}$ to $\frac{2}{3}$ the number of vertices than panels.

Again, considering each of the formulations used to solve the potential flow equation:

For the potential approach:

$$[AIC_{I_\psi}^G](\vec{\phi}) = [AIC_{I_\phi}^G](-V_\infty^\vec{\cdot} \cdot \hat{n})$$

Here the Galerkin approach is applied to the matrices, while the vectors in this equation are the values at each of the vertices. The resulting RHS when multiplied is a Galerkin expression of the boundary conditions. The normal term, \hat{n} , is best provided as the actual normal with the discretization data, since extracting vertex normal data from vertices and connectivity is not accurate.

For the single layer velocity approach:

$$[AIC_{I_\phi}^G](\vec{\sigma}) = (-V_\infty^\vec{\cdot} \cdot \hat{n})^G$$

In this case both the *AIC* and the RHS are computed in a Galerkin manner.

For the double layer velocity approach:

$$[AIC_{I_\psi}^G](\vec{\mu}) = (-V_\infty^\vec{\cdot} \cdot \hat{n})^G$$

Again, in this case both the *AIC* and the RHS are computed in a Galerkin manner.

3.9 The Lifting Cases : Including the Wakes

Inclusion of wakes is only demonstrated for the linear strength case. Since this work is in a preliminary stage, only a simple wake model is used. In the future, further extension of the wake modeling capabilities is recommended. Using models similar to Ramsey, [36], would be beneficial to the solution of complex aerodynamic problems.

The discretization must be changed to incorporate wakes. Primary discretization concerns are the trailing edge vertices. They must be separated into an *upper*, *lower*, and *wake* vertex all superimposed, but with individual unique shape function values. This is presented in Figure 3-59.

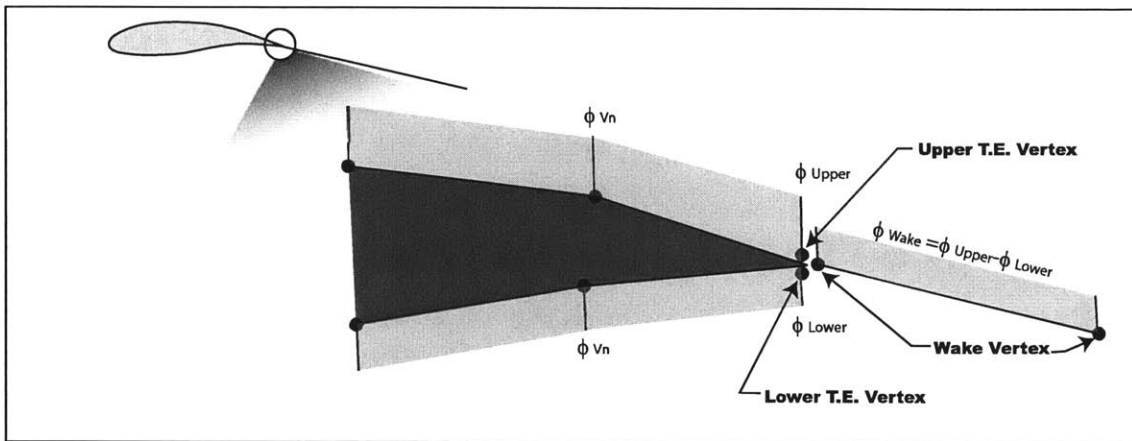


Figure 3-59: The pictorial description of the wake. The three trailing edge vertices are coincident in space, however, they are 3 distinct individual vertices as shown.

The overall discretization is also modified to include the effects of the wake. In figure 3-60 an example of a high aspect ratio wing discretization with a simple trailing wake is shown.

The governing equations for a wake can be found discussed in Chapter 2. In this work the wake equation is simply [40]:

$$\phi_{wake} = \phi_{upper} - \phi_{lower}$$

The influence matrix is computed in a similar manner as the non lifting case, except the wake panels are dipole panels, but not evaluation panels. The panel strength

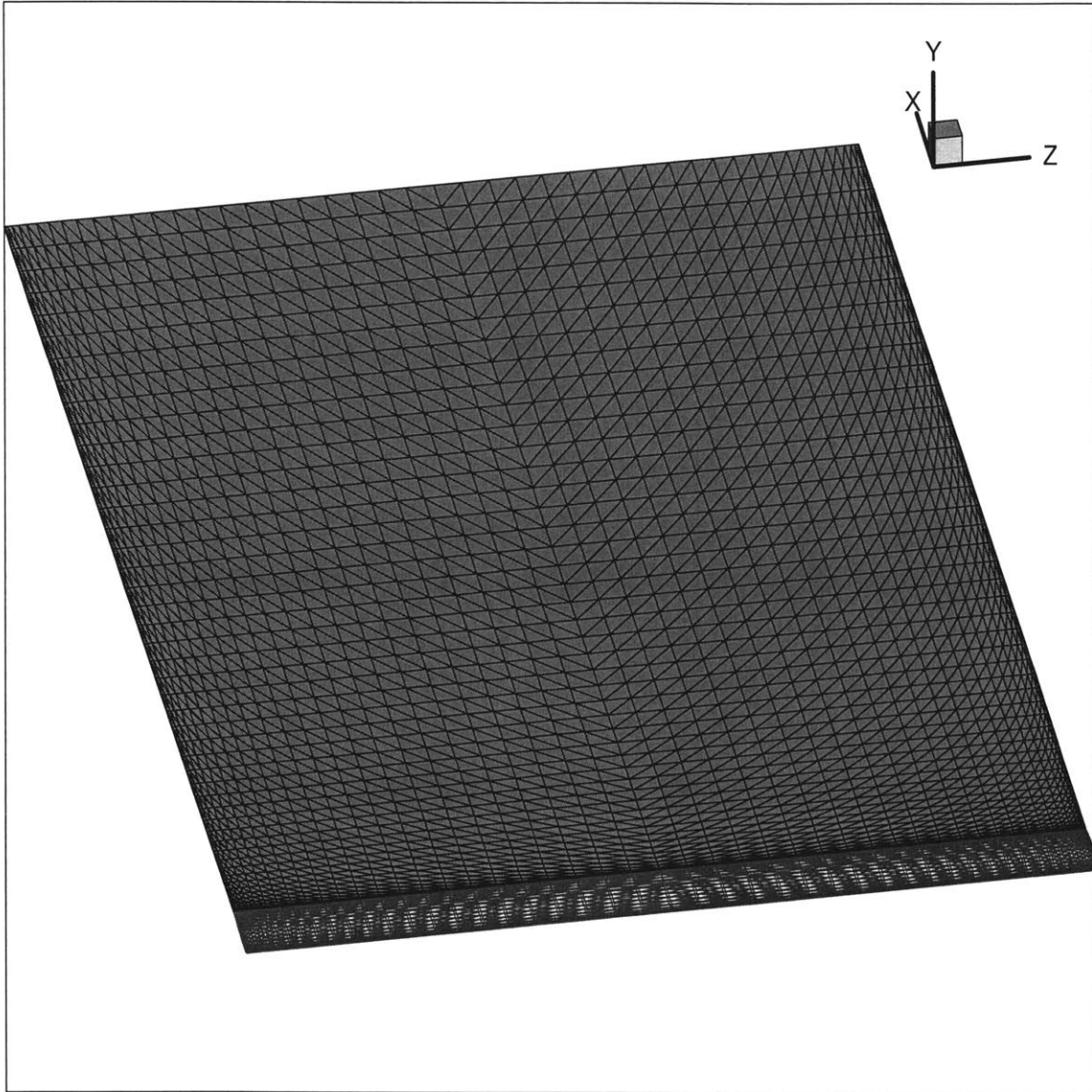


Figure 3-60: A high aspect ratio wing, with a trailing discretized wake. Note, the panel distribution, and panel aspect ratio is not optimal in this example, due to the net-like construction of the case

is determined through the wake condition. In the lower portion of the influence matrix, the wake relation is inputted to result in a $(NV + NV_{wake}) \times (NV + NV_{wake})$ system. The matrix entries representing the wake strength condition correspond to:

$$[\dots, 1, 0, \dots, -1, \dots, 0, -1, \dots] \cdot [\dots, \phi_{upper}, \phi, \dots, \phi_{lower}, \dots, \phi, \phi_{wake}, \dots]^T = [0]$$

This represents a line of the matrix corresponding to:

$$\phi_{wake} = \phi_{upper} - \phi_{lower}$$

The modification and extension of the wake model is recommended to allow more versatility in the panels trailing the aircraft lifting surfaces.

3.10 Conclusion: Discretization of the Boundary Integral Equations

The preceding Chapter demonstrated the Boundary Element Method for numerical implementation. Assuming that no computational time and memory bounds exist, the tools developed in the above chapter will solve the discrete potential flow problem. The methods described above are capable of yielding accurate results for small problems with minimal number of panels. With a direct approach, cases on the order of 1,000-2,000 panels represent a maximum memory and time tolerable system. Since, in real engineering applications, computation time and efficiency are extremely important, faster methods to determine the solution must be determined. These methods are investigated in the following Chapter.

Chapter 4

Acceleration Via a precorrected Fast Fourier Transform Method – pFFT

4.1 Introduction to Faster Methods

In the previous two chapters methods for solving the potential flow around arbitrary 3-Dimensional bodies were presented. No assumptions of the solution time or memory requirements were made. Assuming that direct matrix solution methods are implemented, the solution requires $O(n^3)$ solution time, $O(n^2)$ memory and $O(n^2)$ setup time. This is an adequate cost for solving coarsely discretized problems. However, for most modern practical applications in aerodynamics faster more efficient solution methods are necessary.

4.1.1 Iterative methods

Implementing an iterative solver, such as GMRES (Generalized Minimal Residual – [42]), can reduce the solution time significantly. The solution of the system reduces from $O(n^3)$ to $O(kn^2)$ complexity, where k represents the number of iterations required to achieve a desired residual. When the linear system is well conditioned the

number of iterations, k , is small.

Figure 4-1 demonstrates the iterative solver in its most general form, including an approximate cost for each of the operations.

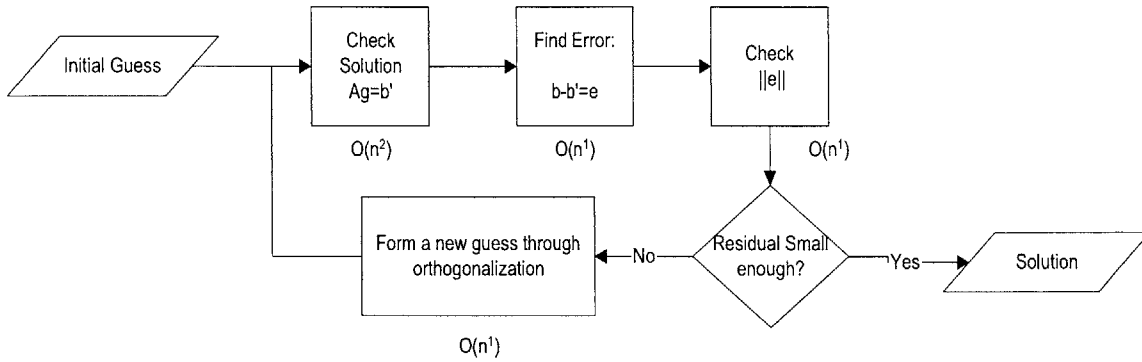


Figure 4-1: Basic flow chart of iterative methods.

Considering iterative solution methods, the computational 'bottle-neck' is the matrix vector multiply, or matrix vector product (MVP), which is an $O(n^2)$ process in the explicit matrix direct form. In addition to this, the set-up and storage of the full matrix are also $O(n^2)$ processes. Introducing an iterative method provides significant speed advances, however, it does not reduce the complexity to a sufficient level for modern engineering computations.

4.2 Fast Algorithms

Fast methods were developed to minimize the matrix vector product complexity. By invoking farfield approximations and panel effect clumping schemes the MVP can be approximated without constructing a full influence matrix. There are several fast algorithms applicable to the BEM potential flow problem:

- 1) Fast Multipole Method/Algorithm (FMM, FMA) [23], [24]
- 2) Pre-Corrected Fast Fourier Transform Algorithm [29]

4.2.1 Introduction to current pFFT Method, pFFT++ implementation [9]

To date the pFFT algorithm has been exploited to solve the constant collocation BEM formulation. The most recent and generalized implementation by Zhu, Song et al. [9], [10], pFFT++, is a general object oriented approach for constant collocation only. It is implemented using some of the generic principles of C++ programming.

The modifications required to implement pFFT++ as a constant and linear strength, collocation and Galerkin fast matrix vector product computational engine are outlined. The algorithm is easily extensible to an n -th degree BEM approximation, however this is not considered.

4.3 The pFFT Algorithm

The pFFT algorithm is easily described by a flow chart accompanied by diagrams of the various steps in the process. Figure 4-2 outlines the fast matrix vector product portion of the pFFT algorithm.

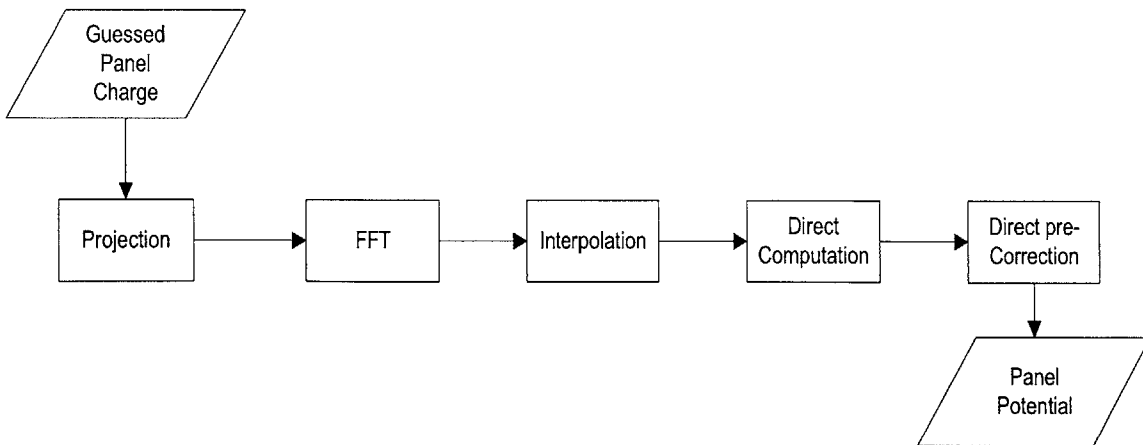


Figure 4-2: pFFT++ algorithm flow chart.

4.3.1 Overview of the Components of the pFFT Fast Matrix Vector Product

First a uniform grid is laid over the geometry under consideration, as in figure 4-3.

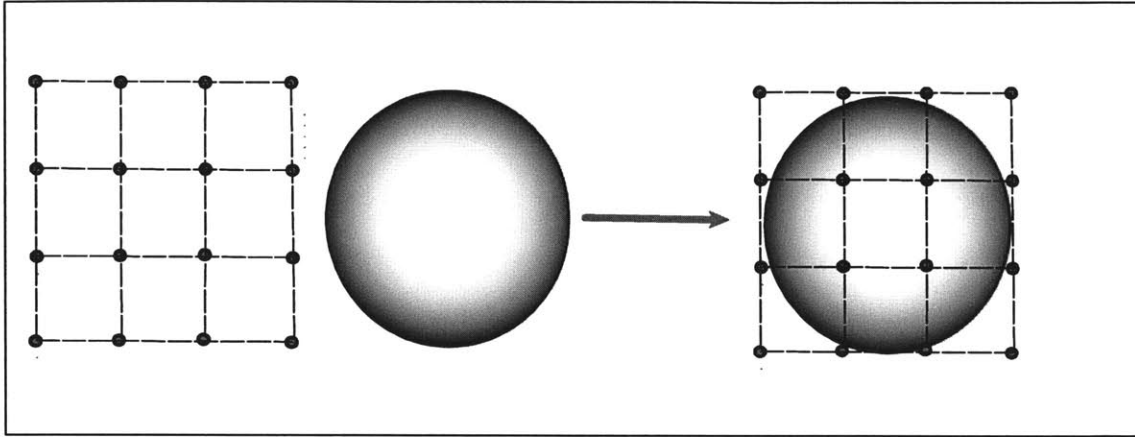


Figure 4-3: The uniform FFT grid is overlaid on top of the geometry.

The panel charges are projected onto the grid, as in figure 4-4

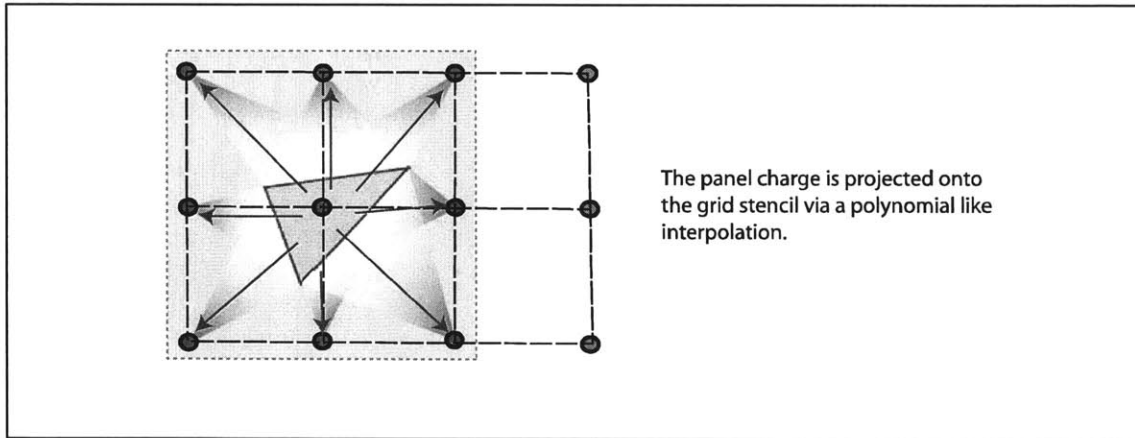


Figure 4-4: The panel charges are projected onto the uniform grid via a polynomial interpolation.

A fast Fourier transform provides an $O(n \log n)$ computation of the convolution integral across the 3-D grid. The FFT computes the grid potentials from the grid charges. The FFT is outlined graphically in figure 4-5.

And finally, the grid potential is interpolated back onto the panels, to finally get the panel charges (Figure 4-6).

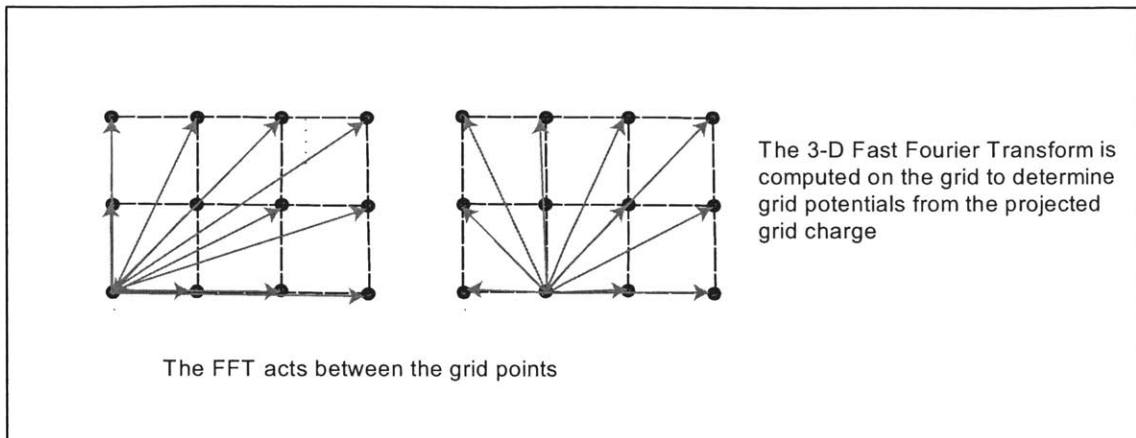


Figure 4-5: A FFT computes the convolution integral of the $\frac{1}{r}$ type integrals. This computes the grid potentials as a result of the prescribed grid charges.

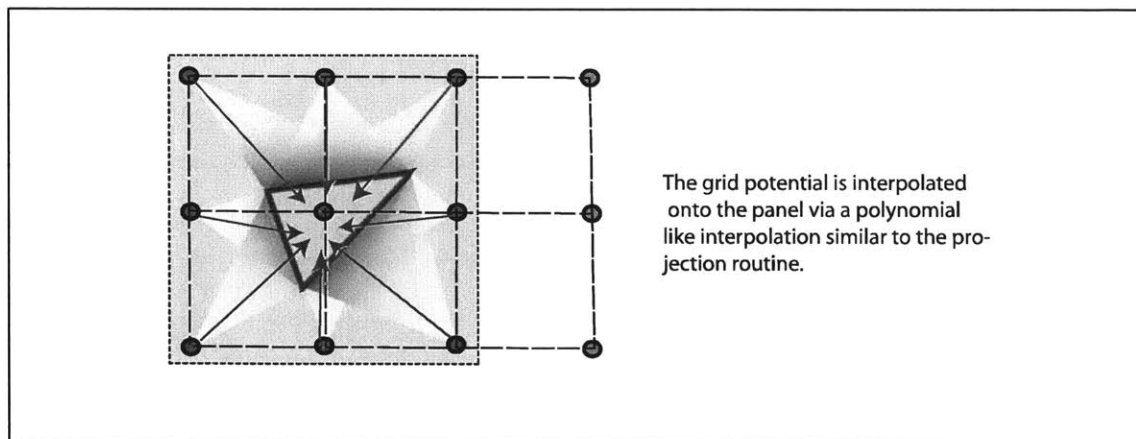


Figure 4-6: The grid potentials resulting from the FFT are interpolated back onto the panels.

The last step is to modify, or precorrect for the nearby interaction effects which are not captured accurately by the grid to grid interactions (Figure 4-7).

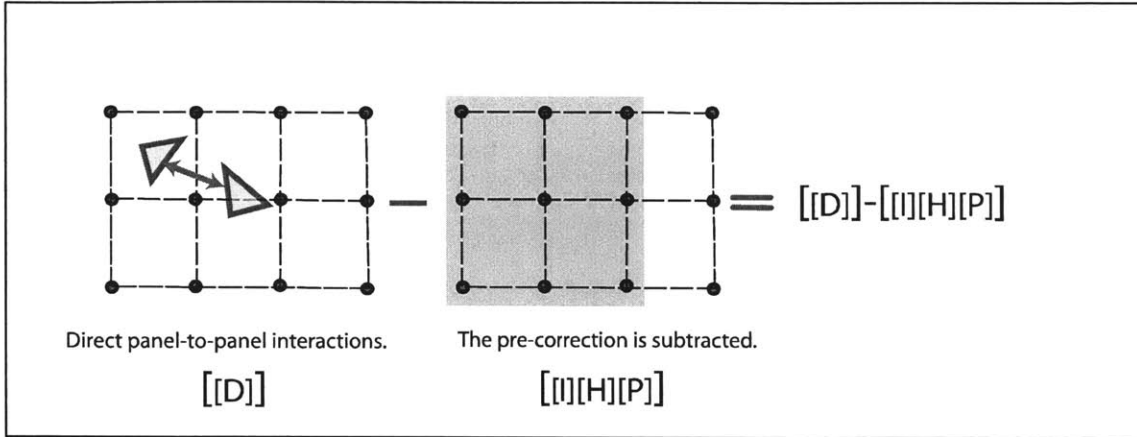


Figure 4-7: The nearby influences are computed directly and a correction is made to eliminate the influences of the grid-to-grid approximation of the nearby influences computed in the FFT approximation section.

The resulting fast matrix vector product is computed by performing a sparse matrix computation of the following operations:

$$[AIC] \cdot \vec{\rho} = [IHP + [\tilde{D} - \tilde{I}\tilde{H}\tilde{P}]_{Local}] \cdot \vec{\rho}$$

where,

I : Is the interpolation matrix.

H : Is the FFT matrix.

P : Is the projection matrix.

\tilde{D} : Is a matrix containing the direct interactions. The matrix represents a direct interaction of elements within a certain radius of the panel, or stencil.

\tilde{I} : Is the interpolation sub-matrix corresponding, to the elements contained in the direct stencil.

\tilde{H} : Is the FFT sub-matrix, corresponding to the elements contained in the direct stencil.

\tilde{P} : Is the projection sub-matrix, corresponding to the elements contained in the direct stencil.

Since all of the matrices are sparse, the matrix multiplies all scale like $O(n)$. The computation of the Fast Fourier Transform is a slightly more costly $O(n\log(n))$ process. The FFT calculation is an $O(n\log(n))$ process, representing the step with the largest complexity in the algorithm.

4.4 Linear pFFT : Modifications to the Constant pFFT Method

The pFFT algorithm is implemented for a constant collocation scheme in the work by Zhu and Song [9]. This work was taken and modified to incorporate a linear basis Galerkin approach. In section 4.4.1 through section 4.4.2, several possible approaches to incorporate a linear basis in the pFFT++ implementation [9] are presented. Following that in section 4.5, the detailed descriptions of the modifications are presented.

4.4.1 Intuitive approach : Tent-to-Tent Interactions

The intuitive approach to the computing the linear basis pFFT acceleration would be to mimic the traditional implementation by using the full linear basis functions rather than individual panels, as the pFFT elements. This is suggested by Zhu, Song and White [10] as a plausible approach. The full linear tent-basis is used in each step (projection, interpolation and direct computations). The result of this is a compact, low degree of freedom final system relying on many intermediate computations in the setup of the system.

There are several advantages to this approach:

- 1) The memory requirement is low (approximately $\frac{1}{2}$ to $\frac{2}{3}$ the memory requirement compared with constant collocation methods of the same size. This is due to the reduction of degrees of freedom when moving from a panel based constant scheme to a vertex based linear scheme).
- 2) The method is close to optimal for the linear panels, and has a fast pre-correct routine when compared with all of the other methods considered.

There are several disadvantages of this approach:

- 1) The tent footprint is large. As a result the nearby interaction stencil in the pFFT may need to be larger than optimal. The direct integrals being computed have a larger footprint than optimal, and as such many more direct integrals are computed than necessary.
- 2) The tent-to-tent interactions, although, maybe a fast and efficient means to computing the MVP via a pFFT algorithm, are linear shape function specific. This would result in a significant loss of generality of the final code.
- 3) A significant modification of the original pFFT++ code would be required for the successful implementation of this approach.

The matrix vector product equation resulting from this approach would be:

$$M\vec{V}P_{l_{vertex}} = ([I][FFT][P] - [D])_{vertex} \vec{\sigma}_{vertex}$$

Where each of the matrices are vertex shape-function based.

4.4.2 pFFT++ Approach: Panel-to-Panel Interactions

The panel-to-panel approach is the appropriate modification of the pFFT++ code to easily enable a linear basis approach.

By separating the linear tent basis into individual panels with three shape functions per panel, a pseudo-panel-based approximation results. After computing a panel-to-panel pFFT interaction of linear basis functions, the linear-tent basis must be reconstructed using the connectivity data before computing the MVP. The reconstruction of the vertex-based approach is done in two different ways, presented below.

pFFT++ Approach: Panel-to-Panel Interactions – Panel Based Matrices

The panel based approach performs the reconstruction as follows:

$$M\vec{V}P_{l_{vertex}} = T_C^T \cdot ([I][H][P] - [D])_{panel} \cdot T_C \cdot \vec{\sigma}_{vertex}$$

The transform matrix T_C contains the connectivity data for the panels. This method requires a pFFT system comprised of the following matrices:

$[I]$ - A $3 \cdot NP \times NG$ matrix

$[P]$ - A $NG \times 3 \cdot NP$ matrix

$[H]$ - The FFT matrix

D - A $3 \cdot NP \times 3 \cdot NP$ matrix.

The source strength vector in the MVP is $NV \times 1$ in dimension. The operations are performed in the following order:

First,

$$\vec{\sigma}_{panel} = T_C \cdot \vec{\sigma}_{vertex}$$

To produce a panel based, $\vec{\sigma}_{panel}$, charge vector. Following this the panel-to-panel pFFT approach is implemented

$$M\vec{V}P_{l_{panel}} = \vec{\phi}_{panel} = ([I][FFT][P] - [D])_{panel} \cdot \vec{\sigma}_{panel}$$

The potential is computed for each panel. Through connectivity, the panel potential must be transformed back to a vertex based potential and be placed in the iterative solution loop. Therefore the reconstruction of the linear-tent-basis functions is required:

$$M\vec{V}P_{l_{vertex}} = \vec{\phi}_{vertex} = T_C^T \cdot \vec{\phi}_{panel}$$

The panel-to-vertex transformation operation and its transpose operation are performed at each iteration. This would be a large disadvantage if the iterations were costly, and large in number. Fortunately for a well conditioned system, such as the potential approach the number of iterations is few, due to the low number of iterations. In addition the MVP is not excessively time intensive to compute compared with the overall setup time for the system.

One main disadvantage of this approach is the increase in memory requirement. The storage of the sub-element enlarged matrices is more costly than any of the other approaches presented.

pFFT++ Approach: Panel-to-Panel Interactions – Vertex Based

The vertex based approach differs slightly from the panel based approach in terms of the order of operations for the MVP computation. The following equation results from the construction of the pFFT matrices:

$$M\vec{V}P_{l_{vertex}} = T_C^T \cdot ([I][FFT][P] - [D])_{panel} \cdot T_C \cdot \vec{\sigma}_{vertex}$$

However, in this case, the vertex-based-matrix-system is constructed prior to computing any matrix-vector-products:

$$\left((T_C^T \cdot [I] \cdot T_C) ([FFT]) (T_C^T \cdot [P] \cdot T_C) - (T_C^T \cdot [D] \cdot T_C) \right)_{panel}$$

The resulting system is:

$$([I]_{Vert.}[FFT][P]_{Vert} - [D_{Vert.}])_{vertex}$$

The result is a similar set of matrices and matrix equations as would have been constructed by the tent-based approach described earlier. With each of the matrices converted by the transformation to the appropriate vertex based linear shape function, the matrix vector product is much less costly, since it acts on a square system of dimension, $NV \times NV$.

In order to justify the additional complexity of computing a vertex based matrix system, it must be shown that the MVP-iterative portion of the solution is excessively costly, which is not the case in the current implementation. The current implementation displays a MVP routine with 10-15 % of the total solution time for the iterative solution, due to the superior conditioning of the potential problem.

One main disadvantage of this approach is the increase in memory requirement. The storage of the sub-element enlarged matrices is more costly than any of the other approaches presented.

4.5 The Modifications to the Implementation

The following sections describe the modifications to the implementation of the pFFT++ constant collocation approach in order to facilitate the linear shape function approach, based on the panel-to-panel interactions with a panel based MVP. This is done in order to maintain generality in the pFFT++ routine. The advantages being the generality of the resulting algorithm, which facilitates both linear and constant strength panels. In addition the low required modification of the original pFFT++ code is a significant advantage.

4.5.1 Projection : The Theory and Linear Panels

The projection of the panel charges onto the grid is performed using a polynomial interpolation. As outlined by Zhu and Song [10] the projection routine is general applying to all orders of panel singularity distribution. This fully generalized implementation was not in the constant code, which favored the more frequently used collocation approach.

Panel Projection Approach in 2D [10]

The theory provided in [10] is re-written here for completeness and to aid the understanding of the modifications. There is little deviation from Zhu te al.'s paper [10] on the subject.

The idea of the projection is to ensure that the grid charges represent the same effect as the original panel. In order to simplify the derivation, a simple point charge, q is considered (figure 4-8).

The effect of the point charge, q , is evaluated at some arbitrary point E , such that the potential $\Phi_E^{(1)}$ at r_E due to a point charge q at the point r_q can be represented as:

$$\Phi_E^{(1)} = G(r_q, r_E)$$

In order for the projection to be consistent, the grid charge(s) ρ_G must produce the

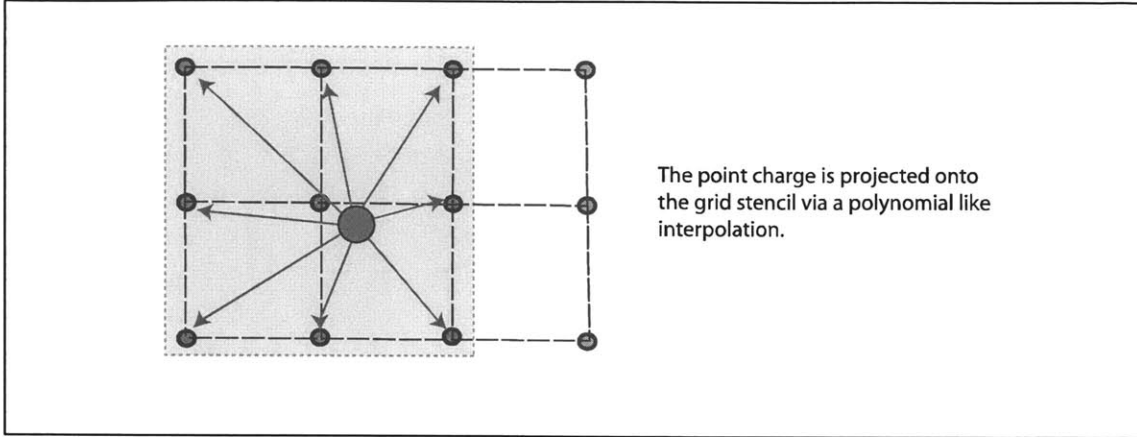


Figure 4-8: The point charge is projected onto the uniform grid.

same potential at the evaluation point E , that the original point charge q did. To do this a second potential $\Phi_E^{(2)}$, due to the grid charges at $r_{G,i}^{\vec{}}$ evaluated at the same position E is expressed as the summation of the effects of individual grid node charges ($\rho_{G,i}$), for the grid stencil being used:

$$\Phi_E^{(2)} = \sum \rho_{G,i} G(r_{G,i}^{\vec{}}, r_E^{\vec{}}) = (\rho_G^T \Phi_G^{\vec{}})$$

The following equality must hold for the grid representation to be accurate:

$$\Phi_E^{(1)} = \Phi_E^{(2)}.$$

Next, the Green's function, $G(\vec{r}, \vec{r}_E)$ is expressed as a polynomial series expansion:

$$G(\vec{r}, \vec{r}_E) = \sum_k f_k(\vec{r}) c_k$$

where,

$f_k(\vec{r})$: Is a set of polynomial basis functions. In the case of a 2-Dimensional grid point stencil, the polynomials are $f_k(x, y) = x^i y^j$, where, $i, j = 0, 1, 2, \dots, 2i + j$.

c_k : are the multiplicative coefficients which must be applied to attain, $G(\vec{r}, \vec{r}_E)$.

To express the potential, in terms of the charges on the grid, the expression of the grid computed potential is presented, where the polynomial functions at the grid

points are evaluated, as $f_i(x_i, y_i)$. Expressing the result in a matrix form:

$$G(\vec{r}_i, \vec{r}_E) = \vec{\Phi}_G = \vec{c}[F]$$

Where $[F]$ is the matrix composed of the $f_{i,j}(x, y)$ evaluations at the grid points:

$$\vec{\Phi}_G = [F]\vec{c} == \begin{pmatrix} f_1(x_1, y_1) & f_2(x_1, y_1) & \dots & f_n(x_1, x_1) \\ f_1(x_2, y_2) & f_2(x_2, y_2) & \dots & f_n(x_2, x_2) \\ \vdots & \vdots & \vdots & \vdots \\ f_1(x_n, y_n) & f_2(x_n, y_n) & \dots & f_n(x_n, x_n) \end{pmatrix} \cdot \vec{c}$$

Rearranging the matrix equation, \vec{c} can be expressed as:

$$\vec{c} = F^{-1}\vec{\Phi}_G$$

The two different expressions for the potential at point E can now be expressed. The potential due to a point charge inside the grid stencil:

$$\Phi_E^{(1)} = G(\vec{r}_q, \vec{r}_E) = \vec{f}^T(\vec{r}_q)F^{-1}\vec{\Phi}_G$$

and correspondingly, the second potential which is a consequence of the grid charge can be expressed as (as shown earlier):

$$\Phi_E^{(2)} = \sum_i \rho_{G,i}G(\vec{r}_i, \vec{r}_E) = (\vec{\rho}_G)^T \vec{\Phi}_G$$

By enforcing that $\Phi_E^{(1)}$ and $\Phi_E^{(2)}$ to be equal, an expression for the grid charge density $\vec{\rho}_g$ due to a point charge at q can be determined:

$$(\vec{\rho}_G)^T = \vec{f}^T(\vec{r}_q) \cdot [F]^{-1}$$

This expression, when solved will give the polynomial interpolation of the point charge onto the grid points, to form the grid charge.

This equation represents a point-to-grid interaction. By further examining and manipulating the equation it can be extended from a point charge projection to a full basis function weighted panel projection. To do this the point charge effect is integrated over the surface of the panel. A single panel with a charge distribution $b_j(\vec{r})$ is considered (here j denotes the j -th shape function on the panel):

$$(\vec{\rho}_G)^T = \int \int_{S_j^b} b_j(\vec{r}) \vec{f}^T(\vec{r}) \cdot [F]^{-1} dS$$

The first version of the pFFT++ code merely implements a constant strength b_j . In the developed linear approach, the b_j can be either a linear or a constant basis. The integration is performed using a numerical quadrature approach (see figure 4-9) and as such, the implementation of a higher order panel basis function is simple.

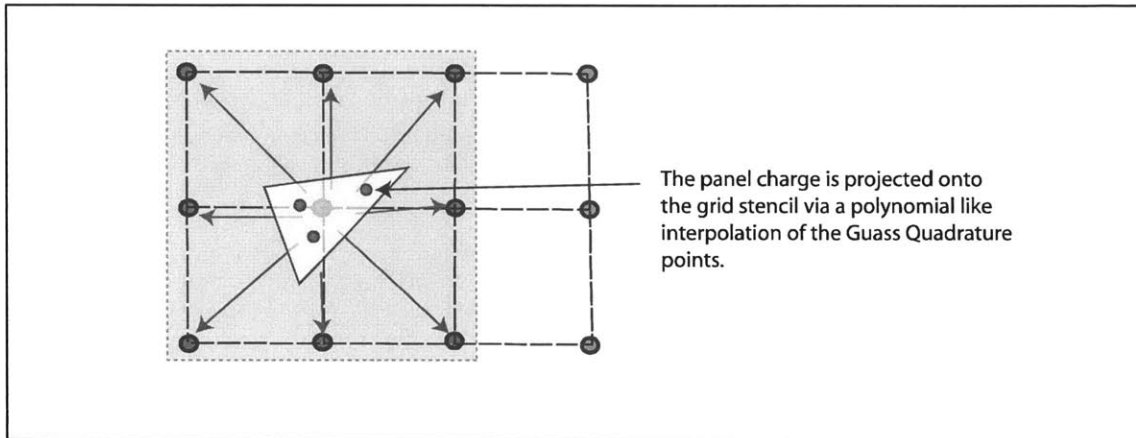


Figure 4-9: The Gaussian quadrature point charges are projected onto the uniform grid. Combined with the shape function b_j effect, the panel integration is computed discretely for the projection.

In order to complete the pFFT algorithm projection requirement, the ability to project multiple panels onto the grid is necessary. The projection of multiple panels results simply in a summation of the panel projected charges at the grid points.

In order to satisfy the additional basis functions in the linear method (three nodal bases, as opposed to a single panel based one in the constant case), the projection matrix is composed as a matrix of vector elements in the implementation. The inner matrix entries for each panel are vectors of size $N_{Shape-Functions} \times 1$. For the linear

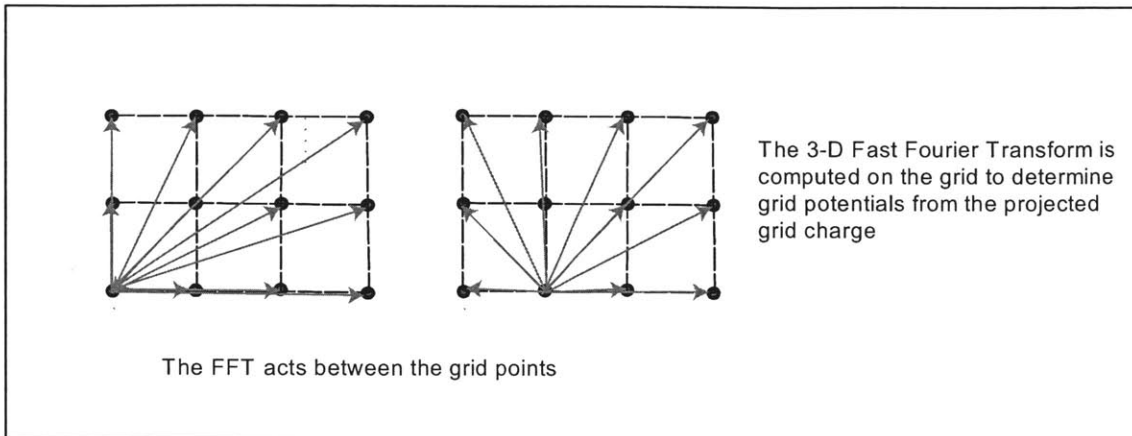


Figure 4-10: The pFFT, Fast Fourier Transform convolution.

case this results in a matrix requiring three times the baseline memory than that used in the constant collocation code.

4.5.2 Fast Fourier Transform

As outlined in papers by pFFT implementation developers [29], [10], the Fast Fourier transform merely computes the convolution of the grid charges to give the grid potential. The FFT is independent of the panel singularity shape function, and as such does not need to be modified for different order shape functions (figure 4-10). The traditional 3-D FFT [43] is computed.

4.5.3 Grid-to-Panel Interpolation [10]

The interpolation routine as described by [10] is easily applied to interpolation panels of arbitrary order with some minor modification. The method implemented in the first version of pFFT++ [10] relies on the collocation concept and is not general to the Galerkin approach. As in the projection matrix, the equations are presented from [10], once again in their most general form. Here the equations are investigated for the sake of clarity and completeness, and are the same equations and presentation as found in [10].

The interpolation matrix derivation is handled similarly to the projection matrix.

The interpolation of the grid potential from the grid to a single point potential in the domain is considered (figure 4-11). After determining the effects of a grid-to-point interpolation, the distribution of potential integrated over the panel weighted with a Galerkin-like-shape function is considered.

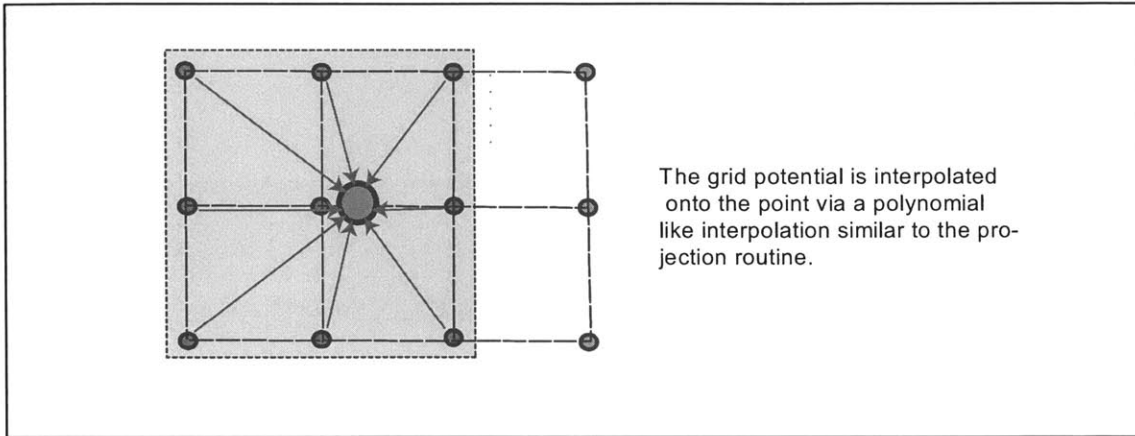


Figure 4-11: The Grid potential is interpolated to a point in the domain.

The potential is expanded as a series, using weights and polynomial function representation, as done for the projection:

$$\Phi(x, y) = \sum_k c_k f_k(x, y) = \vec{f}^T(x, y) \vec{c}$$

Here the $f_k(x, y)$ are a chosen set of polynomials.

When the polynomials in the expansion are evaluated at the grid points a polynomial interpolation relationship between the grid potential and the test point potential is formed:

$$\vec{\Phi}_G = [F] \vec{c}$$

Rearranging this, and using earlier results, a relationship between the grid potential and the point potential at (x, y) , can be written as:

$$\Phi(x, y) = \vec{f}^T(x, y) [F]^{-1} \vec{\Phi}_G$$

This can also be used to express the relationship between the grid and a panel with

a target potential shape function, $t_i(\vec{r})$:

$$\Psi_i = \int t_i(\vec{r}) \vec{f}^T(\vec{r}) [F]^{-1} \vec{\Phi}_G dS = \vec{W}^T \vec{\Phi}_G$$

The interpolation matrix is composed of the various \vec{W}^T vectors, and as a result can be written as:

$$\vec{\Psi} = [I] \vec{\Phi}_G$$

The construction of the interpolation matrix for the linear Galerkin approach uses an almost identical approach to the projection. This results in simplification of the final linear implementation, with several functions being reused. This general approach to the interpolation and the projection is recommended as a starting point for future implementations of the pFFT algorithm.

4.5.4 Direct Terms and Pre-Correction

There are some additional changes required in the direct and pre-correction computations. These are outlined briefly.

Direct Matrix

The direct matrix for the linear shape function case is computed similarly to the panel based constant approach. The difference is that the panel-to-panel interaction results in a 3×3 system, corresponding to the 3-shape function to 3-shape function interaction. This increases the memory usage significantly. In addition the linear panel based integrals as presented in Chapter 3 are also implemented.

Pre-Correction

The pre-correction routine is almost identical to that presented in [10], [9], apart from once again being a 3×3 interaction in the linear case. The same governing equations and concepts apply. The precorrection is evaluated for each of the three

shape functions, i , on the individual panels:

$$[D]_i = ([\tilde{D}_i] - [\tilde{I}_i][\tilde{H}][\tilde{P}_i])$$

4.5.5 Implementation Generalizations

Constant Strength Implementation Conclusions

For the constant strength method the projection and interpolation matrices are composed of elements in a *std :: vector < double >*. The elements are stored in a 1x1 sized vector. Similarly the direct matrix is composed of *std :: vector < std :: vector < double >>* elements. In the Constant implementation these elements are 1x1 matrices. The reason for the vectorized approach is to introduce generality between the linear and constant strength approaches in the same code. As a novice in the realm of C++ programming it is realized that this is not likely the most appropriate approach.

Linear Strength Implementation Conclusions

The linear strength implementation uses identical constructs as that presented above in the constant strength approach. The linear strength projection and interpolation are composed of 1x3 vectors. Similarly the direct matrix is composed of 3x3 matrix elements. This simplifies and generalizes the final code significantly.

Implementation Discussion

Through the use of the *std :: vector < T >* class the computational code is significantly slowed down. The access calls to the *std :: vector < T >* class take a significant amount of time. Due to the intense implementation of the *std :: vector < T >* class it is left as a recommendation to implement a more efficient class for the storage of vector-element and matrix-element entries to the I, P , and D matrices.

4.5.6 Lifting Case : pFFT Implementation of the Kutta Condition

For the lifting cases, the additional Kutta condition must be applied. In the case of linear panels this modification is rather simply performed. The evaluation points for the pFFT influence matrix representation are limited to those control points on the body, while the source panels (either single or double layer), will incorporate both the effects of the body and wake. The Morino [40] condition is applied in the linear pFFT computation by applying the wake strength relation:

$$\phi_{wake} = \phi_{upper} - \phi_{lower}$$

In the MVP routine. Prior to computing the influence effects of the double layer, the wake panel strengths are updated. The new panel strengths provide a better computation of the wake strength.

4.6 The Flow Chart for the pFFTflow Implementation

The final pFFT flow chart is shown in the figure 4-12.

4.7 Conclusions

The pFFT algorithm was considered as the Matrix Vector Product acceleration routine in this work. The implementation of a linear strength pFFT algorithm based on the constant collocation routine developed by Phillips and White [29] and an implementation by Zhu and Song [10] is presented.

The developed linear/constant panel based approach to the pFFT algorithm provides a first implementation of the pFFT method in a higher order BEM environment.

The resulting developed implementation is general. It provides a method to com-

pFFT: GMRES MATRIX VECTOR PRODUCT ROUTINE

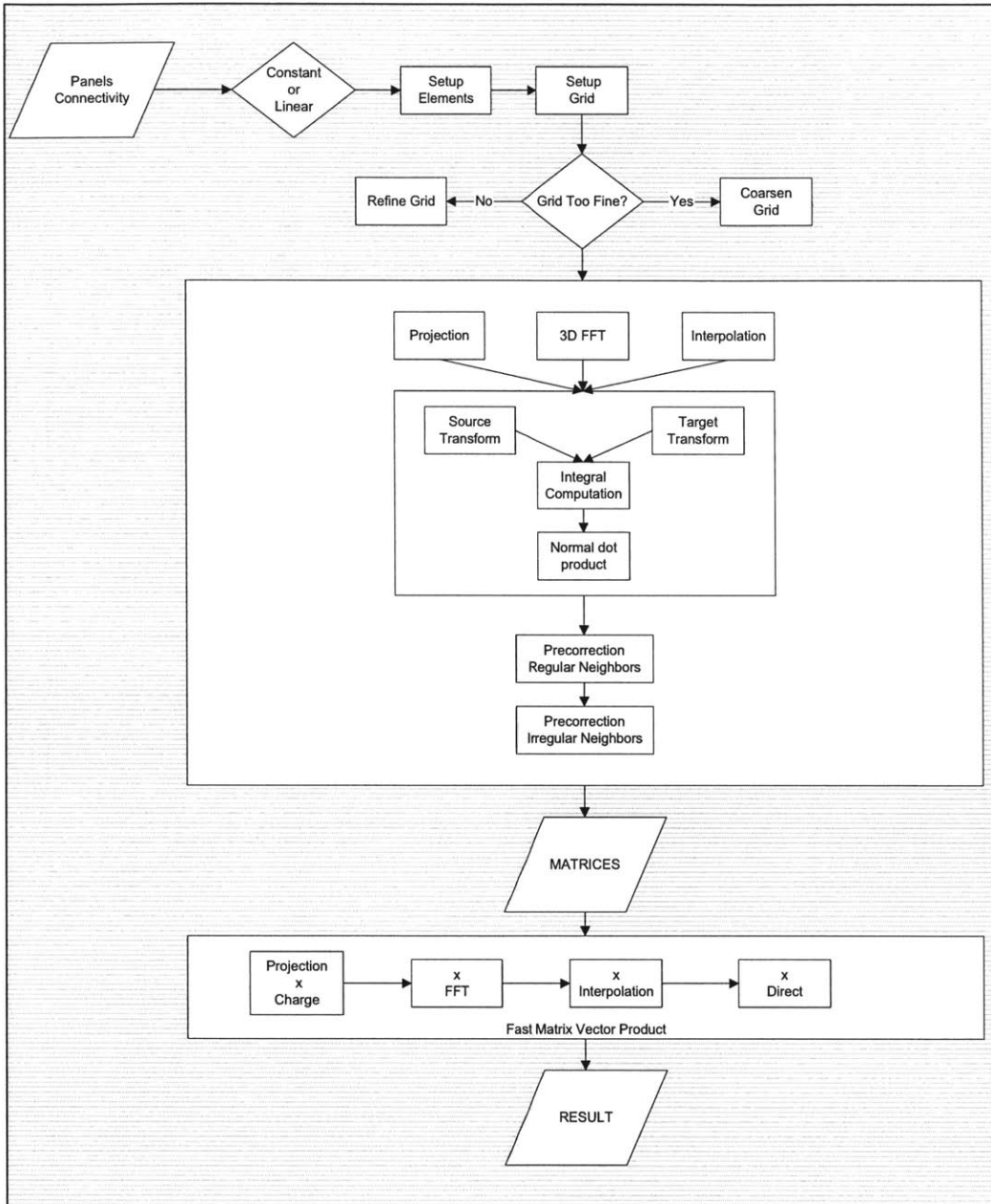


Figure 4-12: The flow chart for the pFFT algorithm.

pute both the linear and constant strength approaches. In addition a Galerkin and collocation approach are developed. This provides a generality not expressed in the original implementations of the pFFT algorithm.

It was decided that should a specific linear strength algorithm be needed, a re-writing of the pFFT code to provide a tent-basis-to-tent-basis approach would be

required. For the current work it was decided that the gains attained through specific linear implementation was exceeded by the benefits of the generality. In addition the modification of the pFFT++ code as a linear specific code would require significant reworking of the framework.

In Chapter 5 the results of the linear implementation are presented and discussed.

Chapter 5

Solution Results and Examples

In this chapter the results of the Boundary Element Method are presented. The direct method is briefly discussed in section 5.1, followed by an in-depth presentation of the results and discussion of the pFFT accelerated method.

5.1 The Direct Method : Validation Though Spheres

The direct method was investigated using 48, 198, 768, and 3092 panel spheres to determine the properties of the various formulations. The discretized sphere geometries are shown in Appendix B. The following investigation was performed to determine:

- 1) Which boundary condition/implementation method is computationally favorable.
- 2) Which boundary condition/implementation method is more accurate.
- 3) The primary results from a linear method compared with a constant strength method (if appropriate).

5.1.1 Analytical Solution for a Sphere

A set of discretized spheres were chosen for the computational comparison. The use of increasingly refined discretizations allows for a consistent comparison between methods. In addition, by superimposing a 3-D point doublet in a freestream flow, the

Comparing the Dirichlet and Neumann Formulations for a 48 Panel Sphere

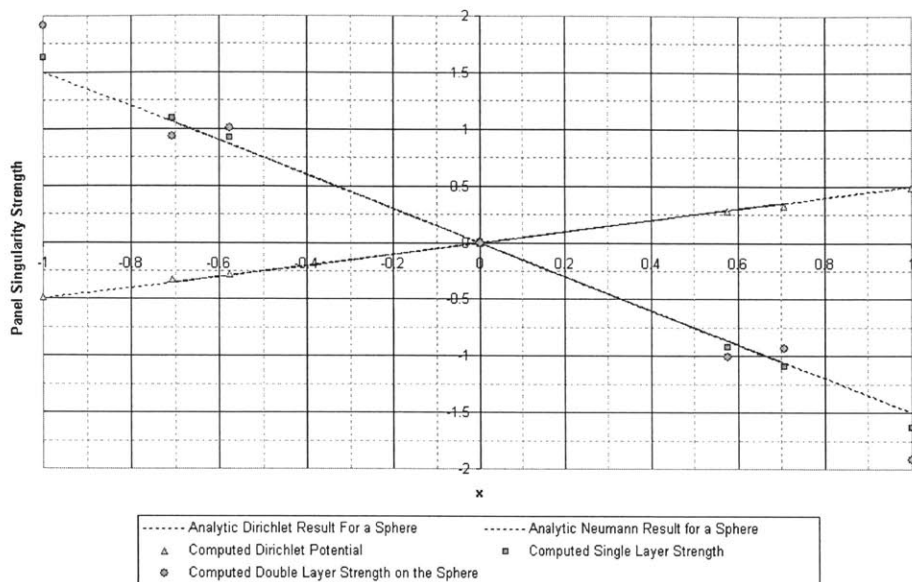


Figure 5-1: The computed direct result for the 48 panel sphere, using both Neumann and Dirichlet approaches.

potential distribution around a sphere can be determined analytically as:

$$\phi = 0.5 \cdot (\vec{x} \cdot |\vec{V}_\infty|)$$

5.1.2 Results for the Spheres

Direct Velocity formulation vs. Potential Formulation Solution : Linear Panel Influence Integral Case

The results for the Velocity formulations and potential formulation cases are compared qualitatively in Figures 5-1 to 5-3 for the sphere test cases. From the plots the double layer Velocity formulation shows significant error in the solution for all of the cases. This is due mainly to the self term calculation which is hyper singular. The single layer velocity formulation and potential formulation show comparable orders in error, with the single layer velocity formulation being slightly more accurate in the overall solution.

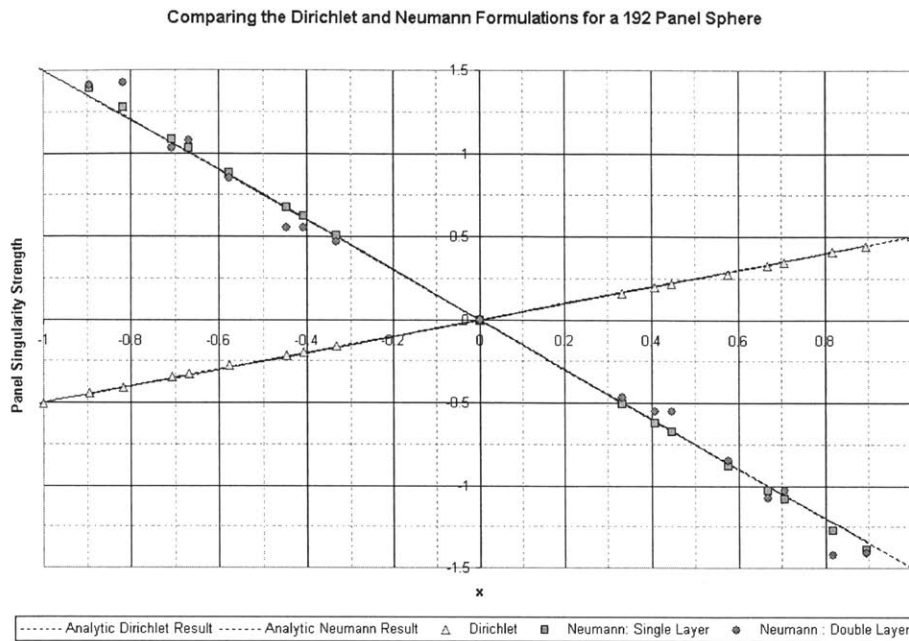


Figure 5-2: The computed direct result for the 192 panel sphere, using both Neumann and Dirichlet approaches.

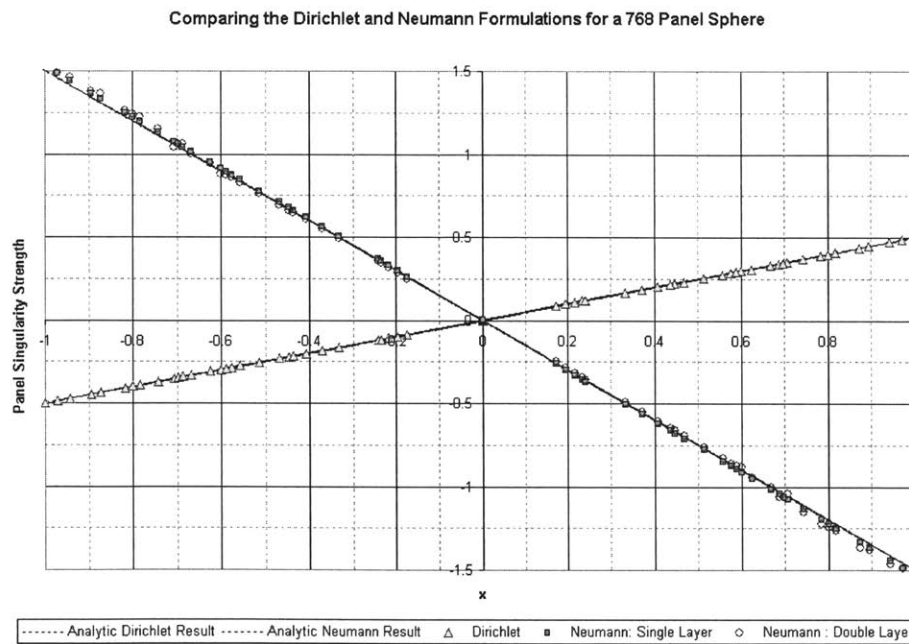


Figure 5-3: The computed direct result for the 768 panel sphere, using both Neumann and Dirichlet approaches.

5.1.3 Boundary Condition Implementation

In the initial linear pFFT development code, the solution of a single formulation was undertaken for simplicity. The potential formulation was chosen due to the following discoveries in the initial direct method investigation:

1) The velocity formulation requires that a panel integral influence gradient be computed at the evaluation point. This requires approximately three times the computational effort, hence making the solution method much slower than the potential formulation which requires one integral per evaluation point.

2) The accuracy of the single layer velocity formulation displayed in the preliminary computations is advantageous, however, significant post processing must be performed to compute the potential and velocity. In addition from the results displayed in figures 5-1 to 5-3, the use of a double layer singularity in the velocity formulation on lifting portions of the body will contribute to the overall solution error significantly. Hence, the lifting body problem would not be well resolved in the velocity formulation implementation.

3) The potential formulation does not require a distinction between lifting and non-lifting portions of the body. The velocity formulation does however require that the double layer singularity be applied on lifting portions of the body, while it is advantageous to apply the single layer velocity formulation on the non-lifting portions of the body.

4) The post processing to determine the body surface velocity in the velocity formulation is significantly more cumbersome than the process required in the potential approach.

In the first iteration of the linear pFFT++ code development, *only the potential formulation* for closed lifting and non-lifting bodies was considered.

5.2 The pFFT-GMRES Accelerated Case : *Potential Formulation*

The results from the generalized linear/constant implementation of the pFFT++ algorithm are investigated in this section.

5.2.1 Validation Results

Cases for spheres with up to 10,800 panels were run in a very short time using the pFFT method. The results are presented in the following sections.

Error Plots

The comparison of the linear and constant strength potential formulation is presented first through error in the computations.

Discussion of the Results in Figure 5-4

The L_2 error plot (Figure 5-4) shows a similar convergence for both the Linear and the Constant strength panel integral methods for a translating sphere case. It is hypothesized that the convergence is governed by the geometric discretization error. The increase in accuracy of the geometry area scales in the first order compared with the element sidelength measure.

It should however be noted that, despite the similar convergence, the linear method is significantly more accurate than the constant strength method when the actual geometric normals are used in the computation. This increase in accuracy easily justifies the increase in cost of the linear method. To gain similar accuracy in the constant method, a method using approximately an additional 50 % computation time must be used.

If the geometric normals are not supplied with the input data, significant error is introduced in the computation of the vertex normal. This increased error in the linear method reduces the accuracy to approximately the same level as the constant

collocation approach.

In addition, the linear method governing system has less degrees of freedom in the solution than its constant strength counter part. Although one would suspect this would prove limiting, this is not a governing limitation in this case. The linear method displays significantly more accurate results on a panel-per-panel analysis. On a degrees of freedom basis, the linear strength method is even more impressive, despite having a similar convergence rate as the constant collocation case. Table 5.1 outlines the reduction in the degrees of freedom of the linear system between a linear and a constant strength approach.

Table 5.1: A comparison between the number of vertices and number of panels for the test sphere data

Number Of Panels	Number Of Vertices
48	26
192	98
768	386
3072	1538

In order to attain a full comparison between the linear and constant strength methods, the construction of an object discretized using quadrilateral panels should be performed. Otherwise, comparison of the linear and constant strength results could be misleading.

Furthermore, an analysis should be performed on an object whose geometric discretization does not influence the convergence rate of the overall case. This is impractical in aerospace computations due to the resulting sharp corners on the discretized geometry which would result in infinity edge conditions. This is deemed not overly important, since many typical aerospace problems have curved surfaces. A sphere example is a realistic measure of the error properties of a conventional aerospace analysis, and as such the reduced order of convergence due to discretization error is accepted.

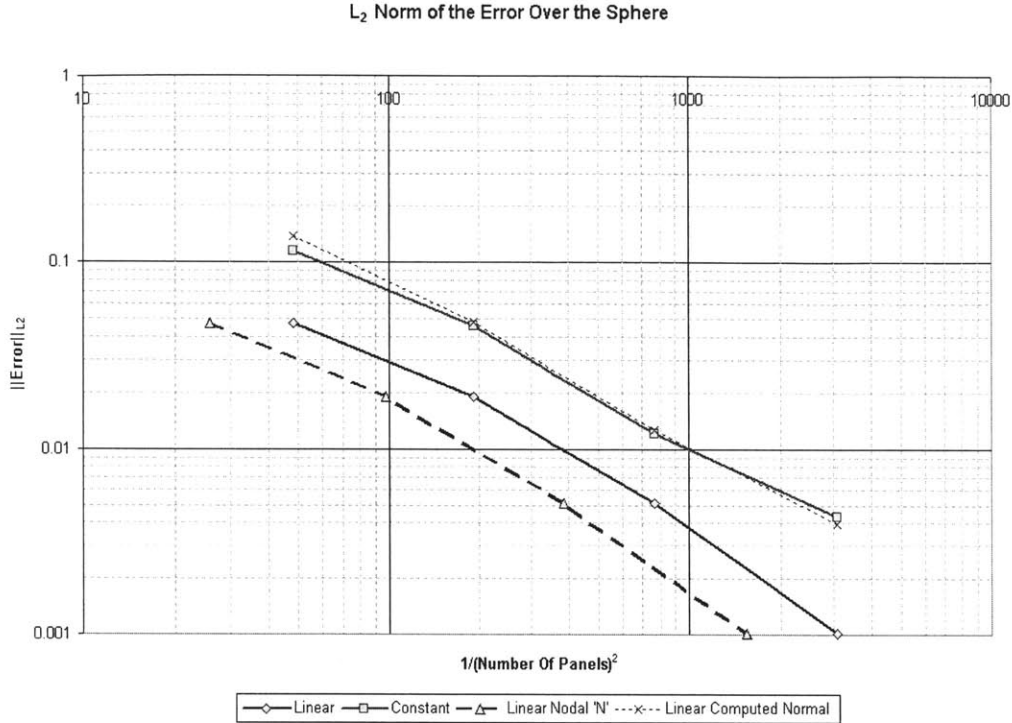


Figure 5-4: The analytical error computed in the L_2 norm. The Linear result is shown for both a Code-Computed normal (less accurate at nodes), and the analytical surface integral at the vertex points (more accurate).

The Integrated Error Result

The error plot shown in figure 5-5 displays an alternate approach to the error comparison. Although it does not fully eliminate the discretization error influence (since that is inherently built into the solution through flat panel analytic integrals), faster convergence for the linear case is seen in this computation of the error. The computation is the L_2 error of an integrated absolute value of the potential over the surface of the sphere, compared with a numerical expression of the absolute value of the exact result integrated over the sphere. It would be expected in a geometry where the discretization has minimal influence governing the error, that the linear strength method would have a faster convergence. If the error were fully independent of the discretization, one would expect an order of magnitude faster convergence. This would be found in a planar constructed object.

As a result of the convergence presented in 5-4 and 5-5, it is recommended that,

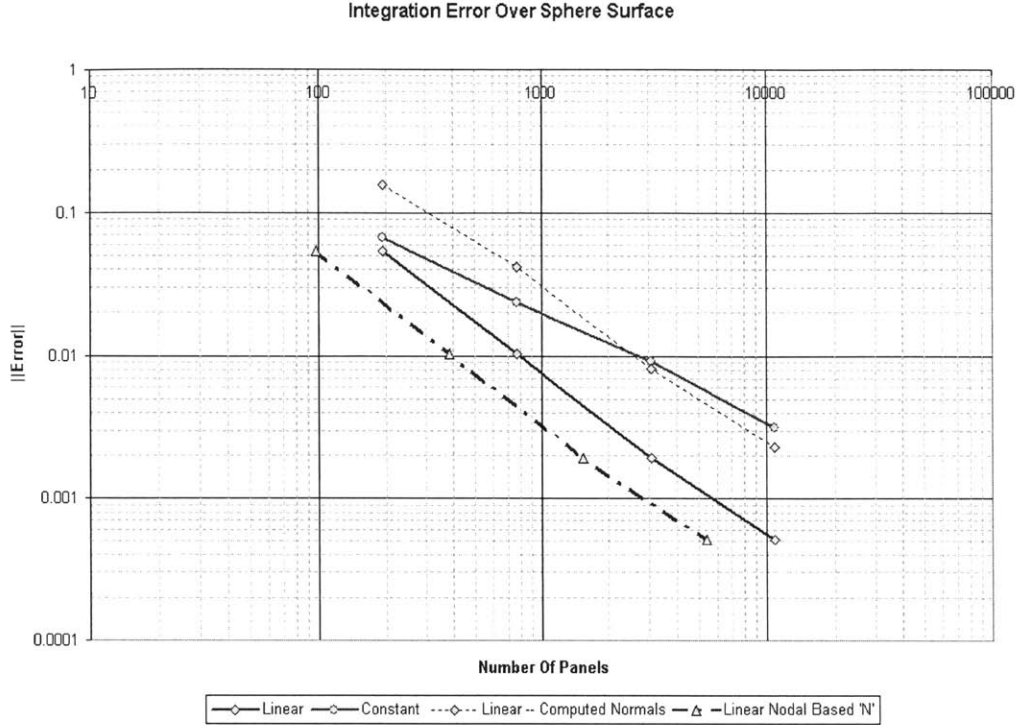


Figure 5-5: A display of the integrated error for the test Spheres. An attempt was made to extract some of the discretization area convergence effect from the computation. The plot shows preliminary results.

should increased convergence rates be required for non-planar curved surface geometries, a higher order curved-panel discretization be used rather than the traditional planar panel. This would eliminate much of the discrepancy in the computation. Using a panel which conforms better with the surface would provide higher accuracy in the results. Methods outlining curved panel geometries are presented by Wang, et al. [44]. These could be appropriately modified if necessary to form a method whose discretization and panel singularity order are consistent.

Recommendations for Measuring and Attaining Improved Convergence

Improved convergence could be verified with a discretized surface which represents the geometry exactly, however, this is difficult to construct in a aerodynamic applications due to the inherent curved surfaces found in many aerospace applications. Constructing a curved surface linear integral representation would prove challenging.

In addition measuring the error properties on a flat surface is not honest for the overall error-behavior for the method in an application where surfaces are curved in more than 90 percent of all applications for increased aerodynamic efficiency.

It is recommended that further investigation of the convergence properties of the linear method be undertaken more rigorously. An investigation such as the one performed by Margason et al. [18], and further investigation into the work of Thomas et al. [45] would be enlightening.

In addition, a more in depth investigation and presentation of the error should be undertaken, similar to the work by Phillips, et al. [46]

5.2.2 Aeronautical Engineering Applications : Non-Lifting Bodies

In order to assess the practicality and the performance of the method some typical aeronautical engineering benchmark analyses are performed. Comparison data was taken from XFOIL [11] with airfoil coordinates from Abbot and Van-Doernhoff [47].

A non-lifting NACA 0012 high aspect ratio wing was analyzed using both the non-lifting, no wake approach, as well as the lifting wake approach. The result is presented in figure 5-6.

As figure 5-6 shows, there is a very good agreement between the predicted 2-D result and the result from the 3-D panel method.

5.2.3 Aeronautical Engineering Applications : Lifting Body examples

Several lifting body examples were analyzed. Results from a high aspect ratio simple NACA 2412 wing section are presented to provide verification and validation of the implemented lifting model.

Lifting NACA 0012 : Wake Model Used

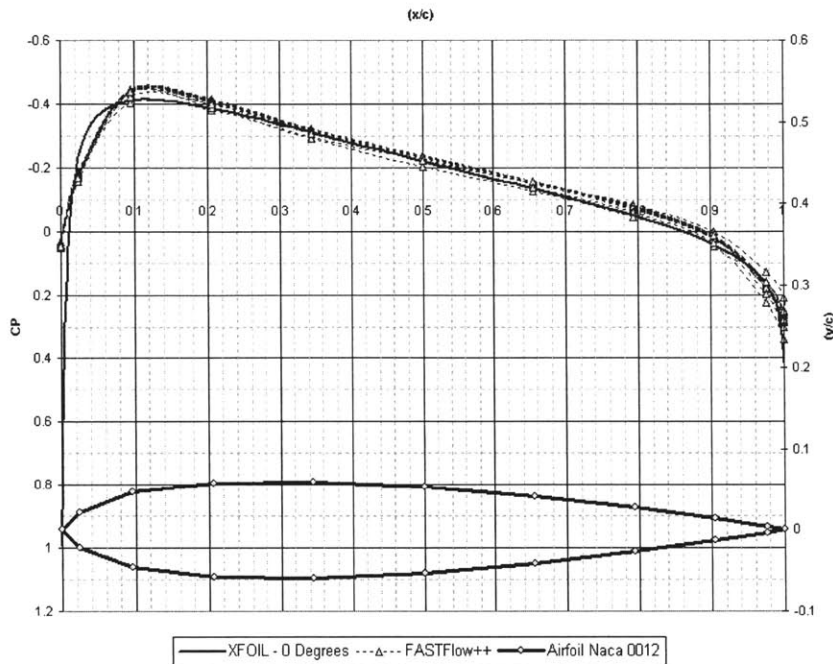


Figure 5-6: The pressure coefficient distribution for the NACA 0012 symmetric airfoil profile high aspect ratio wing at a 0° angle of attack. The result is compared with the 2-Dimensional result from XFOIL [11]

NACA – 2412 Results

The analysis of a rectangular wing with a NACA 2412 profile was undertaken. The following chart outlines the properties of the wing under investigation:

The body and wake mesh geometry investigated is shown in Figure 5-7

The analysis was performed using a three point Gaussian quadrature scheme for the Linear Galerkin formulation.

The pressure coefficient, C_P , is compared in this case rather than the lift coefficient, C_L , or moment coefficient, C_M for several reasons. The distribution of pressure over the airfoil profile can provide significant insight into the overall properties of the section. Airfoil properties and moment, lift and stall characteristics can be extracted more readily from the C_P distribution plot than integrated results. Furthermore, the C_P plot can provide insight into the regions in which the method has significant difficulty with computational resolution. The plot is investigated and compared with

Table 5.2: The information for the NACA 2412 geometry discretization

Variable	Root	Tip
Airfoil	NACA-2412	NACA-2412
Scale	1	1
Aspect Ratio	12	
Spanwise Panels	20	
Chordwise Panels	16	
Number of Wing Nodes	1652	
Number of Wing Elements	E= 3136	
Number of Wake Nodes	2450	
Number of Wake Elements	E= 4608	
Total Nodes	4102	
Total Elements	7744	

results from Drela's 2-D XFOIL [11]. The XFOIL computations are adjusted to compensate for some of the 3-Dimensional effects found in the full 3D-wing applications (such as downwash, tip leakage etc.). The presented 3D results should lie between the XFOIL purely 2-D and the XFOIL corrected 2D-results.

The wing profile is a high-aspect ratio wing, so only the stations on the inboard $\frac{1}{4}$ portion of the wing are presented in the figures, to extract the region in which the flow exhibits the 2-Dimensional flow properties most closely.

Conclusions for the NACA 2412 Lifting Body Case

The results from the 3-Dimensional panel method are comparable with the results from the 2-D XFOIL code. This verifies the simple wake model, and validates the lifting body method. Other examples were run for swept wings and the general properties of the wings were easily realized.

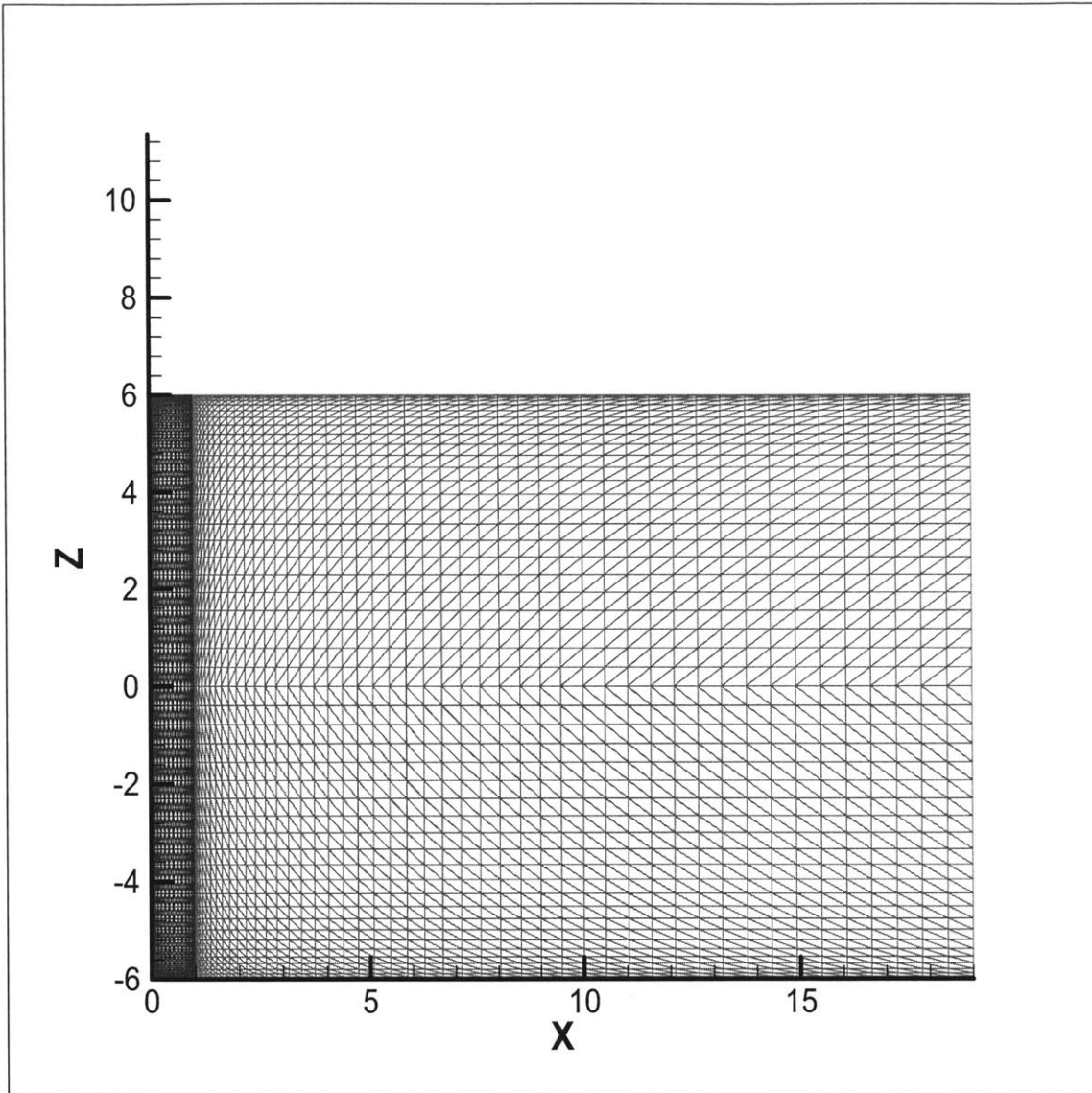


Figure 5-7: The discretization of a NACA 2412 profile high aspect ratio wing with a trailing wake

5.3 pFFT Implementation Time Considerations, and Memory Requirements

The following paragraphs present the memory and time requirements for the simulations. This benchmark was run on a Dell Precision 330, 1Ghz Pentium 4 processor, with 1GB of RAM, in an application free consistent Linux environment.

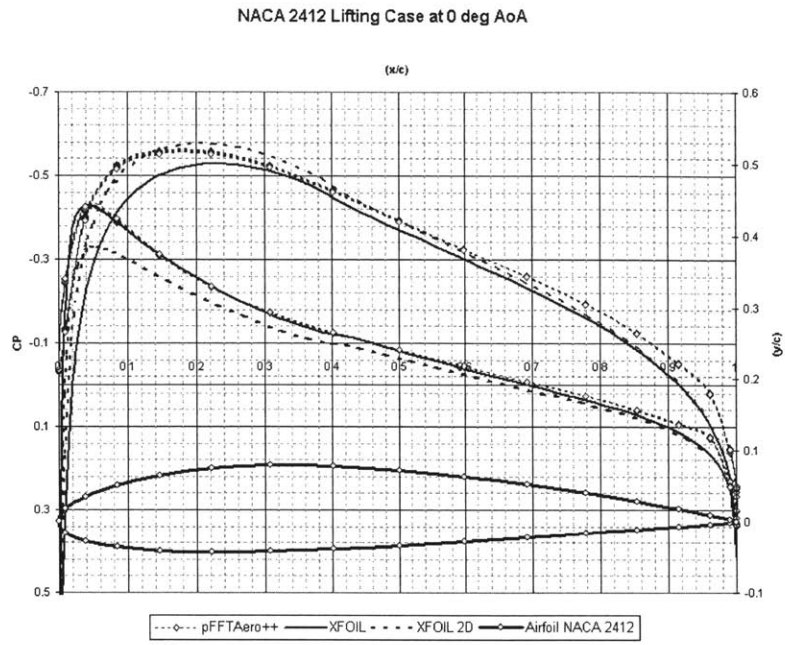


Figure 5-8: The Pressure coefficient for the 2-D XFOIL [11] case compared with the 3D Panel Method Case for $\alpha = 0^\circ$

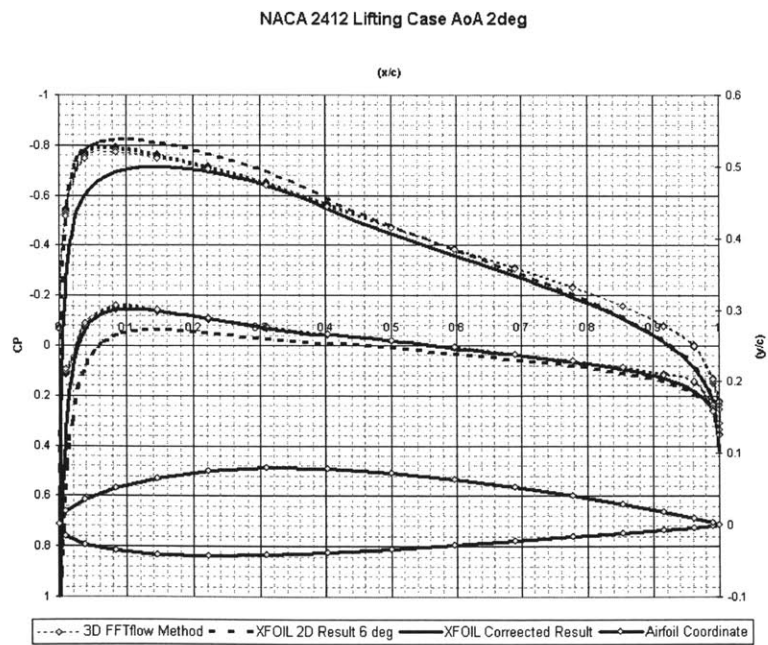


Figure 5-9: The Pressure coefficient for the 2-D XFOIL [11] case compared with the 3D Panel Method Case for $\alpha = 2^\circ$

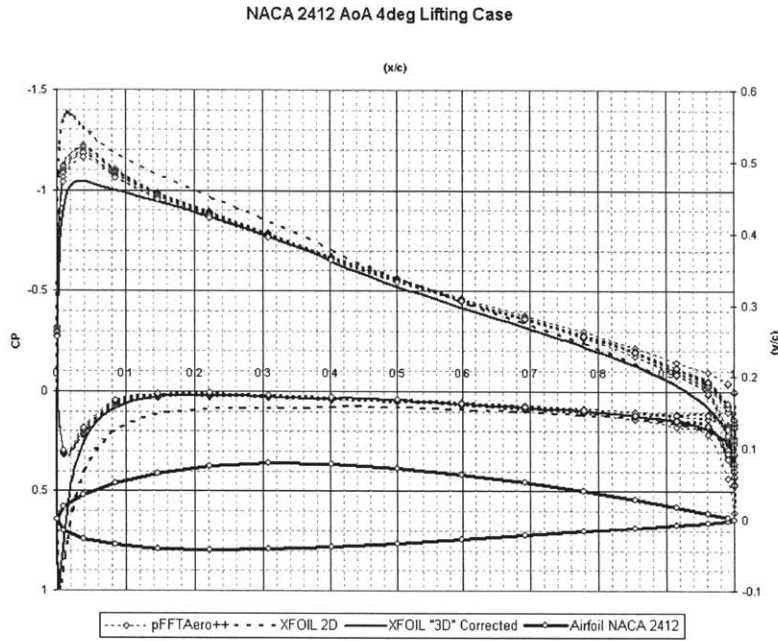


Figure 5-10: The Pressure coefficient for the 2-D XFOIL [11] case compared with the 3D Panel Method Case for $\alpha = 4^\circ$

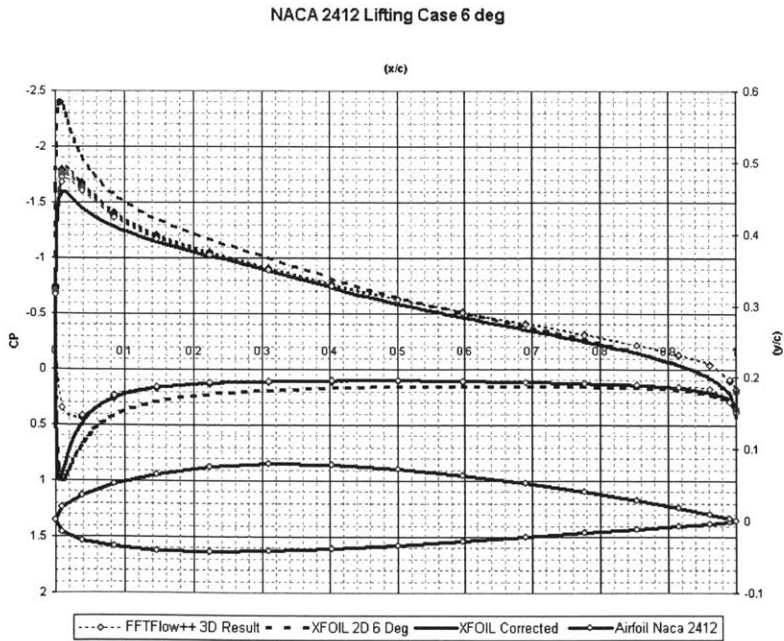


Figure 5-11: The Pressure coefficient for the 2-D XFOIL [11] case compared with the 3D Panel Method Case for $\alpha = 6^\circ$

5.3.1 Time Requirements

The pFFT algorithm scales like $O(n\log(n))$ in time.

Solution Time

The solution time for the accelerated method is significantly improved over the direct solver – matrix approach. Figure 5-12 shows the plot of the direct method solution time compared with the pFFT approach.

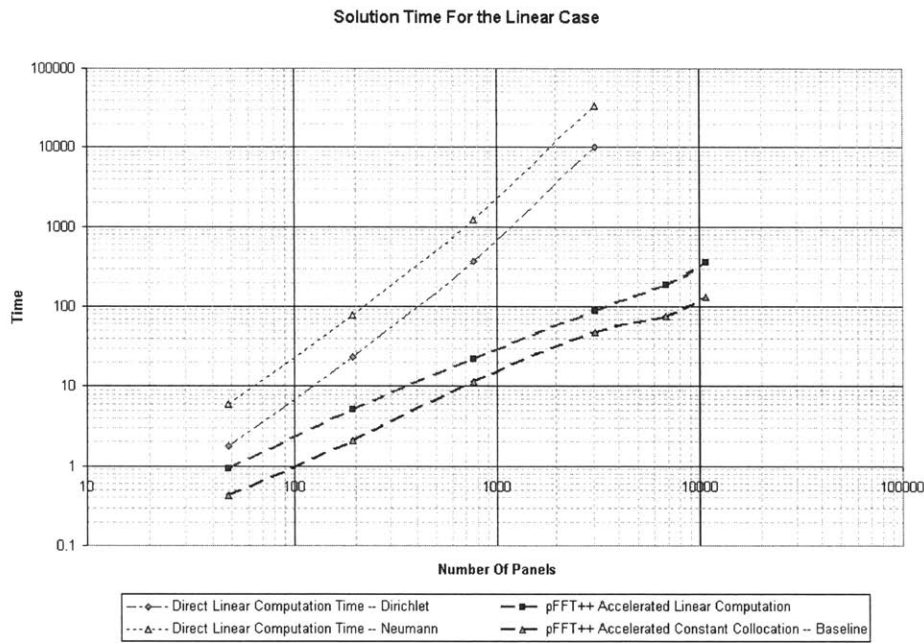


Figure 5-12: The solution time for the pFFT Approach compared with the direct solution approach. Notice the pFFT algorithm scales Like $O(n\log(n))$ here.

The pFFT solution is comprised of several different components. The different components that make up the solution are presented in figure 5-13.

5.3.2 Discussion of Time Requirements

The time requirements for the pFFT approach can be slightly misleading due to their inherent dependencies on the geometry discretization being provided to the method. The following discussion outlines some of the geometry considerations when setting up the pFFT.

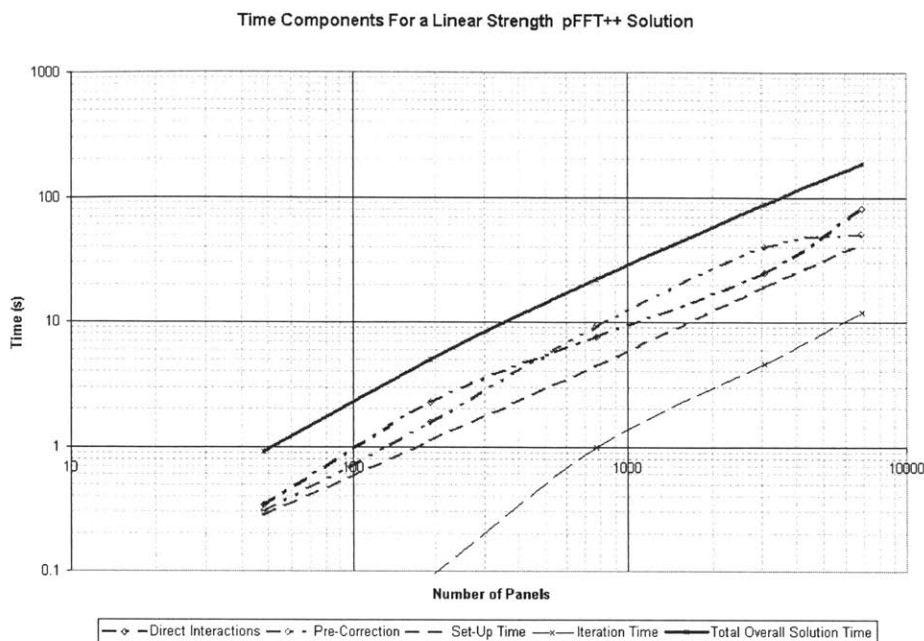


Figure 5-13: The time components of the linear solution for the spheres.

Factors Affecting the total solution time

- The use of linear panel methods is seen to have a 50 percent increase in solution time over the constant strength counter part. This is minimal when compared with the accuracy gains attained in using the linear strength panels.

- The panel discretization is seen to have a large effect on the overall solution time. This is due to the current algorithm being used to determine the FFT-grid in the pFFT method. Large variations in panel side length ratios will result in significant numbers of direct interactions. This causes a reduction of sparsity in the direct and pre-correction routines. This effect increases solution time significantly. In the case of the finite wings, the solution time was seen to take a significantly longer than the similar size sphere problem due to the double cosine grid-like distribution of the panels on the wing surface.

- The current method is not entirely optimized in C++. The implementation of the linear approach was performed in a non-optimized rudimentary C++ approach. With additional optimization significant improvements in overall computation time will be realized.

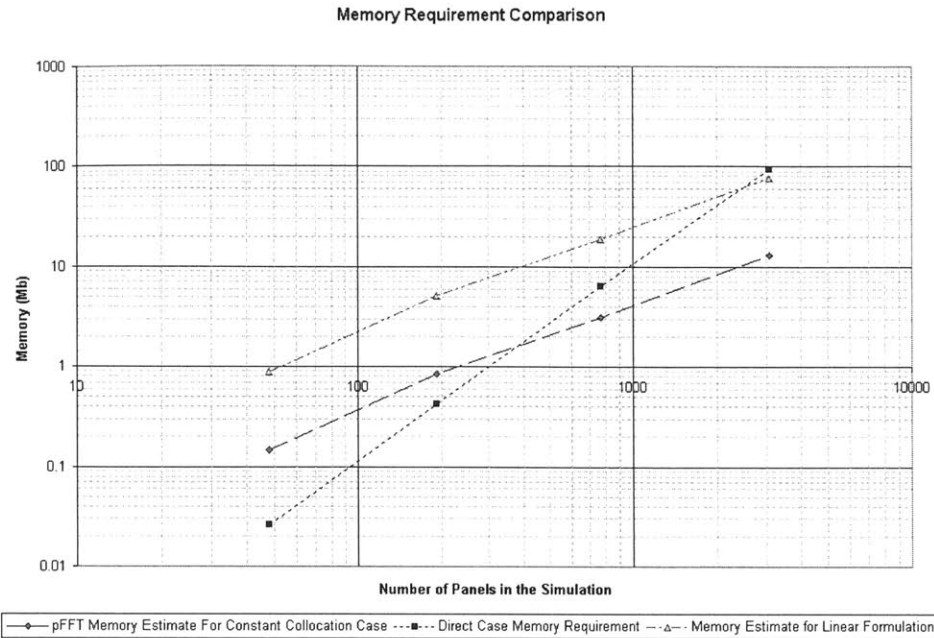


Figure 5-14: The plot of the projected memory requirements for the linear and constant pFFT method compared with the actual memory requirements for the direct method.

5.3.3 Memory Requirements

The memory requirements also scale in an $O(kn \log kn)$ fashion. Figure 5-14 shows the memory estimates for the constant case, for an optimized pFFT code.

The memory requirements make it clear that the pFFT solution allows practical aeronautical problems with panel numbers in excess of 10,000 panels to be solved effectively and efficiently. Although the memory requirement for the linear case is higher, there are significant benefits to the linear panel method with respect to accuracy, which justifies the method.

Discussion of Memory Requirement Reduction for the Linear Panel Influence Integral Case

For the linear computations, memory requirements can be significantly reduced at the expense of some computation complexity. Computing the shape-function-to-shape-function interaction in the pFFT algorithm would result in a method with significantly less memory requirement than the constant collocation approach. The

computational complexity of the Shape-Function-To-Shape-Function approach would result in a method with $\frac{2}{3}$ to $\frac{1}{2}$ the memory requirement of the constant collocation approach due to a vertex based system with $n_{vertex} \simeq \frac{N_{panels}}{2}$. The computational time would increase significantly with the direct interaction computation requiring the computation of far more panel integrals. The result would be a system whose maximum constraints would be based on the number of nodes only. The implemented method relies on the number of panels only.

5.4 Discussion of Results

The successful implementation of a pFFT accelerated linear strength panel integral approach has been realized. The results presented suggest several improvements that can be made to the overall pFFT implementation in the linear case. The conclusions and recommendations are presented in Chapter 6.

Chapter 6

Conclusions and Recommendations

6.1 Conclusions Based on Results from the Computer Code

Based on the results of the panel method the following conclusions are made:

1) The linear BEM method implemented shows significant accuracy benefit over the constant case. Despite the implementation of planar panels the accuracy of the linear Galerkin approach is still superior to the constant strength collocation approach. The use of curved panels for the integration for high order schemes representing curved geometric surfaces will display a faster convergence rate.

2) The use of actual geometric normals in the linear BEM for computations is essential for increased accuracy.

3) The successful application of a linear panel strength pFFT++ implementation has been realized. Results indicate the $O(n\log(n))$ complexity of the method is maintained.

4) A comprehensive set of direct method tools were developed. The constant and linear, velocity formulations and potential formulation were investigated. The choice of the potential formulation in the initial pFFT implementation was made due to implementation simplicity, computational efficiency and accuracy considerations.

5) The computational times for the accelerated method are non-optimal, yet still

display the ability to compute cases with 10,000 and greater panels efficiently and accurately. This provides the opportunity to compute very detailed surface aerodynamic computations. Typically surface resolution was poor in panel methods due to 2,000-5,000 panel limits. With the pFFT accelerated approach these limitations are no longer present, and cases with resolutions of up to 100,000 panels are feasible.

6.2 Recommendations Based on Results and Current Code Status

1) Upgrading the current fast method for the velocity approach is simple and should be considered. Having a mixed Potential-Velocity code would be extremely beneficial for certain aero/hydro-dynamic applications.

2) Upgrading the software subtleties for increased speed will provide significant improvements. The code should be upgraded to a faster access method than the *std::vector<double>* matrix subelements currently being used. In addition better use of the generic programming procedure in C++ could provide a 3-6 times improvement in computation time.

3) Implementing a flexible wake [36] will increase the solution accuracy for lifting applications. The current wake model is simple, yet adequate for most lifting applications.

4) Development of a pFFT specific triangulation routine is recommended. A surface grid generator built into pFFT would allow for rapid optimization and aircraft design capabilities.

5) The application of aerodynamic corrections to the method would be advantageous. Corrections such as the application of boundary layer corrections and compressibility corrections are easily implemented.

6) The implementation of the matrix based transform rather than the vector based transform may display significant increases in efficiency in the MVP routine. In addition the implementation for a specialized reduced memory vertex-to-vertex

pFFT approach should be considered.

7) In order to fully optimize the linear strength panel approach the application of quadrilateral panels combined with triangular panels should be investigated.

8) The extension of the method to solving problems other than the steady aerodynamic problem should be investigated. Unsteady flow analysis and aircraft stability calculations should be investigated. The use of multiple flight conditions through the variation of the right hand side boundary condition should be investigated. In addition, the application of the method to other domains such as hydrodynamic free surface analysis is easily realized [48], [49].

9) The modification of a pre-existing computer code is advantageous, since the student learns alternate coding styles. It is however, difficult for a student to rapidly modify an existing code due to coding intricacies of previous authors. Should significant modifications to pre-existing code be required, a certain required documentation and coding style should be adopted by both the original author and the modifying author. The upgradability of generalized C++ code is only possible through the use of consistent and well documented coding practice. In addition, it should be considered that the student may learn different parts of the routine when developing a code by themselves rather than implementing a modified version of an existing code.

6.3 Overall Recommendations

The accelerated linear strength panel method has successfully been created. There is however significant amounts of additional work which can be performed in order to fully harness the power of the implementation. It is recommended that the project continue informally to develop the code into a simple end-user application for internal use and web based distribution.

Appendix A

Transform the panel

In this appendix, a description of the panel transform is provided. The panel is transformed from an arbitrary 3-Dimensional coordinate system to a panel based coordinate system as shown in figure A-1

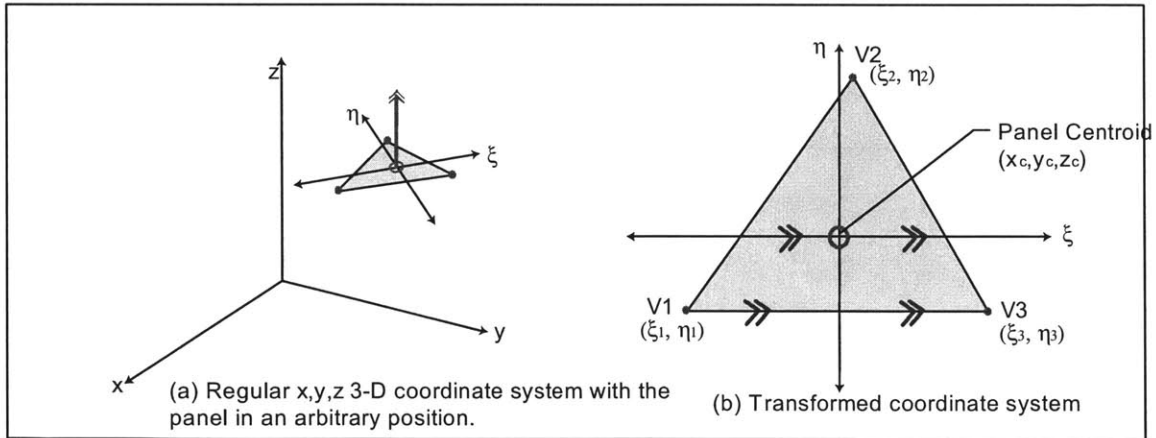


Figure A-1: The coordinate transform. Here the triangle in x, y, z is transformed to an in-plane, ξ, η, z' representation.

A transform is determined, applicable to both constant strength panels and linear strength panels. The steps in determining the transformation are:

- 1) Determine the unit normal, \hat{e}_z , and the centroid of the panel in the original coordinate system (x, y, z) .

$$\hat{e}_z = \frac{(V_1 - V_2) \times (V_1 - V_3)}{\|(V_1 - V_2) \times (V_1 - V_3)\|_2}$$

2) Select the side of the panel along which it is to be aligned with the ξ axis. In this work, side 2 is chosen to lie parallel to the ξ axis.

3) Normalize the side length and call the new unit vector \hat{e}_ξ . In the case where side 3 is chosen (Vertex 1 - Vertex 2):

$$\hat{e}_\xi = \frac{(V_1 - V_2)}{\|V_1 - V_2\|_2}$$

4) Determine the vector normal to the plane formed by \hat{e}_z and \hat{e}_ξ , and normalize it to form \hat{e}_η .

$$\hat{e}_\eta = \frac{\hat{e}_z \times \hat{e}_\xi}{\|\hat{e}_z \times \hat{e}_\xi\|_2}$$

5) Combining the \hat{e}_ξ , \hat{e}_η , and \hat{e}_z , into a matrix $\langle \hat{e}_\xi, \hat{e}_\eta, \hat{e}_z \rangle^T$, the result is a matrix capable of the rotational transformation of the panel into the new coordinate system:

$$Transformation = \begin{pmatrix} \hat{e}_\xi^x & \hat{e}_\xi^y & \hat{e}_\xi^z \\ \hat{e}_\eta^x & \hat{e}_\eta^y & \hat{e}_\eta^z \\ \hat{e}_{z'}^x & \hat{e}_{z'}^y & \hat{e}_{z'}^z \end{pmatrix}$$

6) In order to meet the requirement that the Panel Centroid (x_c, y_c, z_c) , when transformed to (ξ_c, η_c, z_c) , lie at the origin of the $\xi - \eta$ axis system. In order to have this built into the transformation, the following transformation formula should be used for an arbitrary point, $P(x, y, z)$, to transform it to the new transformed system:

$$P(\xi, \eta, z) = \begin{pmatrix} \hat{e}_\xi^x & \hat{e}_\xi^y & \hat{e}_\xi^z \\ \hat{e}_\eta^x & \hat{e}_\eta^y & \hat{e}_\eta^z \\ \hat{e}_{z'}^x & \hat{e}_{z'}^y & \hat{e}_{z'}^z \end{pmatrix} \cdot \langle P(x, y, z) - (x_c, y_c, z_c) \rangle^T$$

Appendix B

Test Spheres

The following are the test spheres used for the Chapter 5 results section:

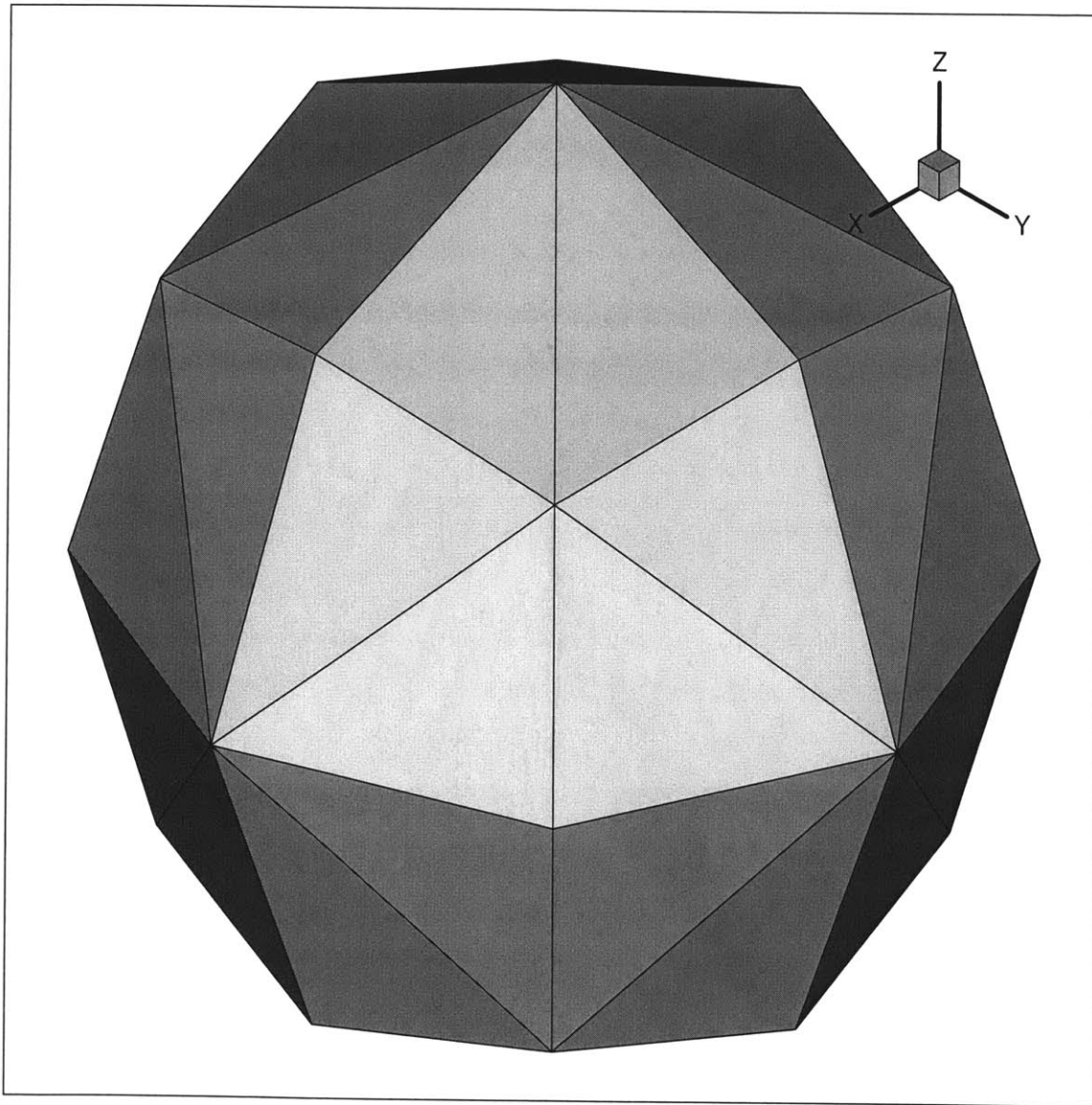


Figure B-1: The discretization of the 48 panel sphere

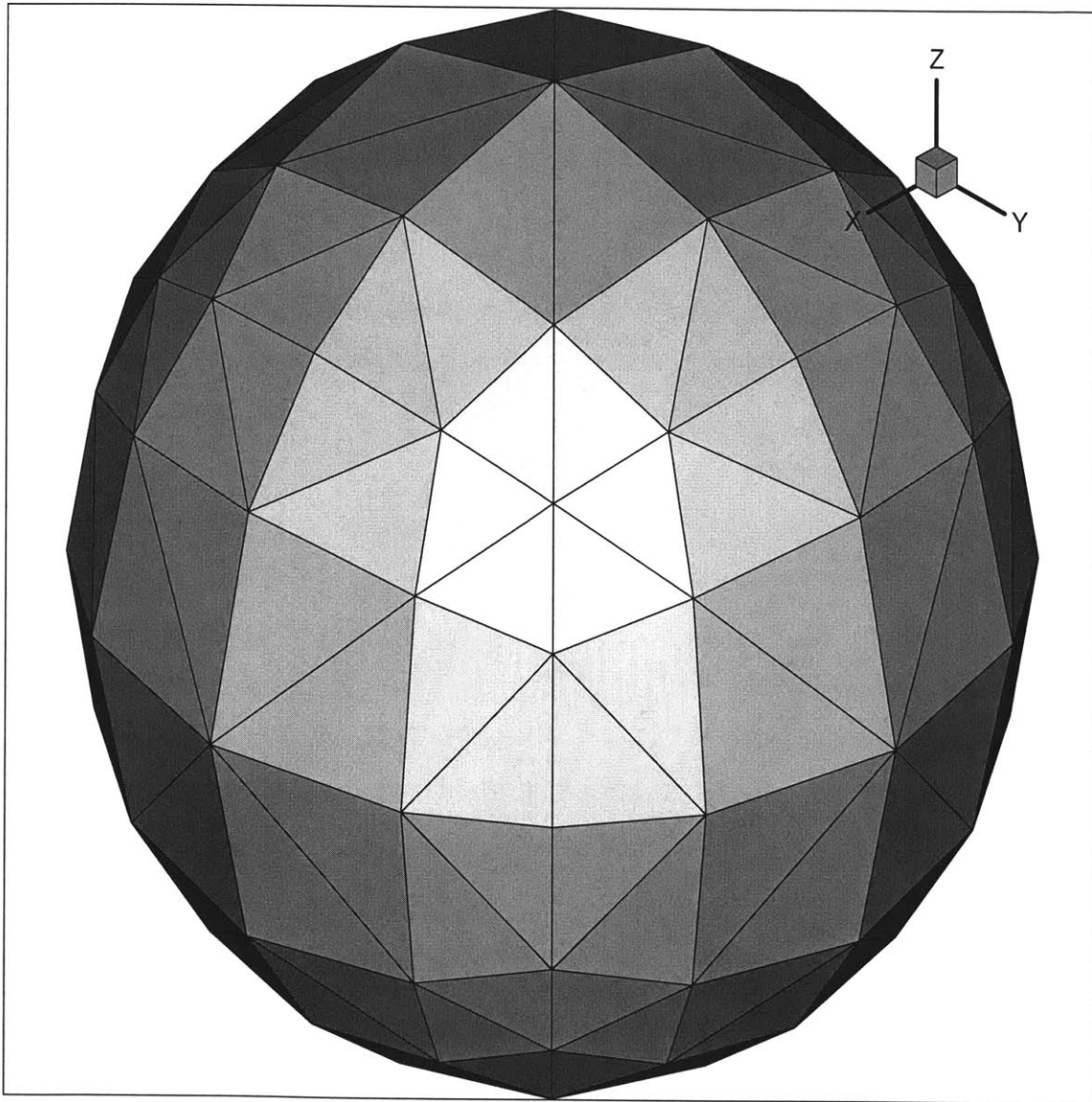


Figure B-2: The discretization of the 192 panel sphere

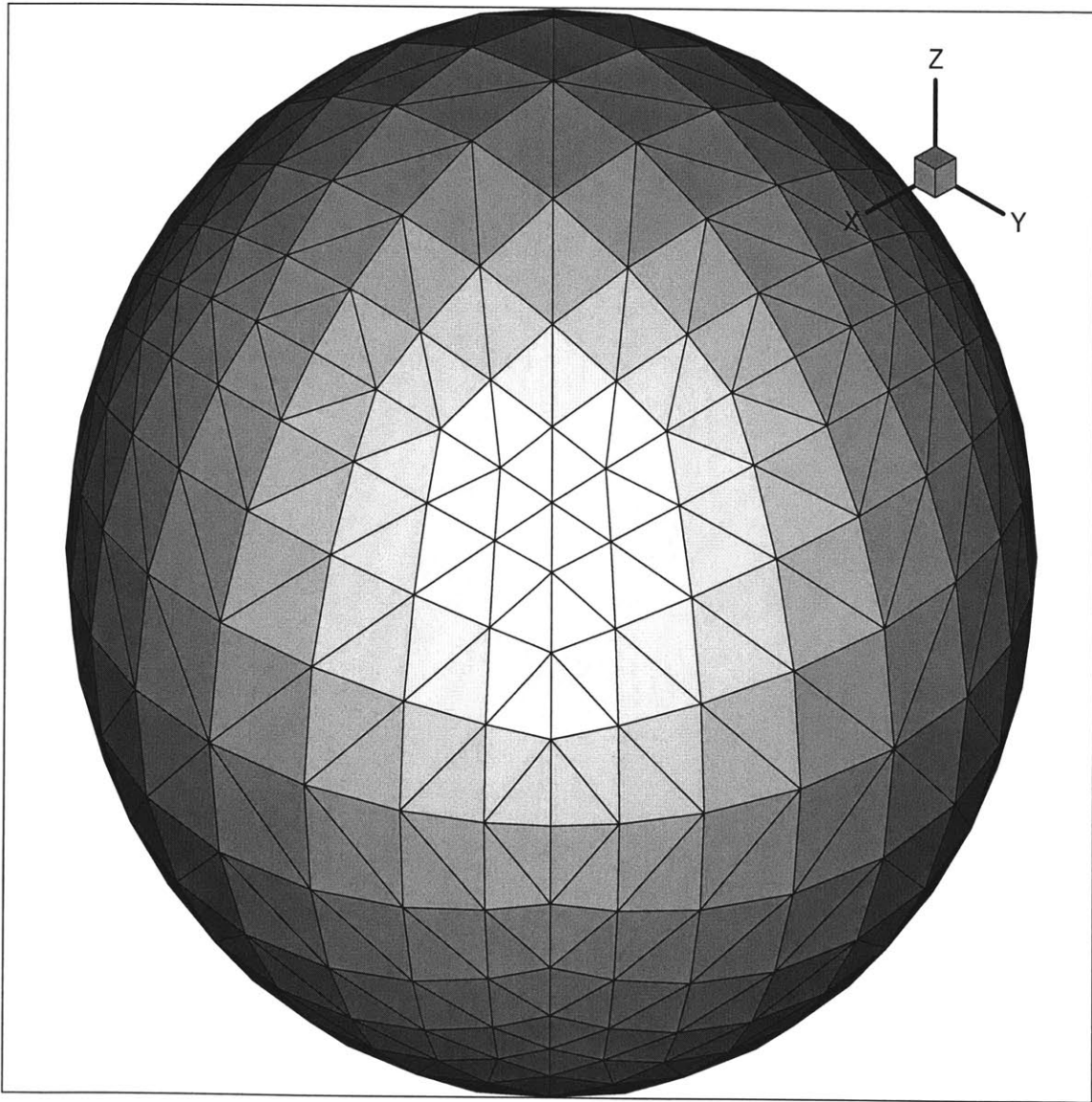


Figure B-3: The discretization of the 768 panel sphere

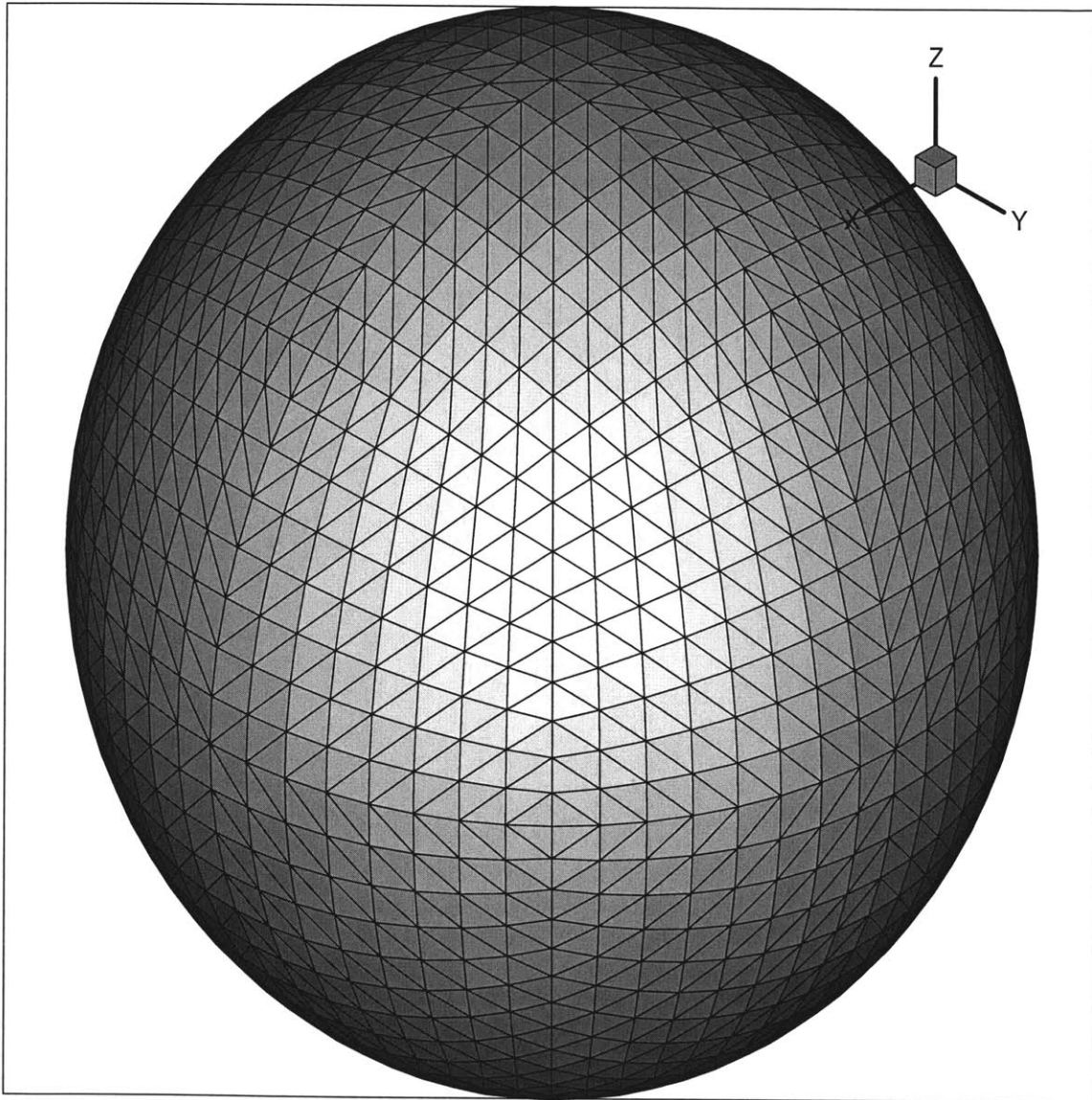


Figure B-4: The discretization of the 3072 panel sphere

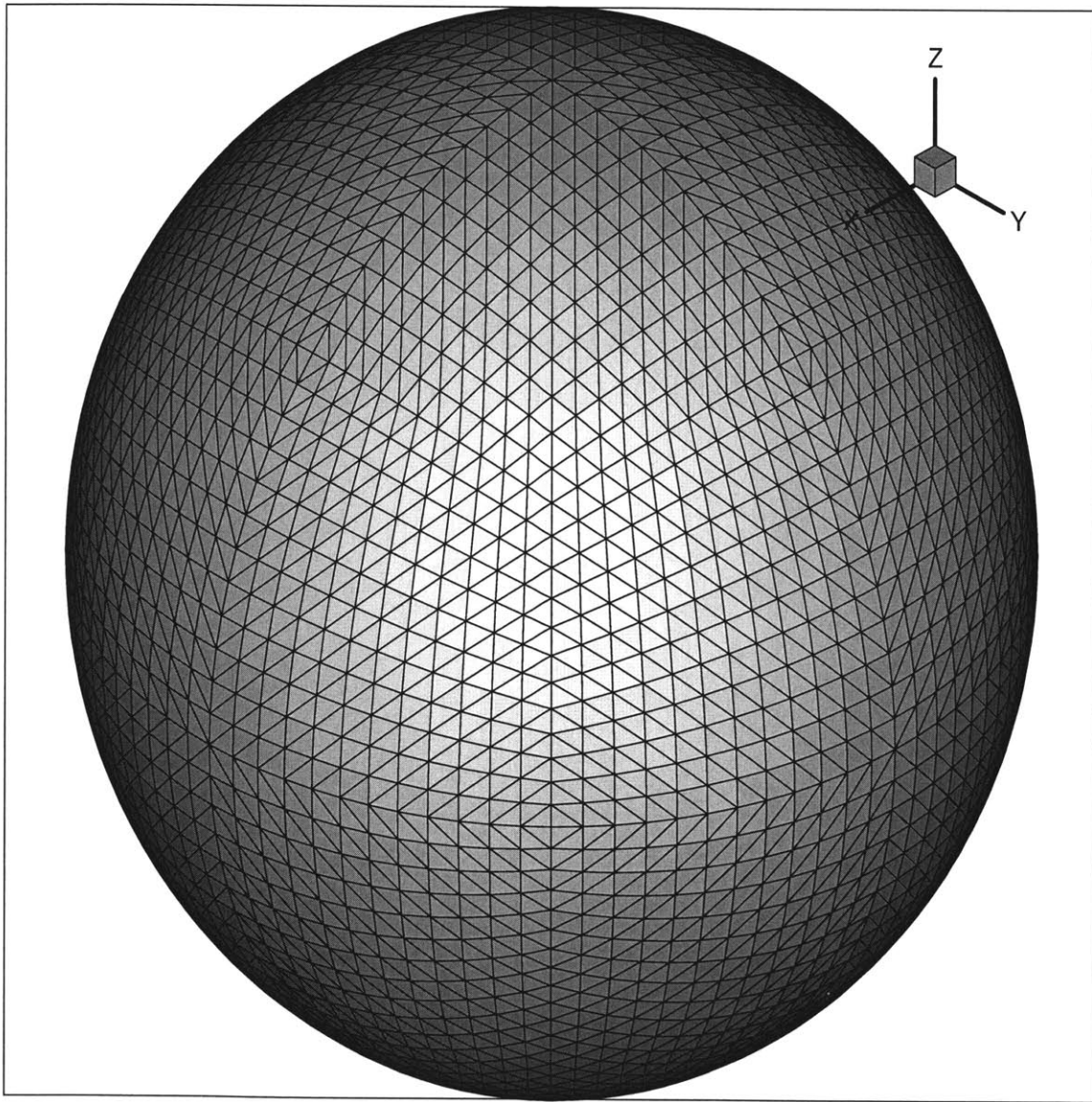


Figure B-5: The discretization of the 6912 panel sphere

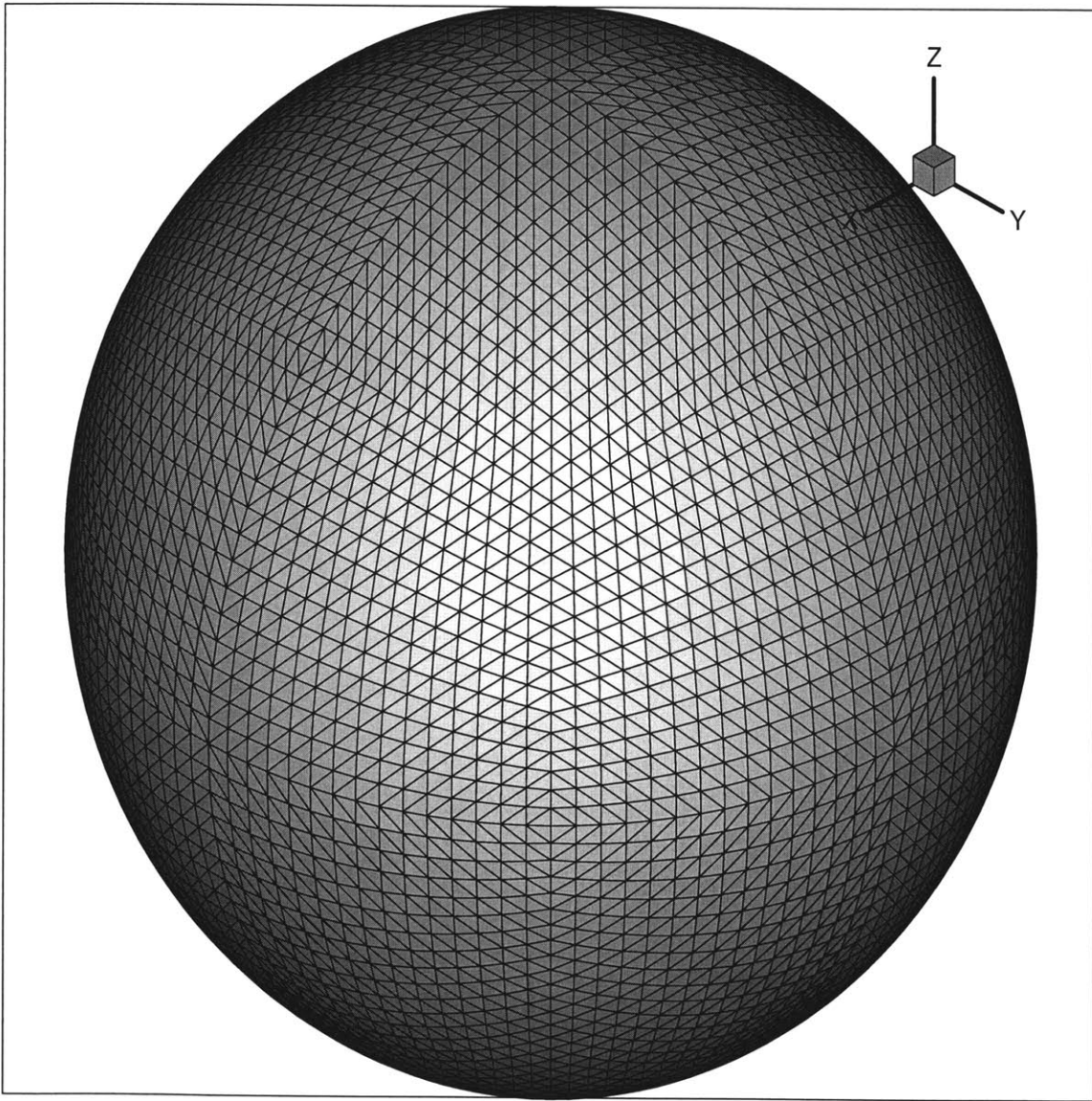


Figure B-6: The discretization of the 10800 panel sphere

Bibliography

- [1] J. D. Anderson. *Fundamentals Of Aerodynamics*. McGraw-Hill, Inc., New York, second edition edition, 1991.
- [2] J. Zhou G. Chen. *Boundary Element Methods*. Academic Press, San Diego, 1992.
- [3] P. K. Kythe. *An Introduction to Boundary Element Methods*. CRC Press, Boca Raton, 1995.
- [4] K.E. Atkinson. Numerical solution of boundary integral equations. *The State of the Art in Numerical Analysis*, 223.
- [5] J.K.White. Panel transform procedure: From 16.910j mit course. Computer code extraction.
- [6] A.M.O. Smith J.L. Hess. Calculation of potential flow about arbitrary bodies. *Progress in Aernautic Sciences*, 8.
- [7] J.N. Newman. Distribution of sources and normal dipoles over a quadrilateral panel. *Journal of Engineering Mathematics*, 20.
- [8] A. Plotkin J. Katz. *Low-Speed Aerodynamics*. Cambridge University Press, New York, second edition edition, 2001.
- [9] J.K. White Z. Zhu, B. Song. pfft++ : An accelerated fast matrix vector program. A constant collocation method implemented in C++. A Computational Prototyping Laboratory Internal Code.

- [10] J.K. White Z. Zhu, B. Song. Algorithms in fastimp: A fast and wideband impedance extraction program for complicated 3-d geometries. to be submitted to IEEE Trans. on Microwave Theory and Techniques.
- [11] M. Drela. Xfoil: An analysis and design system for low reynolds number airfoils. *Conference on Low Reynolds Number Airfoil Aerodynamics*, 1989.
- [12] A.M.O. Smith. The panel method: Its original development. *Progress in Astronautics and Aeronautics*, 125, 1990.
- [13] R.M. Coopersmith H.H. Youngren, E.E. Bouchard and L.R. Miranda. Comparison of panel method formulations and its influence on the development of quadpan, an advanced low order method. *AIAA-83-1827*.
- [14] B. Maskew. Program vsaero – a computer program for calculating the non-linear aerodynamic characteristics of arbitrary configurations: User’s manual. *NASA CR-166476*, 1982.
- [15] A. E. Magnus and M. A. Epton. Pan air-a computer program for predicting subsonic or supersonic linear potential flows about arbitrary configurations using a higher order panel method. *NASA CR-3251*, 1980.
- [16] Dudley M.R. Iguchi S.K. Browne L. Katz J. Ashby, D.L. Potential flow theory and operational guide for the panel code pmarc-12,. *COSMIC Program ARC-13362*, 1992.
- [17] C.H. Berdahl W.Z. Strang. Evaluation of four panel aerodynamic prediction methods (mcaero, pan air, quadpan, and vsaero). *AIAA-85-4092*.
- [18] W.L. Sellers III C.E.K. Morris Jr. K.B. Walkley E.W. Shields R.J. Margason, S.O. Kjelgaard. Subsonic panel methods – a comparison of several production codes. *AIAA-85-0280*.
- [19] J.L.Hess. Linear potential schemes. *Progress in Astronautics and Aeronautics*, 125, 1990.

- [20] B.W. McCormick. *Aerodynamics, Aeronautics, and Flight Mechanics, 2nd Ed.* Wiley, New York, 1995.
- [21] H. Schlichting. *Boundary Layer Theory.* McGraw-Hill Publishing Co., New York, 1979.
- [22] M.B. Giles M. Drela. Viscous-inviscid analysis of transonic and low reynolds number airfoils. *AIAA Journal*, 25.
- [23] V. Rokhlin. Rapid solution of integral equations of classical potential theory. *Journal of Computational Physics.*
- [24] L. Greengard. *The Rapid Evaluation of Potential Fields in Particle Systems.* MIT Press, Cambridge, 1988.
- [25] J.K.White K. Nabors. Fastcap: A multipole accelerated 3-d capacitance extraction program. *IEEE Transactions On Computer-Aided Design of Integrated Circuits and Systems*, 10.
- [26] L. Fornasier. Hisss - a higher-order subsonic/supersonic singularity method for calculating linearized potential flow. *AIAA-84-1646.*
- [27] T.R.Quackenbush A.H. Boschitsch, T.B. Curbishley and M.E. Teske. A fast panel method for potential flows about complex geometries. *AIAA-96-0024.*
- [28] J.C. Vassberg. A fast surface-panel method capable of solving million-element problems. *AIAA-97-0168.*
- [29] J.K. White J. R. Phillips. A precorrected-fft method for electrostatic analysis of complicated 3-d structures. *IEEE Transactions On Computer-Aided Design of Integrated Circuits and Systems*, 16.
- [30] J.K.White N.R. Aluru, V.B. Nadkarni. A parallel precorrected fft based capacitance extraction program for signal integrity analysis. *33rd Design Automation Conference*, 1996.

- [31] X. Wang W. Ye and J. White. A fast stokes solver for generalized flow problems. *International Conference on Modeling and Simulation of Microsystems, Semiconductors, Sensors and Actuators*, 2000.
- [32] Bruce Tidor Jacob K. White Michael D. Altman, Jaydeep P. Bardhan. Fast methods for simulation of biomolecule electrostatics. *ICCAD – 2002 Conference*, 2002.
- [33] V.Zolotov K. Gala R. Panda S.S.Sapatnekar H. Hu, D.T. Blaauw. A precorrected-fft method for simulating on-chip inductance. *ICCAD – 2002 Conference*, 2002.
- [34] C.H. Lee J.N.Newman. Boundary-element methods in offshore structure analysis. *20th International Conference on Offshore Mechanics and Artic Engineering*, 2001.
- [35] F. M. White. *Fluid Mechanics*. McGraw Hill Inc., New York, third edition edition, 1994.
- [36] W. D Ramsey. Boundary integral methods for lifting bodies with vortex wakes, 1996.
- [37] J.D. Jackson. *Classical Electrodynamics, Third Edition*. John Wiley and Sons Inc., New York, 1998.
- [38] O.D.Kellogg. *Foundations of Potential Theory*. Ungar, New York, 1929.
- [39] L.L. Erickson. Panel methods – an introduction. *NASA Technical Paper 2995*.
- [40] L. Morino. *Steady, Oscillatory and Unsteady Subsonic and Supersonic Aerodynamics–Production Version (SOUSSA)*. nasa cr-157130, 1980.
- [41] J. Peraire. Geometry from felissa grid generation tools. Geometry obtained from a volume F-18 discretization from Felissa.
- [42] M. Schultz Y. Saad. Gmres: A generalized minimal residual algorithm for solving nonsymmetric linear systems. *SIAM, Journal of Sci. Stat. Comput.*, 7.

- [43] J.W. Turkey J.W. Coolet. An algorithm for the machine computation of complex fourier series. *Math. Comp.*, 19.
- [44] J.N. Newman X. Wang and J. White. Robust algorithms for boundary element integrals on curved surfaces. *International Conference on Modeling and Simulation of Microsystems, Semiconductors, Sensors and Actuators*, 2000.
- [45] J.M. Luckring J.L. Thomas and W.L. Sellers III. Evaluation of factors determining the accuracy of linearized subsonic panel methods. *AIAA-83-1826*.
- [46] J.R. Phillips. Error and complexity analysis for a collocation-grid-projection plus precorrected-fft algorithm for solving potential integral equations with laplace or helmholtz kernels. *Proceedings 1995 Copper Mountain Conference Multigrid Methods*, 1995.
- [47] A. E. Von Doenhoff I. H. Abbott. *Theory Of Wing Sections*. Dover Publications Inc., New York, 1959.
- [48] B.D. Wood T.W. Chiu, C.A.M. Broers and A.H. Berney. The application of modern panel method techniques to sport aero/hydrodynamics. *AIAA-95-2210*.
- [49] R.M. Coopersmith C.O. Adler. Development of a hydrodynamic free surface capability in a low order aerodynamic panel method. *AIAA-83-1827*.